GRAVITATIONAL RADIATION DETECTABILITY OF THE SUPERNOVA 1987A 'S REMNANT FULLY MATCHED FILTER FOR DOUBLE RESONANT GRAVITATIONAL DETECTOR

A Dissertation
Submitted to the Graduate Faculty of the
Louisiana State University and
Agricultural and Mechanical College
in partial fulfillment of the
requirements for the degree of
Doctor of Philosophy

in

The Department of Physics and Astronomy

by
Giovanni Santostasi
B.S., Maharishi International University, 1995
M.S., Louisiana State University, 1999
May, 2003

DEDICATION

I dedicate this work to my parents Saverio Santostasi and Iolanda Mule'-Santostasi, and my son Saverio. Angelina was my guardian angel all along.

ACKNOWLEDGMENTS

Many people played a fundamental role in helping me to accomplish the task of writing this dissertation. Foremost my thesis advisor Professor Johnson. Professor Johnson has been a precious mentor. I truly admire his well-rounded knowledge in every subject of Physics and many other areas of knowledge. Above all I am very fortunate to have him share with me his great wisdom about life in general. I'm very grateful to Professor Tohline: I thank him deeply for his continuous and contagious enthusiasm for every astronomical subject we discussed, his patience and tolerance for my shortcomings, and his example in professionalism and responsibility required to be successful in life and in particular in the academic environment. I would like to extend my infinite thanks to Professor Bill Hamilton for his financial support during my years of graduate studies. Many thanks to all the teachers of the LSU's Physics Department from which I took courses or I have received guidance: in particular Professor Juhan Frank, I am in awe how he always appears to be a live encyclopedia of Astronomy. I also learned from him what it means to be a rigorous thinker. Also, I would like to mention Professors Svoboda, O'Connell, and Browne.

TABLE OF CONTENTS

LIST OF TABLES

LIST OF FIGURES

ABSTRACT

Part I

There is some observational evidence of the presence of a pulsating light source in the remnant of the supernova (SN) 1987A [1]. This source is considered to be a rotating neutron star. Fourier analysis of the light intensity of this source reveals a main narrow frequency peak and sidebands that are understood as a modulation of the main sinusoidal signal. A particular model of the neutron star invokes a precessing object to explain the modulation. From the Fourier spectrum of the source and changes in the frequency value, we can determine important parameters of the spinning neutron star as rotation frequency, precession frequency and spin down rate. The neutron star is believed to spin down due to the emission of gravitational waves. We give a precise calculation of the strain value of the gravitational waves reaching earth and discuss the possibility of detection of this radiation by existing and soon on line gravitational waves detectors. Our conclusion is that just a few days of integration time will be sufficient to detect the signal using the next generation detectors as LIGO II.

Part II

Historically, in the search for burst signals, the ALLEGRO Gravitational Group used a matched filter constructed in the time domain, and with the particular characteristic of separating the information from the two resonant modes of the bar. The information from the two resonant modes is treated separately until the end when the total energy of the response of the bar is estimated, summing each mode output (we call this filter *partially matched*). We developed a filter (called *fully matched*) that

doesn't separate the two resonant modes and treats the two modes system as a whole. This filter is constructed in the Fourier domain. We compared the performance of partially matched filter with the fully matched filter applying both filters to simulated and real data. The main conclusion is that even in the one mode case, but particularly in the two modes case, the *fast filter* is more efficient than the *slow filter*. In addition, we attempt also to explain why the fully matched is a better filter than the partially matched filter.

PART I
GRAVITATIONAL RADIATION DETECTABILITY OF SUPERNOVA 1987A'S REMNANT

CHAPTER 1
GENERAL INTRODUCTION TO GRAVITATIONAL WAVES AND NEUTRON STAR ASTRONOMY

1.1 General Relativity and Gravity Waves

Gravitational waves are perturbations in the structure of the space-time that are a consequence of the geometrical formulation of gravity by A. Einstein called General Relativity.

The fundamental idea that is at the core of General Relativity is the **equivalence principle**.

This very general principle of physical law is based on the common observation that inertial mass is identical in all the possible experiments to the gravitational mass. Since the time of Galileo and Newton this was considered an experimental fact that is the starting point of the most basic discussion of the physical reality. Einstein in search for a most basic point of view to describe the laws of physics used the identification of inertial mass with gravitational mass to formulate the equivalence principle. It comes in two forms [2]:

The weak equivalence principle:

In a gravitational field a free falling observer will not be able to experience gravitational effects locally. The space time of the observer will be a special relativistic frame, or an inertial one.

The strong equivalence principle

The laws of physics are the same in a free falling frame as if in the absence of gravity.

This form of the equivalence principle is very powerful because it allows us to deduce the correct laws of physics once they are expressed in the special relativistic form. The generalization of the laws can be achieved by describing what an observer in free fall will observe.

The equivalence principle can be used in this way to derive the main laws of General Relativity.

Let's start with a free falling observer that chooses a special relativistic frame ζ^μ, locally we have that:

$$\frac{d^2\zeta^\mu}{d\tau^2} = 0, \zeta^\mu = (ct, x, y, z) \tag{1.1}$$

this is the application of the equivalence principle, that says that a free falling frame doesn't experience the acceleration due to gravity. The relevant space-time is that described by Minkowsky:

$$c^2 d\tau^2 = \eta_{\alpha\beta}\, d\zeta^\alpha d\zeta^\beta, \tag{1.2}$$

where $\eta_{\alpha\beta}$ =diag(1,-1,-1,-1). Any transformation to another frame will obey the transformation:

$$d\zeta^\mu = \frac{\partial \zeta^\mu}{\partial x^\nu} dx^\nu \tag{1.3}$$

Substituting this last expression in the previous equations gives us the main equations of motion in General Relativity:

$$\begin{aligned} \frac{d^2x^\mu}{d\tau^2} + \Gamma^\mu_{\alpha\beta}\frac{dx^\alpha}{d\tau}\frac{dx^\beta}{d\tau} &= 0 \qquad (1.4)\\ c^2 d\tau^2 &= g_{\alpha\beta}\, dx^\alpha dx^\beta, \end{aligned}$$

where:

$$\begin{aligned} \Gamma^{\mu}_{\alpha\beta} &= \frac{\partial x^{\mu}}{\partial \zeta^{\nu}} \frac{\partial^2 \zeta^{\nu}}{\partial x^{\alpha} \partial x^{\beta}}, \\ g_{\mu\nu} &= \frac{\partial \zeta^{\alpha}}{\partial x^{\mu}} \frac{\partial \zeta^{\beta}}{\partial x^{\nu}} \eta_{\alpha\beta} \end{aligned} \tag{1.5}$$

We need to find a set of equations that describe the field laws of gravity and will respect such transformations. We are looking for some similarity with electromagnetism. Consider the Maxwell equation:

$$\Box A^{\mu} = \mu_0 J^{\mu}, \tag{1.6}$$

In this case the 4-current acts as a source for the electromagnetic potential. A parallel can be searched for the case of gravity fields if we recognize matter as a source. Then we can suppose that (at least as a limit for the weak-field case) there is a potential that obeys a law of the type:

$$\Box \phi^{\mu\nu} = k T^{\mu\nu}, \tag{1.7}$$

where k is some constant and $T^{\mu\nu}$ is the energy-momentum tensor. The energy-momentum tensor is the tensorial equivalent of the 4-current in electromagnetism. In fact we can draw a parallel between conservation of charge:

$$\partial_{\mu} J^{\mu} = \dot{\rho} + \boldsymbol{\nabla} \cdot \mathbf{j} \tag{1.8}$$

and conservation of mass:

$$\partial_{\nu} T^{\mu\nu} = 0 \tag{1.9}$$

Intuition suggests that the potential ϕ should be associated with the metric tensor defined $g_{\mu\nu}$ above. In fact in the case of a stationary particle in a stationary

field we should have that:

$$\ddot{x}^i = -c^2\Gamma^i_{00} = 0 \tag{1.10}$$

where $\Gamma^i_{00} = g^{\nu i}(0 + 0 - \partial g_{00}/\partial x^\nu)/2$. Therefore in this limit the equation of state is:

$$\ddot{\mathbf{x}} = -\frac{c^2}{2}\boldsymbol{\nabla} g_{00} \tag{1.11}$$

This means that, considering the analogy with the Maxwell equations in electromagnetism, we are looking for a tensor that contains second derivatives of the metric and that will reduce to equation 11.1 in the weak field limit. Differential geometry tells us that such quantity exists and it is unique, it is called the Riemann tensor $R^\mu_{\alpha\beta\gamma}$:

$$R^\mu_{\alpha\beta\gamma} = \frac{d\Gamma^\mu_{\alpha\gamma}}{dx^\beta} - \frac{d\Gamma^\mu_{\alpha\beta}}{dx^\gamma} + \Gamma^\mu_{\sigma\beta}\Gamma^\sigma_{\gamma\alpha} - \Gamma^\mu_{\sigma\gamma}\Gamma^\sigma_{\beta\alpha} \tag{1.12}$$

It can be contracted to give the Ricci tensor $R_{\alpha\beta}$ and the curvature scalar R :

$$R_{\alpha\beta} = R^\mu_{\alpha\beta\mu}, \quad R = R^\mu_\mu = g^{\mu\nu}R_{\mu\nu} \tag{1.13}$$

The Einstein tensor $G^{\mu\nu}$:

$$G^{\mu\nu} = R^{\mu\nu} - \frac{1}{2}g^{\mu\nu}R \tag{1.14}$$

has the important property that is covariant divergence is zero:

$$\frac{DG^{\mu\nu}}{dx^\nu} = \frac{dG^{\mu\nu}}{dx^\nu} + \Gamma^\mu_{\alpha\nu}G^{\alpha\nu} + \Gamma^\nu_{\alpha\nu}G^{\mu\alpha} = 0 \tag{1.15}$$

From the mass conservation equation we know that the energy-momentum tensor has zero covariant divergence so this leads us to the General Relativity field equations:

$$G^{\mu\nu} = \frac{-8\pi G}{c^4}T^{\mu\nu}. \tag{1.16}$$

The constant is chosen to give the correct answer for the Newtonian, weak field limit case.

1.2 Weak Fields

In the majority of the astrophysical applications, General Relativity can be approximated to almost its Newtonian limit. In particular this approach allows us to predict the existence of gravitational radiation in the case of a slowly moving source. Let's assume that the metric is almost the Minkosky metric and let's add a quantity $h^{\mu\nu}$ to it as a small perturbation:

$$g^{\mu\nu} = \eta^{\mu\nu} + h^{\mu\nu},\ h^{\mu\nu} \ll 1 \tag{1.17}$$

When we are calculating first order effects in $h^{\mu\nu}$ we can use the Minkosky metric instead of the full metric tensor. For example the scalar perturbation h is:

$$h = g_{\mu\nu}h^{\mu\nu} = h^{00} - (h^{11} + h^{22} + h^{33}). \tag{1.18}$$

Then the Ricci tensor $R_{\mu\nu}$ and connection $\Gamma^{\alpha}_{\lambda\mu}$ are:

$$\begin{aligned} R_{\mu\nu} &= \frac{\partial\Gamma^{\beta}_{\gamma\beta}}{\partial x^{\nu}} - \frac{\partial\Gamma^{\beta}_{\mu\nu}}{\partial x^{\beta}} \\ \Gamma^{\alpha}_{\lambda\mu} &= \frac{1}{2}\eta^{\alpha\nu}\left(\frac{\partial h_{\mu\nu}}{\partial x^{\lambda}} + \frac{\partial h_{\lambda\nu}}{\partial x^{\mu}} + \frac{\partial h_{\mu\lambda}}{\partial x^{\nu}}\right) \end{aligned} \tag{1.19}$$

If we define a new field:

$$\overline{h}^{\mu\nu} \equiv h^{\mu\nu} - \frac{1}{2}\eta^{\mu\nu}h. \tag{1.20}$$

we can obtain the field equations in linearized form:

$$\Box\overline{h}^{\mu\nu} = -\frac{16}{c^4}T^{\mu\nu}. \tag{1.21}$$

This is obtained using the gauge condition:

$$\frac{\partial}{\partial x^{\mu}}\overline{h}^{\mu\nu} = 0.$$

In the absence of matter we can have plane waves $\overline{h}^{\mu\nu} \propto \exp(i\mathbf{k}\cdot\mathbf{x} - kct)$; this is equivalent to the electromagnetic case, and the source of gravity is matter, and if we indicate the retarded source with brackets we have:

$$\Box\overline{h}^{\mu\nu} = \frac{4G}{c^2}\int \frac{[T^{\mu\nu}]}{|\mathbf{r}-\mathbf{r}'|}d^3r' \tag{1.22}$$

The wave equations should be solved independently for each component of the energy-stress tensor.

1.3 Gravitational Waves

1.3.1 The Strain h We have seen in the previous section that the field equations of General Relativity predict the existence of waves solutions. These waves are called *Gravitational Waves*. Gravitational Waves are perturbations in space-time that travel at the speed of light. These perturbations will manifest themself as tidal forces that are the true signature of gravity. In Newtonian physics tidal effects can be measured as the relative acceleration of two test particles separated by a distance $\mathbf{X}$:

$$X_i = -\frac{\partial^2\boldsymbol{\phi}}{\partial x_i \partial x_j}X_{j,} \tag{1.23}$$

In the relativistic situation we calculate the equivalent of the previous equation that results to be the geodesic deviation:

$$\frac{D^2}{d\tau^2}X^\mu = R^\mu_{a\beta\gamma}\frac{dx^\alpha}{d\tau}\frac{dx^\beta}{d\tau}X^\gamma \tag{1.24}$$

This means that observers will experience the passage of a gravitational wave as the effect of a tidal tensor $\Delta_{\mu\nu}$ of the form:

$$\Delta_{\mu\nu} = R_{\mu\alpha\beta\nu}U^\alpha U^\beta, \tag{1.25}$$

where the U^μ are the 4-velocity of the test particles.

The Riemann tensor can be expressed to first order as:

$$R_{\mu\alpha\beta\nu} = \frac{1}{2}\left(-\partial_\mu\partial_\alpha h_{\nu\beta} - \partial_\nu\partial_\beta h_{\mu\alpha} + \partial_\mu\partial_\beta h_{\nu\alpha} + \partial_\nu\partial_\alpha h_{\mu\beta}\right) \tag{1.26}$$

In the rest frame $U^\mu = (1, 0, 0, 0)$ the tidal tensor reduces to:

$$\Delta_{\mu\nu} = \frac{1}{2}\frac{\partial^2}{\partial t^2} h_{\nu\beta}, \tag{1.27}$$

Then we can obtain many simplifications using the gauge properties and symmetries of the tensors. The quantity $\Delta_{\mu\nu}$ has to be symmetric because of the symmetries of the Riemann tensor. Because the Ricci tensor vanishes outside matter Δ has to be traceless. Using the Transverse Traceless (TT) gauge:

$$h_{\mu 0} = 0, h^\mu_\mu = 0 \tag{1.28}$$

implies $\Delta_{\mu 0} = 0$ and the radiation Lorentz gauge:

$$g^{\mu\nu} = \Gamma^\lambda_{\mu\nu} \tag{1.29}$$

it is equivalent in this case to $\Delta_{\mu\nu}k^\nu = 0$ meaning that the waves are spatially transverse. So there are just two independent parameters; if we choose a frame of reference where the wave travels in $\widehat{z}$ direction we have:

$$\Delta_{\mu\nu} = \begin{pmatrix} 0 & 0 & 0 & 0 \\ 0 & \Delta_+ & \Delta_\times & 0 \\ 0 & \Delta_\times & -\Delta_+ & 0 \\ 0 & 0 & 0 & 0 \end{pmatrix} e^{-ik^\mu x_\mu} \tag{1.30}$$

The Δ_+ refers to the plus polarization of the wave and $\Delta_\times$ refer to the cross polarization, they are displacement patterns related by a rotation of 45°.

1.3.2 The Energy of Gravity Waves To calculate the energy emitted by a source we have to look to a second order expansion of the field equation. In fact, the field equation solution in vacuum gives us $G_{\mu\nu} = 0$. We can split the Einstein tensor in two contributions one of the background $G^B_{\mu\nu}$ and $G^h_{\mu\nu}$ that is the contribution of the wave. The Ricci tensor vanishes in the absence of matter so the contribution of the wave have to be second order:

The effective source term for the wave is then:

$$T^{GW}_{\mu\nu} = \frac{c^4}{8\pi G} G^{(2)}_{\mu\nu}, \tag{1.31}$$

where $G^{(2)}_{\mu\nu}$ indicates second-order contributions.

It turns out that the equivalent for the pointing-vector in General Relativity is:

$$T^{GW}_{\mu\nu} = \frac{c^4}{32\pi G} \left\langle \overline{h}_{\alpha\beta,\mu} \overline{h_{,\nu}}^{\alpha\beta} - \frac{1}{2} \overline{h}_{,\mu} \overline{h}_{,\nu} \right\rangle \tag{1.32}$$

Using the result:

$$\int T^{ij} d^3x = \frac{1}{2} \frac{d^2}{dt^2} \int T^{00} x^i x^j d^3x \tag{1.33}$$

and after some algebra this leads us to the result called the *quadrupole formula,* for the luminosity or energy emitted through gravity waves by a mass source moving non relativistically:

$$L_{GW} = \frac{dE}{dt} = \frac{1}{5} \frac{G}{c^5} \left\langle \dddot{\underline{I}}_{jk} \dddot{\underline{I}}_{jk} \right\rangle \tag{1.34}$$

where the 3-tensor $\underline{I}_{jk}$is the reduced quadrupole moment of the source:

$$\underline{I}_{jk} = \int \rho \left[x_j x_k - \frac{1}{3} \delta_{jk} \left(x^A \right)^2 \right] \tag{1.35}$$

A useful formula to calculate the strain at certain distance r far away from the source in terms of the luminosity L_{GW} is:

$$h \approx \left(\frac{G}{\pi c^3}\right)^{1/2} \frac{L^{1/2}}{f_g r} \sim 1.77 \times 10^{-22} \left(\frac{1kHz}{f_g}\right) \left(\frac{10Mpc}{r}\right) \left(\frac{L}{10^{46}W}\right)^{1/2}. \qquad (1.36)$$

where f_g is the frequency of vibration of the source.

1.4 Neutron Stars

1.4.1 Degenerate Stars and Chandresakar Limit The existence of a star is determined by the balance of two main forces. The gravity of the matter that makes up the star tends to attract the stellar material in a concentrated region. Some form of pressure inside the star tends to balance the attractive force of gravity with a repulsive action. During star formation the heat produced through the collision of the infalling matter tends to counteract the crushing of the star by gravity. This frictional heat does not achieve balance in gas clouds which are bigger than a few tenths of a solar mass. Nuclear fusion reactions get triggered by the high temperature achieved at a certain point in the dense, infalling matter and the heat produced by these reactions stops the inward force of gravity. A star is formed at this point; and this equilibrium situation is maintained for millions to billions of years according to how massive the star is. The star goes through many different cycles of nuclear reactions, burning heavier and heavier elements. The last element that is possible to burn efficiently in the core of the star depends on the mass of the core. For stars that have central masses of around one solar mass the last elements that can be fused are carbon and oxygen. The observed masses and radii of a certain classes of stars demonstrate the existence of other processes that can sustain the

gravity's inward push. White dwarves, for example, are stars that have solar masses and radii of the same order of the radius of the Earth. In this case the observed luminosity and the inferred pressure and temperature of these objects cannot be explained by the presence of nuclear reactions inside the star. The particular quantum properties of the exclusion principle are invoked to explain the relatively low luminosity of white dwarves and their enormous pressure and temperatures. The matter in a white dwarf occupies different quantum states. The electron in the stars's plasma can occupy at most one quantum state because electrons are fermions. In a normal gas there are many possible states so the exclusion principle does play an essential role. In a very cold gas or an almost relativistic gas at high pressure, like in the case of the white dwarf, the exclusion principle becomes dominant. The matter in this particular state is called degenerate. It obeys the laws of Fermi statistics. The physics of a degenerate electron gas shows us that the limiting self-gravitating mass supported by a degenerate electron gas pressure is:

$$M_{Ch} \approx \frac{3\sqrt{2\pi}}{8}\left(\frac{\hbar c}{G}\right)^{3/2}\left[\left(\frac{Z}{A}\right)\frac{1}{m_H}\right]^2 = 8.7\times 10^{32} g = 0.44\ M_\odot \qquad (1.37)$$

A more detailed and precise calculation gives us a mass of 1.4 $M_\odot$. This is called the *Chandresakar limit.*

1.4.2 General Properties of Neutron Stars Many stars die inconspicuous deaths. Very massive ones die with an enormous explosion that teleases an extraordinary quantity of energy. The stars that die in this dramatic way are called supernovae. Supergiant stars at the end of their nuclear reaction burning cycle are the progenitor of the supernovae. If their inner core has more that a certain mass (the Chandrasekar limit, that is about 1.4

solar masses) it will collapse under the force of gravity once the nuclear fuel is exhausted. In the explosion most of the star is dispersed in the interstellar space. The inner core of the star will go through a transformation and become one of two possible astronomical monsters. One of these objects is known as black hole, the other is a neutron star. Shortly after the discovery of the neutron by J. Chadwick in 1932, astrophysicists W. Baade and F. Zwichy claimed that "supernovae represent the transition from ordinary stars to neutron stars, which in the final stages consist of closely packed neutrons". Neutron stars are very dense and compact astronomical objects. Nuclear reactions are not possible anymore in the core of the supernova and so the entire star is under the crush of gravity. The pressure inside the core of the star pushes the electrons to fall on the protons in the nucleus and form neutrons. The inner part of the supernova becomes in effect an 10 Km wide "neutron". In fact, a 1.4 solar mass neutron star (the Chandrasekar limit can be considered as a good estimate for neutron star masses) will consist of 1.4 $M_\odot/m_n \approx 10^{57}$ neutrons or equivalently a giant nucleus with mass number $A \approx 10^{57}$. The binding force in this nucleus is gravity and the supporting force is neutron degeneracy pressure. In fact, neutrons are fermions and obey the exclusion principle and the Fermi statistics. Applying the laws of Fermi statistics to the neutron star then it is possible to estimate that the radius of a neutron star should be:

$$R_{ns} = \frac{(18\pi)^{2/3}}{10} \frac{\hbar}{G M_{ns}^{1/3}} \left(\frac{1}{m_H}\right)^{8/3} \tag{1.38}$$

Neutron stars are almost relativistic objects. In fact, the ratio of the Newtonian potential energy to the relativistic rest energy is:

$$\frac{GM_{ns}m/R_{ns}}{mc^2} = 0.207 \tag{1.39}$$

The black body luminosity of the 1.4 $M_\odot$ neutron star is derived from the Stefan-Boltzmann law:

$$L = 4\pi R^3 \sigma T_e^4 = 7.13 \times 10^{32} erg\ s^{-1} \tag{1.40}$$

Even if this is similar to the luminosity of the sun the main emission wavelength of the thermal radiation is in the x-rays part of the spectrum in this case:

$$\lambda_{\max} = \frac{\left(5000\ \mathring{A}\right)(5800\ K)}{T} = 29\ \mathring{A} \tag{1.41}$$

1.4.3 The Structure of a Neutron Star The structure of the neutron star will be made of several differentiated levels. It is possible that a neutron star has an atmosphere of ionized particles and electrons. The surface of the star is composed by nuclei of iron. Iron is the last element produced by nucleosynthesis in a star. In fact, any heavier element requires energy to participate in the process of fusion rather than of liberating energy. In old stars iron is left as the final ash of the process of nucleosynthesis and it is found in their core. Because neutron stars are formed by the inner part of a star that exhausted its nuclear fuel, iron and in particular ^{56}Fe is the most abundant element in the outer layers of the neutron star.

One of the most interesting characteristics of neutron stars is that they have a solid crust. The nuclear material in the outer layer of the star is highly ionized and the

lowest energy configuration for electrical charges is a reticular, crystalline lattice. In between the spacing of this reticular structure there is a sea of electrons in a degenerate state. The thickness of the crust could vary from hundreds of meters, in high density neutron stars, to a few kilometers, in stars that have lower density than average. Typical density of the crust is $\rho \approx 10^8$ g/cm^3. Beyond the crust, the density is so high that it becomes possible to trigger the process of neutronization, or inverse β process.

A free neutron is unstable and decays trough the reaction called β decay:

$$n \rightarrow p^+ + e^- + \overline{v}_e \tag{1.42}$$

The density of the inner layers of the neutron star is so high that nearly free electrons are "squeezed on" the protons through the reaction of electron capture:

$$p^+ + e^- \rightarrow n + \nu_e \tag{1.43}$$

This process is a stable one; in fact the neutron doesn't decay because the electrons occupy all the lowest energy states as a consequence of their degeneracy. This creates greater and greater abundance of neutrons *(neutronization)* in the star material 's nuclei as the density increases with depth. At even higher depths inside the neutron star the nuclei are compressed by gravity to be closer and closer until there is a spontaneous release of neutrons by the nuclei. This phenomenon is called *neutron drip.* Finally, the free neutrons start to be so close to each other that they loose their individual identity and they become an undifferentiated highly relativistic gas. The thickness of this last layer should not be more than a few kilometers and its density should be around $\rho \approx 10^{14}$ g/cm^3. The innermost part should constitute a superfluid

of neutrons (in a space of about 10 kilometers) that, speculatively, becomes a solid sphere of a few kilometers diameter with a density of $\rho \approx 10^{15}$ g/cm^3 at the very core of the neutron star.

CHAPTER 2
FREE PRECESSION IN NEUTRON STARS

2.1 Free Precession in Rigid Bodies

When a rigid body undergoes rotation its spin axis will not stay fixed in space if the total angular momentum is not parallel to the spin axis. This motion is called *free precession.*

The term free refers to the fact that all the forces and torques on the rotating body are internal, there are, in other words, not external influences. In the case where external forces are present the precession is called forced.

Free precession is a classical phenomenon discussed in all introductory mechanics textbooks, describing the property and dynamics of rotating bodies as spinning tops and gyroscopes. Gyroscopes are man-made objects that are very useful for missile and satellite navigation. The study of their behavior is an application of the physics of rotating rigid bodies.

Free or forced precession is known to occur also in natural events. For example the interesting phenomenon of Nuclear Magnetic Resonance (that has important medical applications) is due to the precession of the spin of the nuclei interacting with external magnetic fields. Because spin precession is influenced by the characteristics of the surrounding material, nuclear magnetic resonance is a very good tool to create tridimensional images of living tissues in the human body in a non-invasive way.

2.2 Free Precession in Astronomy

Other examples of free precession occurring in Nature happen in astronomical events. Celestial objects that possess a certain rigidity as planets can undergo free precession. The Earth itself undergoes different types of precession. Probably other solid planets precess yet we don't have enough accurate information on their rotation motion. The majority of stars are fluid systems so they can rotate but they do not precess. In fact you need a rigid body (or at least a body with some level of elasticity) to sustain deformation that are not symmetric with the angular momentum vector.

Neutron stars are quite unique among stars in that they have a possible solid crust. This creates the condition for them to precess. The possibility of free precessing neutron stars was contemplated, as soon as the first models of neutron stars with a solid crust were formulated. Indeed, this possibility has been discussed by various authors [3-4].

The existence of precessing neutron stars has important implications for gravitational wave astronomy. In fact, a precessing neutron star requires a certain ellipticity that is not symmetric with the axis of rotation. This implies a changing mass quadrupole that is the requirement for production of gravitational waves.

Relevant to the purpose of this dissertation is in particular the early work of M. Zimmerman [5-6] on the emission of gravitational waves by a free precessing neutron star. In a series of papers Zimmerman derives, using the quadrupole formalism, formulas describing the emission of gravitational radiation by a precessing neutron star. The papers'discussion starts with the simple case of an axisymmetric rigid body and

it gets broadened to the more general case of a triaxial body. Zimmerman also shows that, with due modifications, the radiation formulas derived apply to a non rigid body. Previously to Zimmerman's work (see for example [7]), rotating neutron stars were considered possible continuous sources of gravitational radiation. Mainly discussed was the case of a triaxial object with its rotation and symmetry axis aligned. If the rotation axis is also a symmetry axis the star needs to be triaxial to emit gravitational waves. The centrifugal forces will increase the moment of inertia along the axis of rotation. This deformation will not cause any gravitational wave emission because it doesn't create a changing mass quadrupole. It is necessary to have a further deformation of the star that gives a difference between the moments of inertia along axes perpendicular to the rotation axis. So the object has three different moments of inertia. This makes it a triaxial object. In that case the gravitational radiation is at twice the frequency of rotation. An important quantity in this context is the *ellipticity*, i.e. the fractional difference between the moments of inertia, associated with the axis in the plane perpendicular to the axis of rotation. Looking at the spin down of known pulsars it is possible to determine an upper limit for the ellipticity if one assumes that the spin down is due mainly to loss of rotational energy through gravitational wave emission. We know though, that in most of the cases of known pulsars, the spin down is due mainly to electromagnetic emission. Therefore it is difficult to estimate the level of triaxiality of neutron stars, that are supposed to be quite undeformable objects because of the great strength of their gravitational fields. It is also difficult to envision physical mechanisms that will give triaxiality to these objects even if there is some literature on the subject

[8]. Therefore we are not certain of the possible intensity of the gravitational waves' radiation of rotating neutron stars in general.

The situation is quite different with free precessing neutron stars. Free precessing neutron stars require, in fact, just a deformation along one axis for gravitational wave emission. For example, electromagnetic forces can give enough of a deformation to the star's crust to make a free-precessing neutron star into a good gravitational wave emitter if the rotation axis is not aligned with the symmetry axis of the star. In fact, for free-precession to happen is necessary a misalignment between the rotation and the symmetry axis. It is easy to show (see Chapter 3) that a biaxial object that precesses has a changing quadrupole. For this reason, the evidence for a precessing neutron star 's existence is very interesting for the detection of gravitational waves. The information on the precession, the rotation period and the rate of spin-down will allow a precise determination of the level of deformation of the star's shape. Furthermore, the fact that the rotation axis and the symmetry axis are not aligned guarantees a changing quadrupole. Knowing the level of deformation will allow, consequently, to estimate the intensity of the gravitational radiation on earth. In other words, observation of free-precession in a neutron star guarantees some amount of gravitational wave emission. The negative side of all this is that even if some theorists envisioned [8-8a-9] processes that can cause this misalignment, it is still difficult to believe that free-precession in neutron stars is a common occurrence. Until very recently, we didn't have any sure example of this phenomenon among the known neutron stars. Nature, like always, presents her surprises. In the recent past different articles report and discuss the

discovery of at least three pulsars that have characteristics that can be interpreted as that of a rotating neutron star undergoing free-precession.

The first article [10] on these free-precessing neutron stars (the radio pulsar PSR B1828-11) appeared in the journal **Nature** in the beginning of August 2000**.** The main signal has pulsation with a period of 405 milliseconds, and it is modulated with a period of one thousand days. It is also possible to observe harmonics of this modulation period at 500 and at 250 days. The authors try to explain these observational facts with different mechanisms, but free-precession seems the simplest and more likely explanation that can fit all the data. The quality and duration of the observation makes the radio pulsar PSR B1828-11 a very solid example of a free-precessing neutron star. Unfortunately, its rotation is too slow for this star to be interesting as a gravitational wave source. Its frequency, and even more, its gravitational output are outside the sensitivity of available and next-generation detectors.

2.3 The Remnant of SN 1987A: A Precessing Neutron Star?

In a recent article Middleditch *et al.* [1] discusses fast photometry observations of the remnant of the supernova 1987A. These observations have being carried out at different times over a period of several years. It is reported that the authors have found "no clear evidence of any pulsar of constant intensity and stable timing," but they claim that : " we have found emission with a complex period modulation near the frequency of 467.5 Hz - a 2.14 ms pulsar candidate". Also, it is pointed out that: "In addition, the frequency of the signals followed a consistent and predictable spin-down (˜2-3 x 10^{-10} Hz/s) over the several year time-span ('92-'96). We also find evidence in data, again

taken by more than one telescope and recording system, for modulation of the 2.14 ms period with a ˜1,000 s period which complicates its detection." This observational information about the modulation of the 2.14 ms period can be interpreted as the effect of precession due to the non-alignment of the symmetry axis of the object (that needs to be at least deformed along one axis, or a spheroid) and the axis of rotation. Classical Mechanics tells us that the ratio between the precession frequency and the rotation frequency is proportional to the size of the deformation [12-16]. The deformation and the frequency of rotation then determine the rate of spin-down if the neutron star is assumed to lose energy due, mainly, to gravitational radiation emission. The authors in fact comment: " The characteristics of the 2.14 ms signature and it ˜1,000 s modulation are consistent with precession and spin-down via gravitational radiation of a neutron star with effective non-axisymmetric oblateness of $\tilde{}10^{-6}$".

There are many problems with the Middleditch *et al.* observations, due probably to the very complex nature of SN 1987A environment, that makes the reality of a pulsar with the described characteristics, at best, very suggestive. We will discuss in Appendix C, in more detail the strength of the observational data and method of analysis. The main approach of this work is to assume for the moment that the data are valid and real within the estimated errors and analyze different consequences from the gravitational wave detection point of view.

In Chapter 3 we show that, if we model the neutron star as a rigid body, we can calculate precisely the wobble angle as a function of a single free parameter: the moment of inertia involved in the precession, given the observational information on

the rotation, precession frequency and the spin-down. Knowledge of the wobble angle is important to calculate the strength of a typical pulsar's gravitational wave radiation at earth. The wobble angle also determines the possible strain on the crust due to the re-arrangement of the centrifugal bulge through the precessional motion. This information on the crust strain can give us important clues on the equation of state of the neutron star material. A more detailed analysis of the implication of the calculation of the wobble angle is given in following chapters. It is also possible to show that the data on the supposed SN 1987A optical pulsar obeys a power 2 law between spin down and precession frequency. That is exactly what theory predicts when it is assumed that the main braking mechanism is gravitational radiation back-reaction. This is considered one of the strongest pieces of evidence in the favor of a precessing neutron star driven by gravitational spin-down interpretation of the observed data. In Chapter 4, we review the observational data on the remnant of SN 1987A and the methods used to process the data. Chapter 5 introduces the simple model of a precessing rigid neutron star and the fundamental equations that describe the motion and the gravitational wave emission of this object. In Chapter 6 we examine the possibility of other mechanisms of decay in comparison to the GW hypothesis and put some limits on the strength of the electromagnetic radiation from the pulsar. In Chapter 7, we will look at more realistic neutron star models, that allow for the presence of an elastic crust and the existence of a fluid interior in the star. We show that the data on the characteristics of the precession and the gravitational wave observation will allows us to gather a wealth of information of the structure and the equation of state of the star. In Chapter

8, we talk about the important problem of the strain on the crust caused by the precessional motion of the centrifugal bulge. This strain is a limit factor for the possible values of the wobble angle that are physically allowed. In Chapter 9, we generalize the problem of a precessing neutron star to the case of a pulsar with three different axes. We show that, given the particular parameters of the SN 1987A remnant, the generalization to the three axes case does not change significantly its gravitational wave output. Our conclusion is that the two axes model is sufficient to reproduce the fundamental behavior of the pulsar in terms of its characteristics as a gravitational wave source. Chapter 10 is a review of the literature on precessing neutron stars. Time scales relevant to the study of precessing neutron stars are calculated in Chapter 11. In Chapter 12 we determine the observability of the gravitational wave signal from SN 1987A remnant with present and soon available technology. Our conclusion is that detectors as LIGO II will be able to see the signal from SN 1987A within a few days up to a few months of integration time according to how much of the star's moment of inertia is involved in the precession motion. This makes SN 1987A a very reliable source of continuous gravitational radiation. According Middleditch *et al.* observations the star is undergoing continuous changes that affect its characteristics as a pulsar. For example characteristics as the frequency, spin down and precession periods are not stable within many decimal places, but rather change. Furthermore the orientation of the source with respect the Earth is unknown. All this represents a moderately difficult problem in data analysis. Fortunately, the location and distance of the source is known; therefore the amount of templates used to look for this source is still quite contained.

We discuss in details the problem of the data analysis for this source in section 12.2. Appendix D will show results of a simulation that tries to reproduce the search of a waveform similar to that of SN 1987A remnant (just more intense in amplitude). We then simulate the response to this signal of a computer generated bar detector similar to ALLEGRO (with similar resonant modes quality factors and noise characteristics) but a resonant frequency exactly at twice the rotational frequency of the star.

CHAPTER 3
GRAVITATIONAL RADIATION FROM A PRECESSING NEUTRON STAR

3.1 Relevant Equations for Energy Loss by Gravitational Radiation

We have seen (Chapter 1) that in a system the energy loss due to gravitational wave emission is:

$$L_{GW} = \frac{dE}{dt} = \frac{1}{5}\frac{G}{c^5}\left\langle \dddot{\underline{I}}_{jk}\dddot{\underline{I}}_{jk}\right\rangle \tag{3.1}$$

where $\underline{I}_{jk}$ is the mass quadrupole moment

$$\underline{I}_{jk} = \sum_A m_A\left[x_j^A x_k^A - \frac{1}{3}\delta_{jk}\left(x^A\right)^2\right] \tag{3.2}$$

An axisymmetric object that rotates around its symmetric axis will not emit gravity waves because it has no time varying quadrupole moment. If we indicate the different principal moments of inertia as I_1, I_2 and I_3 then the object can emit gravity waves if two of the moments of inertia are dissimilar, for example, $I_1 \neq I_2$ and the object rotates around the axis a_3. It is also possible to have gravitational radiation if the two moments of inertia are equal, let's say $I_1 = I_2$ but the object rotates around another axis than a_3. In this case the object will also precess if the spin axis is not a principal axis. In most of the cases when continuous sources of gravity waves are considered, the case of the non-axisymmetric body is what is contemplated [11-13]. The particular case we are interested in, instead, is the axisymmetric or the more general one of a rotating non-axisymmetric body which is rotating along any axis. This is the situation when precession is present. We are going to consider both cases to show differences and similarities.

We follow closely the derivation in the book *Black Holes, White Dwarf and Neutron Stars [14].*

Let's set up a reference frame $x_i^{'}$ that is fixed with the rotating body. The quantity $x_i^{'}$ is related to an inertial frame x_i by a rotation transformation R,

$$x^{'} = Rx \tag{3.3}$$

where

$$R_{ij} = \begin{bmatrix} \cos\phi & \sin\phi & 0 \\ -\sin\phi & \cos\phi & 0 \\ 0 & 0 & 1 \end{bmatrix} \tag{3.4}$$

and $\phi = \Omega t$. The quantity Ω is the angular rotational frequency. When there are not applied torques, we have Ω =constant.

We can express the inertial coordinates as:

$$I = R^T I^{'} R, \tag{3.5}$$

where $I^{'}$ is a diagonal matrix with diagonal elements $I_{1,}I_2$ and I_3. The indexes 1, 2 ,3 indicate components in the body frame and x, y, z are the components in the inertial frame.

Developing the equations we have:

$$I_{xx} = \cos^2\phi I_1 + \sin^2\phi I_2 = \frac{1}{2}\cos 2\phi\,(I_1 - I_2) + \text{constant} \tag{3.6}$$

In the same way it is obtained,

$$I_{xy} \;=\; I_{yx} = \frac{1}{2}\sin 2\phi\,(I_1 - I_2)\,, \tag{3.7}$$

$$I_{yy} = \frac{1}{2}\cos 2\phi\,(I_1 - I_2) + \text{constant},$$

$$I_{zz} = \text{constant},\ I_{xz} = I_{yz} = 0.$$

Because of the fact that:

$$Tr\ I^{'} = Tr\ I = I_1 + I_2 = \text{constant}, \tag{3.8}$$

it is possible to use I_{ij} instead of $\underline{I}_{ij} = -I_{ij} + \delta_{ij} Tr\ I$ in the energy loss formula. Thus

$$\frac{dE}{dt} = -\frac{1}{5}\frac{G}{c^5}\left(\dddot{I}^2_{xx} + \dddot{I}^2_{xy} + \dddot{I}^2_{yy}\right) = -\frac{1}{5}\frac{G}{c^5}\frac{1}{4}\left(2\Omega\right)^6 (I_1 - I_2)^2$$
$$\left(\cos^2\phi + 2\sin^2 2\phi + \cos^2 2\phi\right) = -\frac{32}{5}\frac{G}{c^5}\left(I_1 - I_2\right)^2 \Omega^6. \tag{3.9}$$

If we approximate the object by an ellipsoid with semiaxis a, b and c, then

$$I_1 = \frac{1}{5}M\left(b^2 + c^2\right), I_2 = \frac{1}{5}M\left(a^2 + c^2\right), I_3 = \frac{1}{5}M\left(a^2 + b^2\right) \tag{3.10}$$

When we have small asymmetry, $a \approx b$,we get

$$\frac{dE}{dt} = -\frac{32}{5}\frac{G}{c^5} I_3^2 \varepsilon^2 \Omega^6, \tag{3.11}$$

where the ellipticity ε is defined as:

$$\varepsilon \equiv \frac{a - b}{(a + b)/2} \tag{3.12}$$

The above formulae implies that the radiation is emitted at twice the frequency of rotation $\phi/t = \Omega$ and that the intensity of the radiation is proportional to the square of the non-axisymmetric deformation ε.

Let's analyze the case of a non-rigid body rotating around a non-principal axis. We consider the case of an axisymmetric object for which $I_1 = I_2$. The angular momentum vector $\mathbf{J}$ of this system will be an invariant both in size and direction, so we

choose to align the $\mathbf{e}_z$ axis of the inertial frame with the angular momentum. The transformation from the inertial frame to body frame are given in terms of the Euler angles:

$$R_{ij} = \begin{bmatrix} \cos\psi\cos\phi - \cos\theta\sin\phi\sin\psi & \cos\psi\sin\phi + \cos\theta\cos\phi\sin\psi & \sin\theta\sin\psi \\ -\sin\psi\cos\phi - \cos\theta\sin\phi\cos\psi & -\sin\psi\sin\phi + \cos\theta\cos\phi\cos\psi & \sin\theta\cos\psi \\ \sin\theta\sin\phi & -\sin\theta\cos\phi & \cos\theta \end{bmatrix} \tag{3.13}$$

Solving Euler equations for this system (see Appendix A) shows that the symmetry axis $\mathbf{e}_3$, and the angular velocity vector will rotate about the axis $\mathbf{e}_z$ with constant angular velocity $\dot{\phi}= J/I_3$. The angle θ between the axis of symmetry $\mathbf{e}_3$and the angular momentum is called the *wobble angle;* this is a constant of the motion.

In addition to this motion we have precession. Precession refers to the rotation of the angular velocity vector about $\mathbf{e}_3$ with angular velocity $\dot{\psi}= (I_1 - I_3)\dot{\phi}\cos\theta/I_3$ =constant as observed in the body frame.

We solve equation (3.5) for the moments of inertia and obtain:

$$\begin{aligned} I_{xx} &= I_1\left(\cos^2\phi + \cos^2\theta\sin^2\phi\right) + I_3\sin^2\theta\sin^2\phi \\ &= \frac{1}{2}\left(I_1 - I_3\right)\sin^2\theta\cos^2 2\phi + \text{constant} \end{aligned} \tag{3.14}$$

In a similar way we obtain:

$$\begin{aligned} I_{xy} &= I_{yx} = \frac{1}{2}\left(I_1 - I_3\right)\sin^2\theta\sin 2\phi \\ I_{xz} &= I_{zx} = -\left(I_1 - I_3\right)\sin\theta\cos\theta\sin\phi, \\ I_{yy} &= \frac{1}{2}\left(I_1 - I_3\right)\sin^2\theta\cos 2\phi + \text{constant}, \end{aligned} \tag{3.15}$$

$$I_{yz} = I_{zy} = (I_1 - I_3)\sin\theta\cos\theta\cos\phi,$$

$$I_{zz} = I_3 + (I_1 - I_3)\sin^2\theta = \text{constant}.$$

Using $\phi = \Omega t$ and $\dot{\phi}= \Omega$ =constant, we calculate the energy loss equation:

$$\frac{dE}{dt} = -\frac{1}{5}\frac{G}{c^5}\left\langle \dddot{I}^2_{xx} + \dddot{I}^2_{yy} + 2\,\dddot{I}^2_{xy} + 2\,\dddot{I}^2_{xz} + 2\,\dddot{I}^2_{yz}\right\rangle =$$
$$-\frac{1}{5}\frac{G}{c^5}\left(I_1 - I_3\right)^2\langle\frac{1}{4}\sin^4\theta\left(2\Omega\right)^6\left(2\cos^2 2\phi + 2\sin^2 2\phi\right)$$

$$+2\sin^2\theta\cos^2\theta\;\Omega^6\left(\sin^2\phi + \cos^2\phi\right)\rangle = -\frac{2}{5}\left(I_1 - I_3\right)^2\frac{G}{c^5}\sin^2\theta\;\Omega^6\left(16\sin^2\theta + \cos^2\theta\right). \tag{3.16}$$

These equations show that the radiation emitted by a precessing body is both at the frequency of rotation Ω and at twice the rotation frequency, at 2 Ω. Also we notice that the intensity of the radiation depends on the wobble angle θ. The polar angle indicates the line of sight angle. The energy tensor for gravitational waves can be used to calculate the energy flux for the neutron star gravitational radiation [23]. Starting with the moment of inertia in the traceless gauge I^{TT} we have that the strain h is:

$$h^{TT}_{ab} = \frac{2}{r}\frac{d^2 I^{TT}_{ab}}{dt^2}\left(t - r/c\right) \tag{3.17}$$

where r is the distance of the source from the observer and t is time. The energy-momentum tensor is:

$$T^{GW}_{\alpha\beta} = \frac{1}{32\pi}\left\langle h^T_{\mu\nu,\alpha} h^T_{\mu\nu,\beta}\right\rangle \tag{3.18}$$

In the particular case of the precessing neutron star we have:

$$T_{0r}\left(i,\dot{\phi}\right) = k\frac{\sin^2\theta}{r^2}\left(\sin^2 2i + 4\sin^2 i\right) \tag{3.19}$$

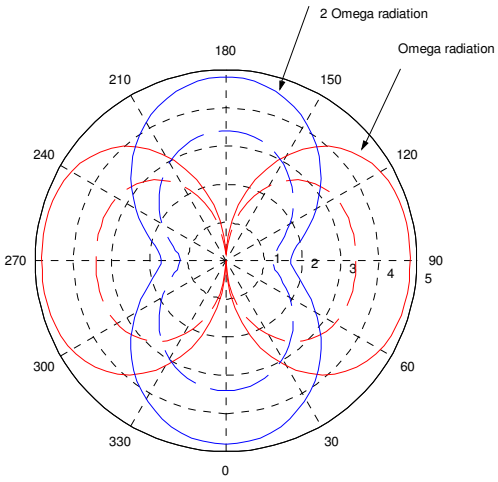

Figure 3.1: The radiation pattern for a precessing neutron star. The angle i is the angle between the source angular momentum and the oberver plane.

for the $\dot{\phi}$ radiation and

$$T_{0r}\left(i,\dot{\phi}\right) = 64k\frac{\sin^4\theta}{r^2}\left\{\left(1+\cos^2 i+4\cos^2 i\right)\right\} \tag{3.20}$$

for the $2\,\dot{\phi}$ radiation. The quantity k is defined as:

$$k = \frac{1}{128\pi}\,\dot{\phi}^{\,6}\,\left(I_{zz}-I_{xx}\right)^2 \tag{3.21}$$

The following Figure is a diagram of the radiation pattern for a source with angular momentum on the y axis, and angle $\theta \approx 30^\circ$.

CHAPTER 4
OBSERVATIONAL DATA ON SN 1987A REMNANT

4.1 The Data

In this section we will summarize Middleditch *et al.*' observations [1]. Since the appearance of the Supernova 1987A there have been attempts to see the signature of a compact remnant in the region near the explosion. The existence of a compact remnant will be revealed by the presence of a pulsating signal somewhere in the electromagnetic spectrum. Middleditch and his collaborators observed the region the sky where the Supernova appeared for many years. They used fast photometry to take measurements of the intensity of light (in the optical and the infrared) coming from that region . That part of the sky is very populated and it was not possible to isolate a star as a candidate pulsar. The light from the region near the explosion was Fourier analyzed and manipulated to bring out eventual signals from the noise (manipulations such as folding certain stretches of Fourier coefficients and adding together harmonics of a particular candidate signal were used). This procedure shows that the frequency around 467.5 Hertz grows over the background noise.

What is even more interesting is the presence of sidebands around the main frequency. These sidebands are equally spaced at 10^{-3} Hertz from the 467.5 Hertz frequency. These sidebands are due to an amplitude and a phase modulation of the main signal. Middleditch and collaborators tried to give possible physical explanation for such modulation. The simplest scenario able to account for the presence of both amplitude and phase modulation is that the neutron star is precessing. A neutron star

Table 4.1: Observational parameters (averages) of the SN 1987A's according Middleditch and alt.

angular frequency ω	2π 467.5 radians / sec
spin down $\dot{\omega}$	2π 2×10^{-10} radians/sec^2
precession frequency Ω_p	$2\pi 10^{-3}$ radians / sec
distance r	50 Kparsec

can precess because of the presence of a solid crust. The sidebands separation from the main rotation frequency is the precession frequency. Figure 4.1 shows a time series of the rotation frequency, derivative of this quantity and the precession frequency.

The change in rotation frequency is due to loss of energy through gravitational wave emission. In fact, a precessing neutron star will emit gravitational waves. Demonstration of this was given in the work of Zimmerman, see for example [5-6]. Using the General Relativity energy loss equation and the Classical Mechanics relationship between ellipticity, rotation and precession frequency we have that the spin-down is proportional to the square of the precession frequency, under the assumption that all the energy is lost due to gravitational back reaction. This will be proved in the following Chapter 5. The Middleditch 's data seems to suggest that there is such relationship between these parameters in the SN 1987A remnant. In fact during the period of observation substantial changes in the precession and spin-down were observed. The values of the spindown and the inverse of the corresponding square of the precession perionds are displayed in Figure 4.2. It can be seen that there is a good linear correlation between these parameters and the linear fit goes through zero. This is what is expected

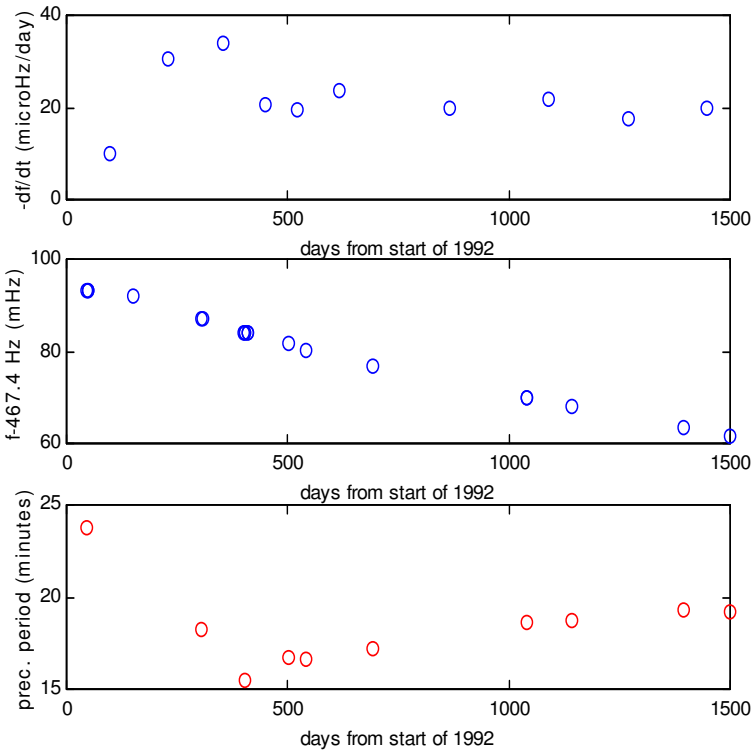

Figure 4.1: Observational data for SN 1987A. The data points are taken from Middleditch et. al paper [1].

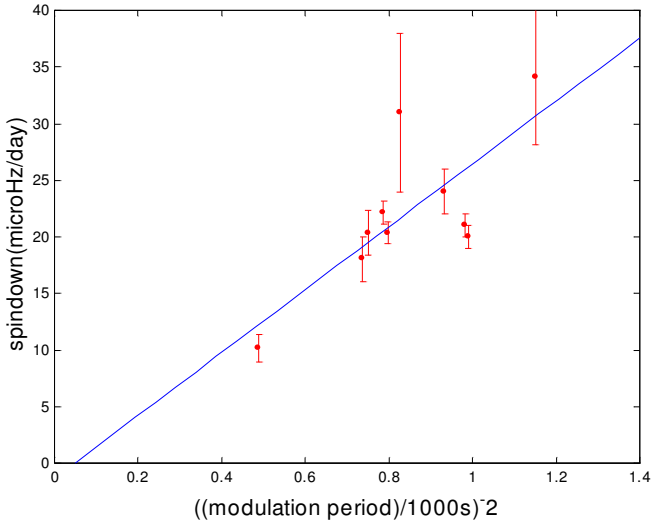

Figure 4.2: The relationship between spin down and precession frequency in the SN 1987A observational data.

if the SN 1987A remnant would loose energy through gravitational waves' radiation exclusively. If an electromagnetic contribution to the spin-down rate is also present, this term will be independent of ellipticity and will be approximately constant during the time span of the observation. This will make the straight line in Figure 4.2 to have a positive constant vertical axis crossing, that is not what is observed. This implies that all the energy loss has to be attributed to gravitational spin-down.

CHAPTER 5
A MODEL FOR THE PRECESSING NEUTRON STAR

5.1 The System Geometry

Neutron stars are supposed to be very smooth objects because of the incredible strength of their surface gravity. Though, because of the great density of the nuclear material even small bumps and irregularities could contribute significantly to the value of the angular momentum along the different axes. The neutron star could be smooth but deformed along different axes, in this case looking like a football or ellipsoid. It is even possible that its shape will be more complicated as in the case of the Earth that has the shape of a pear. In addition a realistic neutron star will have a fluid interior and the crust will not be perfectly rigid. This means, among other things, that the star will have some deformation along the rotation axis and that we will have to consider the effect of the elasticity properties of the crust in our discussion.

Rotating neutron stars are often mentioned as a possible continuous source of gravitational radiation. Usually what is envisioned is that the star has an axissymmetric deformation perpendicular to the axis of rotation to allow for a changing mass quadrupole that will generate gravity waves. This star will emit gravity waves at twice the rotation frequency.

If the star is deformed on an axis that is at any other angle with the rotation axis then it will process as a spinning top. This star will emit at twice the rotation frequency and also at the rotation frequency. The simplest situation is that the star is a rigid body and has just two non-equal principal moments of inertia. Let's assume

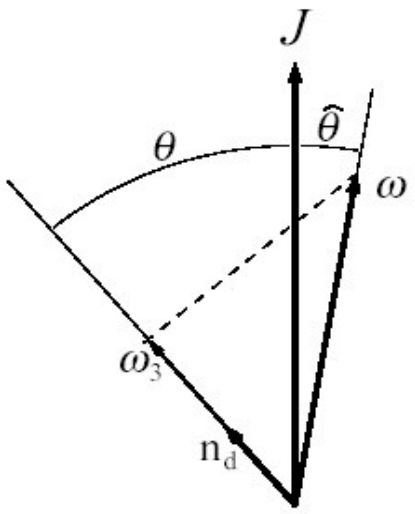

Figure 5.1: The relevant vector quantities in the precessing neutron star in the inertial reference frame. The total angular momentum **J** is fixed in space. The other vectors rotate aroun **J** with constant angles θ and $\widehat{\theta}$.

for simplicity that we are dealing with a smooth object squeezed symmetrically along one axis, this object is called a *spheroid*. We define the symmetry axis as a_3. The axis a_1 and a_2 are perpendicular to a_3. If the object has uniform density we then have $I_1 = I_2 = I_0 - \Delta I_d/3$, $I_3 = I_0 + 2/3\Delta I_d$, so that we have $I_3 - I_1 = \Delta I_d$. I_0 is the average value of the moment of inertia and ΔI_d is a small quantity.

A more complete and realistic model is considered further; but the simplest case remains the basis for the discussion of precessing neutron stars. The main equations are the same even in the more realistic case, with minor modifications. Figure 5.1 shows our convention in the orientation of the important vectorial quantities involved in the problem.

The spheroid rotates with angular frequency ω and the total angular momen-

tum **J** has fixed orientation in space. The object looses angular momentum which is carried away by gravitational waves but on a longer time scale than the one set by the rotation or precession. So, for all purposes, we can consider the angular momentum as conserved. A discussion of the damping time scales due to gravitational radiation and other mechanisms is given in later Chapters. An important parameter for the geometry of the system is the angle θ between the angular momentum vector **J** and the axis a_3. The angle γ is the one between the axis a_3 and the rotation axis $\boldsymbol{\omega}$. See Figure 5.3. It is possible to show [15] that $\widehat{\theta} = \gamma - \theta = \varepsilon = \frac{I_1 - I_3}{I_1}$. The ellipticity ε is a measure of the deformation from perfect spherical symmetry. In neutron stars ε is supposed to be a small quantity (in general $\varepsilon < 10^{-2}$ otherwise the crust will crack due to the deformation stresses). So we will assume often $\gamma \approx \theta$.

We can define the total moment of inertia as:

$$\mathbf{I} = I_0\boldsymbol{\delta} + \Delta I_d \left(\mathbf{n}_d\mathbf{n}_d - \boldsymbol{\delta}/3\right), \tag{5.1}$$

where $\mathbf{n}_d$ is a unit vector pointing along the body symmetry axis a_3 and δ is the unit tensor. Now, let's define the quantity $\epsilon = \Delta I_d / I_0$. It is a well known result of Classical Mechanics (see Appendix A) that:

$$\varepsilon = \frac{\Omega_p}{\omega_3} = \frac{\Omega_p}{\omega\cos\gamma} \approx \frac{\Omega_p}{\omega\cos\theta} \tag{5.2}$$

where Ω_p is precession frequency and ω_3 is the projection of ω on the symmetry axis a_3. We will proceed from the assumption that we know the parameters Ω_p and ω from the observations of SN 1987A by Middleditch *et al.* (2000) [1].

The observed modulation or precession period varied during the span of the

observations in the range from approximately 935 s and 1430 s while, ω or the spin period varied measurably but relatively little. Consequently the observed variations in Ω_p must be attributed to variations in ϵ or θ or both. Note that the correlation between $\dot{\omega}$ and Ω_p claimed by Middleditch *et al.* requires that θ remain constant. Jones and Andersson (2001) [15] and Jones (2001) [17] have claimed that it is not easy to imagine how significant variations in ellipticity can occur without affecting the wobble angle. We shall return to this question in Section 5.3 and argue that it is, in fact, unlikely that variation in epsilon can significantly change the wobble angle.

5.2 Gravitational Radiation Caused by Misalignment

To determine the size of the deformation and consequently the strain carried by the gravitational radiation on earth we need to evaluate the wobble angle θ.

It turns out that it is possible to determine the angle θ when the frequency ω, its derivative $\dot{\omega}$ and the precession frequency Ω_p are known and it is assumed that the neutron star energy loss is due mainly to gravitational radiation. We already explained that this is the case for SN 1987A. In the following we will demonstrate this in more detail. We can calculate precisely the wobble angle θ when the three parameter ω, $\dot{\omega}$ and Ω_p are known (as in the case of SN 1987A) and a particular value for the angular momentum is chosen. We start with the relationship between ellipticity, precession frequency and rotation frequency:

$$\varepsilon = \frac{\Omega_p}{\omega_3} = \frac{\Omega_p}{\omega \cos\theta} = \frac{1/P_r}{1/P \cos\theta} = \frac{\varepsilon_0}{\cos\theta} = \frac{0.00214 \text{ s}}{1000 \text{ s } \cos\,\theta} = \frac{2.1 \times 10^{-6}}{\cos\theta}. \tag{5.3}$$

We know also that the power radiated by a precessing spheroid is:

$$\dot{E}= \frac{2}{5}\frac{G}{c^5}\epsilon^2 I_0^2 \omega^6 \sin^2\theta \left(16\sin^2\theta + \cos^2\theta\right), \tag{5.4}$$

this is the General Relativistic formula derived in the previous Chapter 3. It is important to point out that the two terms in parenthesis represent respectively the contribution of the ω and 2 ω components of the radiation.

The main source of energy for the neutron star is its rotational energy reservoir $E = 1/2\ I_0\omega^2$, we have then that

$$\dot{E}= \omega\ \dot{\omega}\ I_0 \tag{5.5}$$

(more exactly calculating the energy using the full inertia tensor it is obtained $E = 1/2\ I_0\omega^2(1 - \varepsilon\cos\theta) \approx 1/2\ I_0\omega^2$).

Equating this and the previous expression, we have:

$$\dot{\omega}= \frac{2}{5}\frac{G}{c^5}\frac{\varepsilon_0^2}{\cos^2\theta} I_0\omega^5 \sin^2\theta \left(16\sin^2\theta + \cos^2\theta\right). \tag{5.6}$$

Let' s define the quantity:

$$A_1 = \frac{2}{5}\frac{G}{c^5}\varepsilon_0^2 I_0\omega^5 = 1.09\times 10^{-9}, \tag{5.7}$$

The numerical estimate of A_1 is calculated using the observed value for SN 1987A and the theoretical canonical value of $I_0 = 10^{45}$ g cm^2 (this is valid only if the star precess as a solid body; see further for a more general result).

Now it is possible to solve for $\sin^2\theta$,

$$\sin^2\theta = \frac{-(A+\dot{\omega}) + \sqrt{(A+\dot{\omega})^2 + 60A\,\dot{\omega}}}{30A}, \tag{5.8}$$

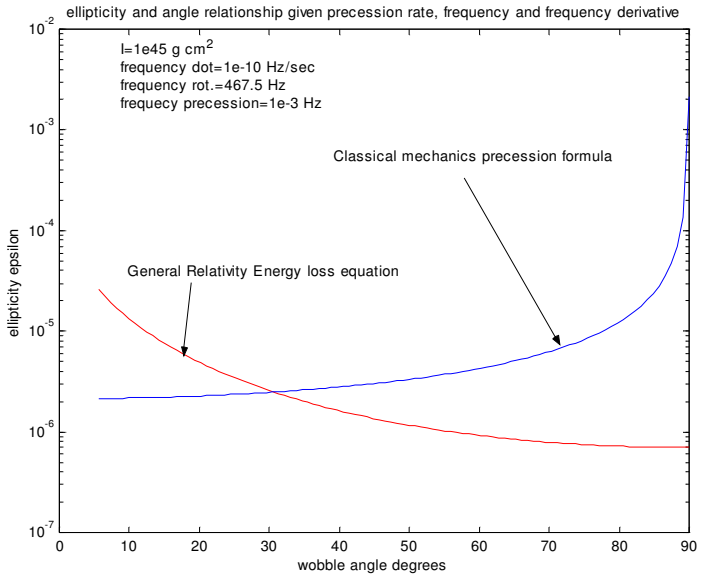

Figure 5.2: The relationship between ellipticity and wobble angle for the Classical Mechanics and General Relativity equations for Precession and Energy Loss. A moment of inertia I of 1e45 is choosen. The meeting point between the two curves determines the only possible physical solution.

and substituting the right values for SN 1987A, we get:

$$\theta \approx 0.53 \text{ radians}=30.6 \text{ degrees}. \tag{5.9}$$

Figure 5.3 shows the dependence of the angle θ on parameters as the frequency and the spin-down. In this Figure are shown the extreme values observed for the different parameters $\dot{\omega}$ and Ω_p. We can see that even uncertainties in the values of these parameters of order 1.5 and 2.25 respectively (similar to that reported in the Middleditch *et al.* study) do not much change the conclusion that the angle θ is in general large. This is a quite interesting and unexpected result. It could be an interesting problem to model a process that can create a precession with such large angle.

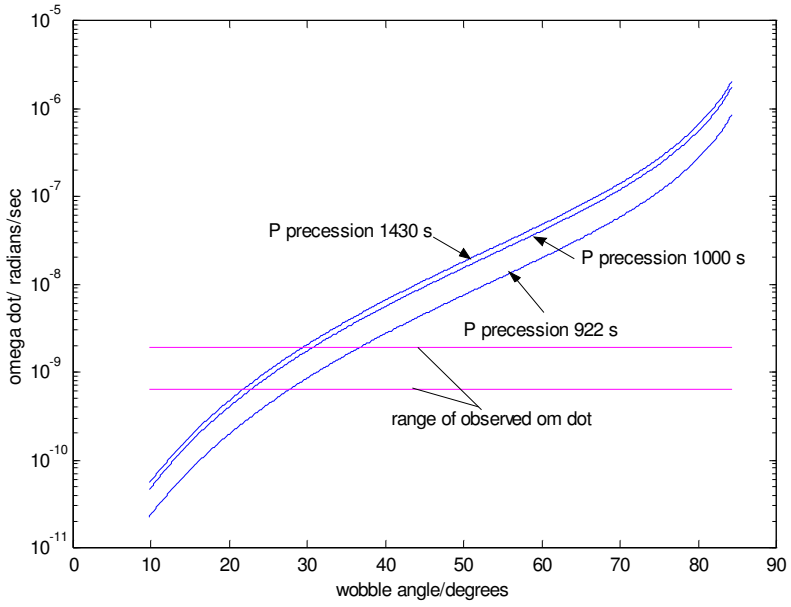

Figure 5.3: Dependence of wobble angle on variation of observed data.

The relativistic equation 5.4 depends on the value of I_0 . This value is the average moment of inertia of star's section that actually participates in the precession. If the star has a solid crust and a liquid interior the I_0 is the crust's moment of inertia and that of any liquid coupled to the crust. In fact, part of the liquid should be stress free and not influenced by the precession. So we can take I_0 to be an arbitrary quantity equal or less than the entire moment of inertia of the star $I_{star} = \frac{2}{5}MR^2 = 1.12 \times 10^{45} gcm^2 M_{1.4} R_6^2$, where $M_{1.4}$ is the mass of the star in units of 1.4 solar masses and R_6^2 is the radius in units of 10^6 cm. If just the crust participates in the precession then according to standard neutron theory the value of I_0 should be 100 times smaller. The Classical Mechanics and the General Relativistic equations have to be satisfied at the same time. This means that for given observed Ω_p, ω and $\dot{\omega}$ and choice of I_0 the functions have

to meet at a point in the parameter space $\varepsilon - \theta$. If we consider the moment of inertia the unknown parameter of our problem, we can determine which wobble angle the star should have given the value of I_0. This is illustrated in Figure 5.4.

It seems that SN 1987A remnant had some relatively big and rapid changes in the precession frequency during the first years of observation. The astrophysical explanation for this can be found in the young neutron star 's very active, dynamic environment which could cause abrupt changes in the density of the crust, fractures and re-arrangement of the surrounding material. Rearrangements in the material in the crust cause changes in the ellipticity. The ellipticity in a precessing body is the ratio between the rotational frequency and the precession frequency. The rotational frequency can be assumed to be constant other than the small and slow changes due to the gravitational wave induced spin-down. Therefore changes in the precession are directly proportional to changes in the ellipticity. Possibly tectonic movements of the crust could raise or lower "mountains" on the neutron star. These mountains need to be just a centimeter high to produce ellipticity values similar to that deduced for SN 1987A. Changes in the height of these mountains by 30 % will cause the observed changes in Ω_p (of order 1.5 the average value). We already mentioned there is an empirical relationship between the observed change in $\dot{\omega}$ and Ω_p. This observed relationship is what theory actually predicts in the case of a precessing neutron star loosing energy through gravitational radiation. If we substitute equation 5.3 in 5.6, we have:

$$\dot{\omega} = \frac{2}{5}\frac{G}{c^5}\frac{\Omega_p^2}{\cos^2\theta} I_0 \omega^3 \sin^2\theta \left(16\sin^2\theta + \cos^2\theta\right). \tag{5.10}$$

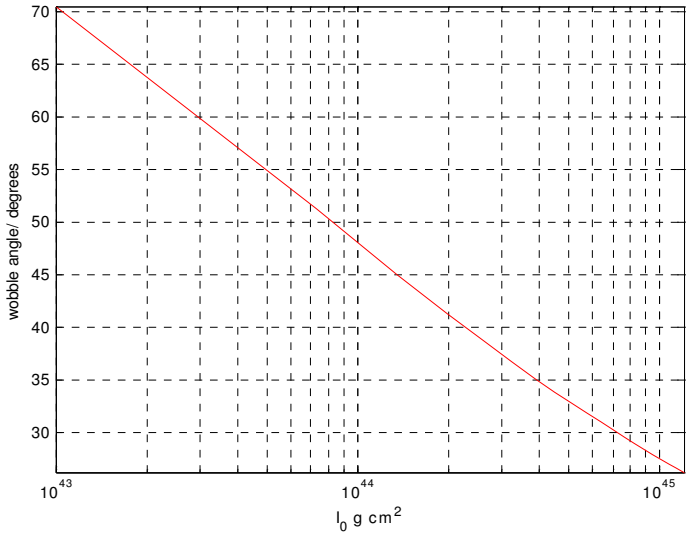

Figure 5.4: The dependence of the wobble angle on the moment of inertia involved in the precession. The range of values for the moment of inertia spans from 10e43 g cm^2 (just the crust precesses) to 1.2e45 g cm^2 (all the star precesses).

Plotting the spin $\dot{\omega}$ versus Ω_p data in a log-log plot we get a good linear fit with less than 10 % error. The measured slope of the fitting line is 2.01. According to equation 5.10, a linear fitting between the logarithms of $\dot{\omega}$ and Ω_p requires that θ remains constant while ε and hence Ω_p vary.

5.3 The Constancy of the Wobble Angle

Middleditch *et al.* (2000) [1] display graphically the correlation between $\dot{\omega}$ and $\Omega_{\rm p}^2$. By reading off the values of these variables and applying the method and equations of Section 5.2 it is possible to determine the values of the wobble angle θ required for each individual pair of values $\dot{\omega}$ and $\Omega_{\rm p}$ for any assumed moment of inertia involved in the precession. This exercise reveals that despite variations of ϵ and $\Omega_{\rm p}$ exceeding a factor of 1.5, the wobble angle does not change by more than a couple of degrees and

appears consistent with remaining constant within experimental errors.

In the case of a freely precessing solid body, the wobble angle is largely determined by initial conditions: taking the principal axes introduced in Section 5.1, if the associated moments of inertia remain constant, then $\omega_3 = \omega\cos\gamma$, also remains constant (see Fig. 5.1). It is easy to generalize Euler's equations to the case in which the principal moments of inertia change due to unspecified internal forces while the external torques vanish and the total angular momentum is conserved:

$$\frac{dI_1\omega_1}{dt} = \omega_2\omega_3(I_2 - I_3) \tag{5.11}$$

$$\frac{dI_2\omega_1}{dt} = \omega_3\omega_1(I_3 - I_1) \tag{5.12}$$

$$\frac{dI_3\omega_1}{dt} = \omega_1\omega_2(I_1 - I_2)\,. \tag{5.13}$$

When the principal moments of inertia are all of the form $I_i = I_0 + \epsilon_i$, then clearly all the time derivatives are of order $\sim \epsilon_i$ and even if the given ϵ_i were to change by factors of a few, the result would be a small wobble of the tip of ω in the body frame. Therefore we conclude that while the variations probably detected by Middleditch *et al.* (2000) in both ϵ and $\Omega_{\rm p}$ were significant, they do not imply any measurable change in θ. Referring back to Fig. 5.1 we see that $\widehat{\theta}$ may indeed change by amounts comparable to itself, but the wobble angle θ would change very little. This conclusion is contrary to what Jones & Andersson (2001) [15] and Jones (2001) [17] have claimed regarding the wobble angle, and thus it makes more plausible that the remnant of SN 1987A is indeed freely precessing while undergoing changes in ϵ and $\Omega_{\rm p}$.

CHAPTER 6
TESTING THE GW EMISSION HYPOTHESIS

One of the main assumptions used to derive the results of the previous section is that the compact remnant of SN 1987A is spinning down mostly due to gravitational wave emission. We relax, for the moment, this hypothesis and try to understand what the consequences will be if the spin down was due to other mechanisms beside gravitational waves. The precession guarantees a certain time-varying quadrupole to the star. Figure 5.2 shows that the dependency of the ellipticity on the wobble angle is not very strong over a big range of angles. The energy loss due to gravitational wave emission (and consequently the strength of the gravitational wave strain on Earth) is strongly dependent on the wobble angle mainly when the angle is less than 5 degrees. As shown previously we need a relatively large wobble angle to explain the observed spin-down even when the star precesses as a solid body. Larger wobble angles are required when less than the entire angular of the star is involved in the precession as in the case of only the crust precessing. Figure 6.1 shows the dependency of the strain of the ω and 2 ω signal on the wobble angle.

The environment of SN 1987A is very complex and, almost certainly, is interacting with the star, causing some additional forms of braking other than the gravitational braking. We do not have enough information on the spin-down over a long time to measure $\ddot{\omega}$ that could determine with precision if gravitational waves are the cause of the spin-down or other forces are involved. Consequentely we cannot rule out completely the presence of other mechanisms for energy loss in the star. If SN 1987A has a strong

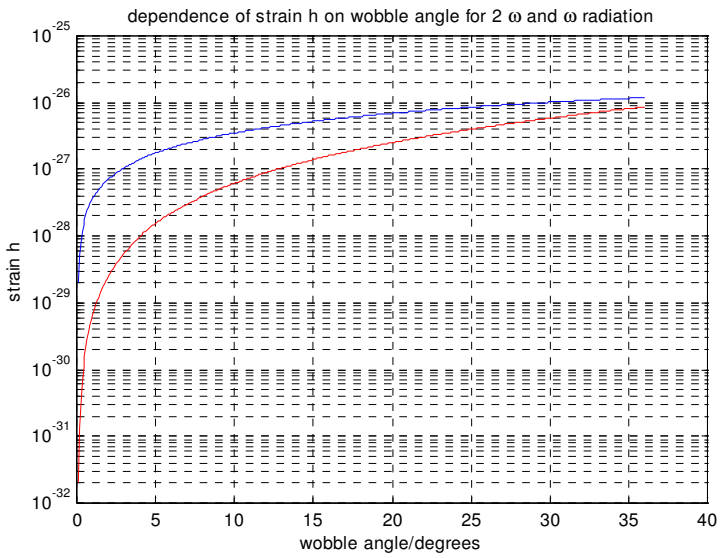

Figure 6.1: Strain h for om. (top curve) and 2 om. (bottom curve) radiation as function of angle.

magnetic field it will spin-down mainly because of emission of electromagnetic radiation. We can show, in fact, that electromagnetism is much more efficient in slowing down the spin of the star.

Lt's start with the usual equation for the energy loss of a rotating magnetic dipole:

$$\dot{E} = -\frac{16\pi^4 B^2 R^6 \sin^2\alpha}{6c^3 P^4}, \tag{6.1}$$

where B is the magnetic field strength at the pole of the star, α is the angle between the rotation axis and the magnetic pole, R is the neutron star radius, c the speed of light and P is the rotational period.

Using the previous formula for the energy loss due to gravitational waves we can calculate the ratio between the period derivative due to gravitational waves $\dot{P}_{GW}$ and

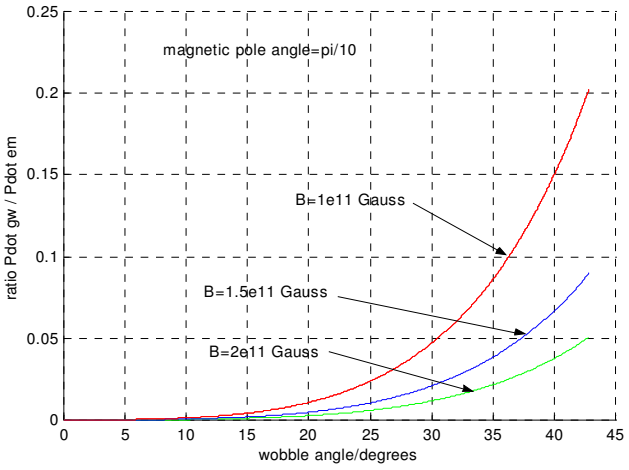

Figure 6.2: Ratio of spin-down due to GW and EM radiation.

the one due to electromagnetism $\dot{P}_{EM}$:

$$\dot{P}_{GW} \; / \; \dot{P}_{EM} = \frac{3 \; G \; \Omega_p^2 \; I^2 \; \sin^2\theta \left(16 \sin^2\theta + \cos^2\theta\right)}{10 \; \pi^3 c^2 \cos^2\theta B^2 R^6 \sin^2\alpha}$$

It is interesting to note that this ratio is independent of the rotational frequency. The main variables are the wobble angle θ and the magnetic field intensity B. We have chosen a moment of inertia corresponding to the entire star precessing. If I was smaller, then the spin-down due to gravity will be even less. We show in Figure 6.2 the ratio between $\dot{P}$ due to gravitational waves and that due to electromagnetism as a function of wobble angle and given magnetic field B. For strong magnetic fields, similar to that of the majority of pulsars, the electromagnetic braking is much more efficient than the gravitational radiation braking, above all at small wobble angles.

If we assume that the spin-down is due to a combination of magnetic and gravitational braking, then we can calculate what strength of the magnetic field B is necessary to account for the observed spin-down. Figure 6.3 shows the relationship between angle

and magnetic field strength necessary to explain the observed spin-down. Two choices of the angle α are given. Looking at the graph it seems that there are two possible regimes. If the wobble angle is close to 30 degrees the magnetic field is very small. This means that mainly the star is loosing energy through gravitational wave emission. Just a few degrees away from 30 degrees we will need the presence of a value of B similar to that of other pulsars in order to achieve the level of spin down of SN 1987A. The other regime is at small values of wobble angle. In this regime the Energy Loss due gravitational radiation is small, therefore most of the spin down is due to electromagnetism.

Of course, the rate of electromagnetic spin-down depends on the angle α between the rotation axis and the magnetic dipole axis. The angle α dependency of the spin-down does not change the main conclusion. A strong magnetic field will require a small angle α if the wobble angle is near 30 degrees. Even small magnetic fields will be enough for electromagnetic braking to dominate if the angle α is large.

Equation 5.10 tells us that if the star's spins-down is mostly due to gravitational radiation, there is a power law between the precession period and the spin-down $\dot{\omega}$. Figure 4.2 illustrates Middleditch's observational relationship between these quantities as the star evolves in time. The data points suggest that indeed, within the estimated uncertainties, there is a power law relationship between precession and spin-down in SN 1987A as if there was not any contribution from the electromagnetic braking. In fact, the straight line will cross the y axis at a value zero for the wobble angle, as the electromagnetic braking should not depend on the wobble angle. The data suggests

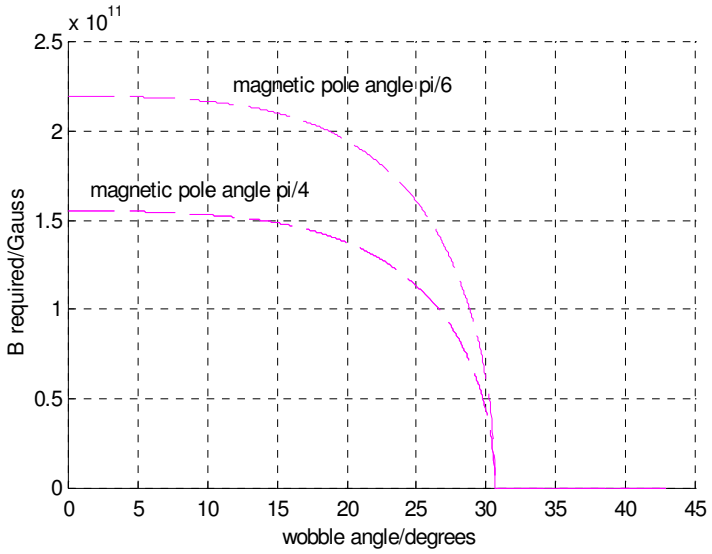

Figure 6.3: Necessary B to account for observed spin-down.

that the straight line goes, within small measurement errors, through the origin.

Another interesting fact about the SN 1987A remnant pulsar that could be suggestive of the emission properties of this star is its location in the $P\ \dot{P}$ diagram.

It can be seen from Figure 6.4 that the SN 1987A remnant occupies a very particular place in the diagram. Most of the known pulsars are loosely clumped on the center-right side of the $P\ \dot{P}$ diagram. This group has spin-down comparable to that of SN 1987A, in general close to 10^{-15} s/s, but it has a much bigger P. There is a minor group of pulsars with very small P, on the order of milliseconds, and quite small $\dot{P}$. This places the millisecond pulsars's group at the left-bottom of the diagram. The pulsar SN 1987A then is quite unique in having a small P and a relatively big $\dot{P}$, locating the pulsar on the center-left of the diagram. What does this mean?

If the spin-down was to be attributed to electromagnetism then the magnetic field of the star will be quite small in comparison with normal pulsars and very high in

comparison with millisecond pulsars. It is reasonable to assume that SN 1987A has a low magnetic field. The usual explanation of the high magnetic fields in neutron stars is the increment of the field line density after collapse of the progenitor star magnetic iron core. In the case of SN 1987A the generally accepted scenario for the supernova explosion is that was initiated by collision of two stars in a close binary system. In this case we will not expect the stars ' magnetic fields to be conserved in a orderly way but quite disrupted by the process of collision. We predict a very low magnetic field for SN 1987A, comparable to that of other millisecond pulsars. All things considered strongly suggest that the high spin-down is due to gravitational wave emission. For other arguments in favor of the gravitational radiation energy loss see the article by S. Nagataki and K. Sato discussed in Chapter 10.

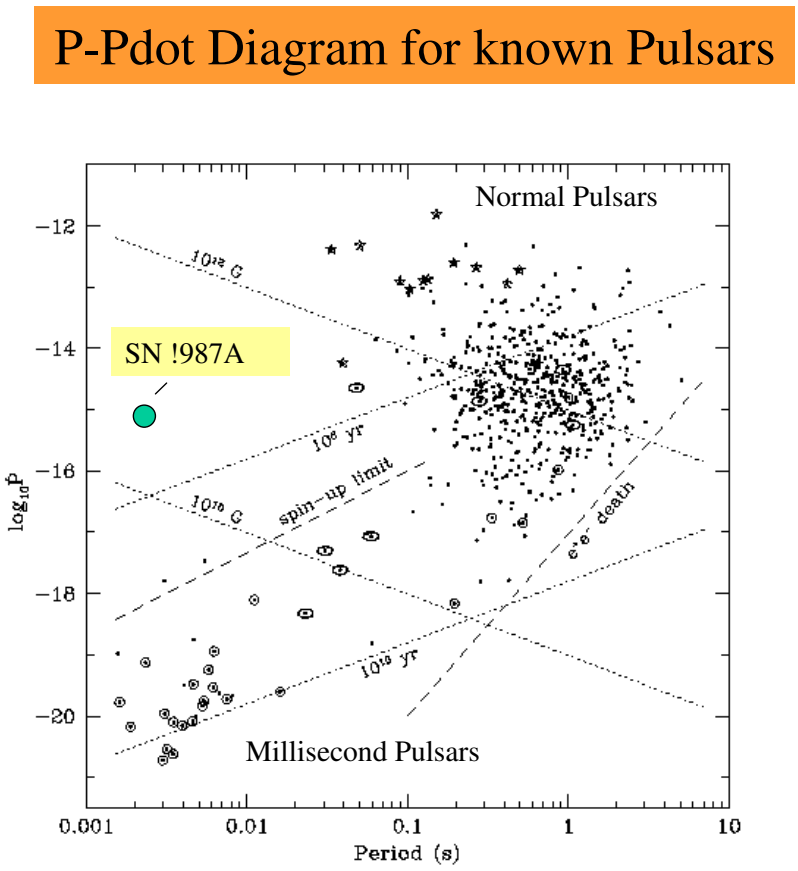

Figure 6.4: The P-Pdot diagram for known Pulsars. The isolated position of SN 1987A compact remnant is maybe an indication that the spin-down mechanism is different from other pulsars: gravitational instead of electromagnetic radiation.

CHAPTER 7
A MORE REALISTIC MODEL: ALLOWING FOR AN ELASTIC CRUST AND PRESENCE OF A FLUID INTERIOR

The textbook discussion of a precessing body implies that the object is rigid. A more realistic neutron star will have a more or less elastic shell, and a fluid interior. The fluid is supposed to be composed of a electron-proton plasma and a neutron superfluid. The plasma fluid interior can couple to the crust because of friction. Under these conditions the system is not simply described by the rigid body model.

Usually the approach taken to explore the properties of a more complicated system such as this is to understand the effect of one additional complication at a time. The paper of Jones and Anderson *Freely precessing neutron stars: model and observations*, address these complications and shows how the more realistic model needs to be modified to account for these complications. In this section we are going to summarize the results of Jones *et al.* paper [15] and apply them to the particular problem of the detection of the SN 1987A remnant.

7.1 The Elastic Crust

In the case of an elastic crust's shell we have to write the moment of inertia as:

$$\mathbf{I} = I_0\boldsymbol{\delta} + \Delta I_d\left(\mathbf{n}_d - \boldsymbol{\delta}/3\right) + \Delta I_\omega\left(\mathbf{n}_\omega\mathbf{n}_\omega - \boldsymbol{\delta}/3\right). \tag{7.1}$$

This is the sum of a spherical part and two quadrupole small contributions. The first term is the moment of the inertia of the undeformed shell, in the absence of rotation. The second term is a deformation due to Coulomb forces and the third is the deformation due to centrifugal forces. The vector $\mathbf{n}_d$ determines the axis of symmetry

of the deformation ΔI_d. The vector $\mathbf{n}_\omega$ lies along the axis of rotation and determines the direction of the centrifugal deformation ΔI_ω's axis of symmetry.

The quantity ΔI_ω is caused by the deformation due to the centrifugal force, its value is determined by:

$$\frac{\Delta I_\omega}{I} = \frac{I_0^2 \omega^2}{4\,(A+B)}, \tag{7.2}$$

where the constants A and B depend on the particular stellar equation of state. The constant A is of the order of the gravitational binding energy and the constant B is of the order of the total electrostatic binding energy of the ionic crustal lattice. The quantity B is much smaller than A so we can make the approximation:

$$\frac{\Delta I_\omega}{I} \approx \frac{I_0^2 \omega^2}{4A} \approx \frac{\omega^2 R^3}{GM} \approx 2.1 \times 10^{-3} \left(\frac{f}{100Hz}\right)^2 R_6^3/M_{1.4}, \tag{7.3}$$

where f is simply $\omega/2\pi$.

In the general situation of non parallel $\mathbf{n}_d$ and $\mathbf{n}_\omega$ we have that the body will precess. As a consequence of $\mathbf{n}_\omega$ being in the direction of the rotation axis (at any given instant) the body will behave as a axisymmetric top even if the body has a triaxial shape. An outline of the proof of this is given in Cutler and Jones [18].

In this case the three moments of inertia are:

$$\begin{aligned} I_1 &= I_0 - \Delta I_d/3 + 2\Delta I_\omega/3 \\ I_2 &= I_1 \\ I_3 &= I_0 + 2\Delta I_d/3 + 2\Delta I_\omega/3 \end{aligned} \tag{7.4}$$

The main conclusion is that even in the case of a elastic crust the star will still behave, for what concerns precession, as a biaxial rigid object. The fundamental

equation (5.2) holds for this situation (with the appropriate inertia moments given above) and this means that the only piece of the moment of inertia that contributes to precession is $\Delta I_d = I_3 - I_1$.

7.2 The Presence of a Fluid Interior

To further improve our model we have to consider the presence of a fluid interior. There are different aspects of this problem.

1) The shape of the cavity for the fluid could be spherical or maybe not be; in the case of a spherical cavity the presence of the fluid, in absence of viscosity, is uninfluenced for what concerns precession. If the cavity is non-spherical then there will be a reaction force that is generated by the tendency of the fluid to assume spherical symmetry around the axis of rotation. The shell will be pushed by the fluid. This problem is solved in the literature [Lamb, 1950] and under the simplification of uniform vorticity of the shell and small cavity ellipticity and wobble angle we have that the usual precession equations described above are still in place. Lamb, for mathematical convenience, assumes a small wobble to obtain simplified equations but even in the most general case of large wobble angle the above described conclusion doesn't change. The only modification to take into account is that ΔI_d refers to the difference in moment of inertia along the axis 1 and 3 of the whole star, and I_0 refers to the average moment of the inertia of the shell only.

2) In the presence of friction between the crust and a part of the interior fluid in contact with the crust we could have some coupling between the motion of the crust and the core. It can be shown that in the case of neutron stars the coupling is very weak

and the core doesn't participate to the precession [19]. If there are frictional forces at work in the interior of the star these will serve just to damp the free precession on time scales between 400 and 10^4 precession periods.

3) The problem of pinning. Jones *et al.* [15] following work of Shaham (see references in [15]) concludes that the presence of pinning of the superfluid to the crusts, at least in the simplest possible configuration doesn't change the form of the equations that describe the precession. The main modification required is that the relevant *effective ellipticity* is generated by combination of the lattice deformation and the moment of the inertia I_{SF} of the pinned fluid , as in the following:

$$\epsilon_{eff} = \frac{\Delta I_d}{I_0} + \frac{I_{SF}}{I_0}. \tag{7.5}$$

The most common theories on pulsar glitches give a precise prediction on the precession behavior in the presence of pinning in a neutron star. The theories require at least a few percent of the total moment of inertia of the star to be in the pinned superfluid. From current understanding of neutron star properties we know that the crust moment of inertia is a few percent of the total moment of inertia of the star. All of this then implies that

$$\epsilon_{eff} = \frac{\Omega_p}{\omega \cos\theta} = \frac{\Delta I_d}{I_0} + \frac{I_{SF}}{I_0} \approx 1, \tag{7.6}$$

in the case of small deformations ΔI_d. The precession and rotation frequency should be close in value if there is a sizable quantity of superfluid that is pinned to the crust. These predictions are not confirmed by observations of the three strongest cases of precession in neutron stars: PSR B1642-03, PSR B1828-11 and SN 1987A remnant, where the

precession is on a time scale much longer than the rotation. The conclusion is that if the free precession interpretation of the modulation of the signal of these pulsars is correct then there is not basically any pinned superfluid in these stars. Recently this apparent conflict between the pulsar glitches theories and the observational data on precessing neutron stars was resolved in Cutler and Link [??]. In this article the authors explain that once the precession is set in motion the inner torques generated by the precession will unpinn very efficiently the superfluid allowing the star to precess undisturbed. This shows that neutron stars with long lasting precession motion are a real physical possibilty.

CHAPTER 8
THE WOBBLE ANGLE AND THE CRUST FRACTURE

8.1 The Centrifugal Deformation

A star that rotates and has a certain level of elasticity will deform under the action of the centrifugal force. Gravity will work as a restoring force so the final shape of the object will be determined by the balance between these forces. Furthermore if the star has a solid crust it will be able to sustain deformations in the Coulomb lattice that form the crust. We can determine the amount of ellipticity ε_Ω, a measure of the deviation from perfect spherical symmetry, by a variational analysis of the energy. In fact, the total energy of a rotating system with a solid crust is:

$$E = E_0 + \frac{L}{2I}^2 (1 - \varepsilon_\Omega) + A\varepsilon_\Omega^2 + B\left(\varepsilon_0 - \varepsilon_\Omega\right)^2, \tag{8.1}$$

where E_0 is the energy of the spherical fluid, L is the angular momentum and I is the moment of inertia, A is the gravitational energy and B is the elastic energy stored in the star as a result of the rotation. The ellipticity ε_0 is the ellipticity that the star would have if the crust will be strain free. Now we can calculate the change in energy as a function of ellipticity. This quantity is:

$$\frac{\partial E}{\partial \varepsilon} = -\frac{L}{2I}^2 - 2B\ \varepsilon_0 + 2B\ \varepsilon_\Omega + 2A\varepsilon_\Omega \tag{8.2}$$

Then the bulge due to rotation is:

$$\varepsilon_\Omega = \frac{I\ \Omega^2}{4(A+B)} \tag{8.3}$$

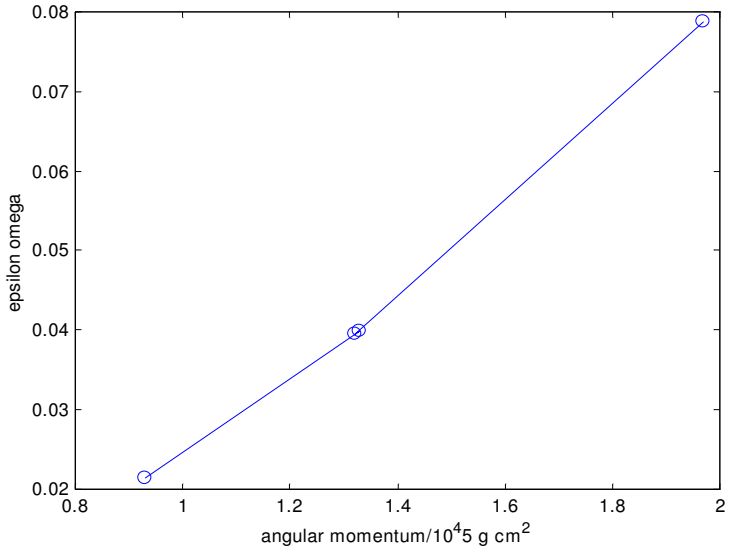

Figure 8.1: The value of the centrifugal deformation using different equations of state.

The values of B and A depend on the properties of the equation of state of the star and the elastic properties of the crust. In general $B \approx 10^{-4}A$ or less so:

$$\varepsilon_\Omega \approx \frac{I\ \Omega^2}{4A} \tag{8.4}$$

Figure 8.1 shows possible values for ε_Ω using estimates of I and A and a value of Ω similar to that of SN 1987A. The estimates of I and A are based on different models for the equation of state as catalogued in the article of V.R. Pandharipande *et al.* [20]. We report the values of I and A used in Table 8.1 .

We do not know which of these models represents the real properties of the neutron star so we are going to calculate the centrifugal ellipticity for a general uniform density self-gravitating star. The energy of a spherical self-gravitating object is:

$$E \sim -\frac{3}{10}\frac{GM^2}{R} \tag{8.5}$$

Table 8.1: Equation of state parameters for different models. The models are discussed in Pandharipande et al. [20]

Model	$(I_{star} + I_{crust})/10^{45} gcm^2$	$A/10^{52} ergs$	ε_Ω
Reid 2,0	0.89+0.04	9.4	0.0213
Reid 2,4	0.87+0.06	9.4	0.0213
Bethe, Johnson 2,0	1.03+0.3	7.2	0.0398
Bertsch, Johnson 2,4	0.94+0.38	7.2	0.0395
Mean Field 2,0	1.31+0.66	5.4	0.0787

and the angular momentum of a spheroid is:

$$I = \frac{2}{5} MR^2 \tag{8.6}$$

and:

$$\varepsilon_\Omega \approx \frac{\Omega^2 R^3}{3\ GM}. \tag{8.7}$$

For a canonical neutron star with SN 1987A rotation frequency we have that $\varepsilon_\Omega \approx$ 0.0153.

Precession will cause the rotation axis of the star to change its position relative to the body frame. This means that the centrifugal force in place will be a function of position and time. The change in the centrifugal force will be on the order of the precession time scale. If the star has an elastic crust, then it will change its shape accordingly to the change in the centrifugal force. The change in shape then causes time dependent stresses in the crust. In the next section we show a relatively accurate estimate of the size of the stress σ on the crust due to precession. The result is that the

strain σ is proportional to the wobble angle and the size of the centrifugal deformation as in the following:

$$\sigma \approx \varepsilon_{\Omega} \ \sin\theta. \approx 7.01 \times 10^{-4} \left(\frac{f}{100Hz}\right)^2 \ \sin\theta \ R_6^3/M_{1.4}. \tag{8.8}$$

From experiment with crystals we have an upper limit for the maximum possible stress sustainable by the crust before breaking, i.e. $\sigma_{\max} \approx 10^{-2}$. This implies that the possible maximum wobble angle for our pulsar is:

$$\theta_{\max} \approx \sin^{-1}(\sigma_{\max} \ 1.4 \times 10^3 \left(\frac{100Hz}{467.5Hz}\right)^2) \approx 0.69 \text{ radians} = 39.79^{\circ}. \tag{8.9}$$

This is a result which differs by a factor of 3 from that obtained using rougher estimates by Jones and Andersonn. We have to point out that these arguments are just order of magnitude estimates and better understanding of the neutron star physical properties is needed. Viceversa, if we do observe gravitational waves from a precessing neutron star we could use the observations to put limits on the equation of state and elastic properties of the crust.

Notwithstanding this precaution statement we can calculate the strain as a function of wobble angle and this is illustrated in Figure 8.2. It is possible to see that there is a range of values, in this particular estimate, that are allowed before the strain reaches values greater than that of the strongest known material on earth. The crust should break at larger angles than 40 degrees and precession should not be possible after the breaking of the crust. This means that if the star precesses then just angles smaller than 40 degrees are those that are realistic.

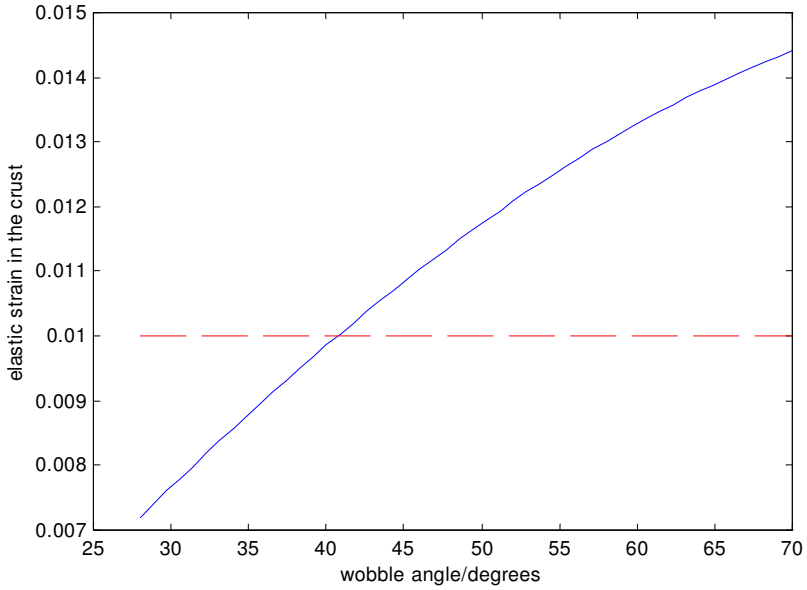

Figure 8.2: The dependency of the elastic strain on the crust as a function of wobble angle. The red line indicates typical maximum strain for known terrestrial materials.

8.2 A More Precise Calculations of the Strain

We saw already that there is a correspondence between how much of the star moment of inertia is involved in the precession and the allowed wobble angles. If we accept the argument of the maximum crustal strain, then we have to conclude that at least half of the moment of inertia of the entire star contributes to the precession. This means that almost all the star mass undergoes precession not withstanding the Chapter 7 arguments that lead us to believe that it is just the crust's moment that precesses.

If the crustal breaking argument is right, and our understanding of the coupling between crust and core is wrong, it means that the existence of an upper limit for

the wobble angle has important implications for gravitational wave detection from the remnant of Supernova 1987A as explained in the previous Chapters. It is important to have the best possible estimate for the strain on the crust.

In this section we will try to use geometric arguments to calculate the strain due to the centrifugal bulge as it displaces because of the precession.. Our strategy will be to calculate the strain as the star shape changes and then take differences between our initial strain and the final point of each transformation. The final difference of this process should be the strain as a function of time due to the precessional motion.

First we calculate the strain that will be caused on the crust by a change in shape from a sphere to a spheroid with semi-axis b<a.

STEP1:

We are going to work in the body reference frame.

Let's call the coordinates on the sphere $x_{0,}$ y_0 and z_0. The coordinates on the spheroid are $x_{1,}$ y_1 and z_1.

We have

$$\begin{aligned} x_0^2 + y_0^2 + z_0^2 &= 1 \\ \frac{x_1^2}{a^2} + \frac{y_1^2}{a^2} + \frac{z_1^2}{b^2} &= 1 \end{aligned} \tag{8.10}$$

We use the transformation:

$$\begin{aligned} x_1 &= x_0\ a, \\ y_1 &= y_0\ a, \\ z_1 &= z_0\ b. \end{aligned} \tag{8.11}$$

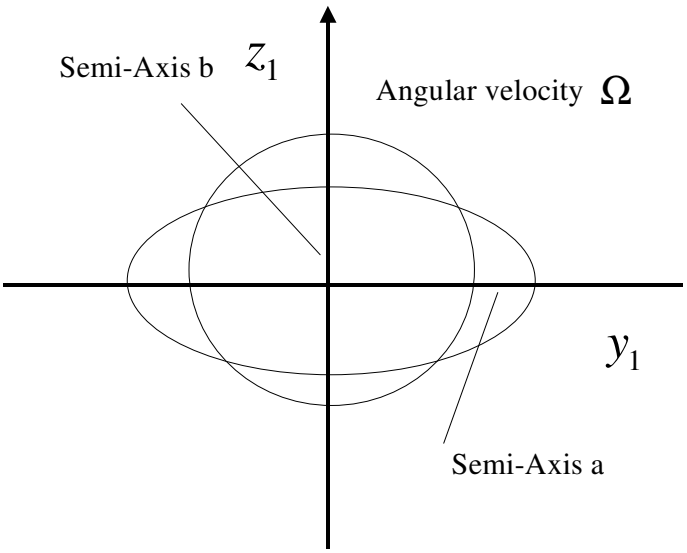

Figure 8.3: The transformation of the sphere of radius 1 to a spheroid with semi-axis b and a.

It is simple to verify that this 1-1 transformation changes the sphere to a spheroid:

$$\frac{x_1^2}{a^2} + \frac{y_1^2}{a^2} + \frac{z_1^2}{b^2} = \frac{a^2 x_0^2}{a^2} + \frac{a^2 y_0^2}{a^2} + \frac{b^2 z_0^2}{b^2} = x_0^2 + y_0^2 + z_0^2 = 1. \tag{8.12}$$

The transformation is illustrated in Figure 8.3.

If a point is located in the plane $y = 0$ then a point that goes from the sphere to the compressed ellipsoid (according to the previously explained transformation) will have the following position, given by the direction vector $\mathbf{r}_{1:}$

$$\mathbf{r}_1 = b(\mathbf{n}_1 \cdot \mathbf{r})\ \mathbf{n}_1 + a(\mathbf{r} - (\mathbf{n}_1 \cdot \mathbf{r})\ \mathbf{n}_1) \tag{8.13}$$

where $\mathbf{r} = (x, y, z)$ is the position of the point on the sphere, $\mathbf{n}_1 = (\sin\theta, 0, \cos\theta)$ is the unit vector in the $y = 0$ plane. The angle θ is the wobble angle. The ellipsoid is

tilted by the wobble angle around the y axis. The z axis represents the direction of the electrostatic deformation. The angular velocity, and therefore the centrifugal bulge is tilted by angle θ relative to the z axis.

STEP2:

Now we want to rotate the ellipsoid by angle ψ around the z axis. This is the motion of the centrifugal bulge in the reference frame. The quantity $\dot{\psi}$ is the precessional angular frequency. Now at any time the position of the deformation is at:

$$\mathbf{r}_2 = b(\mathbf{n}_2 \cdot \mathbf{r})\ \mathbf{n}_2 + a(\mathbf{r} - (\mathbf{n}_2 \cdot \mathbf{r})\ \mathbf{n}_2 \tag{8.14}$$

where:

$$\mathbf{n}_1 = (\cos\psi \sin\theta, \sin\psi \sin\theta, \cos\theta) \tag{8.15}$$

The displacement of any particle on the ellipsoid due to the readjustment of the deformation will be:

$$\mathbf{u} = \mathbf{r}_2 - \mathbf{r}_1 \tag{8.16}$$

This displacement of the material point on the spheroid will create a certain strain. The strain S is defined as:

$$S_{ij} \equiv \frac{1}{2}(\frac{\partial u^j}{\partial x^i} + \frac{\partial u^i}{\partial x^j}),\ \text{where } x^{1,2,3} = x_{0,} y_0 \text{ and } z_0. \tag{8.17}$$

This is equivalent to calculating the change in strain $S^{''}$ due to the initial deformation from the sphere to the ellipsoid and a transformation from the reference frame with Ω as z axis to the body frame of the precessing body. There is an angle $\theta + \widehat{\theta} \approx \theta$ between Ω and the axis I_3. So the transformation is equivalent to a rotation by an angle θ.

The tensor transforms in the following way:

$$S^{'} = R^{T} S^{''} R, \tag{8.18}$$

where:

$$R = \begin{bmatrix} 1 & 0 & 0 \\ 0 & \cos\theta & -\sin\theta \\ 0 & \sin\theta & \cos\theta \end{bmatrix} \tag{8.19}$$

Then the final transformation is a rotation about the a_3 axis by an angle ψ so that:

$$S = \Psi^{T} S^{'} \Psi \tag{8.20}$$

where:

$$\Psi = \begin{bmatrix} \cos\psi & -\sin\psi & 0 \\ \sin\psi & \cos\psi & 0 \\ 0 & 0 & 1 \end{bmatrix} \tag{8.21}$$

The strain on the deformed object is now the difference between the strain tensor $S^{''}$ in the Ω frame and the tensor $S^{'}$ calculated in the body frame. This step is justified because we want to subtract the strain due to the stretching from the sphere to the spheroid. What we obtain is the maximum strain possible on the spheroid. The difference between the strain tensors $S^{'}$ and S gives us the final strain tensor.

STEP 3:

Let's now define the quantity:

$$\varepsilon_{\Omega} = \frac{a - b}{a} \tag{8.22}$$

We have a further condition that to conserve volume in the transformation between the sphere and the ellipsoid we have to require

$$\text{Volume spheroid}=ba^2 = 1 = \text{Volume sphere} \tag{8.23}$$

This implies:

$$a = \frac{1}{(1-\epsilon)^{1/3}} \approx 1 + 1/3\ \varepsilon,\ b \approx 1 - 2/3\ \varepsilon \tag{8.24}$$

When all this is used in the equation for the components of the strain we get that to first order in ε :

$$\begin{aligned} S_{11} &= \varepsilon \sin^2\theta - \varepsilon \cos^2\psi \sin^2\theta,\ S_{22} = -\varepsilon \sin^2\theta \sin^2\psi \\ S_{33} &= 0,\ S_{12} = S_{21} = -\varepsilon \sin^2\theta \cos\psi \sin\psi \\ S_{13} &= S_{31} = \varepsilon \cos\theta \sin\theta\,(1-\cos\psi)\,,\ S_{23} = S_{32} = -\varepsilon \cos\theta \sin\theta \sin\psi. \end{aligned} \tag{8.25}$$

Therefore the transformed strain tensor is:

$$S = \begin{bmatrix} \varepsilon \sin^2\theta - \varepsilon \cos^2\psi \sin^2 & -\varepsilon \sin^2\theta \cos\psi \sin\psi & \varepsilon \cos\theta \sin\theta\,(1-\cos\psi) \\ -\varepsilon \sin^2\theta \cos\psi \sin\psi & -\varepsilon \sin^2\theta \sin^2\psi & -\varepsilon \cos\theta \sin\theta \sin\psi \\ \varepsilon \cos\theta \sin\theta\,(1-\cos\psi) & -\varepsilon \cos\theta \sin\theta \sin\psi & 0 \end{bmatrix} \tag{8.26}$$

STEP 4.

The maximum strains can be found calculating the eigenvalues of the strain matrix S. These eigenvalues are:

$$\begin{aligned} S_{ein1} &= -\varepsilon \sin\theta \sqrt{3 + \cos 2\theta + 2\cos\psi \sin^2\theta} \sin\frac{\psi}{2} \\ S_{ein2} &= -S_{ein1} \\ S_{ein3} &= 0. \end{aligned} \tag{8.27}$$

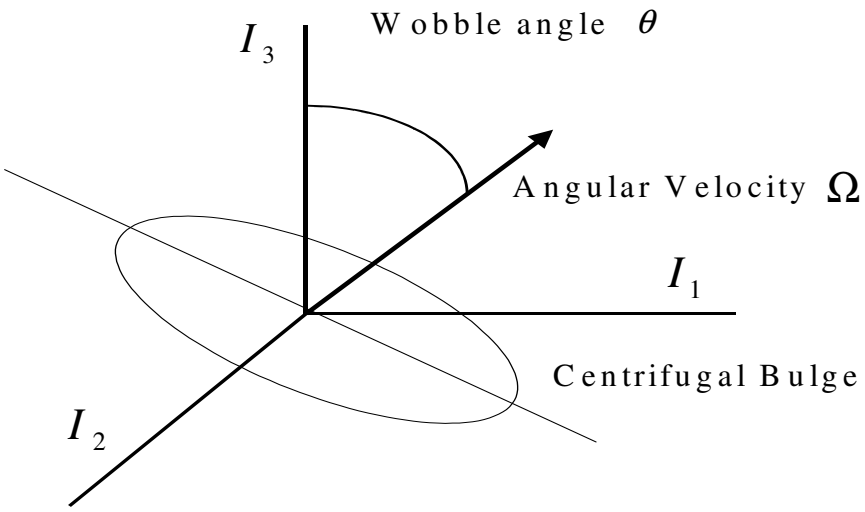

Figure 8.4: The second transformation in the calculation of the strain.

The average of the quantity S_{ein1} over a precession cycle is:

$$\langle S_{ein1} \rangle \approx -\varepsilon \sin\theta \tag{8.28}$$

The following figures show the dependency of the eigenvalue strain on the angle ψ for a given angle θ and the dependency of the strain on the angle θ for fixed ψ.

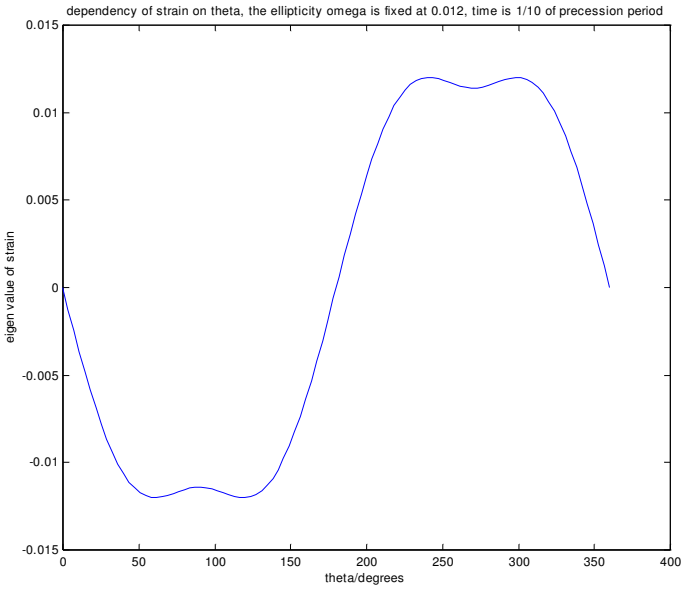

Figure 8.5: The strain depends on the angle theta almost in a sinusoidal fashion. The figure shows a particular moment in time. In average, over a precession period, the strain is proportional to the sine of theta.

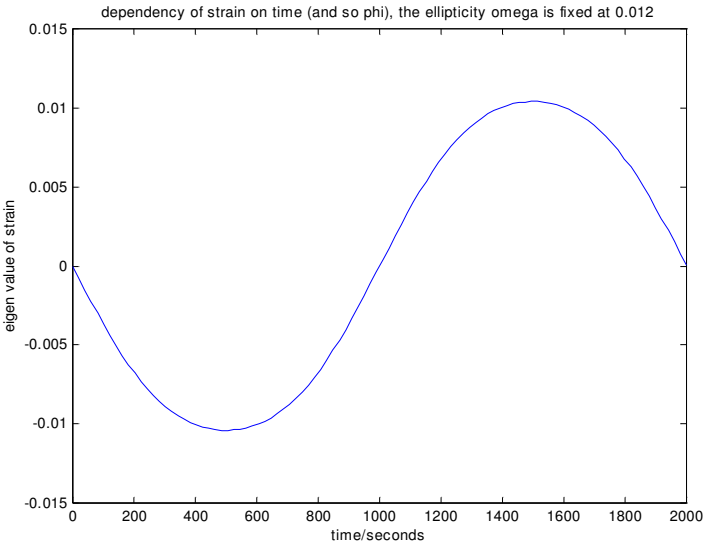

Figure 8.6: The strain is also a function of time. The strain depends on time as the sine of phi dot times the time.

CHAPTER 9
THE CASE OF TRIAXIALITY OF THE NEUTRON STAR

Our model for the precessing neutron star has been, up to this point, based on a star with an effective axissymmetric shape. We showed that, even in the presence of an additional deformation along the axis of rotation due to the centrifugal forces, the neutron star will have a precessional motion identical to that of a biaxial object. It is possible though that there are more than one Coulumb deformation in the crust and this will result in an effective triaxilaity of the body. The triaxial body precession motion is discussed in details in Classical Mechanics textbooks such as the L. D. Landau and E. M. Lifshits, *Mechanics* [16]. The gravitational emission of this object is described in the second of the Zimmerman papers [6].

The precession motion of a triaxial object is more complex than that of a biaxial one and its gravitational wave radiation spectrum has more than two emission frequencies. We are going to show though that when the ellipcity is small and the rotational frequency relatively high (in the hundred of Hz) the triaxial object motion is almost indistinguishable from that of the biaxial case. If we model SN 1987A remnant as a triaxial star, the power of the gravitational wave radiation is mainly at the rotational frequency and twice that, as in the biaxial case. The power in the sidebands is just 10^{-4}less than the power in the principal emission frequencies. This is an interesting result because it shows that, when studying the SN 1987A gravitational wave observability, we can model safely our neutron star as a biaxial object without loosing generality. This is going to be very important in the search for the gravitational wave

signal of the star, using a filter bank similar to that discussed in section 12.2.

9.1 The Most General Case of Precession

It is a very well known result of Classical Mechanics that the inertial properties of a rotating body of any shape can be reduced to that of an equivalent body with just three principal moments of inertia. For this reason the motion of a triaxial object is the most general case of precession. A discussion of the motion of a triaxial rigid body is given in Landau and Lifshits [16]. For reference we are going to write down the main equations that describe the motion of the triaxial object. The moments of inertia are all different and we have two quantities that define how much different is the object from being a perfect sphere. This object with three different moment of inertia is called an *ellipsoid*. Let's assume that $I_1 < I_2 < I_3$. The total angular momentum of the ellipsoid is L.

The *ellipticity* ε is:

$$\varepsilon = \frac{I_3 - I_1}{I_1} \tag{9.1}$$

and the *oblateness* η is:

$$\eta = \frac{I_2 - I_1}{I_1} \tag{9.2}$$

The motion of the triaxial object is more complicated than that of a biaxial object. Here the relevant equations for the Euler angles as a function of time t:

$$\psi(t) = \arctan\left(\sqrt{\frac{I_1\,(I_3 - I_2)}{I_3\,(I_2 - I_1)}}\frac{cn\,(\tau)}{sn(\tau)}\right) \tag{9.3}$$

and

$$\theta(t) = ar\cos\left(\cos\theta_0\ dn(\tau)\right) \tag{9.4}$$

also we have that:

$$\varphi(t) = -\sum_{n=1}^{\infty} \frac{2q^n}{n\left(1-q^{2n}\right)} \sin\left(\frac{4n\pi\ t}{T}\right) \sinh\left(2n\pi\alpha\right) + L\left(\frac{1}{I_1} + \frac{2\cos\theta_0}{KI_2}\sqrt{\frac{\left(I_3-I_2\right)\left(I_2-I_1\right)}{I_1 I_3}} \sum_{n=1}^{\infty} \frac{q^n}{1-q^n} \sinh\left(2n\pi\alpha\right)\right)\ t \tag{9.5}$$

where $\tau = \frac{L}{I_3}\sqrt{\frac{(I_3-I_2)(I_2-I_1)}{I_1 I_3}}t$, $sn(\tau),\ cn\left(\tau\right),\ dn(\tau)$ are the Jacobi functions, K is the complete elliptic integral of the first kind, T is the period of the Jacobi functions and the quantity $\alpha = G\left(\varepsilon,\eta,\theta_0\right)$, $q = H\left(\varepsilon,\eta,\theta_0\right)$ are functions of the ellipticity, oblateness and initial wobble angle θ_0.

It is possible to show [6] that in the astrophysically, relevant cases where the ellipticity and the oblateness are small quantities, the motion of the triaxial object approximates that of the biaxial one. For example we have that $\dot{\varphi} \ggg \dot{\psi}, \dot{\theta}$ and we have that $sn(\tau) \to \sin\left(\tau\right),\ cn\left(\tau\right) \to \cos\left(\tau\right),\ dn(\tau) \to 1$.

9.2 Sidebands in the GW Signal

S. Frasca and C. Palomba, presented at the Gravitational Wave Data Analyis Workshop in Trento, Italy (2001) the paper entitled *Gravitational radiation from triaxial neutron stars: Implication for data analysis [21].* In this paper the authors studied the gravitational wave emission characteristics of a triaxial neutron star. Zimmerman second paper gives the complete form of gravitational wave strain h as a function of time. It is difficult to interpretate the equations because they are very complicated involving elliptical integrals and Jacobi functions. The work of Frasca and Palomba points out that the main frequencies of emission are at $\dot{\varphi}\ /\pi$ and $\dot{\varphi}\ /2\pi$ with $\dot{\varphi}\ /\pi$ being close to the rotational frequency plus the small precessional frequency. The tri-

axial motion contribution is to modulate the main sinusoidal signal. The modulation frequency and its amplitude are:

$$A_{\phi} = 2\pi f_0 \varepsilon g\left(\theta_0\right) \tag{9.6}$$

and

$$f_m = 2\pi f_0 \eta g^{'}\left(\theta_0\right). \tag{9.7}$$

where $g\left(\theta_0\right)$ and $g^{'}\left(\theta_0\right)$ are functions of the initial wobble angle θ_0. The modulation splits the spectrum lines. The number of side lines and their power can be parametrized by the *modulation index* β*:*

$$\beta = \frac{A_{\phi}}{f_m} = \frac{\varepsilon}{\eta} g^{''}\left(\theta_0\right) \tag{9.8}$$

Frasca and Palomba have determined that for $\beta \leq 0.2$ there are two side bands at frequencies $f_0 \pm f_m$. For $0.2 \leq \beta \leq 0.5$ four sides appear at frequencies $f_0 \pm f_m$, $f_0 \pm 2\ f_m$. The power at these frequencies is $\frac{\beta}{2}$ and $\frac{\beta^2}{8}$ of the power at the main emission frequency. In the case of SN 1987A we have that the oblateness should be on the order of the ellipticity or less because otherwise the spin-down will be greater than what is observed. In fact, in Zimmerman is shown that the power is equal (in order of magnitude) in the ellipticity and oblateness contributions, in a triaxial precessing neutron star. Frasca and Palomba plotted graphs of f_m and β as a function of the ratio $\frac{\eta}{\varepsilon}$ and initial frequency f_0. Using the observed parameters of SN 1987A we get a value of $\beta < 10^{-4}$. We wrote a numerical code to simulate the rigid motion of a triaxial precessing neutron star and we used the quadrupole formalism to calculate the gravitational strain of this source. We also calculated the spectrum of the signal and

Table 9.1: The parameters used in the simulation for the 3 axis neutron star.

Angular momentum	400
angular frequency Ω_3	2π 1000
precessional frequency Ω_P	2π 200
wobble angle θ_0	35^o

verified the Frasca and Palomba results in order of magnitude. The following Figures show the Euler angles as a function of time and the spectrum of the strain h for a similar source with initial rotational frequency and precessional period as in Table 9.1. These values were chosen to evidentiate more clearly the results in their qualitative aspect. Finally we used the general solutions from Zimmerman second paper and solved them numerically. We compare the case of a biaxial star with total gravitational power equal to that of a triaxial star with same order of magnitude ellipticity. The ellipticity is of order 10^{-3}. The wobble angle is 30°. The large ellipticity is used for computational convenience. For smaller ellipticities we get even less power in the sidebands. Figure 9.2 shows the spectrum of these two cases and Figure 9.3 compares the cumulative power as a function of the frequency. We can see that even at a rotational frequency of 80 Hz the power in the sidebands is much less than the power in the main emission frequency. The ratio between the power in the main frequency and the one in the sidebands depends on the rotational frequency. As the star rotates faster and faster the power in the sidebands is less and less. We calculated this ratio for different rotational frequencies and kept the total power the same. We found a power law that describes the dependency on velocity

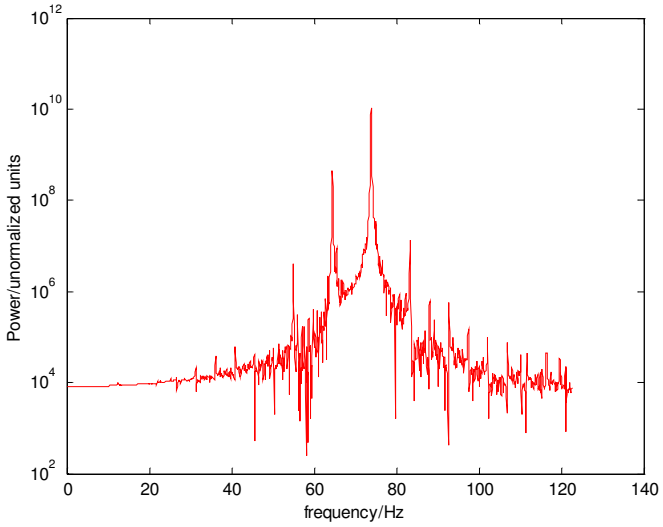

Figure 9.1: The power spectrum for a triaxial neutron star. This is the result of a computer simulation that solves the differential equation of motion of a precessing object.

of the ratio of the spectral power in the main emission frequency and the spectral power in the sidebands:

$$P_{main}/P_{sidebands} = 6.2951x10^{-41}\ f^{-3.3219}/10^{-45} \tag{9.9}$$

When we extrapolate this law to the rotational frequency of SN 1987A compact remnant we get $P_{main}/P_{sidebands} \approx 10^{-4}$.

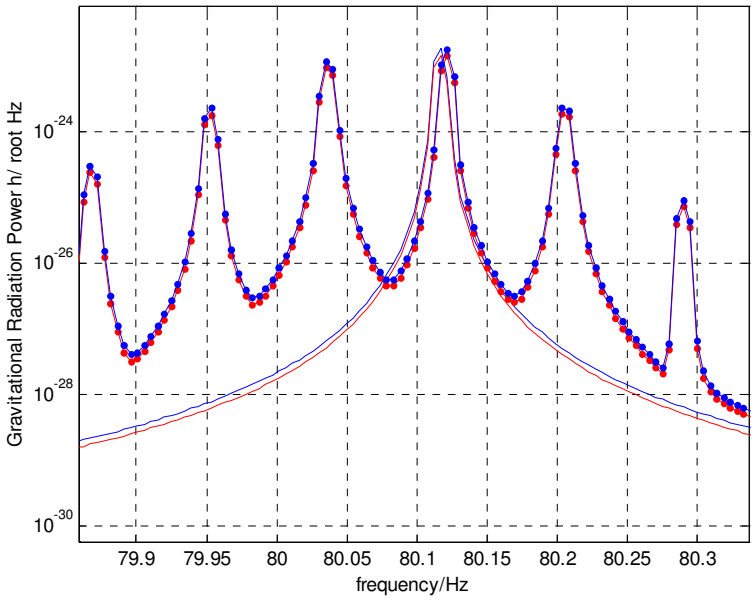

Figure 9.2: The comparison of the gravitational wave spectrum of a biaxial star compared with that of a triaxial star with same total power output. The frequency of rotation is at 80 Hz. The graph was derived using the Zimmerman expressions for the gravitational wave strain h.

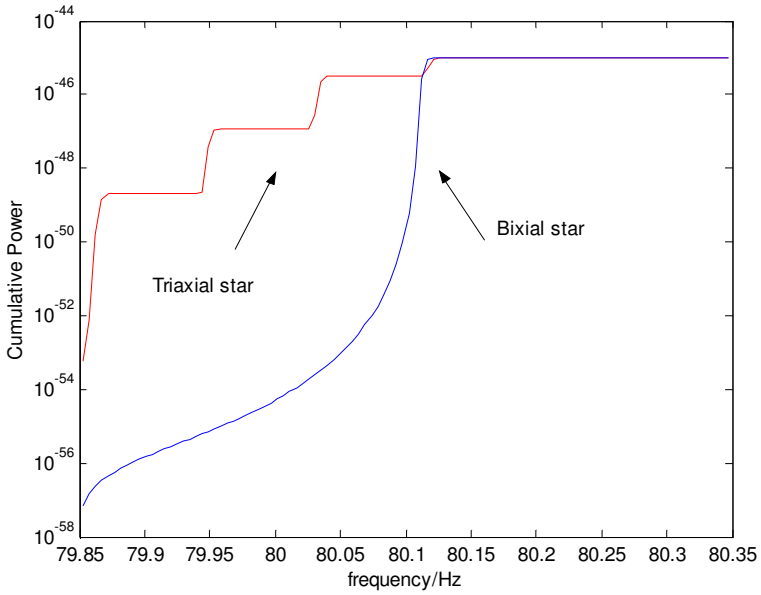

Figure 9.3: Cumulative power between frequency close to one of the main emission frequency. It is possible to notice that the energy in the sidebands is much less than in the the main emission frequency.

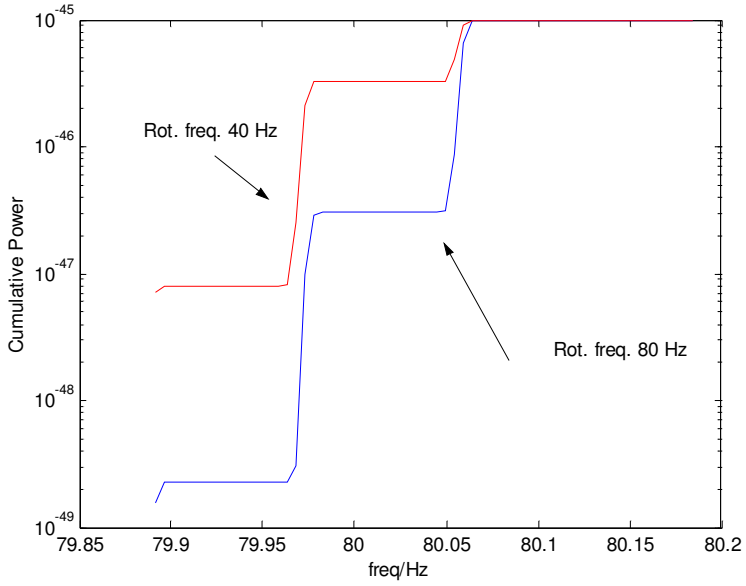

Figure 9.4: The energy in the sidebads it is dependent on the velocity of rotation. For a triaxial star rotating at 500 Hz the energy in the sidebands is 1e4 less than in the main emission frequency.

CHAPTER 10
LITERATURE ON PRECESSING NEUTRON STARS

In this Chapter is given a summary of some of the most relevant papers on the subject of precessing neutron stars and gravitational wave emission from these objects. Many authors speculated about the possibility of neutron star precession but just recently strong evidence of the existence of this phenomenon has emerged. We report here the findings of these observational evidence. A quite complete work that studied the many aspects of precessing neutron stars is the Ph. D. dissertation of I. Jones from University of Whales, Cardiff. Jones 's dissertation work resulted in the publication of a series of papers to which we referred extensively in this dissertation Two main papers are historically important in the discussion of the relevance of precession for gravitational wave detection. These are the paper of Zimmerman (actually the work it is a set of two papers) and the paper by M. A. Alpar and D.Pines. We review these papers in the following sections.

10.1 Zimmerman

Gravitational waves from rotating and precessing rigid bodies. Physical Review D, vol. 20, (1979).

This is the first set of papers that considers the emission of gravitational radiation from a precessing neutron star [5-6]. Prior to the year 1979, rotating neutron stars were considered as possible sources of gravitational radiation. Though it was assumed that the radiation was at twice the frequency of rotation. The model imagined was a star with a deformation on the plane perpendicular to the rotation frequency. This

object, of course, would not have any precessional motion. Zimmerman points out the more general case of a precessing rigid neutron star. In first paper Zimmerman consider the biaxial case, and the case of a triaxial object with a small wobble angle. In the second the author studies the most general case of a triaxial object for any possible wobble angle. The author uses the quadrupole formalism to calculate the waveforms of the strain h and the gravitational wave power. In particular he uses the equations (using the convention $c = G = 1$):

$$h_+ = h_{vv}^{TT} = -h_{vv}^{TT} = (-1/r)\left(\ddot{I}_{vv} - \ddot{I}_{ww}\right) \tag{10.1}$$

and

$$h_\times = h_{vw}^{TT} = (-2/r)\ \ddot{I}_{vw.} \tag{10.2}$$

.

The vectors v and w are mutually perpendicular and perpendicular to the direction of the observer. The vectors are transverse to the direction of wave propagation. The gauge used to calculate the above equations is called Transverse-Traceless, (the symbol TT refers to this gauge). Zimmerman shows in his paper graphs of the waveforms. It also shows how it is possible to obtain important information as the wobble angle, the level of ellipticity and the inclination of the angular momentum relative to the direction of the observer when we can obtain precise measurament of the plus and cross polarization of the gravitational wave signal of the precessing neutron star. Finally, Zimmerman makes the conjecture that the equations for the rigid body will also apply to the case of a star with elastic crust.

10.2 Alpar and Pines

Gravitational radiation from a solid crust neutron star. Nature vol. 314, 334-336, (1985). *[15].*

The main goal of this paper is to show the importance of gravitational radiation in understanding the properties of the crust of millisecond pulsars. The main finding is that if the effective triaxiality ε_{eff} of the star is bigger than 10^{-9} then the gravitational radiation emitted by the star will be enough to spin down the millisecond pulsars at a faster rate than the one observed. Different astrophysical phenomena are discussed: pinning of the crust by superfluid, the influence of the equation of state on the crust properties and different decay mechanisms.

10.3 Jones and Andersonn

Jones dissertation [23] is a very complete work on gravitational waves from precessing neutron stars. The rigid body case is studied and it is discussed the different modifications to the equations of motion needed when the elastic crust and a fluid interior is allowed. Jones consider the possibility of astrophysical mechanisms that can generate and can sustain the precessional motion. In fact, Jones also points out that the precessional motion will be damped by internal friction. The thesis of Jones is the source of a series of papers (with N. Anderson or Cutler as co-authors) to which we referred extensively in this work [15-17-18]. Jones and Anderson arrive to the pessimistic conclusion that there is not a large population of precessing neutron stars that can be detected by current or soon available gravitational observatories. We want to point out that the presence of one precessing neutron star, with a rotational frequency

in the hundred of Hz, will be a very important gravitational source and all what it is needed to establish the field of Gravitational Wave Astronomy. Jones and Anderson discuss SN 1987A remnant as a possible precessing neutron star but they show strong criticism towards the reality of this source. We already offered a rebuttal of some of their arguments in Section 5.3.

There are been different articles on the evidence of other precessing pulsars beside SN 1987 A in the recent past. Here a review of some of these papers.

10.4 I. H. Stairs, A. G. Lyne and S. L. Shemar

Evidence of free precession in a pulsar. Nature Vol. 406 August 2000 [10].

This article appeared in August 2000 in the journal Nature and can be considered the best evidence of free precession in a neutron star. It is reported that the pulsar PSR B1828-11 presents long-term periodical variations both in the shape of the pulse and the rate of slow down. This two parameters follow similar periodical patterns. The main periods are of order 250, 500 and 1000 days, clearly harmonically related. The pulsar time behavior has been followed in the last 13 years and the data is of very good quality. The authors suggest different kind of possible explanations for such time variations. They suggest the presence of planets that can interact with the magnetosphere of the star and cause in this way changes in the pulse profile. This is considered, though, unlikely because to reproduce the observed changes it will be required at least two planets with orbits at a very short distance from the pulsar. Another mechanism considered is timing noise due to random movement of the fluid inside the neutron

star but this will not be able to reproduce the sustained and periodical variations in the pulse shape. The simplest explanation for the observed data and the correlation between changes in the pulse shape and spin-down is that the star precesses. In fact, this will cause changes in the geometry of the beam as it is pointed towards the Earth reproducing the observed changes in the pulse. Moreover the precession will cause changes in the electromagnetic torque that will follow precisely the changes in the pulse profile. The authors also point out that the other two pulsars that present long term profile shape changes are PSR B1913+16 and B1534+12. These pulsars are undergoing precession due to general relativistic effects that it is a very different physical situation from the one of PSR B1828-11 but the final result is similar in the sense of long term changes in the shape of the pulse. Also in the case of the pulsar in question there are not other bodies to influence the motion implying that the precession is free. Finally it is pointed out that PSR B1828-11 is the only isolated pulsar (at the time of the discussion) that has such strong periodical variations in both the pulse shape and the spin down. The authors comment on the fact that the strong evidence of the existence of the precession phenomenon in a neutron star brings some theoretical problems to the model of pinned superfluid in neutron star. Table 10.1 shows the important parameters of the pulsar. The wobble angle is deduced by the changes in the width of the pulse. The ellipticity can be calculated by the usual ratio between the precession and rotation frequency..

$$\varepsilon = \frac{\omega_{rot}}{\Omega_{prec}\cos\theta} = \left(\frac{500 \text{ days}}{\Omega_{prec}}\right)\left(\frac{\omega_{rot}}{405ms}\right)\left(\frac{2/180\pi}{\cos\theta}\right) = 1.06 \times 10^{-8} \tag{10.3}$$

Table 10.1: Table of parameters from Stairs. et.al.

Period, P	405.03 ms
Period derivative, $\dot{P}$	60.03×10^{-15}
Period second derivative, $\ddot{P}$	$-1.7\times10^{-25}s^{-1}$
Magnetic field, B	$5.0\times10^{12}G$
Characteristic age, τ	0.11 Myr
Precession Period, P_{prec}	500, (250,1000 harmonics) days
Ellipticity, ε	10^{-8}
Dispersion Measure, DM	159.7 cm^{-3} pc
Wobble angle, θ	2-3 degrees

The result indicates that the ellipticity is very small, 100 times smaller than the one for SN 1987 A. This combined with the slow rotational speed makes this object not interesting for gravitational wave detection even if PSR B1828-11 stengthen the argument for the existence of precessing neutron stars.

10.5 B. Link and R.J. Epstein

Precession Interpretation of the Isolated pulsar PSR B1828-11 [25].

This article improves on the interpretation of pulsar PSR B1828-11 as a precessing pulsar. The authors main contribution is considering the effect of the coupling between the electromagnetic torque and the precession. They indicate that the precession induced geometrical effects on the beam pulse as seen by an observer are not sufficient to explain the observed data. They point out that it is necessary to consider

real physical coupling between magnetic torque and precession to more precisely fit the data with a model. They obtain parameters for this pulsar as the wobble angle, the angle between the magnetic field poles and the symmetry axis and the ellipticity. We have already seen that this pulsar is not useful for gravitational waves but represents the best evidence to date of the existence of long duration precessing neutron stars. This is a challenge to the idea of pinned to the crust superfluids inside the neutron star as also indicated by the authors.

10.6 T.V. Shabanova, A.G. Lyne, J. O. Urama

Evidence of Free Precession in the Pulsar B1642-03 [26].

This pulsar was discovered more that 30 years ago and it has interesting timing behavior. The main parameters of the pulsar are a period of 0.387 s, spin down rate of $1.78\times10^{-15}s/s$. This shows that the pulsar is relatively young with $\dot{P}\ /2P \approx 3.4$ Myr. The changes in the timing behavior that are attributed to precession are in the timing residuals and not in the pulse shape. The authors says that this could be due to the small magnitude and cyclical variation of the changes. They observe spectral features in the residuals that have frequencies of $2\times10-4$, $4\times10-4$ and $8\times10-4$ day^{-1} corresponding to periodicity of the order of 5000, 2500 and 1250 days. Their analysis suggests that this behavior can be explained with a free precession model of the star with a wobble angle of 0.8 degrees. Also this precessing neutron star is a not a good source for gravitational radiation but it is a further evidence that precessing neutron star indeed exist.

10.7 S. Nagataki and K. Sato.

In their article *Implications of the Discovery of Millisecond Pulsar in SN 1987 A* arXiv:asto-ph/0011363, 20 November 2000 [27] the authors address some of the astrophysical consequences of the discovery of a fast rotating neutron star in the remnant of SN 1987A. Most of their analysis is based on the fact that if we take seriously the information on the angular momentum and spin down of the pulsar, as given by the Middleditch observation, we should get some upper limits on energy loss mechanism and the radiation spectrum of SN 1987A. They try to extend these results to young pulsar in general. Using the known spin-down and rotational frequency we have already seen that we can calculate the energy loss $\dot{E}= I\Omega\,\dot{\Omega}$:

$$\dot{E}= -(4-6)\times 10^{39}\left(\frac{M}{1.4M_{\odot}}\right)\left(\frac{R}{10\text{ km}}\right)^{2}[\text{erg } s^{-1}] \tag{10.4}$$

this is much larger than the observed combined ultra violet, optical, infrared bolometric luminosity that is of order (1-2)$\times 10^{36}$ erg s^{-1}. Nagataki and Sato argue that this supports the idea that the observed spin-down should be attributed to the loss of energy due to only gravitational radiation. The situation is not very different when we are looking at other electromagnetic frequencies. The radio spectrum of SN 1987 A follows the following distribution:

$$S\sim 10^{-15}\left(\frac{\nu}{1GHz}\right)^{-1}[\text{erg } s^{-1}\text{cm}^{-2}\text{GHz}^{-1}],. \tag{10.5}$$

To create this fit, data was taken at the radio frequencies of 1.4, 2.4, 4.8 and 8.6 GHz. It is possible to extrapolate this power law to all the radio frequencies and

integrate such function to obtain the total luminosity:

$$L_{radio} = 3 \times 10^{32} \left(\frac{D}{50kpc} \right)^2 \log_e \left(\frac{\nu_{\max}}{\nu_{\min}} \right) \tag{10.6}$$

where D is the distance from the Earth and ν is the radio frequency. Also in the radio spectrum as in the optical and infrared it is possible to see that the loss in energy is much less than the rotational energy loss. The authors also make the argument that actually the energy in the radio spectrum comes from relativistic electrons generated in the supernova shock encountering the circumstellar matter, so not directly related to the rotating neutron star. The discussion moves further to the soft X-ray spectrum. It is known by Chandra telescope observations that there is an upper limit of 2.3×10^{34} erg s^{-1}in this part of the spectrum Theoretical calculations show that the debris around the pulsar should be opaque to soft X-rays. In the case of hard X-rays there is not much information available. We can estimate the gamma ray luminosity to be:

$$L_{gamma} \sim 8 \times 10^{37} \left(\frac{D}{50kpc} \right)^2 \left(\frac{E_{\max}}{100KeV} \right) \tag{10.7}$$

where $E_{\max}$ si the maximum energy of the gamma-ray photons. This radiated energy is comparable with the loss of rotational energy observed in SN 1987 A. The current understanding though is that the energy in this frequency comes from the radioactive decay of elements as ^{56}Co and ^{57}Co. The authors make the remark that it will be also very difficult to imagine a radiation mechanism that will emit so much energy in the gamma ray frequency but many order of magnitude less energy in the other part of the electromagnetic spectrum. Next the authors try to use some reasoning similar to that of Chapter 6 to put some upper limits on the magnetic field of the pulsar assuming

that all the observed spin down is due to dipole radiation. Against the energy loss due to the dipole radiation can be written as:

$$\dot{E}= -\frac{B_p^2 R^6 \Omega^4}{c^3}, \tag{10.8}$$

where B_p is the intensity of the magnetic field and Ω is the rotation frequency in the authors notation. Using the known data they conclude that:

$$B_p \leq (4-5) \times 10^{10} \left(\frac{M}{1.4 M_\odot}\right) \left(\frac{10km}{R}\right)^4 \tag{10.9}$$

This result is similar to the one derived in Chapter 6 that shows that the magnetic field of SN 1987 A remnant has to be small.

The discussion that follows in the Nagataki and Sato article is about gravitational radiation from the pulsar. This discussion is quite imprecise for different reasons. First the authors use the equation

$$\dot{E}_{grav}= -\frac{32}{5}\frac{G}{c^5} I^2 \varepsilon^2 \Omega^6 \tag{10.10}$$

to characterize the loss of energy due to gravitational wave emission. This equation is the one valid in the case of absence of precession and the presence of a deformation in the crust perpendicular to the axis of rotation. We already seen that actually in the case of precession the energy loss is "split" between the two "modes" of radiation at Ω and 2Ω. The exact ratio of energy loss in the split is determined by the wobble angle. The authors take this formula as a kind of upper limit for the energy loss due to gravitational radiation. The problem with this is when they use this formula to

calculate the strain h of the radiation on Earth. They use the expression:

$$\langle h \rangle \approx 5.1 \frac{G}{c^4 D} I \varepsilon \Omega^2 \tag{10.11}$$

to arrive to the result that:

$$\langle h \rangle \sim 7.8 \times 10^{-27} \left(\frac{I}{1.1 \times 10^{45} g\ cm^2} \right) \left(\frac{\varepsilon}{10^{-6}} \right) \left(\frac{\Omega}{2936 s^{-1}} \right) \left(\frac{50 kpc}{D} \right) \tag{10.12}$$

This result again doesn't specify if we are talking about the radiation at Ω or 2Ω. Also there is not consideration of the fact that the moment of inertia involved in the precession could be less than the total moment of inertia of the entire star.

Their value of h is not also so good as an upper limit because we get that the radiation at Ω is about 30 % higher than what they calculate when an angle of 40 degrees is used (equivalent to all the star involved in precession). Finally it seemed that there is a mistake in the calculation of the integration time because they use a formula that has a linear dependence in time for the minimum noise required in the instrument that is not the case. In fact, improvements in Siganl to Noise Ratio of the detector grows with the square root of time. The authors conclusion that it will be possible to observe the SN 1987A remnant gravitaional wave output using detectors with noise level around $h \sim 10^{-22}/\sqrt{Hz}$ is quite unlikely.

CHAPTER 11
RELEVANT TIME SCALES

In this chapter we discuss some of the relevant time scales and other important parameters for the understanding of precessing neutron star as sources of Gravitational Waves.

11.1 Dynamical Time Scales

Neutron stars can be, at a first approximation, treated as a thermal system in equilibrium. Perturbations from this equilibrium can be studied in terms of statistical mechanical laws. According to the virial theorem in average the absolute value of the potential energy is equal to twice the kinetic energy per unit mass.

In a star the kinetic energy is due to the thermal motions of the atomic particles whose speeds are of the order of the speed of sound v_s :

$$\frac{GM}{R} \approx v_s \tag{11.1}$$

where G is the gravitational constant, M is the mass and R the radius of the star. We can do an order of magnitude estimation of the stellar vibration frequency by noting that the period P_{vib} should be of the same scale of the time that it takes to transmit information about pressure changes across the entire star. This time, of course, is equal to $2R/v_s$, so we have [22]:

$$P_{vib}^{-1} = \nu_{vib} \approx \frac{v_s}{2R} \approx \sqrt{\frac{GM}{4R^3}} \approx \sqrt{\pi G \rho} \tag{11.2}$$

where ρ is the density of the stellar material.

Table 11.1: Dynamical time scales for neutron stars.

density	ρ	3×10^{15} g/cm^3
Period vibration	P_{vib}	10^{-4} seconds
Period rotation	$P_{rot-\min}$	$3\times\ 10^{-4}$ seconds

The maximum rotational frequency is given by the equilibrium between centrifugal and gravitational forces. At a higher frequency the star will be broken apart. So we have that:

$$R\nu_{rot-\max}^2 = \frac{GM}{(2\pi R)^2} \tag{11.3}$$

and the minimum rotational frequency:

$$\nu_{rot-\min} = P_{rot-\min}^{-1} = \frac{1}{\pi}\sqrt{G\rho} \tag{11.4}$$

We can summarize the important dynamical scales and parameters of the neutron star, as in Table 11.1.

These are upper limits but the presence of magnetic fields can reduce the mimimum rotational period. We also know that neutron star densities can vary considerably and the vibrational period can be different by a factor of 10 from the one reported in the Table 11.1. The crust of the neutron star is in general less dense than the the average density value of the star, therefore a typical value for its resonant frequency is around few thousand Hz.

11.2 Decay Time and Mechanisms

In the paper *Gravitational Wave Damping of Neutron Star Wobble* [18] by Cutler and Jones there is a discussion on the time scale in which the precession of the neutron

star can exist. The main question that is explored is how the loss of energy due to the gravitational wave emission effects of the precession motion. We already seen that because of the loss of energy the spin of the star decreases. There is also another mechanism that affect the precession motion. The torque due to the gravitational wave back reaction causes the wobble angle to decrease over time. Their conclusion is that the wobble angle will decrease exponential with a characteristic damping time τ_θ.

From Cutler and Jones paper the gravitational damping time is:

$$\tau_\theta = -\frac{\theta}{\dot{\theta}} = \frac{\omega\theta^2 I_0 \epsilon_{eff}}{\dot{E}} \tag{11.5}$$

This can be parametrized as:

$$\tau_\theta = 1.8 \times 10^6 yr \left(\frac{10^{-7}}{\Delta I/I_0}\right)^2 \left(\frac{kHz}{f_{rot}}\right)^4 \left(\frac{10^{45} gcm^2}{I_0}\right) \tag{11.6}$$

When the following equation is applied to SN 1987A compat remnant we get a value for the gravitational damping time equal to 9.42 10^4 years. This shows that the wobble angle has not changed very much since the birth of the neutron star if gravitational radiation is the main dissipation mechanism in SN 1987A. A much more efficient mechanism for damping the precession motion is any strong dissipation processes inside the star. In particular crust-core interaction and the pinning to the crust of vortices in the superfluid are very efficient in damping the wobble angle.

The damping time τ_w due to crust-core coupling [16-17] is:

$$\tau_w = \frac{\omega}{\Omega_p}\tau = \left(\frac{3}{2} b\epsilon_0\right)^{-1} \tau \tag{11.7}$$

where τ is the crust-core coupling time. The value of τ is about 20 P, where P is the precession period, for the case of a superfluid with electrons and protons. The value of

τ becomes 400 P for the case of neutron superfluid [19]. The value is $b\epsilon_0 \approx 10^{-7}$ for SN 1987A. This gives a maximum crust-core coupling decay time about 0.2 years. This implies that there is no much coupling between the crust and the superfluid material in SN 1987A. The presence of the precession in SN 1987A tells in general that there are not very efficient dissipation mechanisms inside the neutron star.

CHAPTER 12
OBSERVABILITY OF SN 1987A WITH PRESENT AND FUTURE DETECTORS

12.1 The Gravitational Strain h on Earth

Zimmerman in his papers [6-7] treats the case of a spheroid first ($I_1 = I_2 < I_3$ and any angle θ) and obtains the following expressions for the strain parameter h of gravity waves from a neutron star at a distance r from Earth and moment of inertia I_1.

$$\begin{aligned} h_+ &= \frac{G}{c^4}\frac{2I_1\omega^2\varepsilon\sin\theta}{r}\left[(1+\cos^2\ i_s)\sin\ \theta\cos 2\omega t + \cos i_s \sin i_s \cos\theta\cos\omega t\right], \\ h_\times &= \frac{G}{c^4}\frac{2I_1\omega^2\varepsilon\sin\theta}{r}\left[2\cos\ i_s \sin\ \theta\sin 2\omega t + \sin i_s \cos\theta\sin\omega t\right], \end{aligned} \tag{12.1}$$

where i_s is the angle between the angular momentum vector **J** and the plane of the observer sky. This quantity is unknown. It is important to notice that the time dependence of the wave forms is sinusoidal with two main frequencies at ω and 2ω. If the object was rotating along its symmetry axis it will emit just at a frequency 2ω (it will have also to be deformed along the axis perpendicular to the rotation axis). Knowing the angle θ restricts the possible waveforms of the signal to a simply related family parametrized by the unknown angle i_s. This should simplify greatly the search for the SN 1987A signal by gravitational wave detectors.

From the previous sections we can summarize that the relevant parameters are: the rotation frequency f_r the of pulsar:

$$f_r = 467.5\ Hz. \tag{12.2}$$

In the case of a precessing neutron star the gravity wave emission will occur at the

frequencies f_r and f , where:

$$f = 2f_r = 934.5\ Hz,$$

the distance r of the object, located in the Large Magellanic Cloud:

$$r = 50Kpc = 1.5 \times 10^{21} m, \tag{12.3}$$

Another important parameter is the ellipticity ε:

$$\varepsilon = (a-b)/\sqrt{ab} = \frac{\Omega_p}{\omega_3} = \frac{2.1 \times 10^{-6}}{\cos\theta}, \tag{12.4}$$

where a and b are the major and minor axis of the spheroid. In the section 5.2 the minimum wobble angle θ was calculated to be around 30 degrees.

Then we can apply the usual formula for the average size of the strain parameter h, due to the emission of gravity waves from a rotating neutron star with axisymmetric deformation ε, as given by Zimmerman [6-7]:

$$\begin{aligned} h(\omega) &= \frac{G}{c^4}\frac{2I_1\omega^2\varepsilon\sin\theta\cos\theta}{r}, \\ h(2\omega) &= \frac{G}{c^4}\frac{2I_1\omega^2\varepsilon\sin^2\theta}{r}, \end{aligned} \tag{12.5}$$

where the value of the moment of inertia I_1 for a neutron star (depending on equation of state), should be $3\times10^{44} g\ cm^2 \lessapprox I_1 \lessapprox 3\times10^{45} g\ cm^2$, we choose an average value for I_1.

When the above listed values are substituted in equations 12.5, we get a value for our SN 1987A gravitational wave signal h_s:

$$h_s(\omega) = 1.026 \times 10^{-26}, \tag{12.6}$$

$$h_s(2\omega) = 6.002 \times 10^{-27}. \tag{12.7}$$

This very small value for h can appear to require an impossible level of sensitivity from the bar detectors or interferometers existing today or soon available. It is important to notice that the source is a continuous source of radiation, of which all the fundamental parameters (besides the phase of the signal) are known. So it possible, in principle, to integrate the detector data over a long period (even years) to extract the signal from noise. A detailed calculation of the necessary integration time τ is required. To do so we use the following equation:

$$h_n = \sqrt{S_h(f_0)}\sqrt{BW}, \tag{12.8}$$

This equation expresses the level of the stain h_n of the noise in the data from a detector with characteristic noise spectrum S_h. The equation evaluates the value $S_h(f_0)$ of the spectrum at the precise frequency f_0 of the looked for gravitational wave signal. The quantity BW is the bandwidth of the periodic signal. From Fourier Analysis theory in the case of a sinusoidal signal, the value of BW is:

$$BW = \frac{1}{\tau}, \tag{12.9}$$

where τ is the observation or "integration" time.

So we can rewrite equation as:

$$h_n = 10^{-19}\frac{1}{\sqrt{Hz}}\sqrt{\frac{1}{\tau}}. \tag{12.10}$$

The value for $\sqrt{S_h(f_0)}$ it is extracted from the observed spectrum of the ALLEGRO detector, see Figure 12.1.

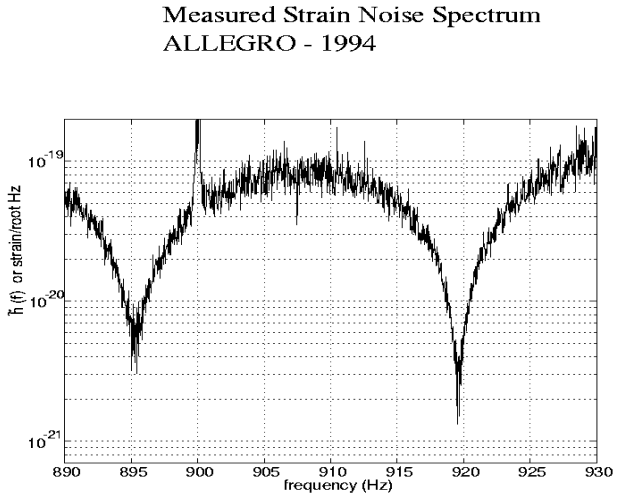

Figure 12.1: Spectrum of stain noise in ALLEGRO in 1994. The spectrum is represented as if all the noise was due to gravitational waves.

Solving for τ we have:

$$\tau = \left(\frac{10^{-19}}{h_n}\right)^2 \text{ seconds.} \tag{12.11}$$

Now we require that the noise level in the data from the detector be at least of the same size of the signal (it should less, 4 times less for a 4 σ confidence level in the statistics, for example). So if h_n is chosen to be $\approx h_s = 10^{-26}$ then we get that:

$$\tau = \left(\frac{10^{-19}}{6 \times 10^{-27}}\right)^2 \text{seconds} \approx 2 \times 10^{14} \text{ seconds} \approx 6 \times 10^6 \text{years.} \tag{12.12}$$

This is of course too long a time to conduct an experiment.

We could also ask what is the required level of sensitivity $\widetilde{h}_{f_o} = \sqrt{S_h(f_0)}$ of our detector at that particular frequency of observation to require a more acceptable time of integration, let's say 3 years, to have a positive detection of a gravity wave signal from our source SN 1987A. In this case we solve for $\sqrt{S_h(f_0)}$ to get:

$$\widetilde{h}_{f_o} = \sqrt{S_h(f_0)} = \left(\frac{h_n}{\sqrt{\left(\frac{1}{\tau}\right)}}\right), \tag{12.13}$$

and substituting the above mentioned values for h_n and τ, we have:

$$\begin{aligned} \widetilde{h}_{f_o} &= \left(10^{-26}/4\ \sqrt{\tau}\right) = \left(10^{-26}/4\ \sqrt{3 \times 3.1 \times 10^7 \text{ seconds}}\right) \\ &= 3.1 \times 10^{-23}/\sqrt{Hz}. \end{aligned} \tag{12.14}$$

This value for $\widetilde{h}_{f_o}$ could be reached by the next generations of gravity wave detectors. In fact preliminary estimates of the noise spectrum of the second generation Laser Interferometer, LIGO II are very promising. LIGO II will be built on the experience of the first LIGO and will be much better gravitational wave observatory. It

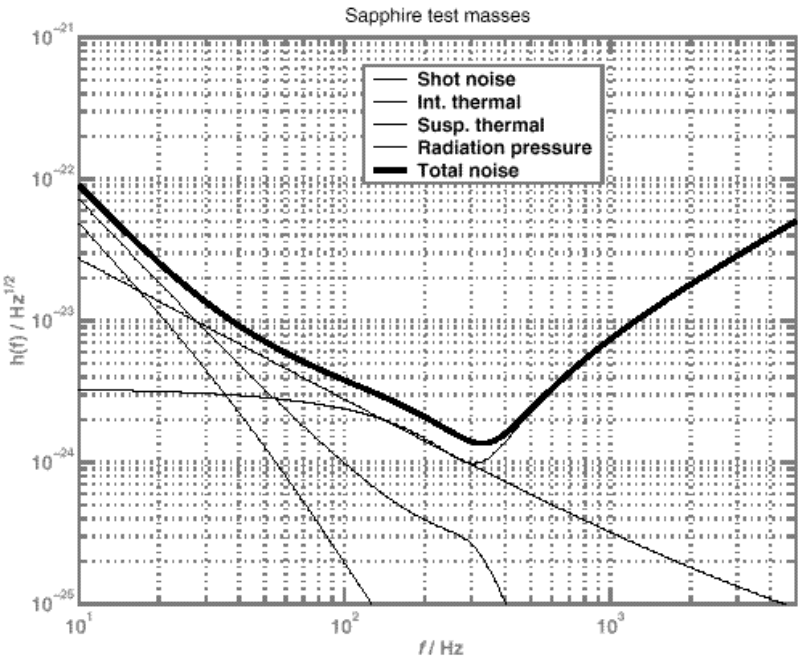

Figure 12.2: Projected LIGOII total strain noise and different sources of noise.

will be on line in 4 or 5 years from now. According Figure 12.2 there is a lowest point in the total strain-noise (the sum of different kind of expected noises). This point is about $h(f_r)$ =1.3×10^{-24} /$\sqrt{Hz}$ at a frequency of 350 Hz. But the LIGO II detector will be able to use narrow banding to shift this lowest point in noise level to higher frequencies. So we could take this as the level of noise at the frequency of emission of SN 1987A. This means that, if the totality of the spin-down is due to gravity emission, it will be needed just 5 days of integration time of Ligo II data to see the signal from the pulsar SN 1987A (at the ω frequency).

Figure 12.3 shows the general dependency of the integration time on the possibles moments of inertia of the star's mass involved in the precession. It is clear that LIGO

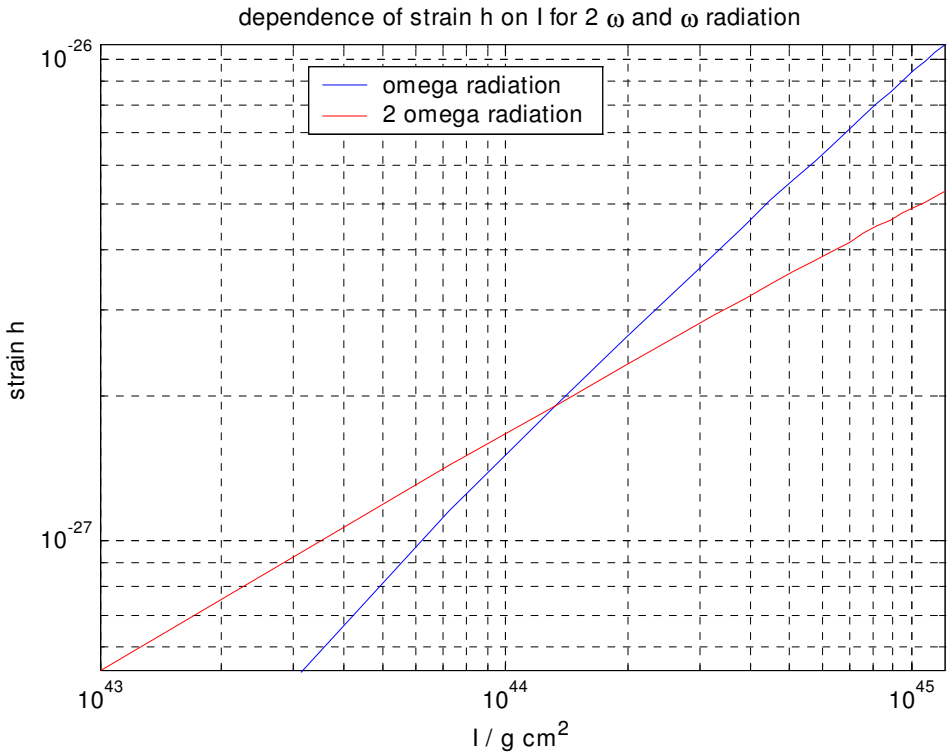

Figure 12.3: The value of the starain h for the ω (blue) and 2 ω (red) radiation at Earth as a function of the moment of inertia involved in the precession. Higher values of the moment of inertia are the more likely because of the limits on the crust strain.

II could detect a signal coming from SN 1987A even for very small moments of inertia if the integration time is on the order of few years.

It is possible that other sources will be detected before but it will be still a very important scientific discovery to detect gravitational waves from the famous Supernova remnant 1987A.

The ALLEGRO detector is supposed to be soon updated with a new transducer and a new SQUID. The detector, due to the new transducer design will behave as a 3 modes oscillator. Together with improvement in the SQUID this will increase the sensitivity and frequency range of the detector. It is possible that at the frequency

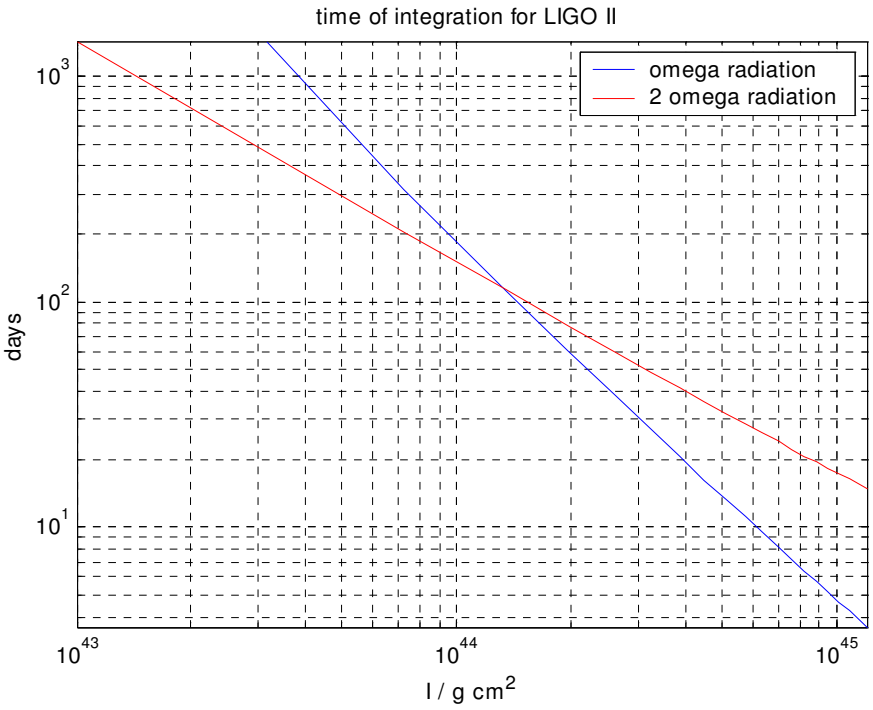

Figure 12.4: The required time of integration for a 4 sigma detection of the ω (blue) and 2 ω (red) radiation using LIGO II.

range of the SN 1987A gravity wave emission at 2 ω (the bar will not be able to see the signal at frequency ω) the noise level $\widetilde{h}_{f_0}$ will be as low as

$$\widetilde{h}_{f_0} = 10^{-21}/\sqrt{Hz}, \tag{12.15}$$

for the updated detector.

So we could ask : with this new sensitivity if we conduct a search for gravity waves from SN 1987A which kind of limit we could put on the ellipticity of the neutron star, if we do the analysis over 3 years worth of data?

If we write the h_s of the signal as

$$h_s(2\omega) = 2.4 \times 10^{-21}\ \varepsilon, \tag{12.16}$$

to isolate the ellipticity contribution to the value of h_s, the we get:

$$\begin{aligned} \varepsilon &= \frac{\widetilde{h}_{f_0}}{2.4 \times 10^{-21}\ \sqrt{\tau}} = \frac{10^{-21}/\sqrt{Hz}}{2.4 \times 10^{-21}\ \sqrt{3 \times 3.1 \times 10^7 \text{ seconds}}} \\ &= 4.3 \times 10^{-5}, \end{aligned} \tag{12.17}$$

where this equation is derived from formula (12.12).

Determining the level of non-axisymmetry of a neutron star with such precision could be a very interesting astrophysical result even if gravity waves will not be detected in this particular search.

The calculated waveforms for the entire signal (h_+ and $h_\times$ polarizations) and its ω and 2 ω components separately are shown in the following figures. The unknown angle i_s is arbitrarily chosen to be close to 90 degrees (to show better the differences between the two polarizations).

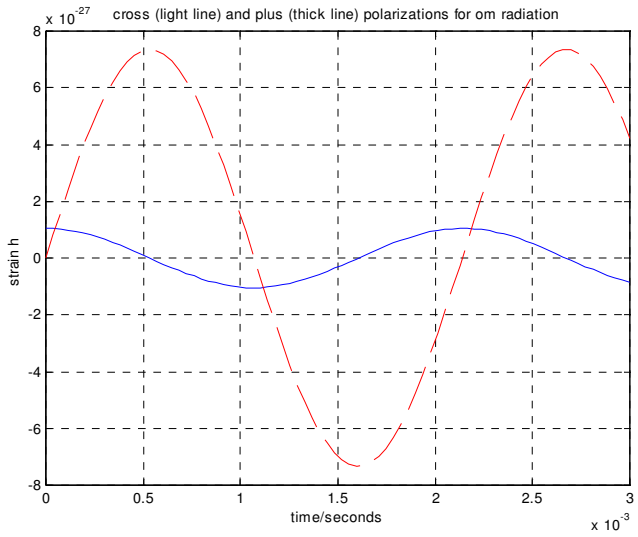

Figure 12.5: The emission for the plus (thick line) and cross (ligth line) polarization of the Ω radiation.

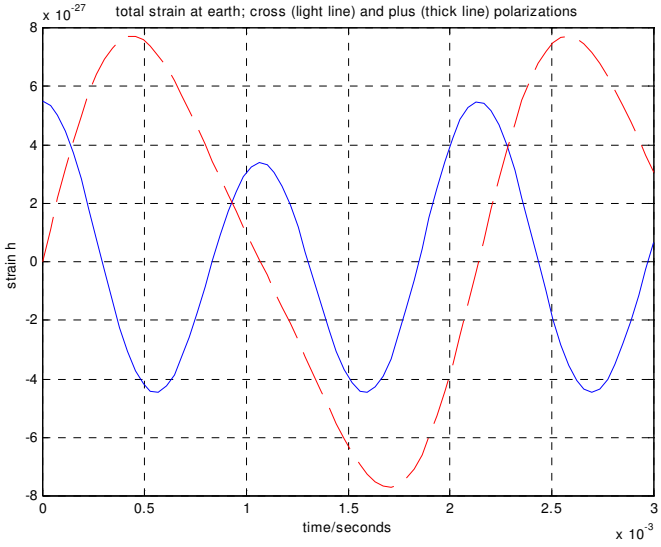

Figure 12.6: Radiation with chosen inclination angle about 90 degrees; wobble angle 30 degrees.

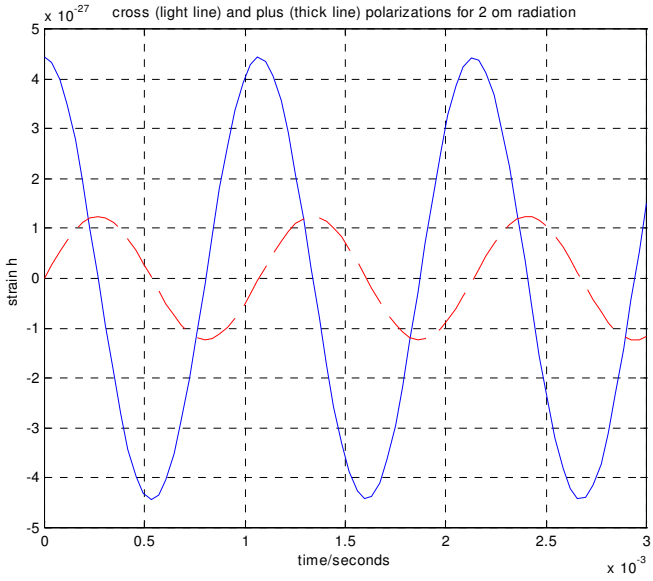

Figure 12.7: Radiation for the 2 omega frequency. The light line represents the cross polarization and the thick line represents the plus polarization. The parameters used are that of SN 1987A.

12.2 Data Analysis Issues: the Search of a Template for the Signal

The discussion of the previous section uses the assumption that the signal from SN 1987A is a sinusoidal function of time with a constant frequency. When this is assumed the analysis of the integration time required to observe the source is exactly valid. To apply the integration algorithm and obtain an increase of the signal to noise ratio proportional to the square root of the integration time one has to follow the phase of the signal quite closely. The model of the previous section is very simple but for what concern establishing the possibility of detection of SN 1987A gravitational wave signal one has to be careful in modelling the characteristic of the source in a more realistic way. We already pointed out that from Middleditch et al. data is possible to observe changes in the precession period, the spin down rate and frequency. This changes suggest that

the motion of the presumptive SN 1987A compact remnant is quite complicated and it cannot be modeled in the filtering process as a simple precessing object. Any attempt to detect the signal from such source will have to construct a template that reproduces the behavior of the source. The changes in the precessing period and spin-down introduce a phase change in the target signal. If this phase changes are not properly taken in consideration the integration procedure will not be effective and actually over time a signal loss will occur instead of a Signal to Noise Ratio increase. An illustration of this is given in Figure 12.8. In this Figure we show the increase of the Signal to Noise Ratio as a function of time for a search of a signal of which parameters are perfectly known (we used the exact of behavior of SN 1987A as in the first few days of observation). We compare this calculation with the result for the Signal to Noise Ratio of a signal search that uses a template that is a simple monocromatic source with parameters similar to that of SN 1987A but without changes in the phase induced by the changes in spin-down and precession period. The filter used in this case is often called non-perfectly matched filter. We notice that after a few days there is not a further increase in the SNR for the case of the non-perfectly matched filter. During the period Middleditch et al. conducted their observations we had some information on the changes in the parameters of the pulsar as the precession period, spin-down and frequency and we could have used this information to construct an adequate template if we could have conduct the search at the time. We cannot rely on such detailed information in future searches (when LIGO II will be on line for example) because as we explained before the optical source has faded away. What has to be done then is a blind search of parameters

that characterize the source. There is an extensive literature on this subject [28-29] and one of the main techniques to deal with this problem is to model the phase changes with a Taylor expansion of the phase. Then the detection problem consists in searching for the appropriate spin down derivatives that determine the shape of the phase function of time. A template bank is constructed made of a multidimensional grid of parameters that need to be tried in modelling our source. The dimension of the grid is determined by how many derivatives of the spin we need to explore and how fine the grid needs to be is determined by how much close our model needs to be to the real signal. The number of dimensions and how fine the grid is determines subsequentely the size of the grid. In the end the search for the signal using filtering techniques becomes a computational problem because the size of the grid determines the computer time required to extract the signal from the noise. One can think that the apparent complicated motion of SN 1987A will require a very intensive search over the parameter space making the computational task of such search completely impossible. But this turns out not to be the case. The first thing to point out is that even if there are changes in the precession period, spin-down and frequency we have already shown that other parameters as the wobble angle don't change. This is consistent with our model of a precessing neutron star with an effective biaxiality that endures changes in the ellipticity by a factor of 1.5. The precession period and spin down are not independent parameters but they seem to be related with the relationship General Relativity suggests is appropriate for a precessing object. The precession changes introduce a change in phase indirectly through the related changes in spin down. The next thing to point out is that looking

at the data it seems that the changes in the spin down are quite smooth and they happen over a relatively extend period of time. The biggest changes seem to have happened in the first 400 days of observation while in the other 1200 days the changes seem to subside and become much smaller. This can be interpreted as a stabilization of the source as the crust solidification process becomes more advanced and the crust tends to be more uniform. So it likely that in the future the source is going to be even more stable. But even if we consider the biggest changes observed we can see that they are actually quite small when compared in a frame time of few days that is what is required for detection of most of the model sequence considered in the previous section. This indicates that maybe the problem of detection is not so impossible after all. We can make this more precise. We are going to estimate how big the parameter space needs to be. We show here that simple templates that describe the observed behavior can be constructed, and that the required number of such templates and the total computational effort needed to adequately keep track of the phase and to detect a signal with the presumed properties is within current computational capabilities as long as there is phase stability over a time series of length comparable or longer than the integration time. Since the required integration times are on the order of 10-30 days, and the phase stability in the Middleditch data was comparable or better than that, this requirement is likely to be satisfied. Following standard treatments we write the time-dependent frequency as a Taylor series

$$\phi(t) = \sum_{n=o}^{\infty} \frac{\omega_n(0) t^n}{n!}, \tag{12.18}$$

where $\omega_n(0)$ indicates the n-th derivative at some arbitrary reference time taken to be zero without loss of generality. A given choice of the parameters $\omega_n(0)$ constitutes a particular choice of template. Then the phase difference between two different templates is:

$$\Delta\phi(t) = \sum_{n=o}^{\infty} \frac{\Delta\omega_n(0)t^n}{n!} = \Delta\omega_n(0)t + \frac{1}{2}\Delta\,\dot{\omega}\,t^2 + ..., \tag{12.19}$$

where $\Delta\omega$ and $\Delta\,\dot{\omega}$ refer to the separation in our parameter grid in the frequency and spin down dimensions. To determine then how fine the grid needs to be we impose the 1/4 of a cycle criterion [29] or:

$$\Delta\phi = \Delta\,\dot{\omega}\,\frac{t^2}{2} \leq \frac{\pi}{4}. \tag{12.20}$$

Now for most of the range in the moment of inertia considered in the previous section a typical detection time is of order of 10 days $\approx 10^6$. The spacing in frequency dot then is of order

$$\Delta\,\dot{f} = \frac{\Delta\,\dot{\omega}}{2\pi} = \frac{1}{2}\pi t^{-2} \approx 2.5 \times 10^{-13}\ Hz/s \tag{12.21}$$

Finally the number of nodes N_d needed is:

$$N_d = \frac{\text{range of spin down change}}{\text{spin down spacing}} = \frac{1 \times 10^{-10} Hz/s}{2.5 \times 10^{-13} Hz/s} \approx 400\,(\tau/10\text{ days})\,, \tag{12.22}$$

where τ is the integration time.

We could make our model even more precise including higher derivative of the spin down but again the relative small changes in the spin down don't really require including higher derivatives. In any case the number of nodes in the grid for higher

derivatives should not be so high. We need to perform also a search around the frequency itself. We can predict the future frequency using the average spin-down observed but because the spin-down is not constant we need to look for values of the frequency around the estimated frequency. During the observations a typical value for the spin-down was $\dot{f} \approx 10^{-10} s^{-2}$ Since the earliest opportunity for LIGO to observe this source is T ∼10 years away, we take the uncertainty in the frequency to be on the order of $\dot{f}\ \ T \sim 3 \times 10^{-2} s^{-1}$or a $BW = 3 \times 10^{-2} Hz$. This is an estimate for the total range of frequencies to be explored. The standard phase stability requirement (Jaranowsky & Krolak 2000 [29]) $\Delta\omega\tau \lesssim \pi/4$ over the integration time, yields an estimate of how closely spaced the frequency templates have to be. For τ ∼10 days∼106 s, this argument yields $\Delta f\ \approx \Delta\omega/2\pi \approx 10^{-7} Hz$. Consequently the total number of frequencies to be sampled is of the order of $BW/\Delta f \approx 3 \times 10^5 \left(\tau/10 \text{ days}\right)$.

Finally, the total number of two-parameter templates N_f we require is given by the simple product of the number of frequency values times the number of frequency derivative values: $N_f \approx 1.2 \times 10^8 \left(\tau/10 \text{ days}\right)^3$.

The computational time $\wp$ in floating operations per second required to analyze this data is then given by the expression:

$$\wp = 6f\ N_f\ \left[\log_2(2\ f\ \tau) + 1/2\right] \tag{12.23}$$

where f is the maximum frequency of our search (say 500 Hz) and τ is the integration time.

A plot of the quantity $\wp$ is given in Figure 12.9 in terms of integration time. It

is possible to see that even after a few days of integration time the computational task of this search is realistically manageable.

With the values derived above, this yields a total computational load of approximately $1.1 \times 10^{19}(\tau/10\mathrm{d})^4$ floating-point operations, which would require 3 months of calculations for a Teraflop machine. While this load is not trivial, it can be achieved by either processing the data offline or using a machine clocking at least $11(\tau/10\mathrm{d})^3$ Teraflops for online processing. However, the above estimate is an upper limit that makes little use of our prior knowledge of the expected frequency and frequency range of the signal. We need only to search over the BW of 3×10^{-2} Hz, whereas the standard argument above assumes we are searching for signals over the entire band from 0 to 500 Hz. The computational task can be significantly reduced by first 'demodulating' or filtering the signal to the bandwith BW estimated above and then 'decimating' or reducing the signal sampling rate to the bandwith. This technique cuts the processing rate essentially by a factor $BW/f \sim 6 \times 10^{-5}$ to approximately $0.7(\tau/10\mathrm{d})^3$ Gigaflops, well within the capabilities of current computers (see blue line in Figure 12.9). Finally we notice that the above discussion refers to one of the two frequencies of emission of the precessing neutron star. The presence of a second emission frequencies can be treated similarly and it is a important element in the statistical considerations on the reality of an eventual detection. In fact it will be a very convincing evidence if a detection of both frequencies is achieved and the respective stain h are as predicted by the previous calculations.

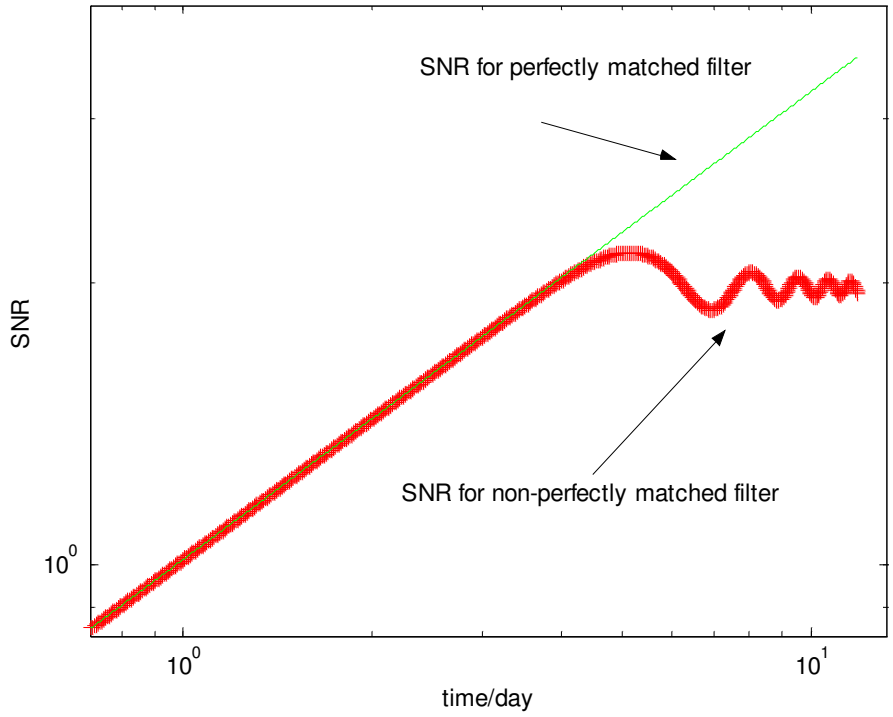

Figure 12.8: The comparison of the SNR (as a function of time) between a perfectly matched filter and a filter that is matched to a signal template that is close but not exactly the real signal.

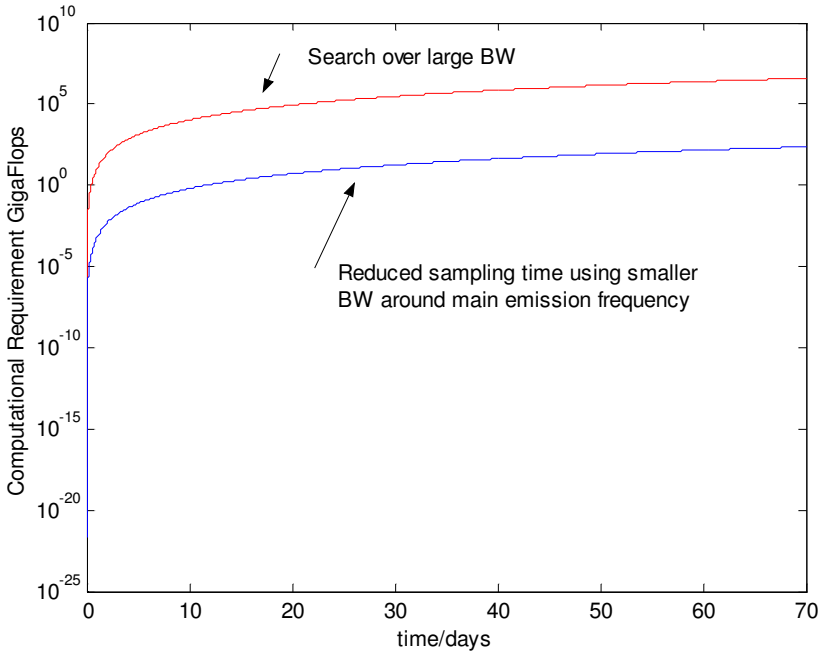

Figure 12.9: The computational requirement in Gigaflops as a function of the integration time.

CHAPTER 13
SUMMARY AND CONCLUSION

In this dissertation we discussed the implications for gravitational wave detection of the optical-infrared observation of a precessing neutron star in the remnant of supernova 1987A . We used the observed data on rotational velocity, spin-down and precession rate to determine the value of the possible asymmetric deformation that causes the precession.

To estimate the size of deformation it is important also to determine the wobble angle between the axis perpendicular to the deformation and the rotation axis. General Relativity gives us an equation for the loss of energy, through gravitational waves. Knowledge the rate of spin-down, the rotation frequency and the precession frequency allows us to find the wobble angle. This is possible under the assumption that the main mechanism for the loss of rotational energy is due to emission of gravitational radiation. Once we know the wobble angle, we can calculate the strength of the radiation on earth. In fact the value of the dimensionless strain parameter h depends on the value of the wobble angle quite strongly.

Our discussion shows that even with a more a realistic model of a precessing neutron star that takes in consideration the presence of a crust, with a certain elasticity and the eventual presence of a fluid interior the precessional behavior is similar to that of the simple biaxial model. The ratio of precession frequency and spin frequency determines the order of magnitude of the ellipticity, but a complete solution requires an estimate of the wobble angle. The preceding discussion shows that it is possible

to obtain such self-consistent models as a function of essentially one parameter: the moment of inertia I_0 that is involved in the precession. Given this parameter, the observational data allow to determine the wobble angle, the size of deformation and consequently the strength of the radiation on Earth.

We saw in previous Chapters that to avoid crust breaking the wobble angle has to be relatively small. In fact, formally, even the smallest wobble angle among the possible range of solutions violates the maximum crustal strain. Given the uncertainties in the model and in the interpretation of the data, we conclude that even if the limits on the maximum strain $\sigma_{\max}$ are relaxed, any viable solution is likely to have a wobble angle near the small end of the range and consequently the moment of inertia must be near the high end of its range. At least half of moment of inertia of the star has to participate in the precession to avoid crust fracture. In turn this means that a short integration time on the order of days is enough to observe with confidence the gravitational wave signal from SN 1987A using advanced detectors as LIGO II. Unfortunately the present generation of detectors such as the resonant bars and LIGO I would require observation times of the order of a million years to extract the signal from the noise. Thus if the precession interpretation is correct, the SN 1987A remnant would be the best candidate for continuous source of gravitational waves. In any case, it is clear that a targeted search for gravitational waves from this source is worthwhile since both detection and absence of detection over a relatively short time will yield interesting constraints on models for precessing neutron stars.

PART II
FULLY MATCHED FILTER FOR DOUBLE RESONANT GRAVITATIONAL DETECTOR

CHAPTER 14
INTRODUCTION

The existence of gravitational waves was predicted theoretically by A. Einstein in 1915. Einstein understood gravitational waves as a fundamental consequence of General Relativity, a theory that revealed a deep parallelism between the field properties of Electromagnetism and Gravity. Einstein, considering the enormous quantity of energy necessary to generate detectable waves, stated that it would be impossible to ever observe directly this phenomenon. In the early sixties J. Weber designed and built the first devices to attempt to observe gravitational waves generated by possible astrophysical sources. The effort by Weber attracted an extraordinary interest, because detection of gravitational waves would be a strong test for gravitational therories and it would open a new window to study and understand the universe.

Notwithstanding the early claims of detection by Weber, subsequent experiment by various groups around the world were not to able to verify any detection of gravitational waves. Weber's contribution was to show that the detection of gravitational waves was within our technological capabilities. Consequently, there has been an intense effort in improving the detectors over the last 30 years.

In experimental physics, the development of the instrumentation equipment is of major importance. Fundamental advances in exploring and understanding new phenomena is often determined by even small improvements in the capability and sensitivity of detectors and other hardware. Of equal, or sometimes even more importance, are the mathematical methods that are used to analyze and interpret the data so painstak-

ingly obtained by the instruments. In the field of gravitational wave detection this fact is particularly true. At this point in time, the working equipment (now resonant bar detectors, and soon, light interferometers) is subject to the limitation, that in the best of scenarios, the signal is unlikely to be far above the noise. Under these circumstances data analysis becomes of extreme importance and the mathematical tools used to accomplish this task are valuable as the instrumentation itself. The major tool used in Gravitational Wave data analysis is *optmal filtering*, a mathematical process that allows us to most effeiciently extract a signal from noise given some characteristic of the signal and noise.

14.1 Filters for Gravitational Wave Bursts' Search

In this particular work, we are going to investigate the performance of two specific filters, called the *slow* and the *fast* filters, or *partially-matched* and *fully-matched* filters. The LSU's ALLEGRO detector group uses a form of the slow filter. We want to explore if we can improve the performance of our data analysis using the fast filter.

14.1.1 Previous Results: The *slow-fast* terminology is borrowed from that used in a certain paper by the research group of Professor Coccia and Pizzella located in Rome at the University of the Sapienza and Tor Vergata [30]. It is claimed by the Italian groups that the *fast* filter gives an improvement by a factor of 2 in the *Signal to Noise Ratio* in comparison with the *slow*. This result was obtained applying the fast and slow filter algorithms to the EXPLORER's gravitational wave detector's data. It was also established that the fast filter is better in estimating the arrival time of a signal in the presence of noise. The paper by Astone *et al. [30]* describes the mathematical

properties of the output time sequence of the fast and slow filter. Comparing these mathematical properties, and in particular the form of the distribution functions of the two filtered outputs, the authors arrive at a conclusion as to why the fast filter is better than the slow.

14.1.2 Our investigation: The main purpose of this research is to confirm or deny (and eventually explain and justify) the claim of the Roman group that the *fast* filter has a better performance in the search for *burst* gravitational wave signals in the resonant bar detectors'data. One particular advantage of our approach to studying the slow and fast filter properties is that, at first, we didn't need to use real data from the detector. Instead, we created an effective simulation for a mechanical one mode and two modes oscillator, with physical parameters that are matching the real detector. We then applied the filtering procedures to the output of the simulated bar detector

The actual filters are found to be nearly equivalent when there is just one mode, but they significantly differ when there are two modes.

The two filters are based on similar basic principles, however the steps to prepare the data for the final filtering procedure differ considerably. In this study we will sometime loosely refer to a filter as the entire filtering sequence.

14.1.3 Fast and Slow Filters: We are going to explain in detail in the following Chapters, about the slow and fast filters and show their similarities and differences. The following Figures are an introduction to the filtering procedure steps in the two cases.

Figure 14.1 shows the ALLEGRO detector 's data taking procedure and the first data analysis steps, done at the hardware level by the data acquisition system.

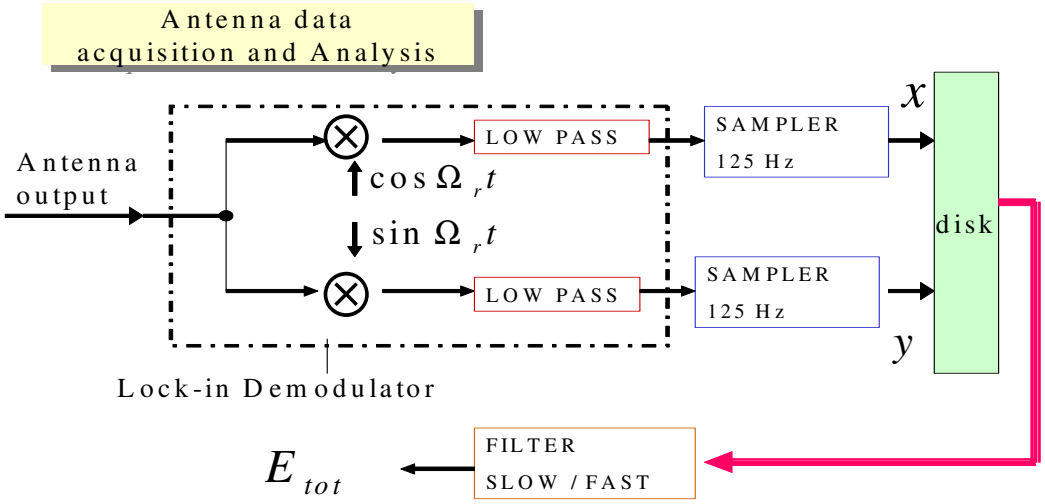

Figure 14.1: The Acquisition and Data Analyisis procedure implemented in the ALLEGRO detector. The antenna output is the relative motion of the bar and the transducer. The lock-in demodulator shifts the zero frequency to the reference frequency Ω_r (a frequency between the two resonant modes Ω_+ and Ω_-). The data is low-pass filtered, to avoid aliasing, and sampled at a relative slow pace (at 125 Hz). The demodulation separates the data in two channels: the in-phase x and in-quadrature y components of the data sequence. The data is stored on disk, with information on the antenna's environment and on the time. The data is consequentely processed through software to produce a final time series called the "Energy Innovation".

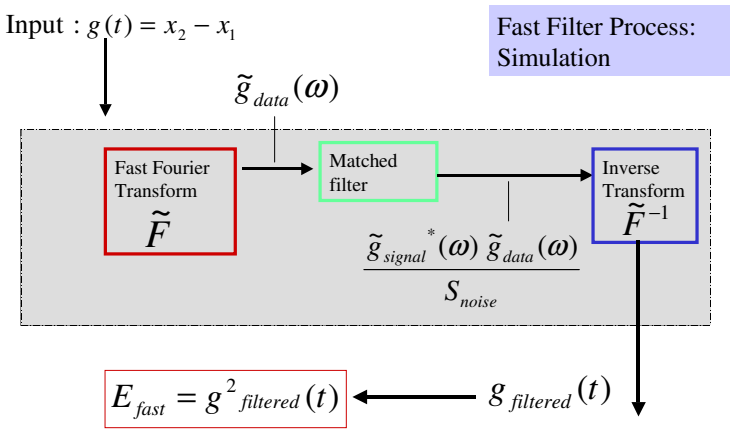

Figure 14.2: The block-diagram for the fast filter. This is a relative straigthforward procedure. The input data is sampled at a fast rate (4096 Hz) and not demodulated. The fast filter is implemented in the Fourier domain. The input data $g(t)$ is the difference $x_2 - x_1$in the displacement of the bar and the transducer. The Fourier transform of the input data (noise+eventual signal) $\widetilde{g}_{data}(\omega)$ is multiplied by the conjugate of the Fourier transform of the template signal $\widetilde{g}_{signal}(\omega)$. This product is divided by the total noise spectrum S_{noise} to obtain the filter data $\widetilde{g}_{filtered}(\omega)$. To go back to the time domain we perform an inverse Fourier transform. The energy E_{fast} is determined by the square of the time domain filtered data $g_{filtered}(t)$.

The fast filter is a direct application of the matched filter, in the frequency domain, applied directly to the data recorded directly without the demodulation and decimation shown in Figure 14.1. We also show that if in addition, we pre-filter the data with a *whitening* filter (that is going to be described later) the results obtained are similar to the case of a direct application of the fast filter. The advantage of using the pre-filter is to recover the initial impulse force and be able to characterize the signal as a short duration impulse. This allows to apply the Fourier transform to a shorter stretch of data with the consequent saving of computational time in the analysis. Figure 14.2 is an illustration of the filtering procedure for the fast filter.

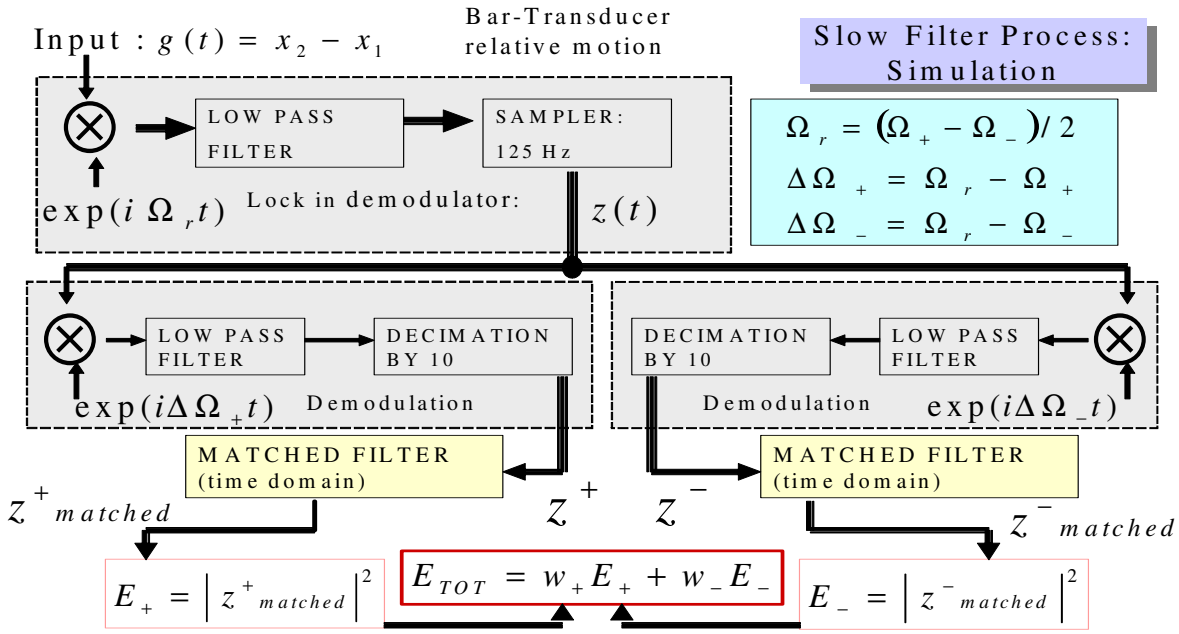

Figure 14.3: The block diagram for the slow filter. The first gray block is the equivalent in our simulation of the lock-in demodulator in the real antenna. We use the phasor function $\exp(i\omega t)$ to demodulate the data. This is equivalent to separate the data in the in-phase and in-quadrature components. The outputs of the demodulation are then complex variables. We use in our diagram thick lines to indicate the flow of these complex variables (as if composed of two channels x and y). After the first demodulation we shift the zero frequency to the plus and minus mode. Then we low pass filter and decimate the data to keep just a narrow window of frequencies around the two resonant modes. We apply the matched filtered to the plus and minus part of the data. The absolute square of the plus and minus filtered data is summed together (with appropriate weights to take in consideration differences in the temperature of the two modes). This final operation gives the energy innovation of the slow filtered data.

The slow filter implemented in the simulations is supposed to closely follow the actual filtering procedure used by the LSU gravitational wave group to analyze the data from its ALLEGRO detector. Figure 14.3 shows the steps followed in the simulation.

In chapter 15 we describe the theoretical basis for gravitational wave detectors and describe their interaction with gravitational waves and discuss the noise sources that characterize the physical detector. In chapter 16 we give some details about the methods of our simulation and we demonstrate that it reproduces the main expected

behavior of the bar. Real life bar detectors are sophisticated and complex machines that contain many different mechanical and electronic parts, all possible sources of noise. In fact, it is very common to find unexplained modes in the spectrum, sudden changes in the average temperature and similar. Our simulation is a complete controlled environment that allows better understanding of the proper characteristic of the filters independent of the ideal behavior of a particular bar. We describe how we modeled the one mode oscillator and how we extended our simulation to the two mode case. In Chapter 17 we write down the analytical form and mathematical properties of the unfiltered and filtered data.

Chapter 18 describes the pre-filtering done before the actuation of the fast filter. This is done to recover the impulsive forces that act on the bar or the transducer. The main purpose of the pre-filter is to allow us to characterize the target signal directly without the response of the bar. This is done because the high Q of the bar requires a very long fast Fourier transform in the matched filter to contain all the Fourier components of the signal after the response of the detector. We show that pre-filtering doesn't alter the result of the fast filtering operation. Chapter 19 gives a short introduction to fast matched filters. In chapter 20 we describe the slow filtering sequence and the motivation behind the idea to separate the data information from the two modes. In Chapter 21 we show the performance characteristics of the two filters over identical simulated stretches of data, reproducing the bar behavior when excited by thermal noise and transducer (electrical) noise. We found that in the case of the one mode oscillator the slow and fast filter are apparently equivalent. When a more precise

analysis of the performance of the two filters is implemented it can be shown that the fast filter is consistently a more efficient filter. Essentially this means that both in estimating the energy of an impulse and its arrival time, the fast filter is more accurate than the slow. This accuracy is a consequence of the fact that after normalization (that assigns to both sets of filtered data the same energy for very large impulses) the Signal to Noise Ratio is higher for the fast. In the two mode case, similarly, different tests were used to demonstrate the superiority of the fast filter versus the slow, in terms of enhancing the detection of a signal buried in noise. It seems that in the two mode case the improvement obtained using the fast filter is more evident. Sections 21.2 and 21.3 describe these results and the different tests used. Different methods give different quantitative estimates on how better one filter is with respect to the other according to the task assigned to the data analysis. In general, however, a value close to the Italian groups' claimed improvement by a factor of 2 in " Signal to Noise Ratio" was found. Chapter 22 explains that is not necessary to sample at a very fast rate and the performance of the "fast" filter is maintained when a much slower rate is used. This indicates that "fast' filter is a misnomer, and a better terminology could be partially and fully-matched filter.

ALLEGRO demodulates and decimates the data in hardware before recording. Therefore an important question is what happens when we apply the fast filter to demodulated data without having complete knowledge of the phase of the demodulation clock. We arrive at the conclusion that not much information is lost when the phase is unknown. The problem and results of applying the filters to the output of the real

detector is described in Chapter 23. Finally Chapter 24 suggests some reasons why the fully matched (fast) filter works better in picking up signals from noise than the partially matched (slow) filter.

CHAPTER 15
GRAVITATIONAL WAVES BAR DETECTORS

15.1 Interaction of Gravitational Waves with an One Mode Resonator

In this section we will show the effect of a gravitational wave on an idealized detector with one natural mode of resonance. In other words we will derive an equation of motion for a simple bar detector. The equation will display the coupling between the gravitational field and the detector.

We closely follow the treatment of the classical textbook of Schutz [31]. The detector consists of two point particles of mass m in a free falling reference system and Traceless and Transverse coordinates. The particles are connected with a spring with spring constant k. We suppose that there is some damping process proportional to the velocity of the mass (internal friction, for example) with damping constant ν. The unstretched spring has a length l_0. The system then can be described by the following system of equations:

$$mx_{1,00} = -k(x_2 - x_1 + l_0) - \nu(x_1 - x_2)_{,0} \tag{15.1}$$

and:

$$mx_{2,00} = -k(x_2 - x_1 - l_0) - \nu(x_2 - x_1)_{,0} \tag{15.2}$$

Let's define the quantities:

$$x = x_2 - x_1 - l_0, \quad \omega_0 = 2k/m, \quad \gamma = \nu/m \tag{15.3}$$

the quantity ω_0 is called the resonance frequency of the system. We can combine the above equations to get:

$$x_{,00} + 2\gamma x_{,0} + \omega_0^2 x = 0, \tag{15.4}$$

The free particle will be at rest in the TT coordinate frame. The action of the gravitational wave will keep the particle at rest. We suppose that the only relevant motions are the ones created by the gravitational waves and so $x = O(|h_{\mu\nu}|^2) \ll l_0$. In the local frame the velocities will also be small and then we can use Newtonian equations in the inertial frame of reference $\{x^{\alpha'}\}$:

$$m x^{j'}_{,0'0'} = F^{j'}, \tag{15.5}$$

The difference of this coordinate system with the TT coordinate system is in second order terms in h then:

$$m x^{j}_{,00} = F^{j} + O(|h_{\mu\nu}|^2), \tag{15.6}$$

The spring restoring and damping forces are the only non-gravitational forces acting on the system. At any given time the motion of the masses are non-relativistic and the restoring force will be linearly proportional to the given extension of the proper distance between the masses at any instant. The metric will determine such distance. In the TT gauge we have the proper distance is changing with time. In fact, if we position particle one at the origin and the other at the point $x = \varepsilon$, $y = 0$, $z = 0$ then we have:

$$\begin{aligned} \Delta l &= \int \left|ds^2\right|^{1/2} = \int \left|g_{xx} dx^\alpha dx^\beta\right|^{1/2} \\ &= \int_0^\varepsilon \left|g_{xx}\right|^{1/2} dx \approx \left|g_{xx}\left(x=0\right)\right|^{1/2} \varepsilon \\ &\approx \left[1 + \frac{1}{2} h^{TT}_{xx}(x=0)\right] \varepsilon \end{aligned} \tag{15.7}$$

We can apply this result to our problem of the effect of a gravitational wave on a idealized resonant detector. We get that the proper distance l between the masses

changes with time as:

$$l(t) = \int \left[1 + h_{xx}^{TT}(t)\right]^{1/2} dt \tag{15.8}$$

Writing explicitly the forces we get:

$$m x_{1,00} = -k(l_0 - l) - \nu(l_0 - l)_{,0} \tag{15.9}$$

and:

$$m x_{2,00} = -k(l - l_0) - \nu(l - l_0)_{,0} \tag{15.10}$$

Using the result on the value of the proper distance we have:

$$x = l - l_0 = x_2 - x_1 - l + \frac{1}{2} h_{xx}^{TT}(x_2 - x_1) + O(|h_{\mu\nu}|^2) \tag{15.11}$$

or solving for the separation between the masses:

$$x_2 - x_1 = l_0 + x - \frac{1}{2} h_{xx}^{TT} l_0 + O(|h_{\mu\nu}|^2) \tag{15.12}$$

The response of the detector can be described by the following equation.

$$x_{,00} + 2\gamma x_{,0} + \omega_0^2 x = \frac{1}{2} h_{xx,00}^{TT}, \tag{15.13}$$

The conclusion is that the bar responds to the gravitational field like a damped harmonic oscillator driven by the gravitational wave as an external force. This result is illustrated in Figure 15.1.

15.2 The Noise

The final crucial element in a description of a detector is a description of all the noise sources, meaning random waveforms that appear in the output of the detector, and are superimposed on any possible signal.

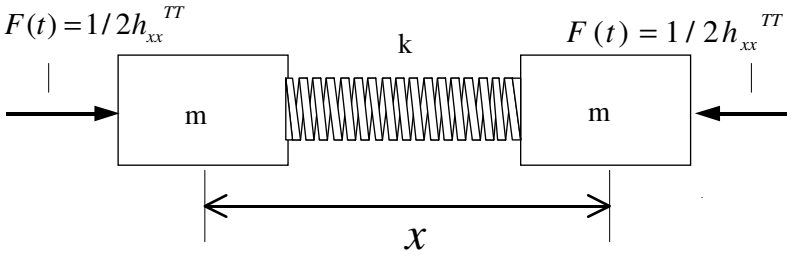

Figure 15.1: The gravitational wave interaction with a massive bar in the case of one mode system. The gravitational wave acts as a external force on the mass of the bar that can be described as two separate masses m attached by a spring with spring constant k.

The detector is subject to many different types of noise that interfere with the observation of gravitational waves. We can divide sources of noise into those that are external and those that are internal to the detector [33].

a) The main source of external noise is the seismic motion of the earth. The spectrum of the earth motion peaks at low frequencies, with a broad spectrum around 5 Hertz. Beyond this lowest frequency the spectrum of the noise can be modeled by the following ground motion amplitude function x_s:

$$x_s = \alpha f^{-2} m/\sqrt{Hz}, \tag{15.14}$$

where f and α depends on the particular environment of the geographical location.

The bar detector has an isolation system consisting of springs and rubber rings. The isolation system has the function to very efficiently stop high frequency motion of

the environment to reach the bar. Low frequencies can go through the isolation system but that is not considered a problem because the range of interest for our detector is around and in between the resonant peaks that are at about thousands of Hertz. In our simulation of the detector we assume that the damping is perfect and no seismic vibration goes through our ideal isolation system.

b) The main source of internal noise is the thermal noise. The bar is kept at a very low temperature to minimize such noise. Even if the bar is frozen to the temperature of liquid helium the thermal noise of the molecules of the material that makes the bar is still a dominant source of noise as compared to the possible astrophysical gravitational wave signals. The noise can be understood as a Brownian motion and its mean expressed in terms of the strain is:

$$h_B \sim \left(\frac{k_B T \tau_{meas}}{M \omega_m l^2 Q}\right)^{1/2} \tag{15.15}$$

where k_b is the Boltzmann's constant, T is the temperature, τ_{meas} is the time of the measurement, M is the mass of the detector, the ω_m, l, Q is the resonant frequency of the detector, the length of the bar and its quality factor respectively. The main frequency of resonance in the longitudinal direction is related to the speed of sound in the material:

$$\omega_m l = \pi \nu_s, \tag{15.16}$$

so the strain is expressed as:

$$h_B \sim \left(\frac{k_B T \tau_{meas}}{\pi^2 v_s^2 M Q}\right)^{1/2} \tag{15.17}$$

substituting physical units we have:

$$h_B \sim 3 \times 10^{-21} \left[\left(\frac{f_m}{1kHz} \right) \left(\frac{10^{10} J}{M v_s^2} \right) \left(\frac{10^9}{Q} \right) \left(\frac{T}{1K} \right) \left(\frac{\tau_{meas}}{10^{-2} s} \right) \right]^{1/2} \tag{15.18}$$

When we use the ALLEGRO's parameters, we have that $h_B \sim 10^{-21}$ (speed of sound in aluminum is 5000 m/s).

c) The SQUID noise is mainly due to the transducer losses. This is a combination of the series noise that is the equivalent of thermal noise in an electromagnetic system and back-reaction of the transducer and amplifier on the bar. The combined effect of the SQUID noise is:

$$h_s \sim \left(\frac{2\hbar}{\pi^2 M v_s^2} \right)^{1/2} \sim 1.1 \times 10^{-21} \left(\frac{f_m}{1kHz} \right)^{1/2} \left(\frac{10^3 kg}{M} \right)^{1/2} \left(\frac{10^4 ms^{-1}}{v_s^2} \right) \tag{15.19}$$

15.3 Two Mode Detector with Different Noise Sources

In this section we extend the discussion of the effect of gravitational waves on a coupled harmonic oscillator, a more realistic model for the bar detector. The real detector has a second mechanical resonator attached to the end of the bar. The purpose of adding a second resonator is to "amplify" the motion of the bar. Using the formalism from Evan Maucelli's dissertation [32], we can write the equation of motion as:

$$\begin{aligned} & m_1 \ddot{x}_1(t) + c_1 \dot{x}_1(t) + k_1 x_1(t) - c_2 \dot{x}_2(t) - k_2 x_2(t) \qquad (15.20) \\ = \; & F_1(t) - F_2(t) + F_T(t) + \frac{1}{2} m_1 L_1 \ddot{h}_{xx}(t) \\ & m_2 \left(\ddot{x}_2(t) + \ddot{x}_1(t) \right) + c_2 \dot{x}_2(t) + k_2 x_2(t) \\ = \; & F_2(t) - F_T(t) \end{aligned}$$

m_1 and m_2 are the effective masses of the bar and the transducer. L_1 is the length of the bar. k_1 and k_2 represent the spring constant of the two resonators and c_1 and c_2 are the damping coefficients. F_1 and F_2 are the random noise forces acting on the bar and transducer. The thermal noise forces on the bar and the transducers can be considered as independent random variables with a normal distribution. The damping coefficients are related to the quality factors Q_1 and Q_2 by the equation:

$$Q_{1,2} = m_{1,2}\ k_{1,2}/c_{1,2}. \tag{15.21}$$

As explained in the previous section the gravitational waves can be considered as an external force. One of the main characteristics of the gravitational wave is that it will excite just the bar with nearly no interaction with the transducer.

This is due to the fact that the strength of interaction of the gravitational wave is proportional to the mass. The mass of the transducer is about a 1000 times smaller than that of the bar. Therefore the effect of the passage of a gravitational wave through the detector is to deposit many order of magnitude more energy in the bar than in the transducer. This explains why the gravitational wave component of the external force is only present in the first equation of motion, which describes the forces acting on the bar mass m_1. In the simulation of the detector we will use this important aspect of the gravitational wave force impulse to characterize the gravitational wave signal. The following Figure 15.2 shows the different forces acting on the bar and transducer.

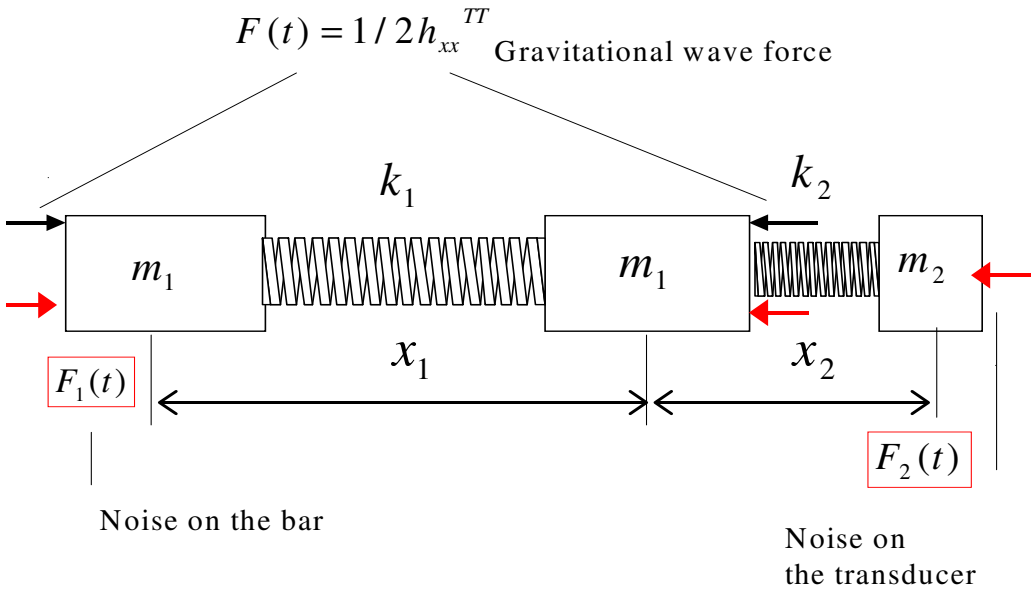

Figure 15.2: The two mode oscillator, with all the different sources of force noise and gravitational wave driving force.

15.4 Details of the ALLEGRO Bar Detector

The ALLEGRO bar detector is located at Louisiana State University. Its precise geographical location is:

$$\text{latitude}=30^o25' \text{ North ; longitude}=91^o10' \text{ West} \tag{15.22}$$

The detector is constituted by a massive aluminum bar and a mechanical-electrical transducer, and other electronic devices to amplify and record the data. The system can be described as a two mode coupled harmonic oscillator. ALLEGRO is a very typical gravitational wave resonant detector and for later use we list in the following tables some of its physical characteristics.

The bar is very massive to offer a bigger cross section to the gravitational waves.

Table 15.1: Physical parameters of the ALLEGRO detector

Mass of bar (Aluminum alloy)	2296 kg (effct. mass=1148 kg)
Mass of transducer	$\sim$ 0.64 kg
resonant frequency bar	913.83 Hz
resonant frequency transducer	902.58 Hz
temperature noise in the bar	4.2 K
temperature of noise in the transducer	4.2 K
spring constants, length	300 cm

On one end of the bar is a transducer that converts the mechanical motion of the bar in a voltage potential difference. This electrical output is amplified by a SQUID (superconductive quantum interference device). The mixing angle α is a parameter that determines the level of "tuning" between the bar and the transducer. In other words the mixing angle tells how close the resonant frequencies of the bar and transducer are. Perfect tuning is equivalent to the mixing angle α equal to 45^o (see following section for a more detailed discussion of the mixing angle formalism). The bar is supposedly excited by a bath of gravitational waves from continuous and burst sources in the sky. Unfortunately the gravitational waves' forces on the bar are much weaker than the thermal noise impulses. The bar is in contact with a liquid helium reservoir through the cable from which the bar is suspended. This limits the thermal noise in the bar, but even when cooled down to a few kelvins, the thermal noise dominates over the majority

of gravitational wave impulses. Another important source of noise is the electrical shot noise due to the SQUID. The bar is supposedly isolated from influences of the external environment, in particular, seismic vibrations of the ground. The isolation is achieved through a sophisticated suspension system that very efficiently dumps the high frequency vibration of the ground. The choice of material, in this case a special alloy of aluminum, and the size of the bar is designed in such a way to have the bar resonant mode close to that of the resonant frequency of typical compact astrophysical sources, the best candidate for gravitational wave sources.

This frequency can be derived from basic principles and it is around 1000 Hz. See Chapter 11 for a discussion of the astrophysical time scales. The suspension system is designed in such a way to have its main resonant mode at a quite lower frequency than 1000 Hz, so no ground motion around the astrophysical interesting frequency can reach the bar. Occasionally very large ground motions do go through the suspension system. A series of seismometers sits around the detector to register information on the surrounding environment. A veto procedure is in place in the ALLEGRO data analysis protocol to discard the data that coincide with large responses from the seismometers.

Table 15.2: Parameters of the normal modes of the detector.

plus normal mode frequency	896.8 Hz
minus normal mode frequency	920.3 Hz
Q of plus mode	$\sim$10ˆ6
Q of minus mode	$\sim$10ˆ6
Mixing angle α	30.8 ^{o}

CHAPTER 16
ANALYTIC FORM OF THE SIGNAL AND NOISE

In this chapter we write the equations for the analytic description of our oscillator system for the one mode and two mode cases. These equations are continuous and so able to reproduce the analog response of the real system. The goal of this chapter is to derive equations that describe the response of the bar to both a gravitational signal and enviromental noise. We calculate the analytic spectrum for our system and then use this to show that our simulation is a good representation of a damped harmonic oscillator with the given characteristics. Our simulation is digital and so discrete in form, reproducing the process of sampling and collection of the data in a real life experiment. The continuous and discrete representations should be in general similar to each other and give comparable answers.

The presence of noise creates a random behavior for the displacement response of the detector, but the statistical properties of the system can be determined when we consider averages over a long time. The response of the detector to a large specified signal can be described deterministically solving the equations of motion. When the noise mean amplitude is larger than the signal we have to be content to describe the average behavior of the bar with statistical quantities such as the power spectrum and auto-correlation functions. In an experiment the spectrum can be measured taking spectra of relatively short time intervals and then averaging many of these intervals. This is a good description of the noise if the noise is stationary, i. e., the spectrum converges when many averages are taken. In many real life detectors the stationarity

of the noise is some kind of an approximation or simply assumed to be the case. Real time measurements of the spectrum are done on a regular basis for a realistic, current estimate of the noise. In our simulation the noise is perfectly stationary and the spectrum will certainly converge if we take enough averages.

The optimization of any filter requires knowledge of the noise. The most informative characterization of the stationary noise is the spectrum. We use explicitly the analytical form of the spectrum for the construction of the data analysis fast filter (see following chapters). The spectrum and auto-correlation functions are closely related. We use in the slow filter the auto-correlation function so we also give an analytical expression for this quantity.

16.1 Analytical Description of the One Mode System

16.1.1 Equation of Motion The equation of motion of a damped harmonic oscillator is (see previous chapter):

$$m\,\ddot{x} + c_s\,\dot{x} + k = F_{driving}. \tag{16.1}$$

If the force driving the oscillator is a random sequence of delta impulses then the solution of the above equation is a random process and x is a random quantity. The above equation is called a stochastic differential equation. In particular the above equation can be understood as describing the motion of a particle attached to a spring and undergoing one-dimensional Brownian motion. In this case equation (16.1) is a form of Langevin equation [29]. The solution of the stochastic differential equation is not deterministic and the quantity x behavior can be described in terms of statistical properties as the mean, standard deviation, Auto-correlation and Power Spectrum (see

next section for a definitions of the Auto-correlation and Power Spectrum).

A standard form for the driving force $F_{driving}\ (t)$ is a Gaussian *white noise* process with zero mean. We model this process as a sequence of random amplitude force impulses acting on the bar at fixed time intervals Δt. This choice is determined by the sampling of the data in real experiments that happens at regular, discrete intervals. The essemble average Auto-correlation function $R(t_1, t_2)$ of the force noise process is defined to be:

$$R(t_1, t_2) = \langle F_{driving}(t_1) F_{driving}(t_2) \rangle = g\ \delta\left(t_2 - t_1\right) \tag{16.2}$$

this means that the Auto-correlation of the noise is a Dirac-delta function δ, with $t_2 - t_1 = n\ \Delta t$ (n is an positive integer). A standard result of Fourier analysis is that consequentely the Power Spectrum of the force noise is flat containing all the frequencies components . The brackets in equation (16.1) indicate average over a large essemble. We assume ergodicity of the noise, this implies that average over a large essemble is equivalent to time average of a single system. We model the driving force as due to the thermal motion of the particle in equilibrium with a heat bath at a temperature $Temp$. In this case by the equipartition theorem the average kinetic energy is $\frac{1}{2} k_b Temp$, where k_b is the Bolzman constant.

16.1.2 Power Spectrum and Auto-Correlation Function A very important and useful quantity to study stochastic processes is the Power Spectrum (PS). When we are dealing with real experiments we have finite time series of length T for the stochastic variable $F(t)$.

Then the Power Spectrum $S_{F,F}$ is defined as:

$$S_{F,F}(\omega) = \lim_{T\to\infty} \frac{1}{T}\widetilde{F}^{*}(\omega,t)\widetilde{F}(\omega,t), \tag{16.3}$$

where $\widetilde{F}$ indicates the Fourier transform of the variable F and the star signifies complex conjugation.

We can express analytically the Power Spectrum S_{bar} for the amplitude of the oscillator x as:

$$S_{bar}(\omega) = |G(\omega)|^2 \; S_{fb}(\omega) \tag{16.4}$$

where G is the transfer function of the oscillator given by:

$$G(\omega) = \frac{1}{m}\left(\frac{1}{-\omega^2 + i\frac{\omega_0}{Q}\omega + \omega_0^2}\right) \tag{16.5}$$

and $\omega_0 = \frac{k}{m}$, $Q = mk/c_s$.

The MatLab function PSD calculates the Power Spectral Density. To convert the analytical Power Spectrum in the Power Spectral Density we need to divide the Power Spectrum by the sampling frequency. In going from the continuous to the discrete case it is useful to refer to the following equations.

We have that:

$$F_b = P_b\delta(t - t_0) \tag{16.6}$$

where P_b is the moment transfer due to the noise force acting on the bar.

The initial impulse force on the bar F_b is related to the Spectrum of the thermal forces S_f by:

$$S_{fb} = F_b^2\, dT; \tag{16.7}$$

where the term dT is the sampling time. The white noise of the SQUID results in an uncertainty of the voltage output of the detection apparatus. This in turn is equivalent in an uncertainty in the displacement of the bar. The distribution of the SQUID displacement error is Gaussian, with zero mean. If the average displacement error due to the SQUID is x_{asn} then we can write this white noise spectrum S_w as:

$$S_w = x_{asn}^2 \, dT. \tag{16.8}$$

Then the total noise spectrum S_{tot} is:

$$S_{tot}(\omega) = S_f \ \left|G_w(\omega)\right|^2 + S_w(\omega) \tag{16.9}$$

The definition of Auto-correlation $R_{F,F}$ of the variable F is:

$$R_{F,F}(\tau) = \langle F(t_1 + \tau) \, F(t_1) \rangle . \tag{16.10}$$

The Auto-correlation function $R_{F,F}$ of the noise is the inverse Fourier transform of the Power Spectrum S_{bar}:

$$R_{F,F}(\tau) = \int d\omega \ e^{i\omega\tau} S_{bar}(\omega) . \tag{16.11}$$

The following Figures show the comparison between the analytical and experimental (from the simulation) Auto-correlation and Power Spectral Density. The agreement is quite good and the uncertainty is due just to the finite length of the experimental data used to calculate the experimental spectrum.

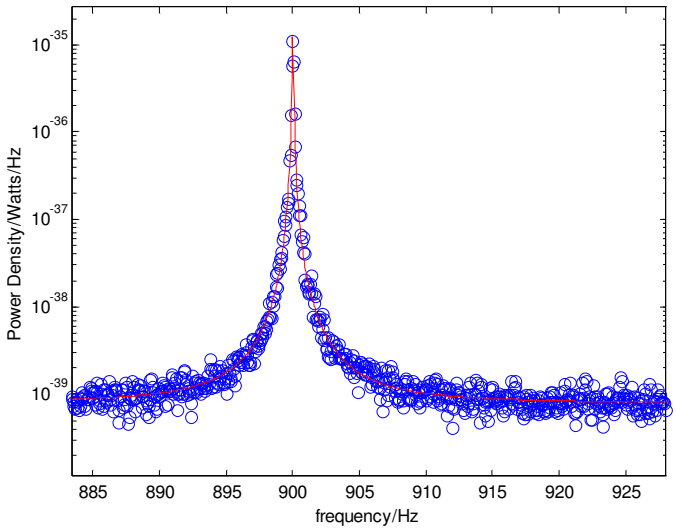

Figure 16.1: The analytical (red) and experimental spectra (blue) are compared.

16.2 The Two Mode System: The Mixing-Angle Representation

Following A. Morse dissertation [35] this is the mass normalization matrix M (see previous chapter 5 for notation refering to the model of a coupled harmonic detector):

$$M = \begin{bmatrix} \frac{1}{\sqrt{m_1}} & 0 \\ 0 & \frac{1}{\sqrt{m_2}} \end{bmatrix} \tag{16.12}$$

Then the system of two coupled oscillator can be described using the displacement vector $\mathbf{u}$ and its second time derivative:

$$\ddot{\mathbf{u}} = -\mathbf{K}\ \mathbf{u} + \mathbf{M}\ \mathbf{F}. \tag{16.13}$$

where:

$$\mathbf{u} = \begin{pmatrix} x_1 \\ x_2 \end{pmatrix} \tag{16.14}$$

and

$$K = \begin{bmatrix} -\left(\omega_1^2 + \frac{m_2}{m_1}\omega_2^2\right) & \sqrt{\frac{m_2}{m_1}}\omega_2 \\ \sqrt{\frac{m_2}{m_1}}\omega_2 & -\omega_2^2 \end{bmatrix} \tag{16.15}$$

The forces acting on the bar and transducer form the vector F. To solve these equations we define the mass-normalized coordinates $\mathbf{a}$ by:

$$\mathbf{a} = M\ \mathbf{u}. \tag{16.16}$$

Then, the equation can be Fourier transformed and solved by usual linear techniques. In the Fourier Domain the solutions for the equations of motion of the detector (ignoring damping) are:

$$\begin{bmatrix} \widetilde{a}_1 \\ \widetilde{a}_2 \end{bmatrix} = \begin{bmatrix} G_{11} & G_{12} \\ G_{21} & G_{22} \end{bmatrix} \begin{bmatrix} \widetilde{F}_1 \\ \widetilde{F}_2 \end{bmatrix} \tag{16.17}$$

where the $\widetilde{a}_1, \widetilde{a}_2, \widetilde{F}_1$ and $\widetilde{F}_2$ are the Fourier transformed displacement functions a_1, a_2 and the impulse delta forces F_1 and F_2. In the case of the noise the force sequences are random variables with normal distributions. In the case of the signal we have that F_1 is a delta function with its maximum located at the instant of arrival of the gravitational wave and F_2 has a constant zero value.

The elements of the transfer function matrix G are:

$$\begin{aligned} G_{11} &= \frac{\cos^2\theta}{m_1\left(\omega_+^2 - \omega^2 + i\omega_+\omega/Q_+\right)} + \frac{\sin^2\theta}{m_1\left(\omega_-^2 - \omega^2 + i\omega_-\omega/Q_-\right)}, \\ G_{12} &= G_{21} = \frac{-\sin\theta\cos\theta}{\sqrt{m_1 m_2}\left(\omega_+^2 - \omega^2 + i\omega_+\omega/Q_+\right)} + \frac{\sin\theta\cos\theta}{\sqrt{m_1 m_2}\left(\omega_-^2 - \omega^2 + i\omega_-\omega/Q_-\right)}, \\ G_{22} &= \frac{\sin^2\theta}{m_2\left(\omega_+^2 - \omega^2 + i\omega_+\omega/Q_+\right)} + \frac{\cos^2\theta}{m_2\left(\omega_-^2 - \omega^2 + i\omega_{-+}\omega/Q_-\right)}. \end{aligned} \tag{16.18}$$

We specify the parameters of the bar and transducer, as the masses m_1, m_2, the resonant frequencies ω_1 and ω_2. Then we proceed to construct the transformation matrix from the mass coordinates to the normal modes coordinates. The mixing angle θ is a measure of the "tuning" between the bar mass m_1 and mass m_2 resonant frequencies. If the resonant frequencies are the same the mixing angle θ is equal to 45^o. The matrix of eigenvalues of the matrix K are the normal mode frequencies ω_+ and ω_-. The eingenfuntion matrix A is the transformation between the mass coordinates to the normal mode coordinates. The matrix A can be written in terms of mixing angle θ, assuming the form of a rotation matrix:

$$A = \begin{bmatrix} \cos\theta & -\sin\theta \\ \sin\theta & \cos\theta \end{bmatrix}. \tag{16.19}$$

16.3 The Spectrum of the Noise for the Observable

In the simulation we can keep track of the values of the displacement variables a_1 and a_2. In a real experiment the transducer is capable to transform the kinetic energy of the motion of the transducer relative to the bar in a voltage potential difference. This is the physical quantity that can be measured by the experimental apparatus. This quantity is proportional to the difference in the displacement variables a_1 and a_2. This means that what we can measure directly is the quantity $a_2 - a_1$. The spectrum of the noise for the two modes system observable $a_2 - a_1$ is:

$$S_{tot} = |G_{12} - G_{11}|^2 \ S_{fb} + |G_{22} - 2\ G_{12} + G_{11}|^2 \ S_{ft} + S_w;$$

where S_{fb} is the force noise in the bar:

$$S_{fb} = \frac{4k_bTemp\ m_{bar}\ \sqrt{\frac{k_{bar}}{m_{bar}}}}{Q_{bar}}, \tag{16.20}$$

and S_{ft} is the force noise on the transducer:

$$S_{ft} = \frac{4k_bT\ emp\ m_{trans}\ \sqrt{\frac{k_{trans}}{m_{trans}}}}{Q_{trans}} \tag{16.21}$$

and S_w is the white noise of the SQUID that is empirically measured in a real detector.

A crucial parameter for any bar detector is the ratio Γ between the narrow band S_{fb} and broad band noise S_w, definde as:

$$\Gamma = \frac{S_f\ G^2}{S_w}. \tag{16.22}$$

where our convention is that the normalizing factor $G^2 = 10^{-21}m^2/N^2$ and N is the unit Netwon. The quantity G^2 is an average measure of the absolute value square of the bar's transfer function away from the resonant frequency where the SQUID white noise dominates. For ALLEGRO we that $\Gamma \approx 10^{-8}$.

In our simulation, because of the low Q that we have chosen our detector, we have to select a smaller value for Γ so that the auto-correlation function changes more gradually over the 31 samples of the filter length. See Table 16.2 for a list of the parameters in our simulation.

16.4 The FFT of the Signal

For a specific force vector, with the Fourier transforms $\widetilde{F}_1$ and $\widetilde{F}_2$, the observable $a_2 - a_1$ will have a specific response given by the Fourier transform $\widehat{a}_2 - \widehat{a}_1$:

$$\widehat{a}_1 \quad = \quad G_{11}\widehat{F}_{1+}G_{12}\widehat{F}_1,$$

$$\begin{aligned} \widehat{a}_2 &= G_{21}\widehat{F}_1 + G_{22}\widehat{F}_{2,} \text{ and} \\ \widehat{a}_2 - \widehat{a}_1 &= (G_{11} - G_{21})\widehat{F}_1 + (G_{12} - G_{22})\widehat{F}_2. \end{aligned}$$

where G_{ab} is the detector transfer function and $\widehat{F}_a$ is the Fourier transform of the force impulse signal.

In the case of a gravitational wave signal we have already mentioned that the only force present is the force on the bar F_1. In this case the FFT for the signal is:

$$\widehat{a}_2 - \widehat{a}_1 = (G_{11} - G_{21})\widehat{F}_1. \tag{16.23}$$

CHAPTER 17
THE SIMULATION

17.1 The Realistic Resonant Detector Versus the Simulated One

The typical bar detector is a large aluminum mass (around 1 ton) and a transducer used to "read" the motion of the main mass. Due to the very small cross section of gravitational interactions, the large mass is necessary to increase the energy released in the detector by the incident gravitational waves. The bar resonant frequency is tuned to particular astrophysical events such as supernova explosions that are supposed to produce gravitational waves with a characteristic frequency of about 1000 Hertz (see the characteristic time scale discussion in the previous part of this dissertation). The transducer, connected to the bar, could be an electric device that transforms the mechanical motion of the main mass in a readable electrical signal. In actuality the transducer is a combination of electrical and mechanical parts. For example in the ALLEGRO detector the mechanical part of the transducer is a "mushroom" shaped piece of metal that is joined to the bar. The mass of this mechanical second resonator is very small. As the bar moves and oscillates the flat part of the 'mushroom' bends and accelerates. The electrical part of the transducer is an inductor in which a small current is constantly going through. The bending metal of the mechanical transducer pushes back and forth the field lines of the magnetic field of the inductor. The inductance, in the inductor, is in this way modulated by the change in shape of the mechanical resonator that reacts to the vibration of the bar. A device called SQUID (Superconducting Quantum Interference Device) is able to convert (and amplify) the changing

flux in a changing voltage which is the physical quantity that is finally recorded in the data acquisition system of the detector. The transducer's total physical characteristics can be translated as that of a mechanical oscillator. Properties such as the natural resonant frequency of this oscillator are chosen to be close to that of the bar. The equivalent mass of the transducer is very small in comparison with the large one (˜1 kilos). This is done to amplify the minute displacements expected to be created by realistic gravitational waves, of the order of 10^{-21} or less than the length of the bar (˜1 meter long). Because of its small mass the transducer is practically not affected by the presence of gravitational waves. The perfect tuning of the bar (mixing angle $\alpha = 45^o$) and transducer is an ideal situation almost impossible to achieve in practice. In our simulation, however, we decided to choose this ideal setting. The perfect tuning should not affect the performance of the two filters but investigations in this particular issue are needed.

In this chapter we explain how to make a discrete time simulation of the antenna dynamics using the mathematical tool called *digital filter.* This approach achieves the purpose of simulating the physical behavior of the oscillator without using for example, ordinary differential equation solvers. Furthermore the digital filter is a representation of the data acquisition system. The real detector is an analog device, it is continuously responding to the different forces that excite it. Instead, our measurements are necessarily finite in time. The process of measurement transforms the analog response of the detector in a digital sequence of information. The digital filter we use creates an output that is discrete in time, and so it represents the digital process of sampling the

analog response of the bar. Hereafter, we will call this filter the digital simulator, to not create confusion with the data analysis filters mention in the following.

17.1.1 Noise Characterization and Simulation The physical behavior of the detector is due to the reaction to thermal Brownian motion force acting on bar and transducer. The random force on the bar and the transducer are independent from each other. We simulate this by a sequence of random force impulses that constitute the input for the digital simulator. The sequence of impulses has a fixed separation in time, determined by the sampling frequency, in our case 4096 samples per second. In reality, of course, the noise impulses arrive at random times. The discreteness of the sampling process in the real experiment allows us in any case to simulate the noise as a sequence of events discrete in time. The amplitude of the impulses is normally distributed with zero mean. In addition to the thermal noise there is another source of noise in the detector; this is the electrical noise from the SQUID. This type of noise is added in the simulation to the response of the bar to the thermal noise. The SQUID noise is white, normally distibuted with mean zero. The ratio of the amplitude of the narrow band noise (the response of the bar to the thermal force) to the wide band noise of the SQUID is an important parameter that determines the characteristics of the detector. This point will be discussed in more details in the following sections.

We are going to consider the simpler case of one mode oscillator. We can build an n-modes oscillator using the same technique applied to n-independent oscillators. Then we consider such oscillators as the normal modes of a n-modes oscillator. To get the output of the oscillator in the mass coordinates we apply the usual linear

transformations to the independent outputs of the n oscillator. We will explain this in details in the following.

17.2 Difference Equations and Filters

In this section we are going to show how to use digital filters to solve the discrete equivalent to differential equations: difference equations. The differential equations that describe the motion of the masses in a coupled harmonic oscillator can be "discretized" writing similar equations that gives the solution y_n at a time t_n as a function the previous status y_k of the system, with $k > n$.

$$u(n) f(n) \longleftrightarrow \mathbf{F}(n) \tag{17.1}$$

If we assume that z-tranform of $f(n)$ is $\mathbf{F}(n)$ where $f(n) = 0$ for $k < 0$.

$$\mathbf{F}(z) = \sum_{n=0}^{\infty} f(n) z^{-n}. \tag{17.2}$$

See the next section for a definition of the z-transform.

Let's define

$$u(n-1) f(n-1) \longleftrightarrow \mathbf{F}_1(n) \tag{17.3}$$

Then

$$\mathbf{F}_1(z) = \sum_{n=0}^{\infty} f(n-1) z^{-n}. \tag{17.4}$$

Let

$$r = n - 1 \tag{17.5}$$

Substituting and manipulating

$$\mathbf{F}_1(z) = z^{-1} \sum_{n=0}^{\infty} f(r) z^{-r}. \tag{17.6}$$

Proceding in a similar way, we can generalize to the previous result and obtain:

$$u\left(n-K\right)\ f(n-K) \longleftrightarrow z^{-K}\ \mathbf{F}(z) \tag{17.7}$$

We used the built in function FILTER in MatLab software to solve the difference equation that models the bar dynamics. The function FILTER in the is a "Direct Form II Transposed" implementation of the standard difference equation:

$$a_1 y_n = b_1 x_n + b_2 x_{n-1} + ... + b_{n_b} x_{n-n_b} - a_2 y_{n-1} - ... - a_{n_a+1} y_{n-n_a} \tag{17.8}$$

If a_1 is not equal to 1, FILTER normalizes the filter coefficients by a_1.

In general, the difference equation of the type above can be written as:

$$\sum_{r=0}^{R} a_r\ f\ \ (n-r) = g\left(n\right) \tag{17.9}$$

where $g\left(n\right)$ is the driving force. Taking the z-transform of both sides of the equation, we have

$$\mathbf{F}\left(z\right) \sum_{r=0}^{R} a_r\ z^{-r} = \mathbf{G}\left(z\right)$$

Solving for $\mathbf{F}(z)$, we obtain:

$$\mathbf{F}\left(z\right) = \mathbf{G}\left(z\right)\ /\ \sum_{r=0}^{R} a_r\ z^{-r} \tag{17.10}$$

This is the general form of the solution of a difference equation in terms of its z-transform.

In the next sections we are going to show how to use this technique to create a model for an one mode and two mode oscillator.

17.3 The One Mode Oscillator

To measure the oscillation of the bar we use a device (called a transducer) that transforms the bar's mechanical motion in some measurable physical quantity. Because the bar needs to be isolated from the environment we want a transducer that forms a self-contained system with the bar. The most efficient way to create such a system is to build a two (or more) mode oscillator, where the bar and the transducer are the coupled oscillators. We want to study the characteristics of the fast and slow filters as explained in the introduction. The best way to do so is to look at a one mode oscillator. We can do a computer experiment where we model the behavior of a mechanical resonator and get directly as an output of such simulation the position and velocities of the bar displacement without the use of a transducer. The presence of two modes can complicate our analysis of the characteristics of the two filters. The simulation also has the advantage of being well controlled. In a simulation we can easily isolate different parameters of the detector and determine their influence on filtering. Once we have understood the behavior of the filters for the one mode oscillator we can extend more confidently our study to the more realistic case of the two modes oscillator. We are going to model the one mode oscillator with a digital filter of the transfer function of one mode oscillator. This procedure is explained in the following section.

17.4 From Continuous System to Digital Filters. The Z-Transformation

17.4.1 The One Mode Oscillator We are going to "digitize" the response of the one mode oscillator with a filter.

This filter is described in Papoulis [40], p. 167. In particular the author explains that the digital simulator of a finite order system $H_I(s)$, obtained by sampling the analog impulse response $h_a(t)$, is a digital filter $H(z)$ of the same order.

In the case of a simple harmonic oscillator we have:

$$H_I(s) = \frac{1}{(s+\alpha)^2+\beta^2} = \frac{1/2j\beta}{s-s_1} - \frac{1/2j\beta}{s-s_2}, s_{12} = -a \pm j\beta \tag{17.11}$$

To obtain the corresponding digital simulator we apply the following z-matched transformation

$$s - s_a = 1 - e^{s_a T} z^{-1} \tag{17.12}$$

obtaining:

$$H(z) = \frac{ATz}{z^2 - bz + c}\ , \tag{17.13}$$

where $z = e^{sT}$, where T is the inverse of the sampling frequency and where

$$A = e^{-\alpha T}\frac{\sin(\beta T)}{\beta},\ b = 2e^{-\alpha T}\cos(\beta T),\ c = e^{-2\alpha T}. \tag{17.14}$$

Now we want to compare this formula with the well known form of the transfer function $H_a(\omega)$ of an harmonic oscillator, described by the typical differential equation $m\ \ddot{x} + c_s\ \dot{x} + k = F_{driving}$, or:

$$H_a(\omega) = \frac{1}{-m\omega^2 + c_s i\omega + k} = \frac{1}{m}\left(\frac{1}{-\omega^2 + \frac{c_s}{m}i\omega + \frac{k}{m}}\right) = \frac{1}{m}\left(\frac{1}{-\omega^2 + \frac{\omega_0}{Q}\omega i + \omega_0^2}\right), \tag{17.15}$$

where ω_0 is the natural frequency of the oscillator and Q is the quality factor.

If we give a value of $i\omega$ to s then we have that $H_I(s)$ in (17.1) is:

$$H_I(s) = \frac{1}{s^2 + \alpha^2 + 2\alpha s} = \frac{1}{-\omega^2 + 2\alpha i\omega + \alpha^2 + \beta^2}, \tag{17.16}$$

Table 17.1: The coefficients for z transform of the one mode oscillator transfer function.

numerator (b coefficients)	denominator (a coefficients)
$z^{-1} \Rightarrow 0$	$z^{-1} \Rightarrow 1$
$z^{-2} \Rightarrow A\ dT$	$z^{-2} \Rightarrow -2e^{-\alpha\ dT}\cos(\beta\ dT)$
$z^{-3} \Rightarrow 0$	$z^{-3} \Rightarrow 2e^{-\alpha\ dT}$

this leads to the identifications (up to constant m):

$$\alpha = \frac{c_i}{2} = \frac{\omega_0}{2Q},\ \beta = \sqrt{\frac{c_i^2}{4} - k} = \omega_0 \frac{\sqrt{4Q^2 - 1}}{2Q}, \tag{17.17}$$

relevant for relating (17.1) to (17.2).

To implement the digital simulator we used the filter command in the mathematical software package MatLab. The filter is specified by two vectors b and a respectively. In our particular case we have that the values for b(1) and b(2) are 0 and $A\ dT$ (dT is equivalent to T in our discrete simulation). The values for a(1), a(2) and a(3) are 1, -b, and c as defined in (2). See the MatLab manual for details on the syntax of the *filter* command.

The input of the filter is a normally distributed random sequence of force impulses. The mean value of the force F_{bar} is established by the given temperature T_{emp} of the bar ($T_{emp} = 4$ mKelvin in our experiment):

$$F_{bar} = \sqrt{\frac{S_{fb}}{dT}}, \tag{17.18}$$

where S_{fb} is the *white noise* spectrum of the random force sequence [27]:

$$S_{fb} = \frac{4k_b T_{emp}\ m\ \sqrt{\frac{k}{m}}}{Q}, \tag{17.19}$$

and k_b is the Boltzman constant.

The output of the filter operation on the force impulses input is the discrete time domain response of the harmonic oscillator driven by the random force. This is a satisfactory digital simulation of the sampling (at a chosen "fast" rate of 4096 samples per second) of the continuous response of a realistic bar detector. Finally we add a certain amount of *white noise* to the output of the digital filter. This is done to simulate the effect of the noise in the SQUID. The ratio Γ between the broad band noise of the SQUID and the narrow band noise in the bar is chosen to be similar to that of the real detector. To determine if our simulation is truly a good representation of the system with the physical characteristics chosen. We tested the response of the simulated bar to a single impulse and measured the typical exponential decay time τ and this turned out to be very close to the theoretical decay time. Also we looked at the spectrum of the simulation data and compared it with a calculated theoretical spectrum for the oscillator (see next chapter for a discussion of the form of the spectrum of the oscillator). The agreement is quite satisfactory as Figure 17.1 shows.

The procedure to create a two modes oscillator from a one mode oscillator is straightforward. It is explained in detail in the following.

17.5 Energy Conservation and Decay Time

17.5.1 Tests for Checking the Simulation Performance As a test, to demonstrate that our simulation behaves as expected, we can check if the total energy of the system is conserved within a short time span. The system is not strictly conservative because of the dissipation due to friction. Nevertheless we expect the energy to decay with a

Table 17.2: The physical parameters used in the simulation for the one mode oscillator.

Temperature T_{emp}	$4 \times 10^{-3}\ K$
Mass m_1	$1000\ Kg$
Quality factor Q_1	10^4
resonant frequency ω	$900\ Hz$
narrow/broad noise ratio Γ	5.1×10^{-9}

predictable time constant. Also we can expect the maximum of the potential energy to be coincident with a null value of the kinetic energy and viceversa. In other words the potential and kinetic energy should have a phase difference of 90^o. In a short time scale the total energy should be conserved. The maximum value of the potential energy of the oscillator should equal the initial impulse energy. The amplitude and energy should decay in an exponential fashion with a typical decay time τ:

$$\tau = Q/\omega \tag{17.20}$$

17.5.2 Convergence of Solutions and the Sampling time of the Simulation There is a important issue that needs to be discussed at this point. The digital filter that we constructed to simulate the behavior of the bar under stochastic forces is a way to solve the dynamical behavior of this system similar to solving a system of differential equations. As in the case of differential equations solved in a numerical fashion it is very important to choose appropriate initial conditions and the size of the time steps used. In our simulations the initial conditions are not so essential because we discard usually (through the use of overlapping windows) the first and last few sample points

in a typical filtered stretch (usually 2^{18} samples long). Any inital transient is therefore uninfluential in our simulation.

The sample time instead is a very crucial element in discretization of our system dynamics. Choosing shorter and shorter sampling time for our filter should bring closer our digital simulation to the real analog behaviour of the bar. The sample frequency we choose in our simulation is 4096 samples per second. We had to decrease the sampling time by a factor of 500 to have a cleaner and smoother result and reproduce more precisely some of the expected characteristics of the system as described in the previous subsection (see Figure 17.4). Even at a lower sampling rate our simulation comes close to the requirement of energy conservation in a short time scale, within an acceptable error. In this case we verify that the solution (consisting of the sample points in the time sequence) is a subset of the faster sampled solution. The results for this test are shown in the following Figure 17.5 and Figure 17.6. This verifies that our simulation behaves as expected and the sample time of 4096 is adequate for our purposes.

17.6 Simulation of the Two Mode System

It is possible to extend the method of the previous sections to the case of a two mode oscillator. The main complication that we have in the two mode situation is that there are two sources of noise in the bar besides the white noise of the SQUID. There are random forces acting on the bar and random forces acting on the transducer. Furthermore the transfer function for such system is a matrix making the problem of creating a filter more complicated. An important property of a two mode oscillator is

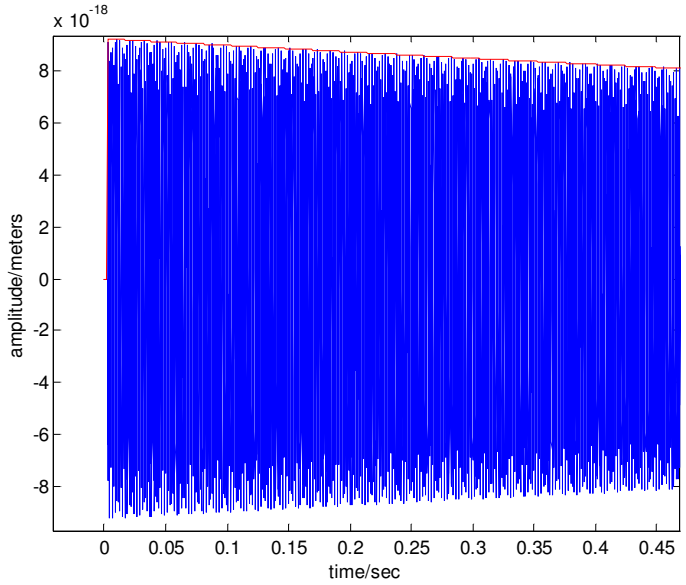

Figure 17.1: The decay of the simulated oscillator (blue) compared with the theoretical decay function (in red). The sampling rate here is 4096 per second.

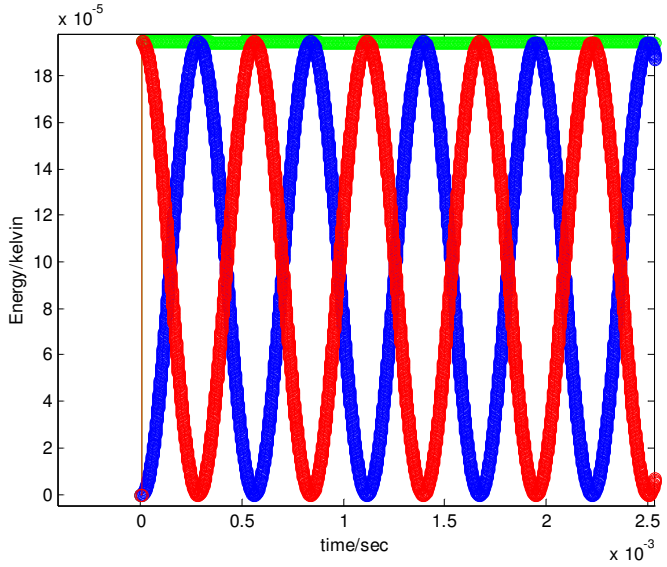

Figure 17.2: The total energy of the one mode simulated oscillator (green), the potential energy (red) and kinetic energy (blue). The sampling time is 500 shorter than in the previous figure. The potention and the kinetic energy are out of phase by 90 degrees as expected.

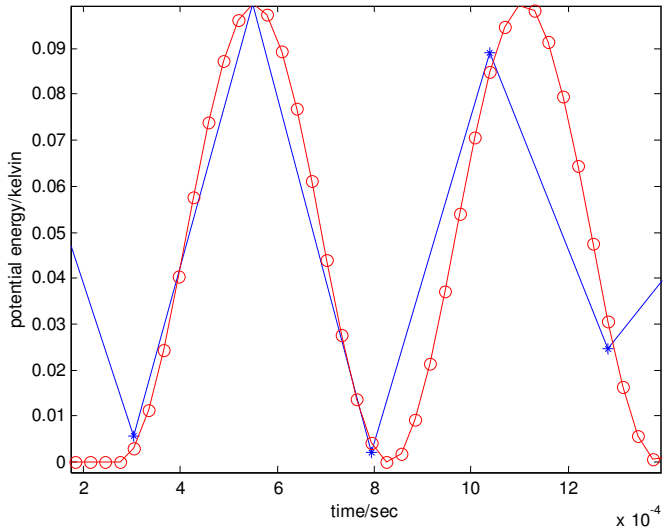

Figure 17.3: The red curve shows the simulation output with a sample frequency of 4096 samples per second. The blue curve is sampled 8 time faster. The blue curve reproduces more precisely the dynamical properties of the bar. The graph shows, anyway, that the slower sampled data is just a subset of the faster sampled data. This means that the essential characteristics of the bar dynamics are preserved in the simulation and that sampling at a lower rate doesn't effect greatly the performance of the simulation.

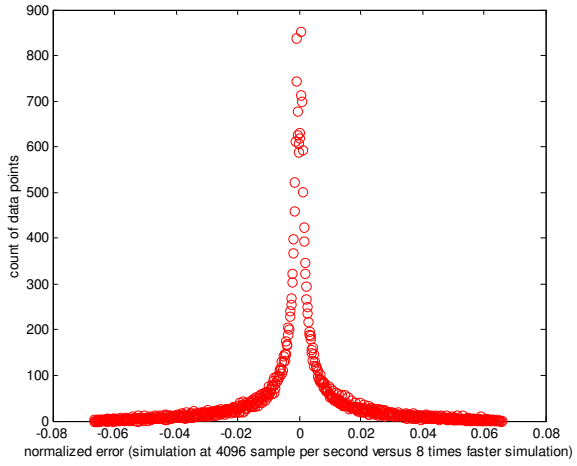

Figure 17.4: This figure shows the histogram for the "error" in the potentail energy in a simulation with 4096 sample per second compared with a simulation sampled 8 times faster. The error is normalized to the average value of the potential energy of the faster simulation. The histogram is sharply peaked around the mean value of about -10^{-4}.

Table 17.3: Physical parameters for the transducer and the bar in the two mode oscillator.

Bar parameters		Transducer parameters	
Temperature T_{emp}	$4x10^{-3}$ K	Temperature T_{emp}	$4x10^{-3}$ K
Mass m_1	1000 Kg	Mass m_2	1 Kg
Quality factor Q_1	5×10^4	Quality factor Q_2	5×10^4
resonant frequency ω_1	900 Hz	resonant frequency ω_2	900 Hz

that we can find a transformation that brings the inertial coordinates of the displacement $x_1$and x_2 to normal modes coordinates η_1 and η_2. The normal coordinates can be treated as two independent one mode oscillators. This result is exact when there is not damping in the system. Damping makes the system non-linear, introducing cross term between the modes. Theoretically that means we cannot consider the two modes completely independent. In our case we have some damping but because of the high Q of the bar and transducer we can think about the system under consideration as almost being without damping. We adopted the following steps in creating the simulation for the two modes system:

STEP1:

We specify the physical parameters for the bar and transducer. Table 17.3 shows these parameters that are similar to the real life detector.

Other parameters for the simulation are also set as the sampling rate that is 4096 sample per second and the length of the fast Fourier transform (fft), that is chosen to be at 2^{18} points. The sampling time is quite faster than the sampling time

of the ALLEGRO data acquisition system. We want to study the effect of the fast sampling time and see if we loose information from slowing down the sampling time. The temperature determines the spectrum S_{fb} and S_{ft} of the random noise in the bar and transducer . The force noise spectrum acting on the bar is independent of frequency with constant value:

$$S_{fb} = \frac{4k_b T_{emp}\ m_1\ \sqrt{\frac{k_1}{m_1}}}{Q_1}, \tag{17.21}$$

and for the transducer we have:

$$S_{ft} = \frac{4k_b T_{emp}\ m_2\ \sqrt{\frac{k_2}{m_2}}}{Q_2} \tag{17.22}$$

where $k_1 = \sqrt{\frac{\omega_1}{m_1}}$ and $k_2 = \sqrt{\frac{\omega_2}{m_2}}$ are the spring constants of the oscillators. The spectrum then can be used to determine the average size of the force impulses $F_{bar} = \sqrt{\frac{S_{fb}}{dT}}$ and $F_{trans} = \sqrt{\frac{S_{ftt}}{dT}}$. The parameter sampling time dT is the inverse of the sampling frequency. The built in random generator of the MarLab program is used to create a force time sequence normally distributed around F_{bar} and F_{trans}. These two sequences are the forces that act on the bar and transducer and the input of our simulation.

STEP2:

We now are ready to make a transformation to the normal coordinates. Following the method of the dissertation of A. Morse [35] we write the matrix $\mathbf{K}$:

$$\mathbf{K} = \begin{bmatrix} -\left(\omega_1^2 + \frac{m_2}{m_1}\omega^2\right) & \sqrt{\frac{m_2}{m_1}}\omega_2 \\ \sqrt{\frac{m_2}{m_1}}\omega_2 & -\omega_2^2 \end{bmatrix} \tag{17.23}$$

This is the mass-normalized elastic matrix. We will explain in the next chapter in more detail the derivation of this matrix. It is important to point out that this

matrix doesn't contain damping terms. To transform to the normal modes coordinates we need to find the eigenfunctions of the matrix **K**. Again we used the built in MatLab function *eig* to calculate the eigenvalues and eigenfunction matrix **A**. The eigenvalues are the normal modes frequencies. These are $\omega_+ = 914.34$ and $\omega_- = 885.88$ Hz. We then use **A** to calculate the friction coefficients in the normal modes' coordinates, that gives us the quality factors Q_+ and Q_-. Finally we calculate the forces F_+ and F_- in the normal modes' coordinates. These two forces are a linear combination of the force on the transducer and on the bar for each normal mode.

STEP3:

Now we are able to define two independent oscillators that have their resonant frequency equal to the frequency of the normal modes. These oscillators are damped and we use the quality factors in the normal modes coordinates Q_+ and Q_-. With the oscillators parameters defined we can assign values to the b and a coefficients similarly as in the previous section. In this case, of course, we have two sets of coefficients b_1, b_2 and a_1, a_2 for the two oscillators. The input of the filters are the two random sequences F_+ and F_-, the output is the time sequence of the normal modes η_+ and η_-.

STEP4:

The next task is to go back to the mass coordinates. To do so we use the inverse transformations matrix $\mathbf{A}^{-1}\mathbf{M}^{-1}$, to go from the normal coordinates η_i to the mass coordinates x_i. The mass matrix **M** was used to normalize the elastic matrix.

$$M = \begin{bmatrix} \frac{1}{\sqrt{m_1}} & 0 \\ 0 & \frac{1}{\sqrt{m_2}} \end{bmatrix}.$$

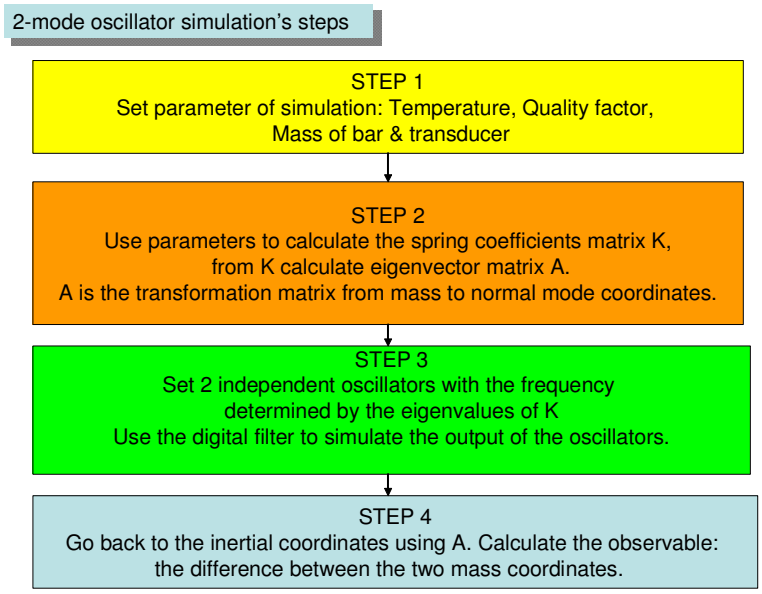

Figure 17.5: The four different steps in the simulation of the two-modes oscillator.

To return to the original mass coordinates we have to multiply by the inverse of the mass matrix **M** after multiplying by the rotation matrix **A**. Finally the measurable variable is the difference between the two mass coordinates, that is the relative displacement between the bar and transducer.

17.7 Energy Conservation and Decay Time for the Two Mode Case

The energy for the two mode system can be expressed as [12]:

$$\begin{aligned} E_{pot} &= \frac{1}{2}\left(k_1 + k_2\right) x_1^2 + \frac{1}{2} k_2 x_2^2 - k_2\ x_1\ x_2; \qquad (17.24) \\ E_{kin} &= \frac{1}{2} m_1\ \dot{x}_1 + \frac{1}{2} m_2\ \dot{x}_2 \end{aligned}$$

Again we can verify that the energy decays with the right time constant and the initial energy response of the bar is equal to the input impulse. Also as, in the one mode case, we have that the potential energy and kinetic energy have a phase

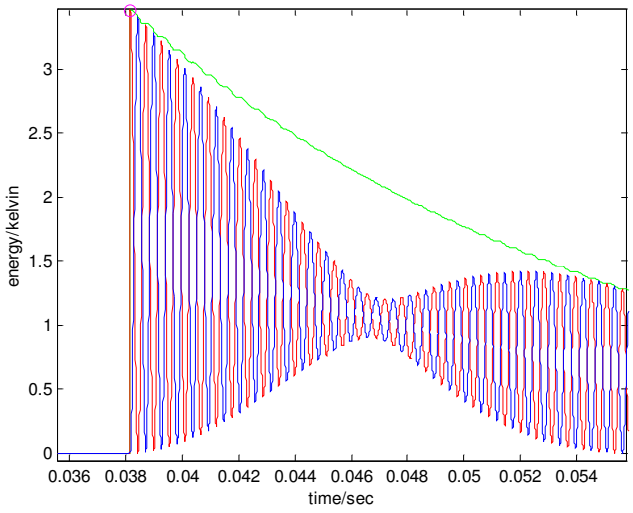

Figure 17.6: The kinetic (red), potential (blue) and total energy (green) for the two modes case. The magenta dot represents the energy of the input impulse. As in the one mode case the potential energy and kinetic energy are out of phase by 90 degrees.The general behaviour of the two components of the energy is more complicated than the one mode case but the total energy (green) is a simple exponential function of time.

difference of 90°. The following Figure 17.3 shows the result of the simulation for the two modes case.

CHAPTER 18
PRE-FILTERING. THE WHITENING FILTER

We want to eliminate the effect of the oscillatory and damping behavior of the antenna. We already have observed that if a large gravitational wave impulse impulse arrives at the antenna it will interact mainly with the bar and it will almost not excite the transducer at all. This is equivalent to say that $\widetilde{F}_2$ in expression 17.22 is equal to zero. So to recover the signal we will multiply our data in the Fourier domain by the transfer function:

$$W(i\omega) = \frac{I}{G_{11} - G_{21}} \tag{18.1}$$

The expression $G_{11} - G_{21}$ is equal to:

$$\begin{aligned} & \frac{\cos^2\theta}{m_1\left(\omega_+^2 - \omega^2 + i\omega_+\omega/Q_+\right)} + \frac{\sin^2\theta}{m_1\left(\omega_-^2 - \omega^2 + i\omega_-\omega/Q_-\right)} \\ & + \frac{\sin\theta\cos\theta}{\sqrt{m_1 m_2}\left(\omega_+^2 - \omega^2 + i\omega_+\omega/Q_+\right)} - \frac{\sin\theta\cos\theta}{\sqrt{m_1 m_2}\left(\omega_-^2 - \omega^2 + i\omega_-\omega/Q_-\right)} \\ = & \frac{A}{\left(\omega_+^2 - \omega^2 + i\omega_+\omega/Q_+\right)} + \frac{B}{\left(\omega_-^2 - \omega^2 + i\omega_-\omega/Q_-\right)} \\ = & \frac{-\left(B+A\right)\omega^2 + \left(i\omega_-/Q_- A + i\omega_+/Q_+ B\right)\omega + \left(A\omega_-^2 + B\omega_+^2\right)}{\left(\omega_+^2 - \omega^2 + i\omega_+\omega/Q_+\right)\left(\omega_-^2 - \omega^2 + i\omega_-\omega/Q_-\right)} \end{aligned} \tag{18.2}$$

where:

$$\begin{aligned} A &= \frac{\cos^2\theta}{m_1} + \frac{\sin\theta\cos\theta}{\sqrt{m_1 m_2}} \\ B &= \frac{\sin^2\theta}{m_1} - \frac{\sin\theta\cos\theta}{\sqrt{m_1 m_2}}. \end{aligned} \tag{18.3}$$

We can rewrite $W(i\omega)$ in the Laplace space with the substitution $s = i\omega$ and after factorization of the polynomials in s we get:

$$W(s) = K\frac{(s-s_1)(s-s_2)(s-s_3)(s-s_4)}{(s-s_5)(s-s_6)} \tag{18.4}$$

Table 18.1: The pre-filter coefficients b and a.

numerator (b coefficients)	denominator (a coefficients)
$z^{-4} \Rightarrow e^{-2(\alpha_1+\alpha_2)T}$	$z^{-4} \Rightarrow 0$
$z^{-3} \Rightarrow -2e^{-(\alpha_1+2\alpha_2)T}\cos(\beta_1 T) + 2e^{-(2\alpha_1+\alpha_2)T}\cos(\beta_2 T)$	$z^{-3} \Rightarrow 0$
$z^{-2} \Rightarrow 4e^{-(\alpha_1+\alpha_2)T}\cos(\beta_1 T)\cos(\beta_2 T) + 2e^{-2\alpha_1 T}$	$z^{-2} \Rightarrow e^{-\alpha_3 T}$
$z^{-1} \Rightarrow 2e^{-\alpha_1 T}\cos(\beta_1 T)\cos(\beta_2 T) - 2e^{-\alpha_2 T}\cos(\beta_2 T)$	$z^{-1} \Rightarrow -2e^{-\alpha_3 T}\cos(\beta_3 T)$
$z^{-0} \Rightarrow 1$	$z^{-0} \Rightarrow 1$

where $K = 1/(A+B)$.

Now we can realize a digital filter that reproduces the properties of the transfer function $W(s)$. In the z space it will have the form:

$$W(z) = \frac{\sum b_{k+1}\ z^{-k}}{\sum a_{k+1}\ z^{-k}}, k = 0, n \tag{18.5}$$

Applying the z-matched transformation [30] we get the expression in Table 17.1. The zeros and poles in 17.5 can be rewritten as $s_k = \alpha_k + i\ \beta_k$. This gives α_k, β_k as follows:

$$\alpha_k = \frac{\omega_k}{2\ Q_k},\ \beta_k = \omega_k \frac{\sqrt{4\ Q_k - 1}}{2Q_k}, \tag{18.6}$$

where $\omega_1 = \omega_+, Q_1 = Q_+$, $\omega_2 = \omega_-, Q_2 = Q_-$, and $\omega_3 = \frac{\sqrt{A\ \omega_-^2 + B\ \omega_+^2}}{A+B}$, $Q_3 = \frac{\omega_3}{\left(\frac{\omega_-}{Q_-}A + \frac{\omega_+}{Q_+}B\right)/(A+B)} = \frac{\sqrt{A\ \omega_-^2 + B\ \omega_+^2}}{\left(\frac{\omega_-}{Q_-}A + \frac{\omega_+}{Q_+}B\right)}$.

CHAPTER 19
FAST FILTER

19.1 Introduction

The expected gravitational waves'signals are extremely weak in comparison to the average noise in the existing gravitational wave detectors. The signals coming from any likely astrophysical sources are many orders of magnitude less, in energy delivered to the bar, than the average thermal energy of the bar environment. For this reason we need to use mathematical techniques to extract the signal from the noise. The process of signal extraction is called *filtering.*

19.1.1 The Matched Filter One of the most common filters is the *matched filter.* The term matched indicates that given the signal $s(t)$ the filter has the same form of the signal except for a reversal in time [38]. So the matched filter has the form $s^*(-t)$. This means that to implement the matched filter we need to have some initial knowledge or guess on the form of the searched signal. The matched filter is an example of a *linear system* $f(t)$. If the resonse of the filter is

$$g(t) = X\left\{f\left(t\right)\right\} \tag{19.1}$$

then the system has the following properties:

$$kg(t) = X\left\{kf\left(t\right)\right\}, \text{ where } k \text{ is a constant} \tag{19.2}$$

and

$$g(t) + g_1(t) = X\left\{f\left(t\right) + f_1\left(t\right)\right\}. \tag{19.3}$$

19.1.2 Known Signal In the case of gravitational wave detection we use our knowledge of general relativity and make models of the astrophysical processes that can cause gravitational waves. Using these models we arrive at a particular wave form for the astrophysical event. Then we use the transfer function of our detector to determine the output response of the detector to the particular astrophysical source signal. In our simulation and in the analysis of the ALLEGRO data we assumed a very simple form for the astrophysical signal. Our analysis is focused on burst signals. A burst signal is an event that occurs in a very short period of time, usually on the order of a tenth of a second or less. Possible sources for such events are supernova explosions. Another possible source of burst signals is the coalescence of neutron stars binary systems. The neutron stars will approach each other because of the loss in kinetic energy due to the emission of gravitational waves. The emission of gravitational waves in this system will span different increasing frequencies but, just before the two stars will touch, the frequency will be in the range of detectability of the bar detectors, i.e. in the kiloHertz region. At that point the orbital velocities are so fast that the last orbit before contact will be swept in a fraction of a second. So also this merging event can be considered, from a detection point of view, an extremely short lived one. This motivates us to make the simplification to model the astrophysical signal as a delta function in the time domain. The delta function represents a sudden increase in the energy of the bar due to the interaction of the gravitational wave and the mass of the bar. The detector response will be as if a large impulse hit the bar. After the initial sudden displacement the amplitude of the motion of the bar will decay exponentially. This response of the

bar to a large delta impulse as input is the template for our signal.

19.1.3 Known Noise The matched filter has the property of optimally enhancing the signal to noise ratio. A signal buried in noise and undetectable before filtering can be made quite visible after filtering. The mathematical theory of matched filters shows that this filter is *optimal* in extracting the signal from the noise and maximizing the signal to noise ratio (SNR). The matched filter, in practical applications, is often implemented using digital techniques and so it is important to understand the effect of discretization on the filter. The fast filter terminology comes from the fact that it is suggested (in the Italian papers we already referred to [30,42,43]) that sampling at a fast rate improves the optimization. Our finding in the following is that fast sampling is not the key element of the fast filter in making it superior to other filtering strategies as the slow filter or Maucelli filter currently used by the ALLEGRO group.

19.2 Known Signal in Noise

In the following we set the formal tools for a formal discussion of the matched filter. The definitions and results of the next sections are going to be used in our simulation. This a very standard treatment that is possible to find in any books on linear systems and data analysis.

In the theory of stochastic processes the estimation of a signal $f(t)$ in the presence of noise $\mathbf{n}(t)$ is an important problem. The complete data is the sum:

$$\mathbf{x}(t) = f(t) + \mathbf{n}(t), \tag{19.4}$$

the nature of the problem is to express $f(t)$ in terms of $x(t)$.

19.3 Linear Estimation

We want to use as input $x(t)$ to a linear system with impulse response $h(t)$. The output $y(t)$ is the sum:

$$\mathbf{y}(t) = \mathbf{x}(t) * h(t) = y_f(t) + \mathbf{y}_n(t), \tag{19.5}$$

where

$$y_f(t) = f(t) * h(t) \text{ and } \mathbf{y}_n(t) = \mathbf{n}(t) * h(t), \tag{19.6}$$

are the components due to signal $f(t)$ and to the noise $\mathbf{n}(t)$, respectively. The symbol $*$ indicates the operation of convolution. We define the *signal to noise ratio* as:

$$\frac{S}{N} = \frac{|y_f(t_0)|}{\sqrt{E\left\{|\mathbf{y}_n(t_0)|^2\right\}}}. \tag{19.7}$$

19.4 Deriving the Matched Filter

Once we have a stream of data that is composed of a signal and noise, we want to pick up the signal and reduce the noise. This goal is achieved by the process of filtering. In the fast filtering we choose a high rate of sampling (this is where the term fast comes from). Then we apply a matched filter to the sampled data. The idea of matched filter is explained in Papoulis [40], p. 325.

Assuming that the noise is stationary with power spectrum $S(\omega)$, then we have:

$$E\left\{\mathbf{y}_n^2(t)\right\} = \frac{1}{2\pi}\int_{-\infty}^{\infty} S(\omega)\,|H(\omega)|^2\,d\omega, \tag{19.8}$$

where $H(\omega)$ is the system function of the unknown system.

At $t = t_0$, the output due to the signal $f(t)$ is equivalent to

$$y_f(t_0) = \frac{1}{2\pi}\int_{-\infty}^{\infty} F(\omega)H(\omega)e^{j\omega t_0}d\omega \tag{19.9}$$

Applying the Schartz's inequality to the above integral and using the identity:

$$F(\omega)H(\omega) = \frac{F(\omega)}{\sqrt{S(\omega)}} H(\omega)\sqrt{S(\omega)}, \tag{19.10}$$

we obtain

$$\left| \int_{-\infty}^{\infty} F(\omega)H(\omega)e^{j\omega t_0} d\omega \right|^2 \leq \int_{-\infty}^{\infty} \frac{|F(\omega)|^2}{S(\omega)} d\omega \int_{-\infty}^{\infty} S(\omega) \left|H(\omega)\right|^2 d\omega. \tag{19.11}$$

Hence

$$\left(\frac{S}{N}\right)^2 = \frac{y_f^2(t_0)}{E\left\{|\mathbf{y}_n(t_0)|^2\right\}} \leq \frac{1}{2\pi} \int_{-\infty}^{\infty} \frac{|F(\omega)|^2}{S(\omega)} d\omega, \tag{19.12}$$

The equality is satisfied if

$$H(\omega)\sqrt{S(\omega)} = k\frac{F^*(\omega)}{\sqrt{S(\omega)}} e^{-jt_0\omega} \tag{19.13}$$

We obtain the optimum filter by

$$\boxed{H(\omega) = k\frac{F^*(\omega)}{S(\omega)} e^{-jt_0\omega}}, \tag{19.14}$$

giving

$$\left(\frac{S}{N}\right)^2 = \frac{1}{2\pi} \int_{-\infty}^{\infty} \frac{|F(\omega)|^2}{S(\omega)} d\omega. \tag{19.15}$$

In the particular case of white noise the spectrum is given by a constant N_0

$$S(\omega) = N_0 \tag{19.16}$$

then:

$$\left(\frac{S}{N}\right)^2 = \frac{1}{2\pi N_0} \int_{-\infty}^{\infty} \left|F(\omega)\right|^2 d\omega. \tag{19.17}$$

For the case of narrow band noise we have to use explictly the form of the spectrum inside the integral.

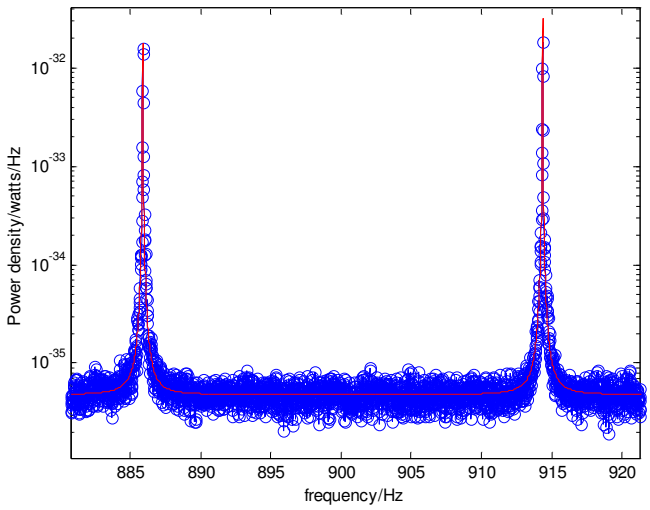

Figure 19.1: The analytical (red) and simulated (blue) functions for the spectrum in the two mode case.

19.5 The Implementation of the Matched Filter

In our simulation the noise is a combination of white and non-white noise. See previous sections for a discussion of the analytical form of the noise for the one mode and two mode systems. When dealing with data from the real detector we used (with due normalization) the MatLab function PSD to extract the spectrum of the noise. We compare in the following figure the analytical (red) and the simulation (blue) measured spectra.

In equation (19.11) we have the quantity k. This is a normalization factor that is arbitrarily chosen in such a way that the filter output maximum value is equal to the maximum value of the signal before filtering. This normalization reduces the floor level of the noise because the filtering process is supposed to maximize the SNR. Also we have to notice, in the filter definition, the presence of the phase shifting function

$e^{-jt_0\omega}$. This implies that the filtering process introduces an arbitrary delay in the time domain. In our simulation we applied large calibration pulses at a certain given time. We make sure that the filtered signal coincides in time with the calibration pulse. This gives us a characteristic constant time-shift that we use to correct the time labeling of the filtered output. The function $F^*(\omega)$ represents the conjugate of the target signal. We have already explained in the previous chapter how we obtain the analytical form of the signal for the one and two mode case. In the implementation of the matched filter the function $F^*(\omega)$ is multiplied in the Fourier domain by the Fourier transform of the data $F_{data}(\omega)$. In real life experiments the function $F_{data}(\omega)$ is noise in most of the cases with the possibility of signal more or less buried in it. We show in Figure 19.2 the result of the matched filter applied to a large signal (in the one mode case) in the absence of noise. Figure 19.3 shows the result of the filtering process in the presence of noise.

The filtered signal has a "compact" form. It has relatively short duration in the time domain. It is symmetric in respect to the maximum. This is a consequence of the atemporality of the filter; the filter uses information on the time sequence before and after the signal arrival time. Another important characteristic is the "beating" oscillations.

The filter signal oscillates about zero. This is not a physically realistic behavior. The amplitude of the filtered signal should increase, reaching the maximum and then decrease in a smooth manner. In the case of the one mode oscillator the filtered output oscillations are at the resonant frequency of the oscillator. The envelope of the

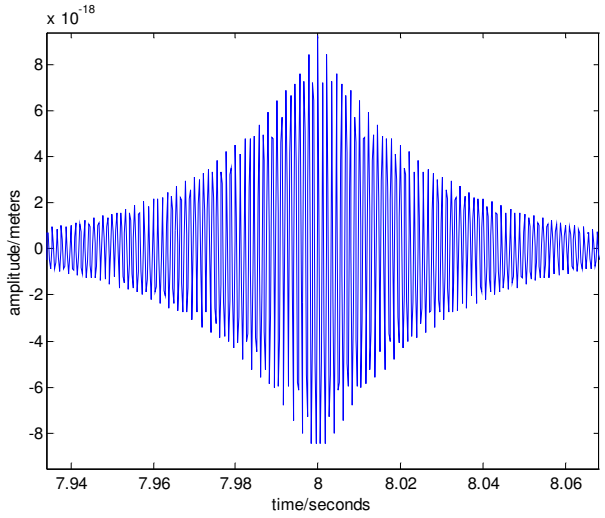

Figure 19.2: The amplitude of the filtered signal; no noise is present. Notice the oscillations through zero amplitude. This is the response when the bar excited by a large delta function. The response is described by a sine wave at the mode frequency (in the one mode case) and amplitude modulated as shown.

matched filter contains the information that is physically meaningful. See Chapter 20 for a discussion of this topic.

19.6 The Digital Fast Filter

In our simulation we start with the raw data of the displacement of the detector. Naturally this quantity is a real valued quantity. In the acquisition system of the real detector an analog demodulation is performed bringing the zero frequency of the raw data to the frequency in the middle of the two resonant modes. This operation is equivalent to multiplying the real valued data by a complex value function; see Chapter 24 on working with real detector data. This means that the raw data becomes a complex valued quantity. In the ALLEGRO acquisition system the real and imaginary components of the complex raw data (called in phase and in quadrature) are treated separately. In our application of the matched filter using real data we combine the

two components in one complex variable and work on this variable directly. In the simulation we don't have to deal with complex raw data. The following is a summary of the steps taken to filter the real detector data but these are similar to the simulated case (beside the difference in real and complex raw data explained above).

I) **Pre-treatment of data**:

The raw data is in the form of in-phase and quadrature components. A single complex number is formed by combining the in-phase and quadrature components of the raw data as real and imaginary parts of a single variable named z.

From z we take out the mean value of z, to eliminate the dc component of the data.

We apply an antialias filter. This is achieved by a low pass filter. The cutoff frequency is 0.85/3 times the nyquisit frequency. The data is then decimated by a factor of 3.

II) **Data Analyis**:

1) Make a spectrum of noise using MatLab psd. The variable that represent the noise spectrum is called **Snoise**.

2) Make theoretical FFT of the signal.

We take the transfer function of the bar in the Fourier domain. We multiply this by a vector that has a F1 component equal to the FFT of a delta function and F2 equal to zero. The FFT of the signal is called **at**.

3) Make the filter. Divide the conjugate of the theoretical FFT of the signal **at** by the spectrum **Snoise.** This varaible is called **H.**

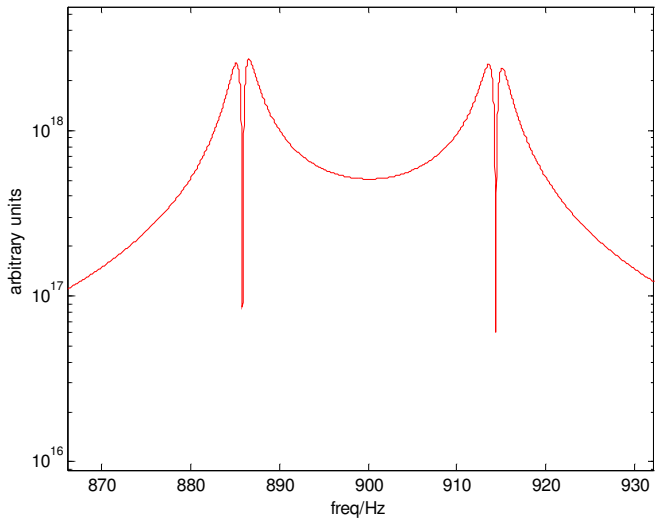

Figure 19.3: The filter H in the frequency domain for the two mode case.

Filtering the data:

4) Multiply the filter **H** times the FFT of the data in order to filter.

5) Use the MatLab function IFFT to go back to the time domain and obtain a time sequence of the filtered output.

Normalization:

6) The result of the IFFT operation gives a complex quantity because of the presence of a non-zero phase component of the time sequence (the imaginary part of the inverse transform filtered data). We take the absolute square of this quantity and call it the "energy" of the filtered data. We normalize this energy in such a way that a large filtered calibration impulse has the same value as the initial impulse in units of kelvins. See normalization section in next chapter. The next figure shows the typical shape of the filter **H,** in the Fourier domain, for the two mode system.

CHAPTER 20
SLOW FILTER

20.1 Introduction

Historically the ALLEGRO experimental gravitational group has used a filtering strategy that is based on separating the information from the two resonant modes of the antenna, through demodulation. Also the data stream is kept in its in-phase and in-quadrature parts and these components are filtered separately. To estimate the final filtered energy output all of these pieces are added together with particular weights based on the difference in the average temperature of the two modes. For reasons of data storage economy and to improve the speed of the data analysis, just a small frequency window around the resonant peaks is saved, using a low pass filter after demodulation. The data is then reduced through decimation. All the filtering operations are done in the time domain without using Fourier analysis. The data acquisition system is relatively slow. The data is sampled every 0.008 seconds or at a frequency of 125 Hz. Compare this sampling rate to the 4096 Hz of our simulation. This slower sampling rate is why this filtering procedure is called *slow*. We are going to show in Chapter 22 that the sampling rate is not a fundamental element in the optimization of the filter when dealing with colored noise detectors. The convention of the slow and fast names will still be used. In the following we are going to summarize, for reference purposes, the main steps of the slow filtering process. We used mainly material from the E. Maucelli article on the data acquisition and analysis of the ALLEGRO detector [41].

20.2 Energy and Noise Temperature

We have already seen that the acquisition system of ALLEGRO separates the raw data stream in the in phase x and quadrature y components. In our simulation we combine these components in one complex variable called z, and we have that $z = x + i\ y$. In the following we are going to describe the important filtering steps according to the usual procedure used by the ALLEGRO group. This is similar enough to our simulation to not justify changing notation.

The first step is to demodulate the data. In the real detector this is done analogically through a lock-in device. The reference frequency is in the middle of the two resonant frequencies. In our simulation we do this multiplying the amplitude output of the detector simulator by a complex function ϕ called *phasor*:

$$\phi = \exp(2\pi f_{ref}\ t), \tag{20.1}$$

where f_{ref} is the reference frequency. The slow changing DC offsets are removed from the data by subtracting the average value of the amplitude from the time sequence. In the simulation the data is then demodulated by a factor of 32. This brings the initial sampling frequency of 4096 Hz close (128 Hz) to the ALLEGRO raw data sampling frequency of 125 Hz. A further demodulation is performed with reference frequencies equal to the minus and plus modes. A low pass filter is applied with a corner frequency of a few Hertz. In the case of the real detector this corner frequency is exactly 2.35 Hz. Both the simulated and real data is decimated again by a factor of 10. This brings the final sampling frequency at 12.5 Hz for the real detector (12.8 Hz for the simulation).

We then apply the time domain version of the matched filter using the MatLab function filter with weights obtained as explained in the following section. The x and y output of the filters is multiplied by its conjugate and then these quantities added to obtain the absolute square of each mode. If we represent the output of the separated in-phase and in-quadrature components for the minus and plus modes as $f_{x\pm}$ and $f_{y\pm}$, we have that the burst energy at each sample is:

$$E_{\pm} = f_{x\pm}^2 + f_{y\pm}^2, \tag{20.2}$$

The next step is to estimate a total burst energy for each sample. The average temperature in the two modes can be different (this depends on how well "tuned" the natural modes of the bar and transducer are). The energy of an event then is distributed in different way in the two modes. To have a statistically correct evaluation of the burst energy we have to assign a weight to each mode and use this weight to calculate the total energy of each sample. The weighted burst energy is:

$$E_w = T_w \left(E_+/T_+ + E_-/T_-\right) \tag{20.3}$$

where the quantity T_w

$$T_w^{-1} = T_+^{-1} + T_-^{-1} \tag{20.4}$$

is the weighted noise temperature.

20.3 The Filter Weights

The MatLab filter function uses as input the sequence of coefficients (weights) b and a of the denominator and numerator of the polynomial representation of the filter

(see section 16.3). The slow filter weight a is equal to 1. The weights b are constructed using the auto-correlation function of the noise. We have that:

$$\mathbf{b} = \underline{R}^{-1}\mathbf{s} \tag{20.5}$$

where $\mathbf{b}$ is a the vector of the numerator coefficients of the filter, $\underline{R}^{-1}$ is the inverse of the auto-correlation matrix of the noise and $\mathbf{s}$ is the detector's response to the signal being sought. To calculate the auto-correlation function in our simulation we use the MatLab built in function CORR. The auto-correlation of the two modes is calculated separately, generating two sets of filter weights.

20.4 The Signal

We need to characterize the nature of the signal that we are hoping to detect. For this purpose we stimulate the bar with a specific, completely know target signal. A delta signal of short duration smaller or equal to the sampling time is used as the input for the digital simulator, without any noise present.

The response of the bar, in the absence of noise, is demodulated, low-pass filtered and decimated. A sample of length 1/2 the length of the weights around the peak of the response of the detector forms the signal characterization. We collect the data points for the in-phase $\mathbf{s}_{\pm}^{x}$ and $\mathbf{s}_{\pm}^{y}$ in-quadrature part of the signal (separately for the plus and minus frequency). The in-phase and in-quadrature parts of the signal are squared, added together and then we take the square root of this quantity that is the final signal characterization $\mathbf{s}_{\pm}$:

$$\mathbf{s}_{\pm} = \sqrt{\left(\mathbf{s}_{\pm}^{x}\right)^2 + \left(\mathbf{s}_{\pm}^{y}\right)^2} \tag{20.6}$$

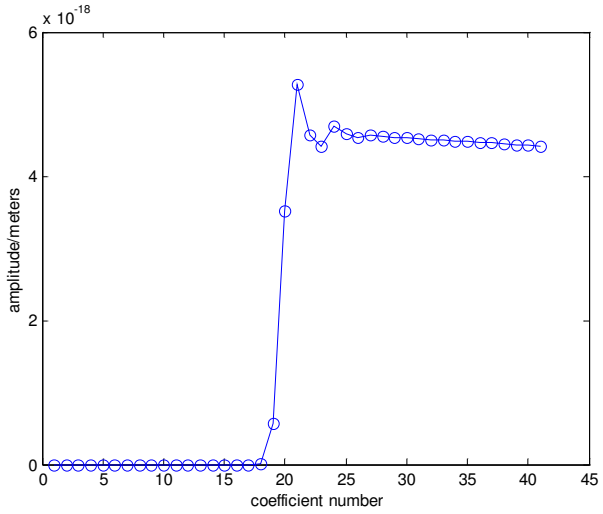

Figure 20.1: The signal vector characterization for the one mode case.

The length of the signal is 41 samples. The following figure shows the result of this process.

20.5 The Noise

Instead of measuring the spectrum of the noise, the slow filter relies on the auto-correlation function $\mathbf{R}$:

$$\mathbf{R}(j) = \frac{1}{N} \sum n_i n_{i+j}, \tag{20.7}$$

where N is the number of coefficients in vector $\mathbf{R}$, in this case 41. The noise amplitude n is the output of the simulated oscillator after demodulation and decimation. The noise in our simulation doesn't need to be cleaned of large non-Gaussian events as happens in the case of filtering the real data from ALLEGRO. We select a few hundred stretches of data 3.2 seconds long (41 samples each onsisting of 0.078 seconds). The segments of data are uncorrelated because they are separated by few minutes in the simulated time sequence. This time is much longer of the relaxation time of the oscillator. For

each segment of data we calculate the auto-correlation function, and obtain a final auto-correlation averaged over the few hundred stretches collected. Finally we assign values to quantities called R^x and R^y, representing the real and imaginary parts of the averaged auto-correlation function. In the case of the two mode oscillator we have to separates sets of auto-correlation for each mode. The next step is to use the MatLab function *toeplitz* to generate the auto-correlation matrix $\mathbf{R}_{\pm}$**:**

$$\mathbf{R}_{\pm} = toeplitz\ (\frac{1}{2}\ (R^x_{\pm} + R^y_{\pm})), \tag{20.8}$$

The matrix $\mathbf{R}_{\pm}$ has the form:

$$R_{ij} = \frac{1}{2}\left(R^{x\ \pm}_{i+j} + R^{y\ \pm}_{i+j}\right). \tag{20.9}$$

The inverse of auto-correlation matrix $\mathbf{R}_{\pm}$ is calculated using the MatLab function INV. Finally we can calculates the filter weights using equation 20.5. Following figures show the auto-correlation and the filter weights for the one mode case.

20.6 Normalization

We already seen that the definition of the filter in equation 19.11 contains a normalization factor k. Also the slow filter needs to be normalized. The motivation of the normalization should be that we can interpret the effect of the filter as maintaining the energy of the signal while reducing that of the noise, improving in this way the signal to noise ratio. So the object of normalization is that to assign the same energy to the response of the bar after to a large signal as to the filtered output. This means in practice that we need to find a normalization constant given the detector parameters.

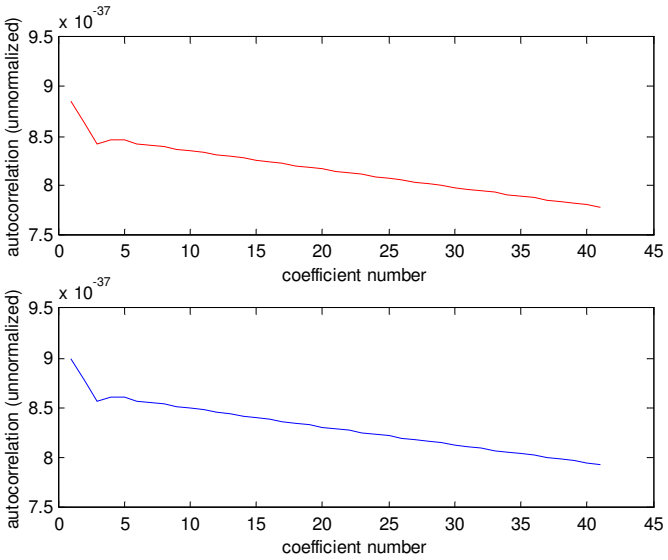

Figure 20.2: The autoccorelation fucntion for the one mode case, a) in phase, b) in quadrature components.

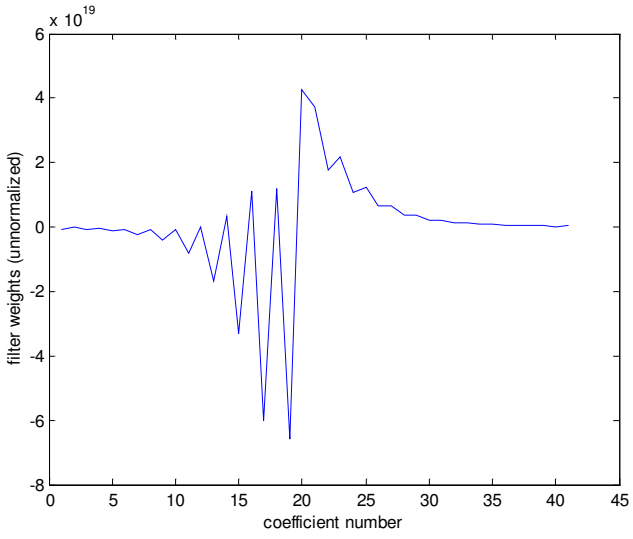

Figure 20.3: The filter weights for the one mode case.

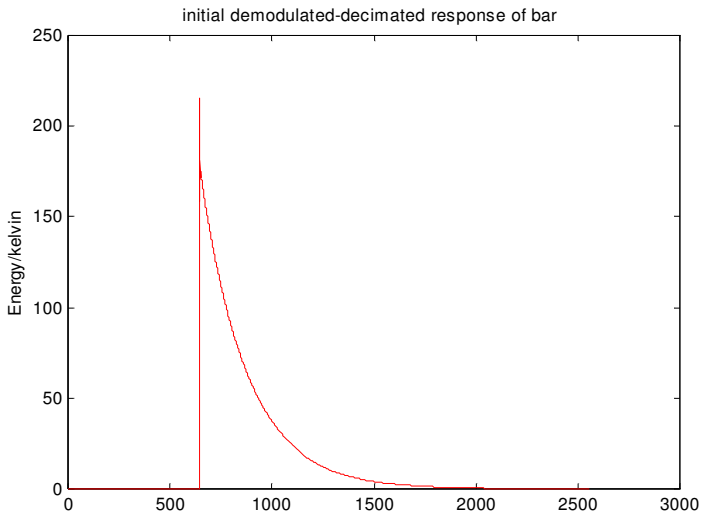

Figure 20.4: The initial demodulated, low-pass filtered and decimated data. No noise present.

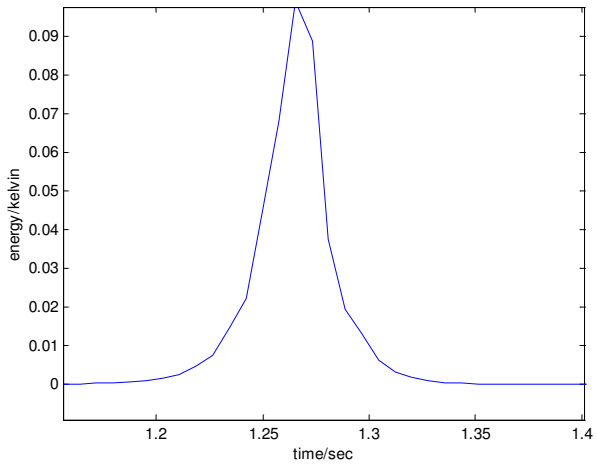

Figure 20.5: The slow filtered output in the presence of a large signal; the one mode case.

In our simulation, we imagine that the bar is kicked by an sudden force. We choose arbitrarily the size of this force (in units of Newtons). Then we calculate the value of the initial *energy impulse.* The energy impulse is calculated from the *impulse momentum* P_{imp} by the formula:

$$E_{imp} = P_{imp}^2/2m, \tag{20.10}$$

where m is the mass of the detector.

The *impulse momentum* P_{imp} is in general calculated from the initial kick force f_{sig} via the following equation:

$$P_{imp} = \lim_{\Delta t \to 0} \int_{t_o - \Delta t}^{t_o + \Delta t} f_{sig}\ dt \tag{20.11}$$

where t_0 is the time when initial impulse takes place. But because we are dealing with a digital simulation the minimum unit of time available to us is the sampling time or the inverse of the sampling frequency $1/f_s$.

Because of this we use the following formula instead:

$$P_{imp} = f_{sig}\ /f_s, \tag{20.12}$$

We already show that the response of the simulated bar in the presence of a signal gives a maximum change in energy that is equal to the initial input energy. The digital simulator is set up to give an amplitude response in meters.

Next we apply the slow and the fast to an identical set of data that represent the response of the bar to a force impulse of given size, in the complete absence of noise. We measure the maximum amplitude square of the real and imaginary part of

Table 20.1: The normalization constants for the one mode and two modes case.

constant (for simulation parameter see Tables 16.2-3)	value
$norm\_const(fast)$ one mode	1.0119×10^{-20}
$norm\_const(slow)$ one mode	9.0194×10^{19}
$norm\_const(slow)$ two modes	2.2388×10^{15}
$norm\_const(fast)$ two modes	1.0571
norm. constant to convert output of the simulator in MKS units	1.0018

the slow and fast filter output. We add the squared real and imaginary components to form a single variable $E^{un}_{tot}(fast, slow)$. The superscript un means unnormalized. This variable is used to calculate the unnormalized energy value, by the formula:

$$E^{un}_{potential} = \frac{1}{2}\ k\ E^{un}_{tot}(fast, slow) \tag{20.13}$$

where $k = \omega^2 m$ is the spring constant of the oscillator, and $\omega = 2\pi f_s$. The ratio $E_{imp}/E_{potential}$ should be 1 if we used the right normalization constant. To find this constant in our simulation we perform the calculation:

$$norm\_const(fast, slow) = \sqrt{E_{imp}/(1/2\ k\ E^{un}_{tot}(fast, slow))}. \tag{20.14}$$

In the case of two modes oscillator we calculate the energy of the slow filter according formulae 20.2 and 20.3. The values for the constants for the slow and fast filtering that we found from our simulation are given in the following table:

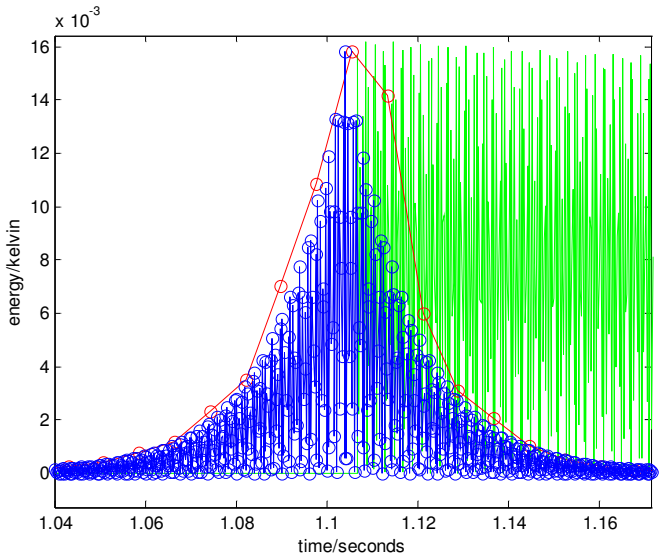

Figure 20.6: The normalization result: the energy of the bar response (green), fast filter (blue) and slow filter (red) output is the same.

The values in the table are set up for the particular choice of noise parameters reported as in the example of Chapter 16. Nominally the rms of the displacement amplitude for both white and non white is of the order of 10^{-18} meters. The initial impulsive force is of the order of 1.6×10^{-4} Kelvin. The following figures show graphically the result of normalization.

CHAPTER 21
COMPARISON OF THE TWO FILTERS

In this chapter we discuss the performance of the fast and slow filters. We want to establish if there are differences in the ability of the filters to identify the presence of a signal in the noise dominated detector. First we analyze the case of the one mode oscillator. We already explained that this case is very useful because we can determine any fundamental difference between the two filters without the complication of the two mode system. In the one mode case we want to isolate the intrinsic properties of the two filters. In the case of one mode oscillator, the two filters'construction seems similar enough that we expect should not be any difference in their performance to exctract a signal from noise. The one mode system can be explored just through analytic calculations or performing a simulation.

We generalize to the case of a two mode system. An experiment using real detectors has to deal with a least two modes because they use a transducer to mechanically amplify and read the motion of the bar, the main resonator. In the case of two modes is not necessarily true that the behavior of the two filters has to be the same than in the one mode case. At first we might think that the two mode system is just an essemble of independent one mode systems. But the gravitational signal excites the bar alone and not the transducer. It is possible that one of the two filters is better able to to distinguish the presence of a signal because it is better in identifing the situation in which the bar receives a big kick and the transducer is almost not excited. This can mean that an improvement in identification of the a signal in noise, using one filter

instead of the other, will be evident just in the two mode system. We will try to test these possibilities in the following sections.

21.1 The Results for the One Mode Case

21.1.1 The Energy of the Filtered Data We already show in the previous chapter that the amplitude of the bar response can be transformed in an *energy innovation* or the change in energy due to some random impulse on the bar. The output of the filter can be

21.1.2 The Distribution Functions of the Fiiltered Data For the one-mode case the distribtution function for the slow and fast outputs is given by Astone *et al.* [30].

The distribution function of the energy $E_{slow} = \rho^2$ of the output for the slow filter is:

$$f_{slow}(\rho^2) = \frac{1}{\sigma_{slow}^2} \exp\left(\frac{-\rho^2}{\sigma_{slow}^2}\right), \tag{21.1}$$

where ρ is the random variable the represents the slow output amplitude, and σ_{slow} is the standard deviation of the random variable ρ.

The distribution function of the energy of the output for the fast filter is:

$$f_{fast}(g^2) = \frac{1}{\sigma_{fast}\sqrt{\pi g^2}} \exp\left(\frac{-g^2}{\sigma_{fast}^2}\right), \tag{21.2}$$

where g is the random variable the represents the slow output amplitude, and σ_{fast} is the standard deviation of the random variable g.

The slow filter is the linear sum of two normal variable so it has a exponential distribution. The fast filter events have a double chi-squared distribution. The following Figure 21.1 shows the two distributions.

It might appear that for an equal number of events, there are fewer events for the slow filter at low energy and more events for the slow filter at high energy. This can lead to the conclusion that the fast filter is a better filter than the slow. We will explain in the following that comparing the two distribution functions of the totality of the events is not very useful in understanding if one filter is better than the other.

Another way to compare the efficiency of the two filters is to measure the relative *temperatures* of the noise after filtering. Because the normalization factors where chosen in such way that the output response to a large signal was the same for both filters, a lower temperature of the noise for one filter will mean a higher signal to noise ratio. In their article in the Nuovo Cimento [30] Astone *et al.* comment "...if we normalize the energy scale to the peak value of the signal, the noise of the fast filter is $kT_{eff}/2$, which we assume as the "apparent" effective temperature of this filter. For the fast filter in other words, we have an improvement of the signal to noise ratio for pulse detection of a factor of two in comparison with the slow filter". This statement has important implications for data analysis. Because noise is so dominant in comparison with even the highest possible gravity wave burst we can hope for, every improvement in the signal to noise ratio in our filtering is very significant. We need to be careful in assessing the claim that the fast filter is an improvement on the slow filter.

The measurement of the temperature of the noise can be very misleading. In fact looking at the following Figure 21.2 it seems that the temperature of the fast filter is quite less that of the slow filter. The ratio between the two temperatures is illustrated in Figure 21.3 and it seem to confirm that the temperature of the fast filter is half of

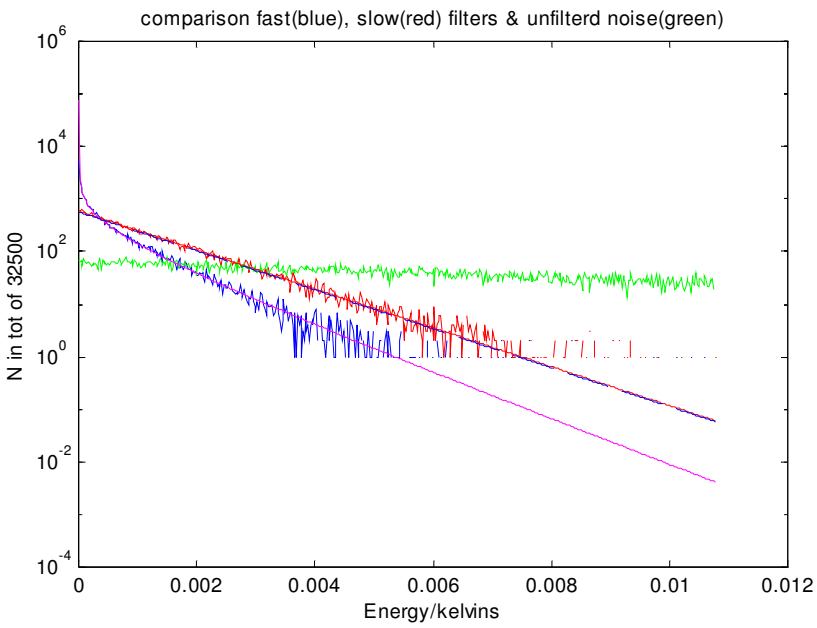

Figure 21.1: The measuread and theoretical (continuos lines) distribution functions for the slow (red) and fast filter (blue). The green points are the unfiltered data. It seems to be a very good match between measured and theoretical distribution functions.

that of the slow filter.

But this can be explained through the fact that the fast filter is oscillating between values that are almost zeros and values that are monotonically increasing or decreasing. We can see the oscillation clearly when a big signal is applied like in Figure 20.6. The random fluctuations of the noise are "modulated" by a sinusoidal function. Analytically the form of the output $g(t)$ of the fast filter after a big input pulse is expressed by the following formula (see Astone *et al.*) [30]:

$$g(t) = \frac{\exp(-d\ t)}{4d\omega_0^2}\cos(\omega_0 t) \tag{21.3}$$

where $d \approx .\frac{\omega_0}{Q}$. The exponential decay is also present in the slow filter output but the oscillatory part of the equation is typical of the fast matched filter.

In the previous section we explain how the displacement of the bar can be expressed in terms of an energy change, or evolution. The energy is then express (through the boltzman constant) in terms of a temperature in units of kelvin. This is an historical practice based on the idea that the interaction of the gravitational wave with the bar has parallel with the interaction of a particle with a calorimeter.

When the temperature of the filtered data is measured (the temperature is proportional to the square of the amplitude of the output), taking averages of the values of all the data points we get a lower value for the fast. The mean value of the square of a sinusoidal function is in fact 1/2 of its maximum value. A similar reasoning can be applied to understand why the distribution functions of the two filters give a lower count of high energy events for the noise after fast filtering. The big number of the low energy events in the distribution of the fast is due to the oscillations that bring periodically the energy function to zero. So for a given number of data points there will be much more events in the high energy range than in the lower energy one. This means that the improvement of the fast filter can be a kind of illusion that doesn't have a real physical meaning.

A more direct way to compare the two filter is to look at the entire data set without averaging. Superimposing the two time series with the right time shift allows to see that the two filters follow quite closely each other and in average the height of the "events" are very similar. See Figures 21.4 and 21.5. In the one mode case it seems that one filter is not better that the other . What we have to do to fairly compare the two filters is to look at the envelope of the data that is the only part of the data that

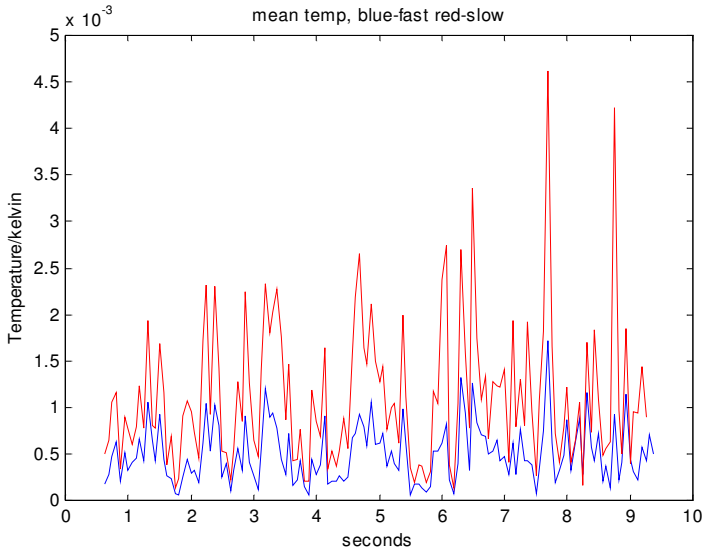

Figure 21.2: The temperature sequence for the fast (blue) and slow (red) filters. It appears that the slow filter output is at higher temperature than the fast.

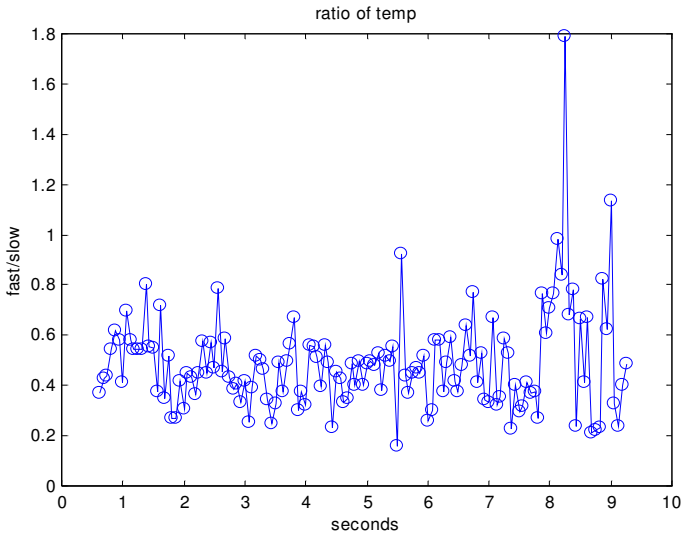

Figure 21.3: The ratio between the fast and slow output temperature as a function of time. In average this ratio is of order 1/2.

contains the physics, the oscillations under the envolope are a mathematical artifact that does not give us any interesting information. The envelope should be the part of the filtered output that contains the physical information of our system and the mean value of this set of data is a better measure of the temperature of the system. The "envelope" can be defined as the smooth curve that bounds the totality of the data points between successive peaks.

. The slow filter output, because of the demodulation and low pass operation is already a slow changing function and it is constituted of just envelope and not fast oscillations. In the case of a very large signal the slow filter output is almost the envelope of the fast filter, as is illustrated in Figure 20.6. Also see similar Figures in Astone et al. [30]. In the presence of noise, the envelope of the slow filter process is not exactly the same than the envelope of the fast filter.

We developed an algorithm that trough different passages "smooths" the fast filter and gives the slow changing behavior of the output, without taking averages. Figure 21.6 shows the result of the algorithm in choosing the points that are considered part of the envelope among the totality of the data set. We then calculate the distribution functions of the envelopes for the fast and slow filter. The result is shown in Figure 21.7. The distribution of the envelope of the fast filter looks almost exponential. This time it seems that the slow and fast filters distribution are very close. Are there more subtle differences between the two filters? The main purpose of the of the filter is to pick up a signal in noise. To answer the question, we have to study the filters behavior in the presence of signal in noise and use more precise comparison tests. Because the

Table 21.1: Statistical parameters for the fast and slow filtered data in the one mode oscillator.

statistical parameter	fast	slow
SNR^2	215.18	170.68
stand. dev. (noise)	1.69e-004	3.01e-004
stad. dev. (signal)/signal energy	0.094	0.11

properties of the filter are statistical in nature we have to perform test that probe the statistical characteristics of the filters. This will be done in the next section.

We just argued that we have to be careful in the interpretation of the mean value of filtered noise. The usual parameter that is used in characterizing the performance of a filter is the Signal to Noise Ratio (SNR) as defined in Section 19.3, equation 19.4. Because the SNR is based on a simple average of the square of the amplitude of the filtered data we think the SNR is not a fully reliable test of comparing the performance of filters with outputs that have different types of distributions.

However, it is still useful to show the result of a typical experiment where we inserted large impulses in the bar in the presence of noise. The signal had a energy of 0.05 kelvin and the noise temperature was 4 milliKelvin. To account for the oscillations of the fast filter we adjust the SNR of the fast filter by a factor of 2. The improvement in SNR, using the fast instead of the slow filter, is about 10 %. Table 21.1 shows the statistical results for the two filters in this experiment.

21.2 Statistical Tests to Compare the Performance of the Two Filters

We performed different tests to understand better if there is a difference in the performance of the two filters and which filter has the better performance.

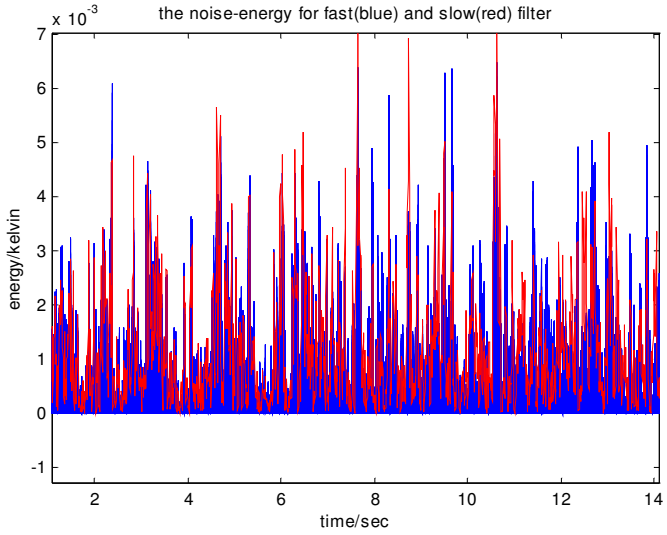

Figure 21.4: The time sequence for the fast (blue) and slow (red) events is superimposed in this figure. We can notice that even if not identical the two time sequence in average follow each other. It seems that one filter is not "quieter" than the other.

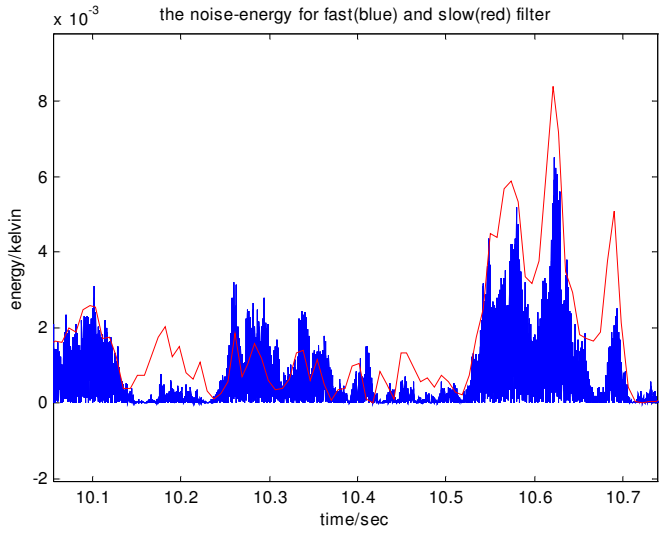

Figure 21.5: A closer look at the time sequence of the output of the two filters.

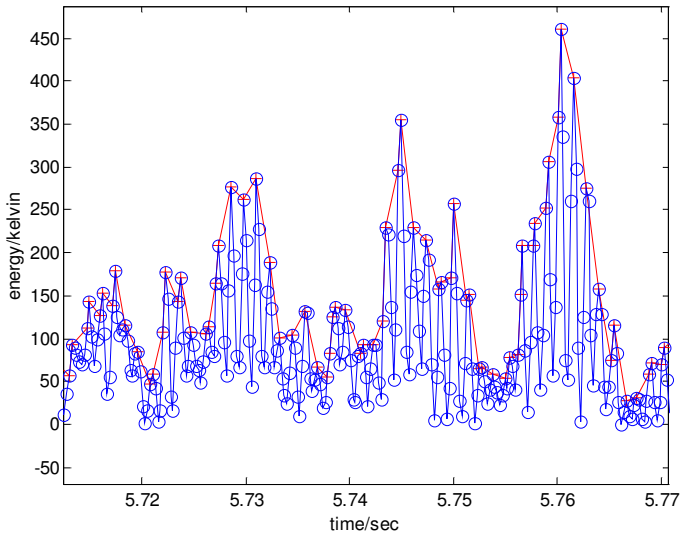

Figure 21.6: The envelope of the fast filter is shown in red, the entire fast time sequence in blue.

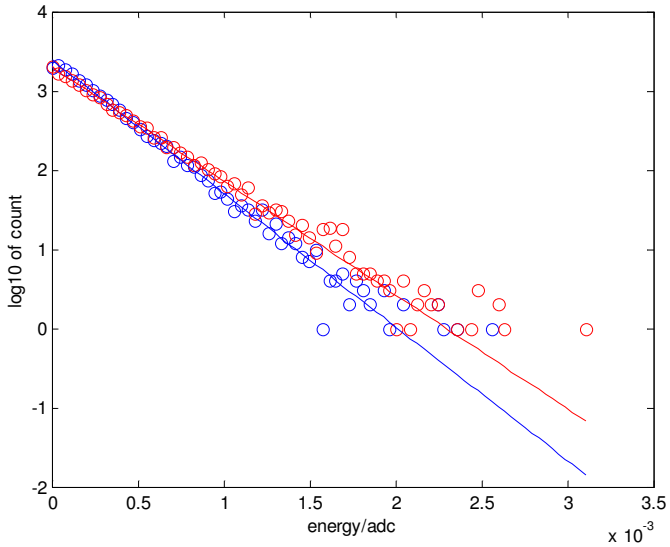

Figure 21.7: The histograms of the envelopes of the fast (blue) and slow filters (red).

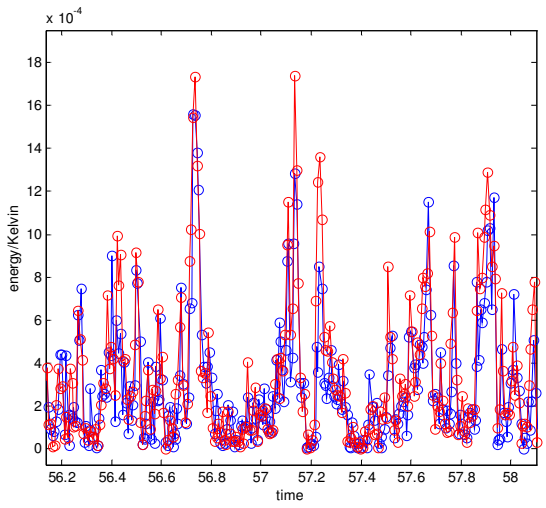

Figure 21.8: The superposition of the envelope of the fast (blue) and slow (red) filter envelopes.

21.2.1 a) The Threshold Test: In real life experiments to search for gravity wave bursts in the noisy data one has to use two or more detectors. In fact there is no real way, using information just from one detector, to determine if large bursts are due to astronomical events or if some local source of noise has excited the bar. What has to be done is to look for coincidences of the occurrence of large events between two or more detectors. We expect environmental noise in different detectors separated by long distances, to be uncorrellated. There might still be coincidences due to chance but a large number of coincidences will be a strong evidence for the presence of gravitational waves that can affect the detectors simultaneously.

The procedure to search for coincidences requires establishing an energy threshold for selection of events. If the filtered time series goes over the threshold the sequence is followed until falls again below the threshold. This group of consecutive data points is considered a single candidate gravitational event and its energy is estimated to be

the maximum of this sequence. A list of such candidate gravitational wave bursts is compiled for each detectors and then compared to look for coincidences [34]. An illustration of the procedure to identify a candidate event is shown in the following Figures 21.09 and 21.10.

We want to analyze the lists of events created using the slow filter and the fast filter in the presence of pure noise and when signal are inserted in the time series. This will be a fair and relevant test to establish the superiority of one filter over the other. It can be seen that the list of events is very similar but that there is a noticeable small difference. The slow filter, for a given threshold produces more events. For example we introduce in a minute of data 9 burst signals with energy 0.0016 kelvin and the threshold is fixed at 0.0012 we see that the slow filter produces a list of 45 events and the fast just 35. This difference, even if not big, can create more events over the threshold for the slow filter and so generating more false alarms for the coincidence search. This makes the fast filter a slightly better filter in this particular test. Figure 21.11 shows the distribution of the energy of the events over threshold. It is clear that for a given energy there are less events for the fast filter.

21.2.2 b) Estimation of Energy and Arrival Time of a Signal in Noise Test: The second test is to include a signal with a certain energy added to the noise.

In this case we introduced three equal pulses, at a certain separation between each other, in a segment 15 seconds long. The random sequence of noise pulses was re-initialized using the final condition of the filter delay (see MatLab filter options). This

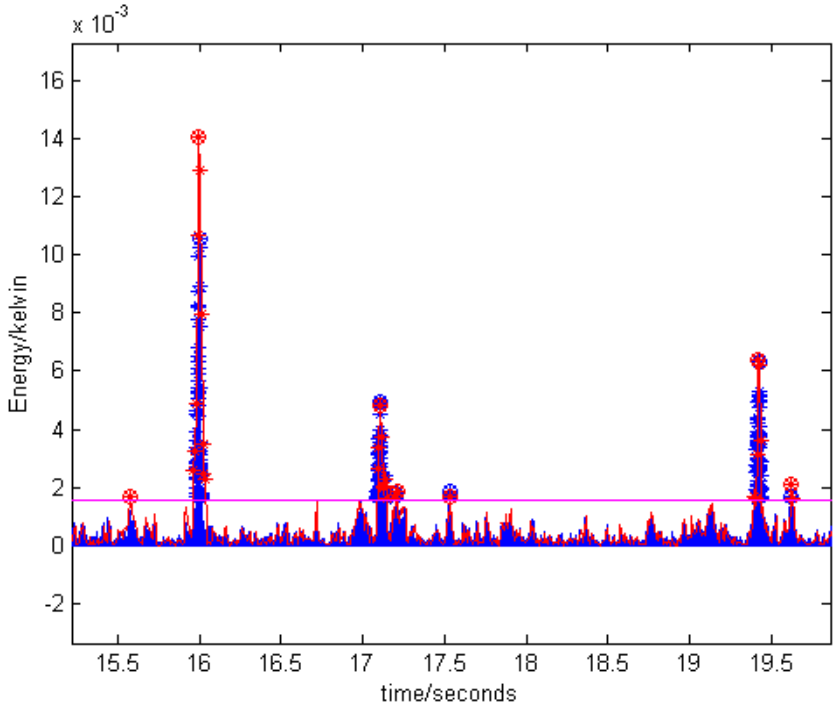

Figure 21.9: The events above threshold.

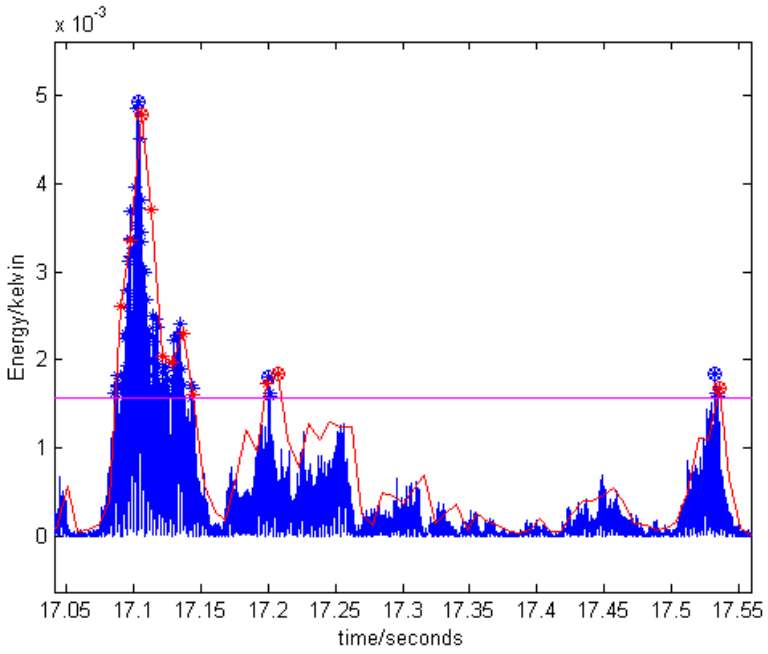

Figure 21.10: A close up of the events ove threshold and the estimation of the maximum energy of the event. The circles indicate the maximum for a given event above threshold.

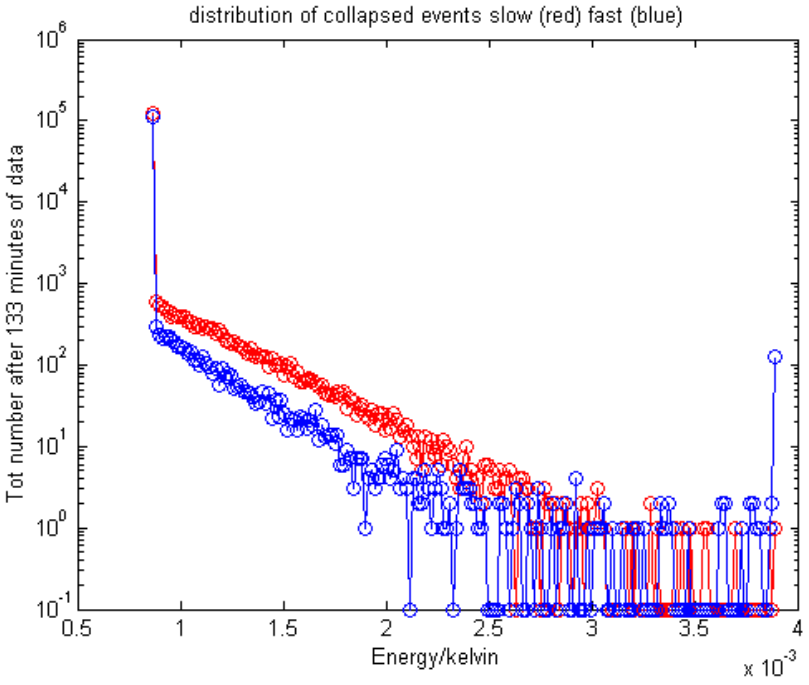

Figure 21.11: Statistics for the energy of the events above threshold. It is easy to see that for given energy there are more events for the slow filter. This produces a higher false alarm rate when performing a coincidence search betweem two detectors.

allows us to construct a very long, continuous time sequence with three large signal pulses every fifteen seconds. We run different tests with pulses with strength 25, 50, 80 and 110 times bigger than the average noise impulse. The experiment collected up to 6×10^4 samples of the arrival time differential of the pulses and their energy after filtering with the two different methods.

The *arrival time differential* is defined as the difference between the known time of insertion of the large delta function pulse, that is our signal, and the time at which the largest impulse in a given "signal window" occurs. The "signal window" is chosen to be a 1/5 of a second wide around the time where the inserted force impulse of the signal is supposed to be. We choose in the given window the largest event after filtering. We measured the energy of the largest event in the window and identified that with the energy of the signal assuming that the highest event in the window is the signal itself. The presence of the noise introduces some uncertainty in the arrival time and energy of the signal. This means that we can treat the energy and time of arrival as a statistical quantity. The distribution functions of the value of the energy estimation of the signal in noise is displayed in the Figure 21.12.

.

It is possible to see that the distribution functions are quite similar but a small effect is noticeable. In the fast filter distribution function there is a majority of events happening at the exact value of the energy of the original signal, that in the example shown is 0.0074 kelvins. The distribution function of the fast filter is slightly more narrower than the slow. The standard deviation of the distribution functions give us

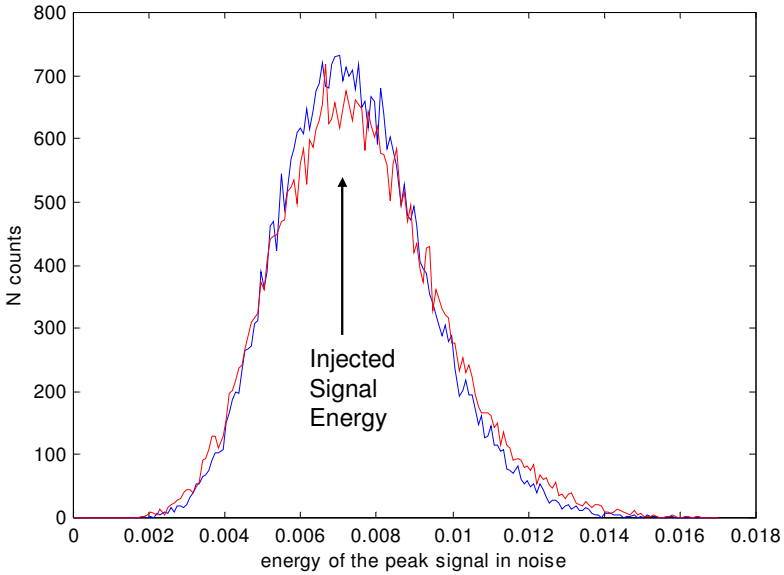

Figure 21.12: The distribution function of the estimation of the energy of the signal in noise. The red curve is the result for slow filter and the blue is that for the fast. It is possible to notice that for the fast filter there are more events near the real value of the signal at 0.0074 kelvins.

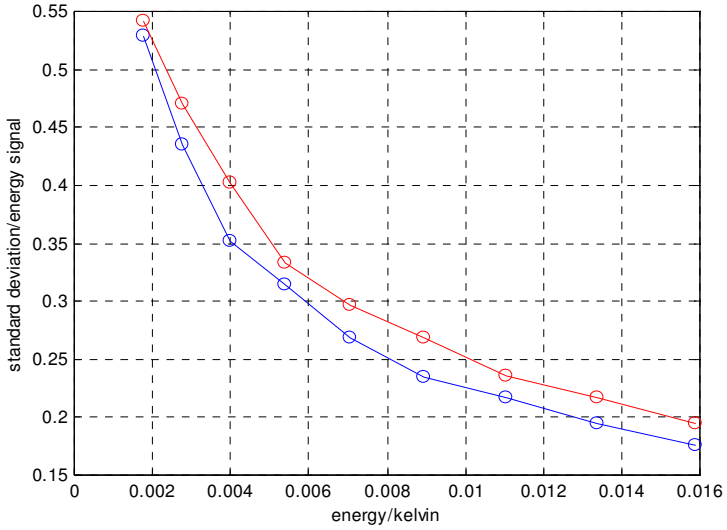

Figure 21.13: This figure shows the standard deviations for the energy estimation for the fast and slow filters. The standard deviation is normalized to the value of the original signal energy and it is displayed as a function of the energy of the signal.

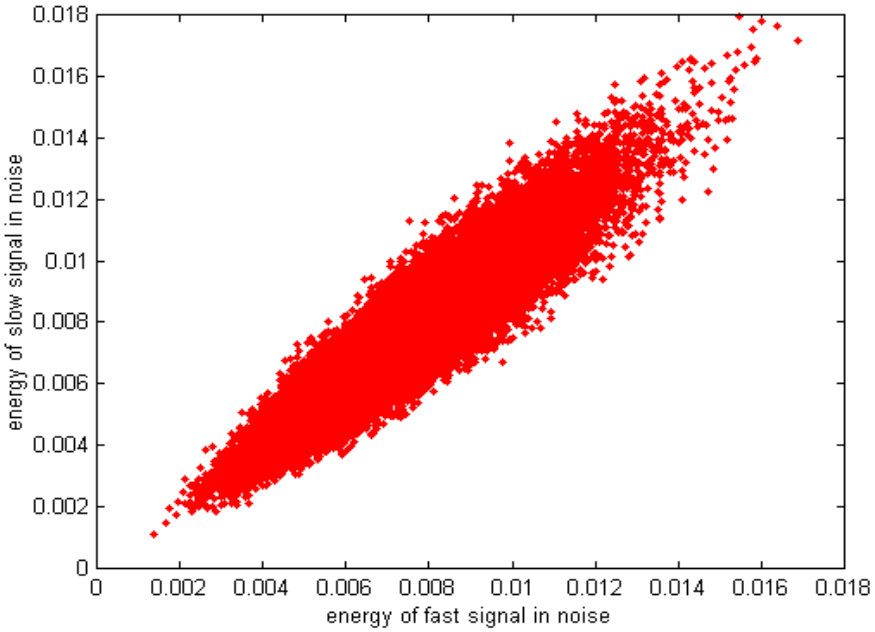

Figure 21.14: The energy of the signal in noise after the operation of filtering with the fast and slow filters are compared against each other. It seems there is a very good correlation between the two data sets.

a way to quantify this effect. The standard deviations for different signal strength is given in Figure 21.12. The difference between the two standard deviations is almost constant over a wide range of values of the initial energy of the signal. Both of the standards deviations grow with energy of the signal. The difference between the two standard deviations is about 10 %. There is also another important difference between the two filters outputs and it is the precision with which the two filters identify the arrival of the signal. Figure 21.14 shows the arrival time differential of the two filters compared to each other. The majority of the events are happening at the exact time where the signal is supposed to be or with zero delay. We can see that there is a bigger dispersion in the slow filter. We show in Figure 21.13 the comparison of the energy

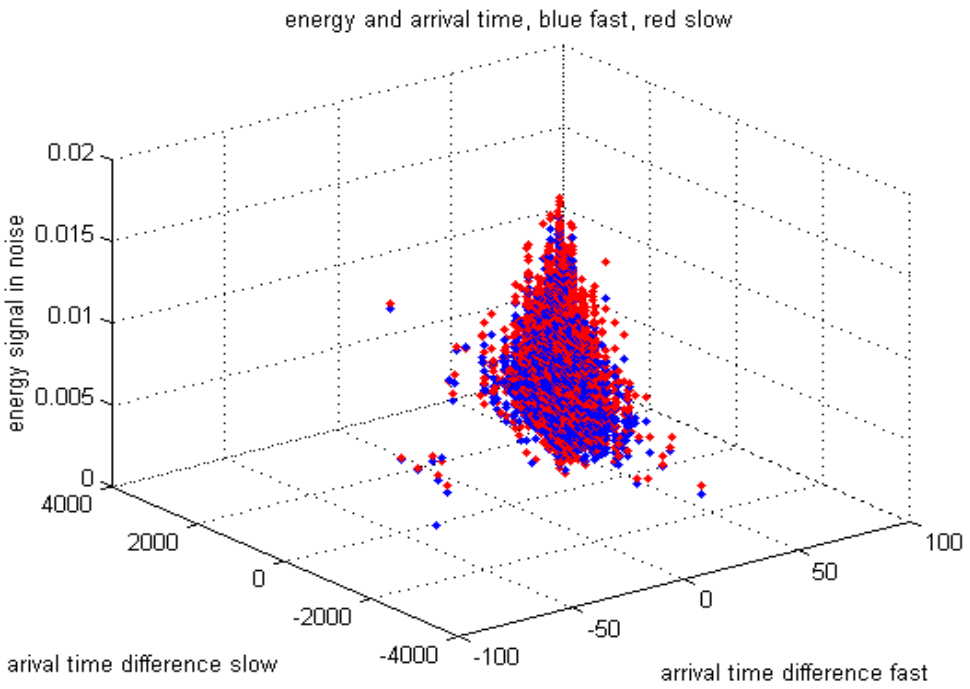

Figure 21.15: The arrival time and energy of the signal in noise for the fast (blue) and slow (red).

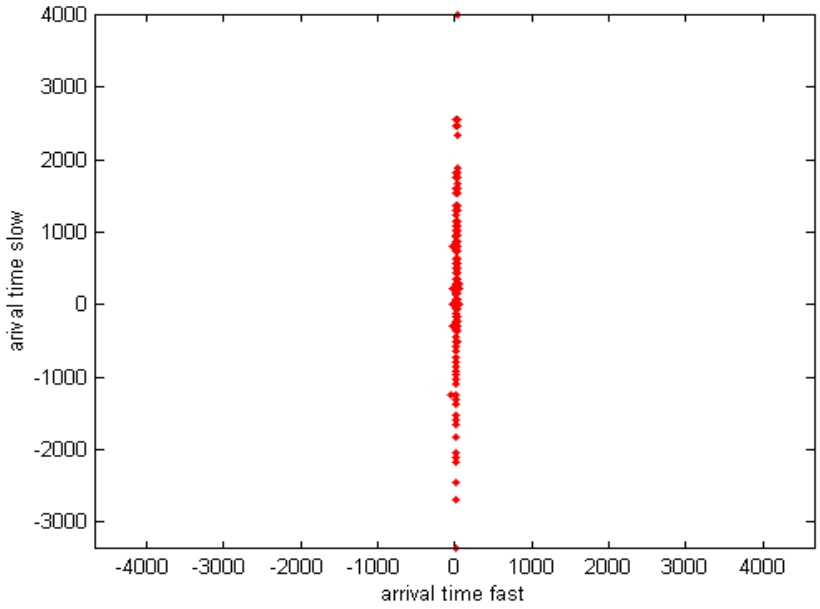

Figure 21.16: The arrival time of signal for the slow filter and the fast filter. The time is given in sampling points (4096 per second). The energy of the injected signal is 0.0074 kelvin.

Table 21.2: The standard deviation of the arrival times normalized to the energy of the signal

energy of signal	std dev. of arrival time/slow	std dev. of arrival time/fast
0.089 kelvins	4.34 x sample time	12.29 x sample time
0.0110 kelvins	3.29 x sample time	10.68 x sample time
0.0134 kelvins	2.38 x sample time	9.04 x sample time
0.0159 kelvins	1.98 x sample time	8.35 x sample time

estimate of all the signal events for the two different filters. There is good correlation between them, perfect agreement of the two data sets will mean the points will lie on a straight line but what is obtained is a configuration of elliptical shape that means the data sets agree just in average. Figure 21.15 shows both the arrival time and the energy for the slow and fast filter in a three dimensional plot. The two colors, red and blue, indicate the energy of the signal for the slow and fast filter. This is a illustration in one single glance that summarize the previous results. Table 21.2 shows the standard deviations for the arrival time differential of the two filters. The difference in arrival time is a much bigger effect than the difference in estimation of the energy of the signal. In general we conclude that also in this test the fast filter is a better filter than the slow even if by a factor of 10 % in the estimation of the energy of the original signal. There is though a real advantage in determining the exact arrival time of the signal when using the fast filter.

21.2.3 c) The Coincidence Test Finally we want to produce a complete random sequence of noise and signal that are arriving at different times. To simulate a realistic

search for coincidences in two detectors separated by large distances we create two set of different noise and one set of identical signal for the two detectors. We produce two event lists using the two filters and compare the efficiency of one filter to identify real coincidences versus random coincidences. We found similar results to test a), indicatinng that there is an excess of false alarm of 10 % for the slow in comparison with the fast filter.

21.2.4 Conclusions for the One Mode Case The slow and fast filter differ in their performance by just 10 % in the one mode case. Temperature difference between the filter is not a fair way to compare them. We have shown that the envelopes of the two outputs are very close to each other and performed different tests showing that the ability of the two filters to extract a signal from noise is very comparable.

It is interesting that there are already differences between the slow and fast filter in the one mode case. Still we don't get a factor of 2 in signal to noise ratio as claimed in the Astone paper [30]. We want to verify if this significant difference appears when the filter is applied to the response of a two mode oscillator. We use our simulated two mode oscillator.

21.3 The Results for the Two Modes Case

We might think that dealing with two modes should not alter significantly the previous results because the two modes are statistically independent. It is possible, tough, that the fast filter is better suited to distinguish between the situation when the signal is present and when it is not. However the gravitational wave signal is different from noise because it intereracts mainly with the massive bar and almost not at all

with the transducer.

It is possible to show that this difference in interaction should be evident in the target waveform which can be used to distinguish between signal and noise. The fast filter function H (see Figure 23.1) has a very different form when is applied to a large event interacting with both the bar and transducer and when the same large event excites just the bar. This difference is not evident in the Fourier domain of the slow filter applied to similar situations. This can happen because the fast filter optimizes the information from both modes, through cross terms in the energy formula for an event (see Chapter 23). The slow filter simply add linearly the energy of the two mode in this way loosing valuable information on the cross correlation between the two modes. So the interaction between the two modes in the presence or absence of a signal can be the significant difference between the one and two mode case with consequence difference in the fast and slow filter performance.

In this section we are going to show the results of tests similar to that used used in the previous sections.

21.3.1 The Superposition of the Outputs and SNR First we show a superposition of the output of the slow filter and the fast filter. Again it seems that the low filter output is consistentely at a high energy that the slow filter.

We introduced many signals with an burst energy of 0.0552 kelvins in the noise and calculated the average signal to noise ratio SNR. We adjusted the signal to noise ratio of the fast filter by a factor of 2 to account for the fast oscillation to zero, that are not physically meaningful. The SNR for the two filter in this particular experiment

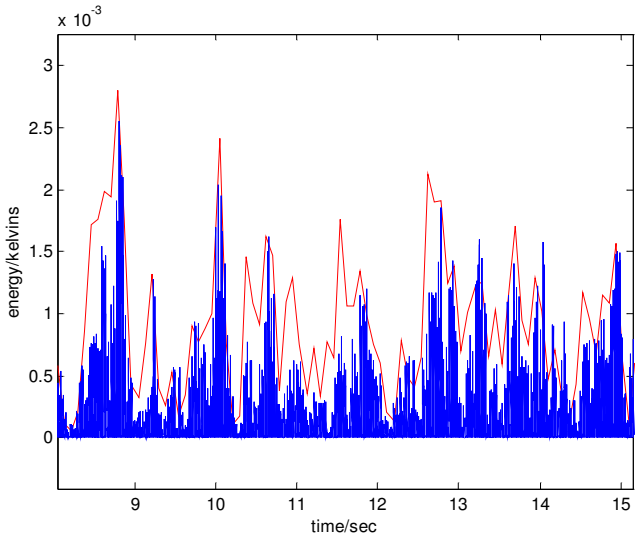

Figure 21.17: The comparison between the energy time series of the slow (red) and fast (blue) output, for the two modes oscillator.

Table 21.3: Statistical parameters for the fast and slow filter. This is the two modes oscillator case.

statistical parameter	fast	slow
SNR^2	155.25	61.18
stand. dev. (noise)	2.6916e-004	9.2317e-004
stad. dev. (signal)/signal energy	0.1198	0.1361

and other statistical data are reported in Table 21.3. The improvement of the SNR given by the fast filter is about 40 %. This improvement is much better than in the case of the one mode oscillator (10 % improvement).

21.3.2 Energy Estimation and Time of Arrival As in the one mode case in our experiment every minute of data contains three equal input signal at a fixed distance from each other. We collected the maximum value in the window where we inserted the signal. This is the value attributed to the signal in the presence of noise. We

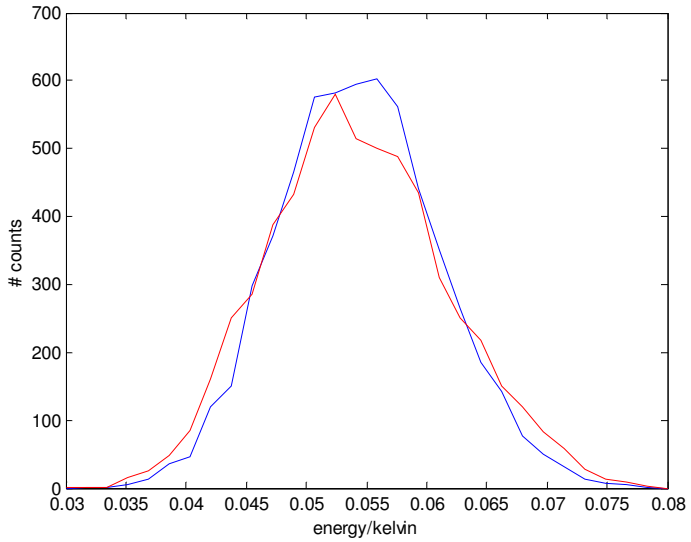

Figure 21.18: The distribution of the energy estimation for the fast (blue) and slow (red) filter in the case of the two modes oscillator. The energy of the injected singnal is at 0.052 kelvin.

show in Figure 21.16 the distribution functions of the energy of the signals after 2000 minutes of simulation time. The distribution of the energy of the signal after the slow filter procedure is noticeably wider. This means that there is a bigger chance for a false alarm trigger when using the slow filter. The percentile difference between the standard deviation of the signal energy estimation of the two filters is around 14 %. This is a small improvement in comparison with the one mode case where the average percentile difference in the standard deviations was around 10 %. Next we are going to show what this improvement means in terms of how fewer events we can find above a given threshold using the fast filter instead of the slow.

The following Figures 21.17, 21,18 and 21.19 show the result of a simulation in which we inserted three pulses at 0.006 kelvin, just above the average 4 millikelvin of the noise temperature. We established a threshold at a given energy and collected

samples above the given threshold. We group together a sequence of samples from the time goes above threshold to when again goes below the threshold. We consider this sequence as a single event above threshold and call it a "collapsed event". The energy of the collapsed event is the maximum of the sequence. The time of arrival of the collapsed event is the time of maximum of sequence. The energy distribution of the collapsed events is shown in Figure 21.17. It is possible to show that the fast filter produces fewer events above a given threshold. The presence of the signals is revealed by the "bump" in the distribution at 0.06 kelvin. This is due to the high density of our signals, 3 of them each minute. In real experiments we can expect that the gravitational wave signal are quite rare. When we are looking for possible gravitational waves we don't know what is the burst energy of the astrophysical signal. The only way to distinguish environmental noise from genuine gravitational wave signals is to look for coincidences between different detectors. We can see that the slow filter can produce more false alarms than the fast filter. Figure 21.19 shows that the ratio between the number of events above threshold can be between twice to 10 times more for the slow filter, when the threshold is at high energy. For comparison we also show the result of the same experiment without any signal, just noise. Again it is possible to see in Figure 21.20 and 21.21 that the slow filter is producing consistently more events above a given energy threshold. The ratio between the number of events above threshold in absence of signal is given in Figure 21.22.

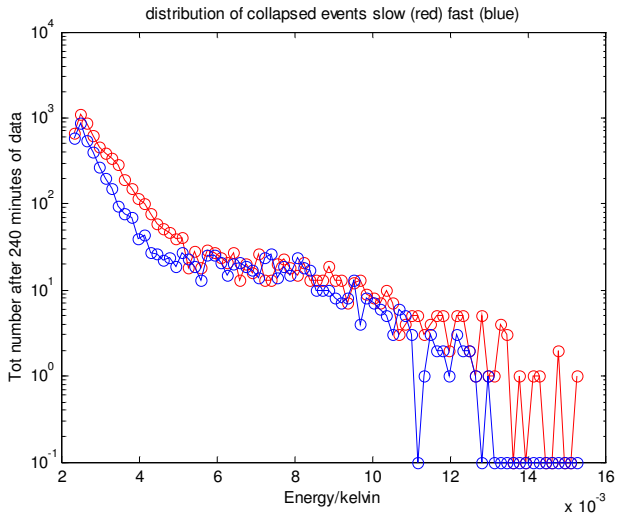

Figure 21.19: The distribution of the collapsed events above threshold for fast (blue) and slow (red). The simulation contains signal plus noise.

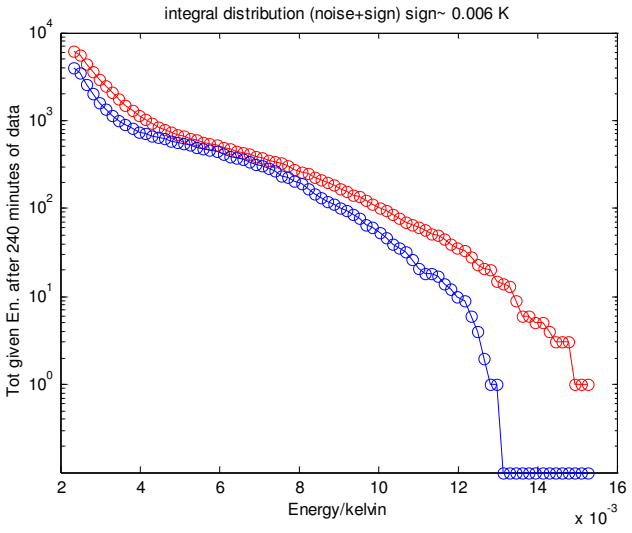

Figure 21.20: The integral distibution of the collapsed events above threshold; i.e the total number events above given energy.

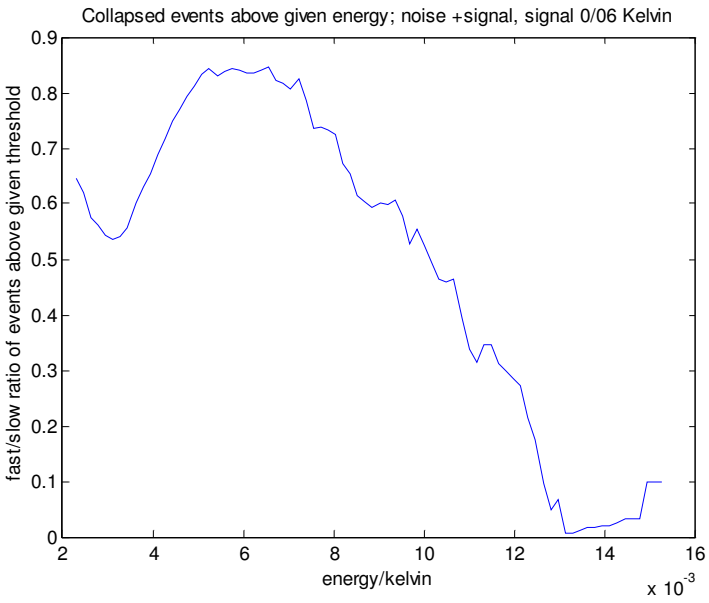

Figure 21.21: The ratio between the collapsed events over a given threshold for the fast filter blue) and slow filter (red).

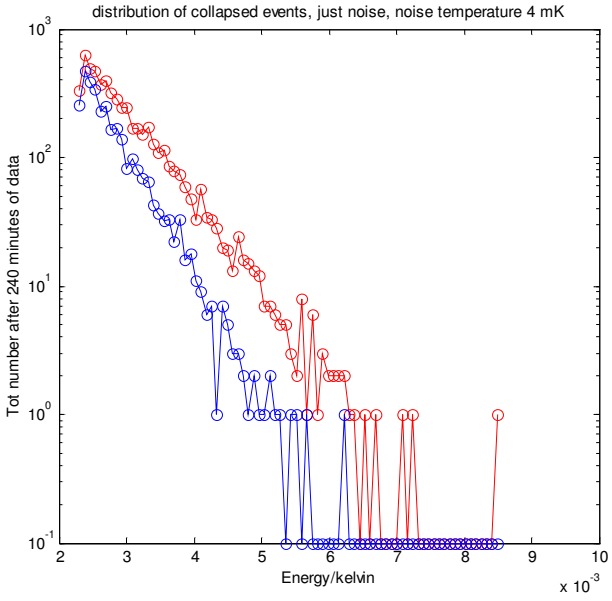

Figure 21.22: The distribution of events above threshold, for fast (blue) and slow (red) filters. No signal is present.

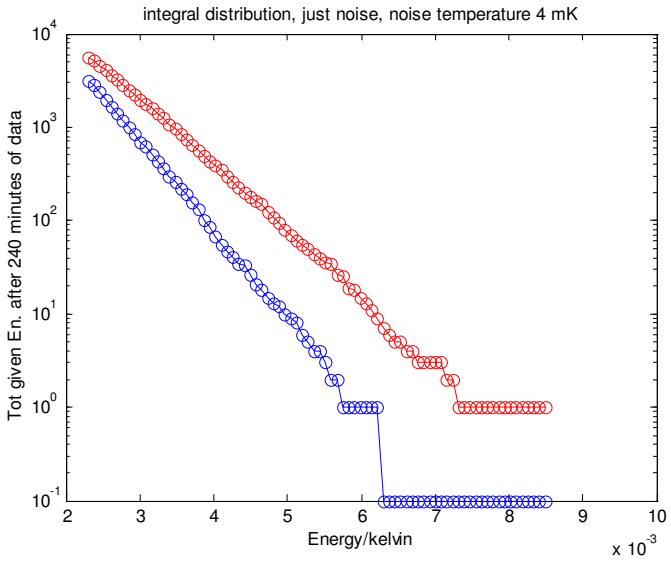

Figure 21.23: Integral distribution of the events above threshold. Just noise is present.

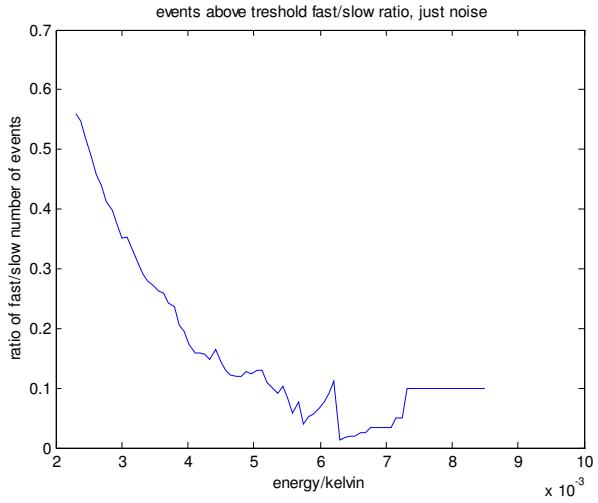

Figure 21.24: The ratio between fast over slow number of events above threshold. Just noise is present.

CHAPTER 22
IS SAMPLING AT FAST RATE ESSENTIAL?

22.1 Effects of Demodulation

There is a problem in applying the fast filtering procedure to the ALLEGRO data. The data acquisition system of the ALLEGRO detector samples data at a certain rate, then demodulates and decimates (this is done through the hardware) and creates two channels of data that are the in phase and in quadrature part of the data. The question that we need to explore is if we can implement the fast filtering procedure to this demodulated and slower sampled rate data. Demodulation can be represented mathematically as a multiplication of the data by a phasor function Φ :

$$\Phi = \exp(2\pi i \ f_d \ t + \phi). \tag{22.1}$$

where f_d is the demodulation frequency, the frequency that will be the zero frequency of the demodulated data. The quantity ϕ is an unknown phase. The real valued amplitude of the raw data becomes a complex value function after has been multiplied by the phasor. The real part x and imaginary part y of the values of this function can be considered as the in phase and in quadrature part of the data. This is equivalent to assuming a phase $\phi = 0$. We used again our simulated detector to understand the effect of demodulation and the loss of information due to not knowing the exact value of ϕ. We performed a comparison of the results of the fast filtering on the original data and the same data sequence demodulated down by 980 hertz. Also we low pass filter the demodulated data with a corner frequency of a few Hertz more than the frequency offset of the mode. Finally we decimate by 3 the time sequence. The original data is

the response of a one mode detector with a resonant frequency at 1000 Hz excited by thermal noise at 4 millikelvin. We also added to the bar response some SQUID noise. When demodulating we tried different values of ϕ.

There are several remarks that should be made about details of the procedure to filter the demodulated data. Demodulation, in the frequency domain, causes a frequency shift. In constructing the fast filter for the demodulated data we need the spectrum of the frequency shifted noise. That spectrum is similar to the original non-demodulated spectrum but with the resonant peak at 20 Hertz from the zero frequency, that is in the middle of the spectrum. In our simulation we used the algebraic form of the spectrum calculated at properly shifted frequencies. Also a demodulated, low pass filtered and decimated signal is used for the template to construct our filter.

Our simulation shows that demodulation doesn't change very much the physical properties of the fast filter output. For example,comparing the demodulated and the original version of the fast filter, in a sample of 400 seconds of simulated data the mean of the two sequences are respectively 0.0022 and 0.0023 kelvins. That is a proportional difference of about 6 percent. We show in Figure 22.2 the distribution of non modulated and modulated data. We selected high energy events, to reduce the effect of the high frequency oscillations of the non demodulated data. It is already possible to see that the two distributions are very close.

The envelope of the data extracts the real physical behavior of the noise after filtering, eliminating the oscillation typical of the fast filter. We used our routine to pull out the envelope of the non demodulated data. The direct comparison of the time

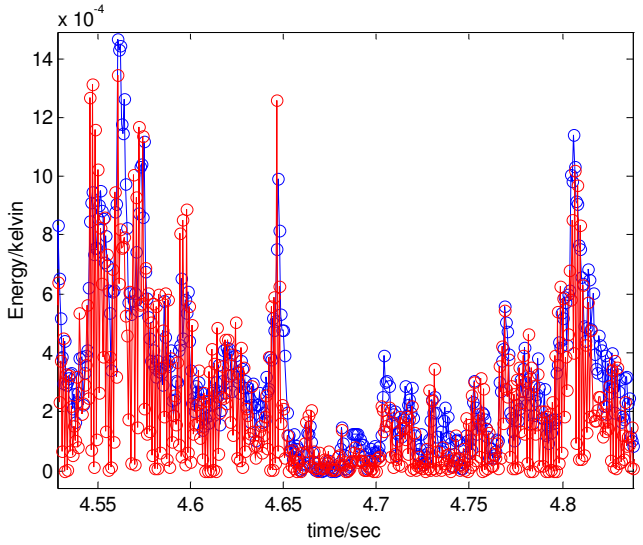

Figure 22.1: The time series of the demodulated data (blue) and the original data (red). It is simple to see that the demodulated data "follows" the original sequence.

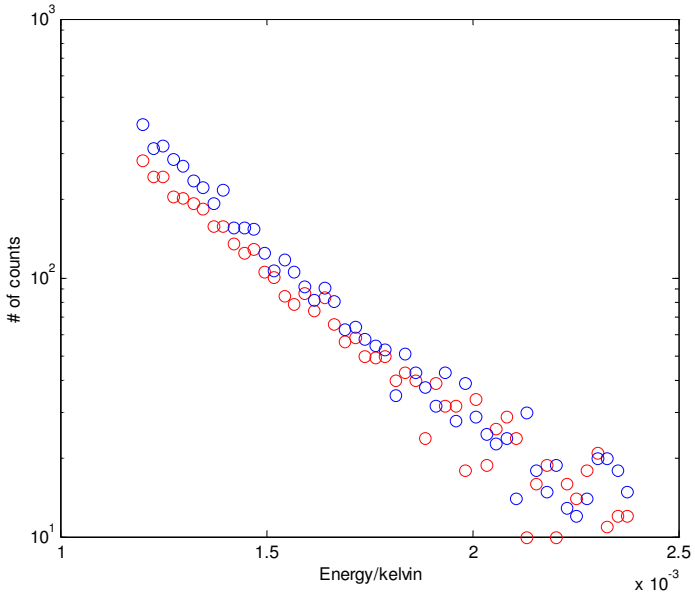

Figure 22.2: The histogram for the demodulated data (blue) and the original data (red). It is clear that at high energy the two histograms are comparable.

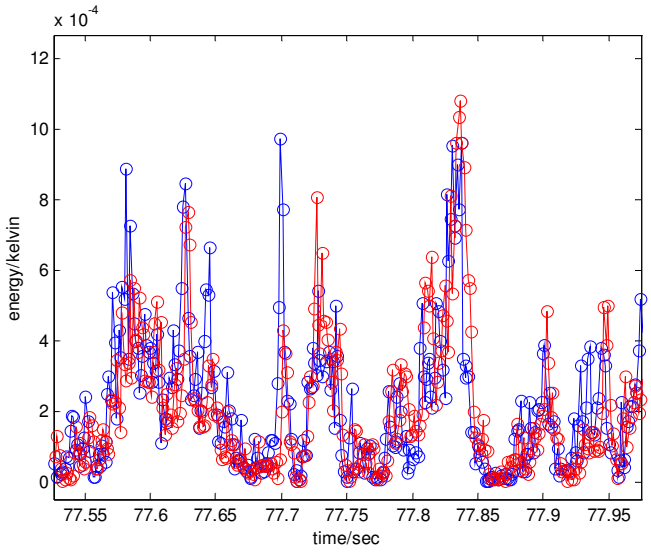

Figure 22.3: The envelope of the non-demodulated (red) data superimposed on the time series of the demodulated data (blue).

series of the envelope of the undemodulated and the demodulated data is shown in the next Figure 22.3.

One could ask why the two outputs are not perfectly identical. Let's define the output filtered time series as $g(t)$. Then the demodulated filtered time series $\widetilde{g}(t)$ is related to the non-demodulated sequence by:

$$g(t) = \text{Real } \left(\widetilde{g}(t)\exp(i\Omega t)\right). \tag{22.2}$$

where Ω is the demodulation frequency and t is the time. We can rewrite the previous expression as:

$$g(t) = x\cos(\Omega t) - y\sin(\Omega t); \tag{22.3}$$

where x and y are the in phase and in quadrature part of the demodulated data: ie x =Real $(\widetilde{g}(t))$ and y =Imag $(\widetilde{g}(t))$.

The envelope of the original time series is $E_{env}(t) = \sqrt{x(t\}^2 + y(t)^2}$. The square of $E_{env}(t)$ in our simulation is the time sequence that we plotted in blue in the previous Figure 23.3. This time series is not perfectly identical to the envelope "extracted" using our smoothing algorithm. If our demodulation calculation is correct we should be able to reproduce our original data sequence using the equation (22.3). We tested the validity of our demodulation procedure on a large signal with no noise present. In this case the demodulation frequency was 1000 Hz. The result is shown in Figure 22.4. The signal is a narrow-band signal, in this case the response of the bar to a delta function impulse. The original time series is plotted in blue. The "reconstructed" time series is plotted in red. The "reconstructed" time series is the application of equation (22.3) using the x and y components of the demodulated signal. We can see that the agreement is excellent (note though that the reconstructed time series is decimated by a factor of 3). This is in agreement with the fact that the extracted envelope square of a large signal in our simulation is always identical to the quantity $E_{env}(t)^2$. In the case of noise we noticed an interesting effect. When we apply equation (22.3) to noise we see that the reconstructed noise agrees with the original time series for a while then it seems to go suddenly out of phase, i.e. it seems to have similar amplitude but shifted in time by a certain amount. The phase of the demodulated data is defined as:

$$\phi(t) = \tan^{-1}\left(\frac{y}{x}\right). \tag{22.4}$$

In the case of a large signal the phase is constant in time. We plotted in Figure 22.5 the phase (as defined in equation 22.4) for a typical noise segment in our simulation.

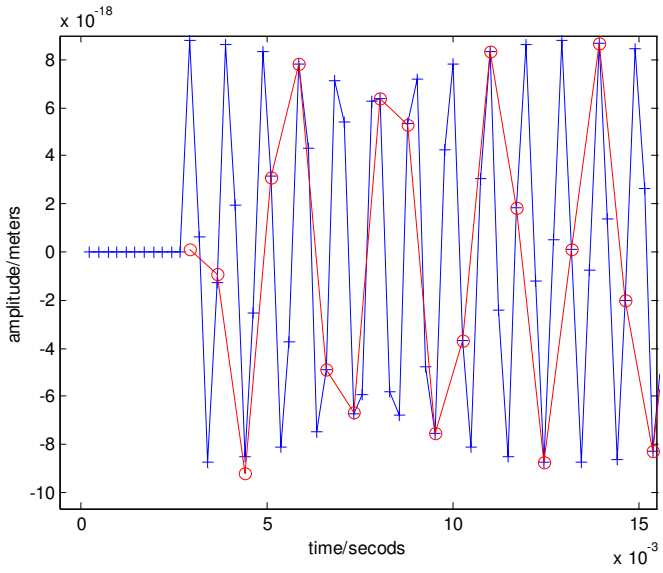

Figure 22.4: The comparison of the large signal (no noise) original time series (blue) and the "reconstructed" from the demodulated data time series. There is complete agreemetn between the two series.

The phase follows a characterestic random walk in time. We noticed that any time that there was a change in phase between the original noise sequence and the reconstructed data, there was a sudden change in the phase. Figure 22.6 shows the changes in phase and we can easily these sudden jumps or "glitches". We think the glitches are due to the discrete nature of or simulation. When we reduced the sample time the glitces are smaller but they still cause a certain time shift in the reconstructed noise time series. This effect is not a serious problem though. All that we care about noise is that the statistical characteristics are maintained if we go from the original time series to the demodulated one.

We compared the histogram of the energy of the extracted envelope of the non-demodulated filtered data with the histogram energy of the demodulated data (the envelope $E_{env}(t)$). The result is illustrated in the following Figure 22.7. The two

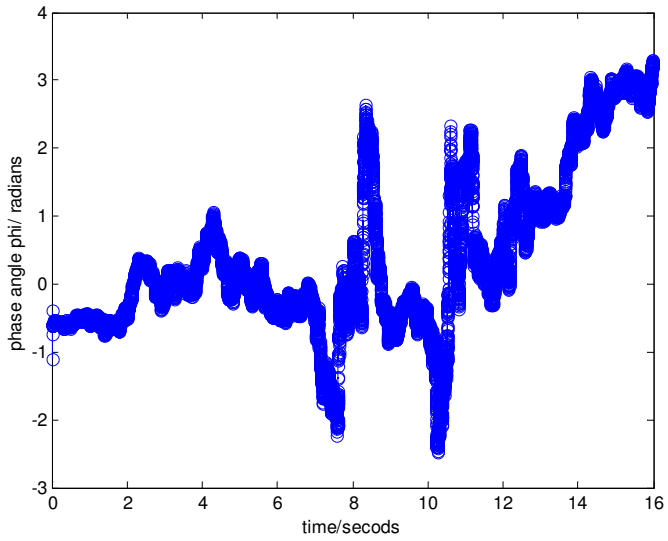

Figure 22.5: The time series of the phase phi for the demodulated data.

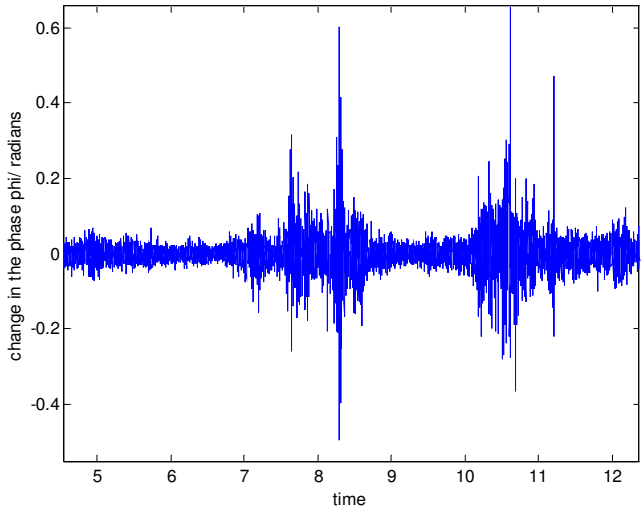

Figure 22.6: The difference of the values of the phase phi. Notice the "glitches" or sudden changes in the phase value.

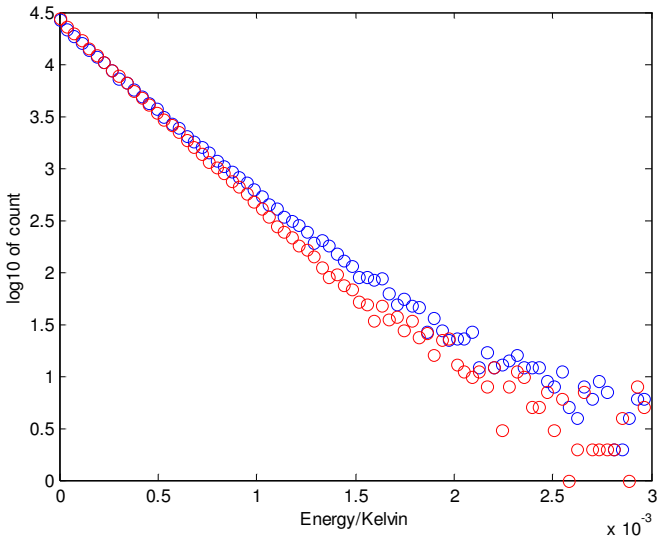

Figure 22.7: The histogram of the energy of the demodulated (red) and not demodulated (blue) data.

distribution are very close to each other.

It is clear that the statistical behavior of the filtered output before and after demodulation is very similar. So we can conclude that the technique of fast filtering can be applied to the demodulated data of ALLEGRO without any serious impediment.

22.2 Effects of Decimation

The other important question we want to answer is what is the effect of the rate of sampling on the performance of the matched filter. The relevance of this question is first at a practical level. In fact, again the acquisition system of ALLEGRO samples the data at a lower sampling rate than that used in our simulation. The term fast filter suggests that an essential element of the filtering process is to work with data that are sampled at a high sampling rate, much higher than the resonance frequency. If the fast sampling rate is fundamental in the improved performance of the fast filter,

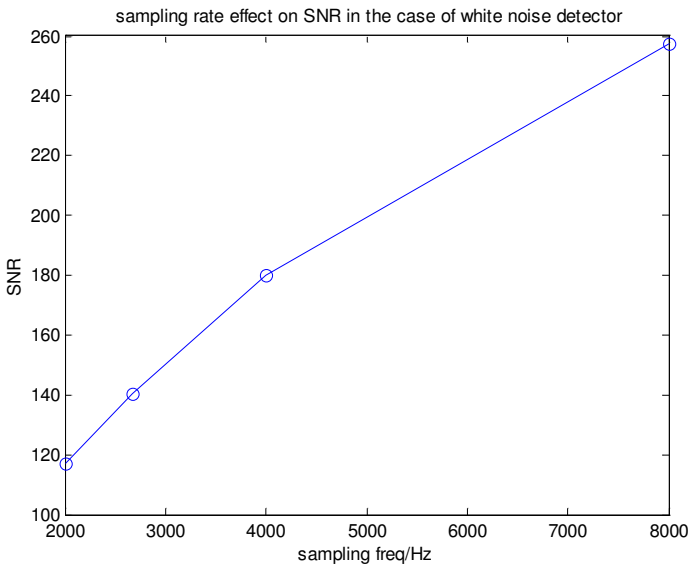

Figure 22.8: The effect of the sampling rate on the SNR. This experiment simulates the presence of a short lived signal in a white noise (broad-band) detector.

then we could not achieve any improvements in applying the fully matched filter to the ALLEGRO data. After demodulation, the resonant frequency is shifted at a very low frequency so it seems that is not really essential to sample the data at a high sample rate. In general, the sampling rate can influence the performance of the fast filter. This depends on the type of noise we are dealing with. For example, we simulated a situation where white noise is the principal type of noise in the detector (as in the case of interferometric gravitational wave detectors). We inserted a short lived sinusoidal signal and sampled the data at different sampling rates. Figure 22.5 shows the measured signal to noise ratio as a function of sampling rate for this particular experiment. It is possible to notice how the sampling rate has an evident effect on the performance of the filter.

In our bar detector our noise is an equal mixture of white and colored noise (the

response of the bar to the Gaussian thermal noise). The effect of this is that most of the power in the noise spectrum is concentrated around the resonant frequency. The shape of the noise spectrum, the FFT of the signal and the Fourier domain fast filter form suggests that most of the information that characterizes the behavior of the filter is in the Fourier coefficients near the resonant frequencies. See figure 19.3 for the shape of the fast filter in the Fourier domain. Because the fast decay of the filter away from the resonant frequency it is reasonable to expect that we don't loose a lot of information just keeping the coefficients close to the resonant peak. In fact, reducing the sampling rate or performing a *decimation* is equivalent to discarding the high frequency part of the Fourier representation of the filter. More precisely if we reduce, for example, by a factor of 3 the sampling rate we cut off a third of the high frequency coefficients of the Fourier representation of the filter. But this operation should not effect too much the qualities of the filter. In fact, most of the Fourier coefficients we discarded have a small value compared to the one close to the resonant frequency. The sampling theorem says that the highest frequency contained in the Fourier transform of the sample data is at half the sampling frequency. This frequency is the Nyquisit frequency. The important requisite in decimating the data is of course that the Nyquisit frequency is higher than the resonant frequency (or its value after demodulation). We performed a simulation using the one mode detector with a very high sampling rate. We decimated the data with different decimation factors and fast filtered the decimated data. No noticeable effect in the signal to noise ratio of the filter was noticed up to the point where the Nyquisit frequency reached less than 10 % of the resonant frequency. So we conclude

when filtering the colored noise of a resonant detector the sampling rate is not a key element in the performance of the optimal filter. The fast filter is a better filter but not because is applied to fast sampled data. So the fast filter name is actually a misnomer and we propose the name of *fully matched filter* instead. This name indicates that the filter is applied directly to the data without separating the information from the two modes. In chapter 24 we are going to indicate few factors that could explain the better performance of the fully matched filter over the partially matched filter both in the one mode case (where the two filter should not show any difference at all) and in the two modes case (where the difference between the two filter can mostly be attributed to how the two filters deal with information from the two modes).

CHAPTER 23
WORKING WITH REAL DATA

The simulation of the one and two mode cases allows us to study the filtering process in a simplified environment. In fact we have pointed out that real detectors are more complicated than the model that we have developed. For example, analyzing the spectrum of a real detector, like ALLEGRO, we notice that there are more than two peaks, suggesting that there are more that two modes present in the detector. Fortunately most of the power in the spectrum is in the two main resonant modes. This means that we can still model the detector as a two mode system within reasonably small error.

23.1 The Spectrum of the Real Detector

One difficulty with real data is that the noise imay be stationary on a short time scale but can change over a longer time frame. The consequence of this is that we need to extract the current spectrum of the detector for the construction of the filter. For this reason, instead of using an analytical form of the noise we rely on an average of the spectrum over a few hours to characterize the noise for a particular day. We eliminate from the data needed to calculate the spectrum high energy events that lie outside the normal distribution of the noise.

The following Figure 23.1 shows a typical spectrum of ALLEGRO.

We can point out different features of the spectrum. The main resonant peaks are at 896.4 and 919.6 Hz. There is a peak at 887.7 Hz the origin of which is not well understood. It is suspected that is a mechanical resonant mode that has its location in

Table 23.1: Parameters of the ALLEGRO detector spectrum.

mode	frequency	quality factor Q
minus mode	896.414 Hz	10^{-6}
plus mode	919.659 Hz	10^{-6}
mystery mode	887.742 Hz	?
15th hrmonics of 60 Hz	900 Hz	10^{-5}
calibration pulse	855 Hz	?

the transducer. At 900 Hz it is possible to notice another peak in the spectrum. This is the fifteenth harmonic of the 60 Hz frequency of the commercial AC electricity line.

Finally we notice the peak at 855 Hz. This is the peak due to the continuous sine wave that is injected to calibrate the detector.

The following Table 23.1 summarizes the main frequency peaks and their measured quality factor Q, when this is known.

At high and low frequency we notice the "attenuation" of the power spectrum due to the low pass (antialising) filter used in the acquisition apparatus. The entire data sequence is demodulated to low frequency in the acquisition system of ALLEGRO. The reference frequency is between the two main modes. Its actual value is 908.03 Hz. This has the consequence that the lower resonant frequency has actually a negative value if we use the reference frequency as the zero of frequency. This explains the common name of the two main frequencies as the minus and plus mode.

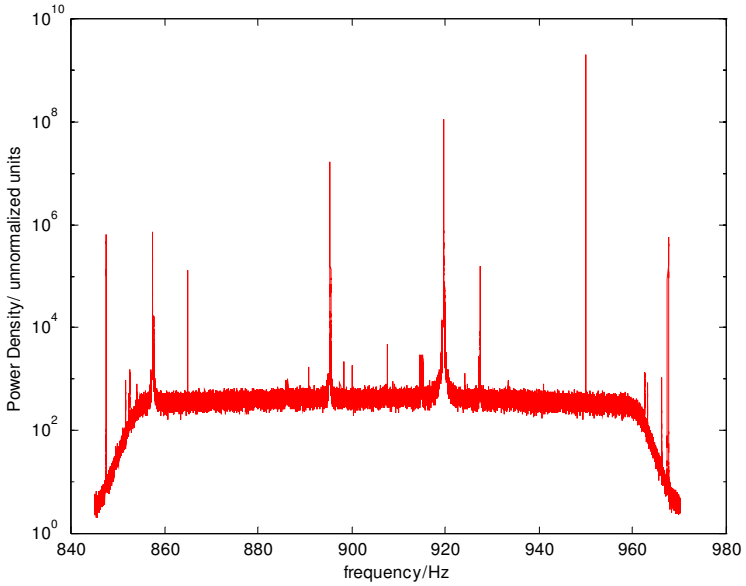

Figure 23.1: The Spectrum of the ALLEGRO detector.

23.2 The Mauceli Filter

The current burst event filter used by the LSU experimental group was developed by different people but mainly by Even Mauceli, a Ph. D. graduate from LSU. The code for the filter is written in the MatLab programming language and its algorithm is explained in section 23.3. We are going here to summarize the main steps of the filtering process in the Mauceli filter. The acquisition system demodulates the analog signal of the SQUID with a reference frequency that is in between the two resonant modes. Then the filters applies a low pass filter and reduces the sampling time trough decimation. The sampling time of this raw data is 0.08 seconds. The data is separate in two sets called the in phase and in quadrature part of the data by a lock in apparatus. The Mauceli filtering program then multiplies the two sets of data with sine and cosine functions (called "mixing") to demodulate the data to the minus and plus modes of

the detector. Then a low pass filter is applied to keep just the frequencies near the resonant modes, and finally another decimation is applied. The final decimation rate is once each 0.0008 seconds. We have at this point 4 sets of data: the in phase and in quadrature components for each of the two modes. On these demodulated and low pass filtered data sets it is applied the slow filter that is described in Chapter 20.

The filter weights are obtained in the time domain using a real calibration pulse as the target signal and the auto-correlation function of the noise of a typical day, eliminating very large energy events. The total energy data sequence is generated summing the square of the in phase and in quadrature components and giving appropriate weights to the minus and plus modes to compensate for the empirical difference in temperature of the two modes.

23.3 DemonTemper Program

The main program that implements the slow filter is the program called DemonTemper.m. This is a program written in the MatLab programming language.

The algorithm of the program is as follows.

1) Read the raw data: the raw data from the acquisiton and collection system is organized in records. These are segments of data 20 seconds long. The sampling rate is 8 ms so one record contains 2500 samples. The raw data contains an header, the in phase and in quadrature output channels, environmental information as seismographic data from devices around the bar, hardware status information, various vetos and the sample time in Coordinate Universal Time (UTC).

2) Remove DC offset: the amplitude of the bar has both rapid and slow changes

(due to environmental changes as the moon tides for example). The gravitational wave relevant changes are the rapid, high frequency changes so the mean value of the amplitude is subtracted from the data.

3) Mixing: the four set of data, the in phase and in quadrature is multplied with sine and cosine functions with frequency values that are the minus and plus frequency (after the appropriate frequency relabeling to account for the first hardware demodulation). We have at this point four data sets the in phase plus and minus x_+ and x_-, the in quadrature plus and minus y_+ and y_- components of the amplitude of the detector.

4) Low pass filter: a 8^{th} order digital Bessel anti-aliasing filter with a corner frequency at 2.35 Hz is applied to the four components of the data, keeping in this way just the frequencies near by the resonant frequencies.

5) Decimation: the data is decimated by a factor of 10 reducing the sample time to 80 ms.

6) Apply the slow filter: the filter described in Chapter 20 is applied to the proceed data in the time domain. Also the weights are already normalized in such way that the energy of the filter output matches the "energy" trnasfer of the calibration pulse.

9) Energy Estimation: the energy is evaluated squaring the separate in phase and in quadrature components for each mode and adding them together.

10) Data selection and storage: an energy threshold is chosen (typically a value 10 times larger than the average noise temperature) and the samples above threshold are collected and tagged with their corresponding arrival time.

Also the average over a record of the amplitudes of the in phase and in quadrature components and the energy for each mode is stored in a file. All the environmental data is also stored.

23.4 The FastDemon

We modified the Demontemper program to implement the fast filter on the ALLEGRO data.

This program is called FastDemon.m. It is very similar in structure to the DemonTemper. The main difference is in the filtering procedure and partitioning of the data set. We are going to explain the main differences.

1) Read the raw data: the reading of the raw data is exactly the same as before except we read many records at once. The MatLab routine for the FFT can handle up to 2^{18} Fourier coefficients without slowing down too much the computational process. In constructing our real data fast filter we choosed a number of coefficients close to $2^{16} = 65536$. The choice of this number limits the amount of data samples we can filter at once. Each record is made of 2500 samples, that means that 27 records have a total number of samples quite close to the ideal 2^{16}. This number is 67500 and it is not a power of 2, but we verified experimentally that FFT processing time is not much affected by this. A group of 27 records is called in our program a *long record.* A long record is exactly 9 minutes of data, and there exactly 160 long records in a 24 hours day.

2) Creating the complex variable z: we combine the in phase (denoted with an x) and in quadrature data (denoted with the variable name y) components to form a

single complex variable (called z). We have that:

$$z = x + iy \tag{23.1}$$

We don't do any further demodulation in software.

3) Apply the fully matched filter: The fully matched filter is constructed in the following way. The measured spectrum of the noise for the day is calculated using the MatLab PSD routine. We clean the noiseof vetoed data and large impulses. The signal template, see Figure 23.2, is formed using the analytical form of FFT of the signal as described in section 17.4. Because demodulation is just a shift of the frequencies in the Fourier domain we simply relabel the frequencies to account for the frequency shift of the acquisition system of ALLEGRO. Then the FFT is calculated using formula 17.22, using the parameter in Table 23.1 for the transfer function of the bar. The idea again is that a gravitational wave signal will affect just the bar and not the transducer. We make sure that the peaks in our FFT are aligned with that in the spectrum. We divide the conjugate of the FFT of the signal by the Spectrum to get the filter H. We apply H to the FFT of z, and calculate the inverse transform to get the amplitude of the filtered data. This is a complex variable because of the demodulation and we calculate the total energy as the absolute value squared of this quantity. We multiply this quantity by a normalization constant derived from a large calibration pulse in the stored data library of ALLEGRO. The pulse that was used for normlization was in day 250 of 1997.

4) Storage: the storage of the data is similar to that of Demon Temper except that we don't have data from two modes, but a single set of data that combine naturally

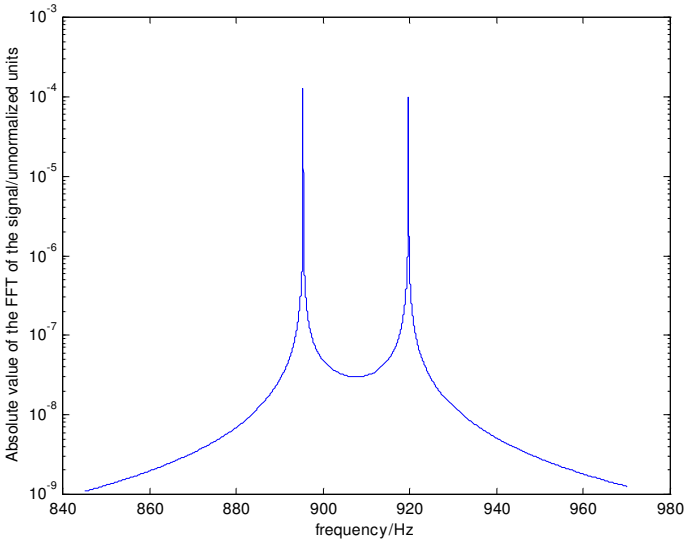

Figure 23.2: The FFT of the template signal using ALLEGRO parameters.

the information from the two modes.

23.5 Results for the Real ALLEGRO Data

We compared the result of filtering using our fully matched filter and the Maucelli filter. We made sure that the response of the two filters to a large calibration pulse was the same. Then we compared the output of the two filters in a section of data where not large events were present. We applied to the fast data our routine to extract its envelope, that contains the physical meaningful information. Figure 23.3 shows the distribution functions of the envelope of the fast filtered data and the Maucelli filtered data. It is evident that a noticeable improvement in reduction of noise temperature is achieved by using the fully matched filter. If we fit the distributions with straight lines the ratio between the two slopes is about 50 %. This should be equivalent to the reduction of the noise temperature.

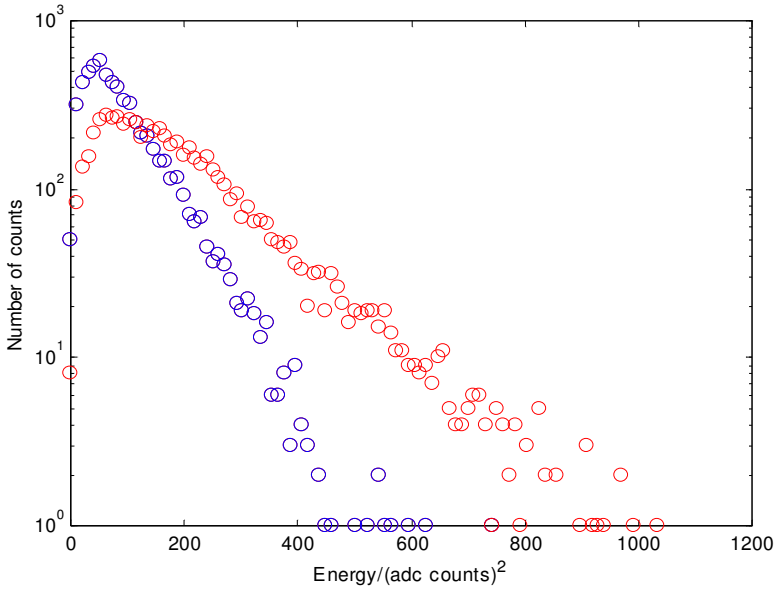

Figure 23.3: The real detector result for the fast filter (blue) and the slow filter (red). This is the hystogram for the envelopes of the data sets.

CHAPTER 24
WHY IS THE FAST BETTER THAN THE SLOW FILTER?

In this Chapter we point out a few important charactersitics of the fast filter that could contribute to its better performance in comparison with the slow filter. We could not find in the literature a convincing explanation on why the fast filters is better than the slow. For example, Astone *et. al* look at the statistical properties of the distribution functions of the two filter to arrive to a conclusion that one filter outperform the other, and they quantify the improvement in signal to noise ratio. We already explained how this is a misleading comparing the statistical properties of the two filters because they have different distribution functions. We have also pointed out that the fast oscillations of the fast filter that contribute to the form of its distribution function don't have a real physical meaning. Also in the paper by Astone *et al.* there is not consideration on the difference between one or more modes in the detector. Actually their analysis seem to be completely independent of how many modes are present in their mathematical model. We showed above that the fast filter is a better filter than the slow but the difference in performance between the two filters becomes more evident in the two modes case. At the moment we don't have an analytic demonstration of why one filter is better than the other. Not withstanding we want to show some qualitative arguments that can point to the relevant characteristics of fast filter that make it a better filter. This can be useful for further investigation on this subject.

24.1 One Mode versus Two Modes

In the two mode case the most important characteristic of the fast filter is that the information of the two modes is not separated and then recombined in quadrature in the end as in the slow filter procedure. At first consideration we can think that the approach followed by the slow filter is acceptable because the two modes are statistically independent. There is though an important characteristic of the gravitational wave signal that can introduce correlation between the modes. This is the fact that the gravitational wave signal excites just the bar and not the transducer which causes the normal modes to be equally excited at the same moment and same phase. The fast filter can distinguish very well between the situation, when a large impulse excites just the bar and when the bar and the transducer are both affected. The first case is typical of gravitational wave signal,s and the second is typical of some of the noise. To illustrate this we show in Figure 24.1 the frequency domain form of the filter applied to the response of the two mode detector when a large impulse is applied to the bar, and also the opposite situation when a force impulse acts just on the transducer. There is a very evident difference between the two cases. The time domain form of the filtered output is shown in Figure 21.2. The energy of the input impulse in both cases is the same. We can see that the energy value assigned to the filtered output in the case of the impulse acting just on the transducer is less than in the case where the force acts just on the bar. This is to be expected because we optimized the filter to signals that act only on the bar. The fractional difference in the filter output energy between the two cases is about 15 percent. When we use the slow filter, the fractional difference is

4 %. Figure 24.5 illustrates pictorially these results.

The difference in the energy output between the impulse on the bar and the impulse on the transducer depends on the parameter Γ (that determines the ratio between narrow and broad band noise, see Section 17.3). Figure 24.3 shows the result for another case, where Γ was incremented the value by a factor of 2. It is easy to see an evident difference between the two cases. Increasing the Γ increases the ability to distinguish between the excitation of the bar and excitation of the transducer. This ability can be quatified with the ratio $R_{bar/trans}$, defined as the ratio of energy outputs for equal excitation of the bar and transducer. A plot of his ratio, as a function of Γ, is shown in Figure 24.4. The slow filter was found to be insensitive to changes in Γ. The Signal to Noise (SNR) was used to compare the performance of the fast filter and slow filter for different values of Γ. We used the Signal to Noise Ratio (SNR) to compare the two filters using the previos justified correction for the fast filter (see Chapter 14). Figure 24.6 shows our final result. The improvement due to the fast filter in comparison with the slow is proportional to the ratio $R_{bar/trans}$ and this ratio, as already shown, is proportional to the parameter Γ. This shows that for detectors with large values of Γ the fast filter has a noticeable higher performance than the slow filter. One last question is, if in our process of increasing Γ, we allowed for the cutoff frequency of the low pass filter, applied to the demodulated data in the slow filter construction, to be beyond the frequency where the white noise contribution becomes smaller than the narrow band noise. This will mean that the improvement in the fast filter is just due to our choice of cutoff frequency and it is not really an intrisic porperty of the fast filter. A

more careful choice of the cutoff frequency, in this case, it will offset the improvement. Figure 24.7 shows that this is not the case. The Figure ilustrates the cumulative power (in meters squared) of the two quantities:

$$\begin{aligned} S_w(t) &= x_w^2\ t, \\ S_f(t) &= |G_{11} - G_{12}|^2\ S_f \end{aligned} \tag{24.1}$$

where the quantity x_w^2 is the mean value of amplitude of the SQUID noise. The two curves cross at a certain point, where the two noise contributions are equivalent. We notice that the cutoff frequency of the low pass filter and decimation is at a lower frequency than this point. This means that the demodulated, low passed and decimated data in the slow filter still contains information on the white noise. We choose the lowest value of the white noise used to generate the graph in Figure 24.6. Our conclusion is that the difference between the two filters as a funtion of Γ is a real effect.

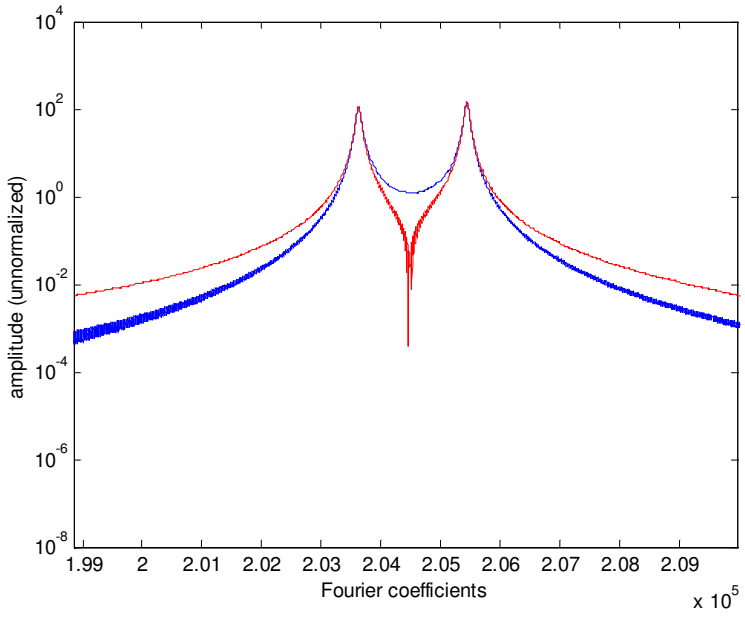

Figure 24.1: The fast filter applied to a large impulse tha excites just the bar (blue, as in the gravitational wave signal) and both the bar and transducer. The filter assigns more energy to the first type of event.

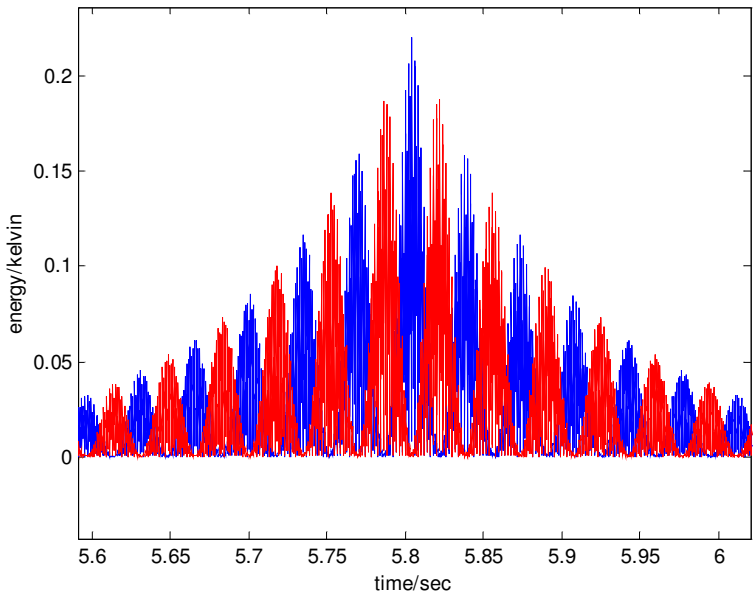

Figure 24.2: The fast filter output in the case of energy being delivered just in the bar (blue) and both in the bar and transducer (red).

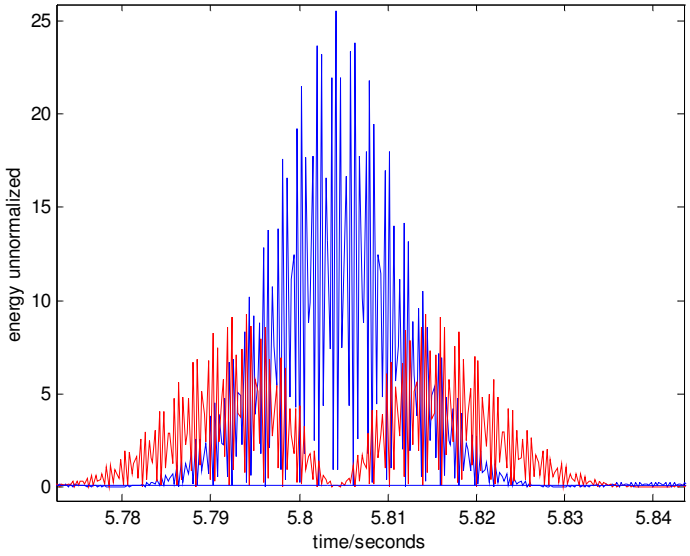

Figure 24.3: The relationship between the impulse on the bar (blue) and the impulse on the transducer (red) for a value Gamma 15 times less than the one used in the previous picture.

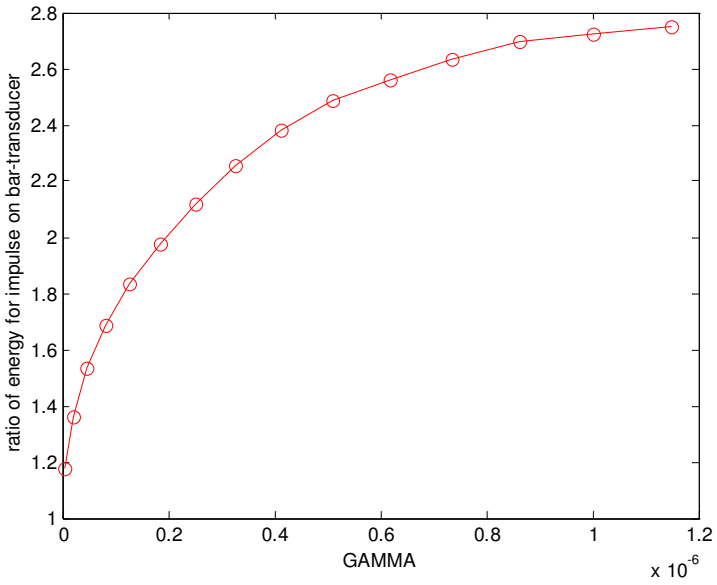

Figure 24.4: The relationship between the value Gamma and the ratio in energy output when the bar is excited and when only the transducer is excited.

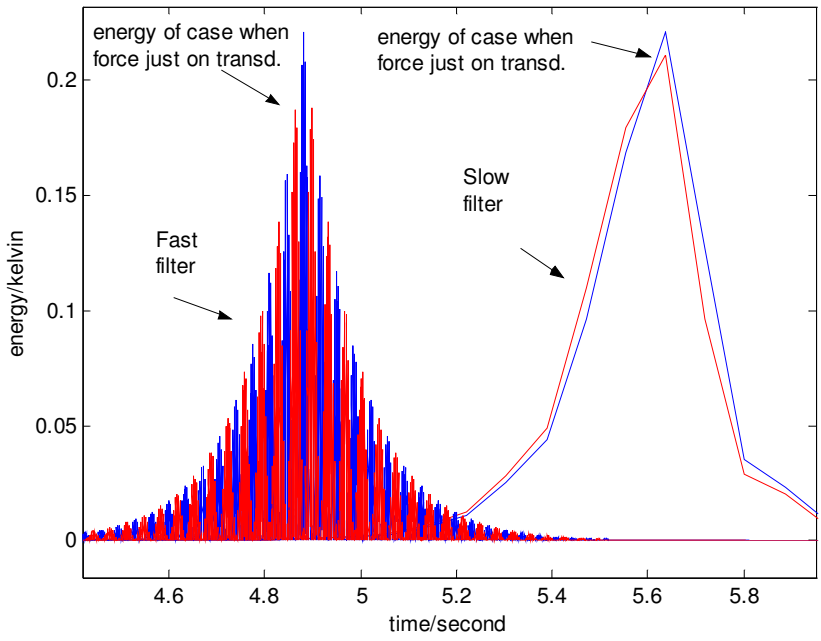

Figure 24.5: The comparison between the case of the force acting just on the bar (blue) and the case of the force acting just on the transducer for both fast and slow filter.

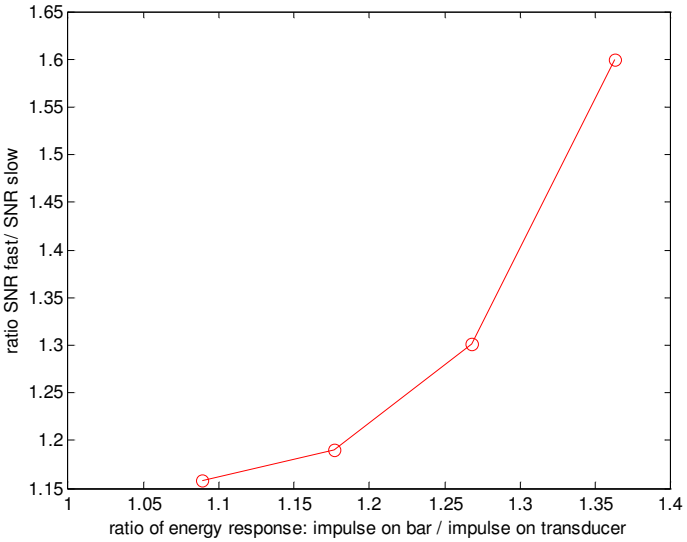

Figure 24.6: This figure shows the relationship between the ratios in Signal to Noise ratio (SN) and the ratio between the energy response of the case of an impulse just on the bar and the case of an impulse just on the transducer.

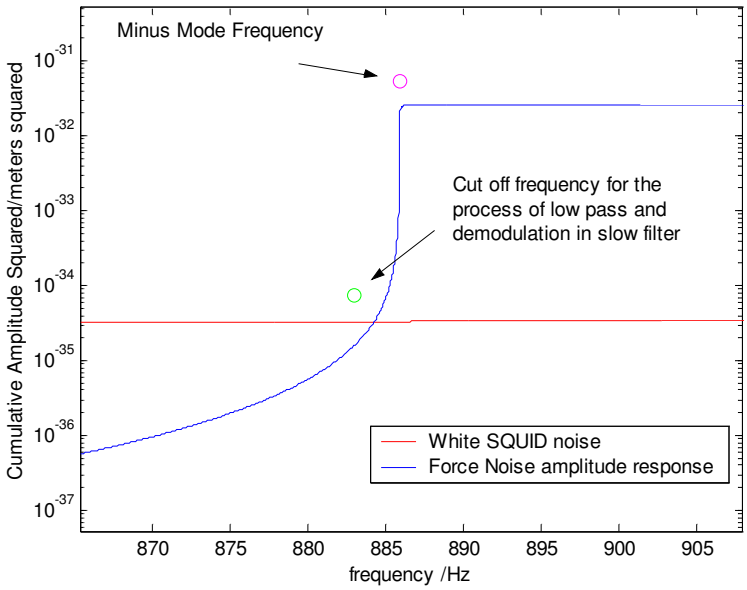

Figure 24.7: The Figure illustrates the cumulative power for the force noise amplitude response and the broad band SQUID noise. The cutoff frequency is at lower frequency than the frequency where the narrow band noise becomes greater than the broad band noise.

CHAPTER 25
CONCLUSIONS

In our study we explored the performance of two different types of filters, the fast filter and slow filter. We used a simulated damped harmonic oscillator with one and two modes. It was shown that there is a small but noticeable difference between the two filters even in the one mode case. In terms of Signal to Noise ratio (SNR) the improvement between the fast and slow is about 10 %. The fast filter is a better filter in the sense that produces less events above a certain fixed threshold used in the coincidence search between different detectors. This in turn means that using the fast filter we have fewer false alarms when producing a list of possible event candidates used for coincidences searches.

The advantage of the fast filter is much more evident in the case of the two mode oscillator. The SNR improvement in this case is about 40 %. The number of events above threshold is a function of the energy of the threshold. When we use threshold energy that are few times the average noise temperature we can have between 2 to 10 times more events above threshold for the slow filter in comparison with the fast filter. This a considerable and useful effect. We also applied the fast filter to the real ALLEGRO data and found similar results. In particular we reduced the noise temperature by a factor of 2 in comparison with the average temperature of the Mauceli filtered noise. We have also shown that the Signal to Noise Ratio improvement of the fast filter over the slow filter is proportional to the parameter Γ. The parameter is the ratio between the narrow band and broad band noise power. This means that for bigger

values of Γ we have higher SNR for the fast filter output in comparison with the slow filtered output.

REFERENCES

1. Middleditch, John; Kristian, Jerome A.; Kunkel, William E.; Hill, Kym, M.; Watson, Robert D.; Lucinio, Richard; Imamura, James N.; Steiman-Cameron, Thomas Y.; Shearer, Andrew; Butler, Raymond; Red , Michael; Danks, Anthony C., *Rapid photometry of supernova 1987A: a 2.14 ms pulsar?* **New Astronomy**, vol. 5, no.5, p. 243-283 (2000).

2. J.Peakock, *Cosmological Physics*, Cambridge Univ. Press 1999.

3. J. H. Taylor and R. N. Manchster, Annual Review of Astronomy and Astrophysics, vol. 15, p. 19 (1977).

4. P. Goldreich. *Neutron Star crusts and allignment of magnetic axes in pulsars.* **The Astrophysical Journal,** vol. 160, L11-L16, (1970).

5. M. Zimmerman and E. Szedentis Jr., *Gravitational waves from rotating and precessing bodies. Simple models and applications to pulsars.* **Physical Review D**, vol. 20, no.2, p.351-355 (1979).

6. M. Zimmerman, *Gravitational waves from rotating and precessing bodies. II. General solutions and computationally useful formulas.* **Physical Review D**, vol. 20, no.2, p. 351-355 *(1980).*

7. W. H. Press and K. S. Thorne *Gravitational Wave Astronomy*, Annual Review of Astronomy and Astrophysics, vol. 10, p. 335-371, (1972).

8. G. Ushormirsky, C. Cutler, L. Bildsten, **Montly Notices of the Royal Astronomical Society**, **319**, 902, (2000).

8-a. P. Haensel, in J. A. Marck and J. P. Lasota, editors, Relativistic Gravitation and Gravitational Radiation, Les Houches, p. 129 (1995).

9. L. M. Franco, B. Link, and R. I. Epstein, *Quaking stars,* Los Alamos e-prints, **astro-ph**/9911105 (1999).

10. I. H. Stairs, A.G. Lyne and L.Shemar, *Evidence of free precession in a pulsar.* **Nature** vol. 406/3, p.484-466.

11. K. S. Thorne, *Gravitational Radiation ,* p. 330-468 in S. W. Hawking and W. Israel, *300 years of Gravitation.* Cambridge University Press, Cambridge (1987).

12. J.B. Marion, S. T. Thornton, *Classical Mechanics of particle and systems,* Saunders College, Forth Worth, Philadelphia (1995).

13. K. C. B. New, G. Chanmugan, W. W. Jonhson and J. Tohline. *Millisecond pulsars: detectable sources of continuos gravitational waves?* **The Astrophysical Journal,** vol. 450:757-762, (1995).

14. S. L. Shapiro and S. A. Teukolsy, *Black Holes, White Dwarfs and Neutron Stars.* Wiley-Interscience, New York (1983).

15. D.I. Jones and N. Anderson *Freely precessing neutron stars: Model and Observation.* arXiv:astro-ph*/0022063 (2000).*

16. L. D. Landau and and E. M. *Mechanics,* Butterworth-Heineman Ltd. (1976).

17. D. I. Jones, *Gravitational Waves From Precessing Neutron Stars.* arXiv: gr-qc/0111007 (2001).

18. C.Cutler and D. I. Jones, *Gravitational Wave Damping of Neutron Star Wobble*, arXiv:gr-qc/008021 (2000).

19. D. Pines and J. Shaham, **Nature** 248, 483-486 (1974).

20. V. R. Pandharipande, D. Pines and R. A. *Neutron Star Sructure Theory, Observation ad Speculation.* **Astrophysical Journal**, vol. 208, 550-566, (1976).

21. S. Frasca and C. Palomba, GWDAW preecedings in Trento, Italy (2001).

22. E. E. Salpeter and J. N. Bahcall, *On the Masses of Quasi Stellar Objects.* **The Astrophysical Journal**, vol. 158, L15, (1969).

23. D. I. Jones, *Gravitational waves from Precessing Neutron Stars*, University of South Wales, Cardiff Ph. D. Thesis.

24. M. A. Alpar and D. Pines, Gravitational radiation from a solid-crust neutron star. **Nature**, vol. 314, 334-336, (1985).

25. B. Link and R. J. Epstein, *Precession of the isolated pulsar PSR B11828-11.* arXiv: astro-ph/0101282 (2001).

26. T. V. Shabanova, A.G. Lyne and J. O. Urama, *Evidence of Free Precession in the Pulsar B1642-03*, arXiv: astro-ph/0101434.

27. S. Nagataki and K. Sato, *Implication of Millisecond Pulsar in SN 1987A.* arXiv: astro-ph/0011363 (2000).

28. Paper on signal analysis: Shutz

29. P. Jaranowsky, A.Krolak. *Data analysis of gravitational wave signals from spinning neutron stars. III.\ Detection and computational requirements.* **Physical Review D** 616 2001.

30. P. Astone, G. P. Buttiglione, S. Frasca, G. V. Pallotino and G. Pizzella, **Il Nuovo Cimento** 20, 9 (1997).

31. B. F. Scutz. *A First Course in General Relativity,* Universtiy Press, New York, (1989).

32. E. Maucelli. *Data Analyis of the ALLEGRO wave detector.* LSU dissertation (1997).

33. L. Ju and D.G. Blair. *The detection of gravitational waves.* **Modern Physics D**, vol. 5: 104-150, (1996).

34. Paper on thermal properties of spectrum (saulson??)

35. C. A. Morse. *Improving searches for gravitational wave burst.* LSU dissertation (1999).

36. L.E. Reichl. *A modern course in Statistical Physics.* John Wiley & Sons, New York, (1998).

37. A. V. Oppenheim, R. W. Schafer. *Discrete-time Signal Processing.* Prentice-Hall, London (1989).

38. A. D. Whalen. *Detection of Signal in Noise.* Academic Press, New York \& London (1971).

39. L. A. Wainstein and V. D. Zubakov, *Extraction of Signal from Noise*, Dover Press, New York, (1962).

40. A. Papoulis. Signal Analysis, McGraw-Hill Inc., New York, 1977.

41. E. Maucelli et al. *The ALLEGRO gravitational wave detector: Data acquisition and analysis.* **Physical Review D**, vol 54: 1264-1275 (1996).

42. P. Astone, S. D'Antonio and G. Pizzella, *Time dispersion and efficiency of detection for signals in gravitational wave experiments.* arXiv:gr-qc/0001030 v2 (2000).

43. S. Vitale, S. Caruso, P.L. Fortini, G. Marcon, A. Ortolan, G. A. Prodi, L. Taffarello, G. Vedovato, J. P. Zendri and M.Cerdonio. *Fast Numerical Data Analysis for Resonant Gravitational Waves Antennas and Antenna Arrays: optimal filtering, signal timing and internal vetoes.* **Nuclear Physics B**, 48, p. 104-106 (1996).

APPENDIX 1
THE PRECESSION OF A ROTATING NON-AXISYMMETRIC ELLIPSOID

The actual shape of the neutron star could be quite complicated. The deformations from perfect spherical symmetry will be however quite small. The fraction of ellipticity allowable before the crust will break is of the order of 10^{-4}.

For simplicity let's assume the star can be approximated as a solid object. Even a small deformation will produce a wobble in the motion of a rotating neutron star . More precisely the rotation axis will change its orientation, relative to a distant observer. The axis will appear to move in a circular pattern with a certain rotation frequency $f_{p.}$ This motion is called precession. There are two possibilities that can create the precession. The first is that the star is deformed along just one of the axis of symmetry, let's say along the axis a_3. If the rotation axis coincides with the axis a_3 then there is not precession. Precession will occur, though, if the axis of rotation is not parallel to the axis a_3.

In this case we derive a simple expression that relates the ellipticity to the precession frequency and the rotation frequency of a rigid body.

This derivation can be found in most classical mechanics books. See for example [12]. Let' s start with the Euler equations for force-free motion, solutions to the

Lagrangian of a rigid body motion:

$$\left.\begin{aligned}(I_2 - I_3)\omega_2\omega_3 - I_1\,\dot{\omega}_1 &= 0\\ (I_3 - I_1)\omega_3\omega_1 - I_2\,\dot{\omega}_2 &= 0\\ (I_1 - I_2)\omega_1\omega_2 - I_3\,\dot{\omega}_3 &= 0\end{aligned}\right\} \tag{1.1}$$

In the case of a spheroid ($a_1 = a_2 > a_3$) we have $I_1 = I_2 \neq I_3$. The we can rewrite Euler 's equations as:

$$\left.\begin{aligned}(I_1 - I_3)\omega_2\omega_3 - I_1\,\dot{\omega}_1 &= 0\\ (I_3 - I_1)\omega_3\omega_1 - I_1\,\dot{\omega}_2 &= 0\\ I_3\,\dot{\omega}_3 &= 0\end{aligned}\right\} \tag{1.2}$$

where we have substitute I_1 for I_2. Let's assume that the center of mass of the object is at rest and the spheroid rotates with angular velocity $\boldsymbol{\omega}$ along an axis non parallel with the symmetry axis a_3. The third equation in (17) gives us $\dot{\omega}_3 = 0$ that implies

$$\omega_3 = \text{const.} \tag{1.3}$$

So we can rewrite (17) :

$$\left.\begin{aligned}\dot{\omega}_1 &= -\tfrac{(I_3 - I_1)\omega_3}{I_1}\omega_1\\ \dot{\omega}_2 &= \tfrac{(I_3 - I_1)\omega_3}{I_1}\omega_2\end{aligned}\right\} \tag{1.4}$$

Define the constant:

$$\Omega = \frac{I_3 - I_1}{I_1}\omega_3, \tag{1.5}$$

to get:

$$\left.\begin{aligned}\dot{\omega}_1 + \Omega\omega_1 &= 0\\ \dot{\omega}_2 - \Omega\omega_2 &= 0\end{aligned}\right\} \tag{1.6}$$

The solution of this equations is:

$$\left.\begin{aligned} \omega_1(t) &= A\cos\Omega t \\ \omega_2(t) &= A\sin\Omega t \end{aligned}\right\} \tag{1.7}$$

where $A = \sqrt{\omega_1^2 + \omega_2^2}$.

This is showing that the projection of the vector $\boldsymbol{\omega}$ onto the $a_1 - a_2$ plane describes a circle with time. This motion of the velocity vector $\boldsymbol{\omega}$ around the symmetry axis a_3 is called **precession.**

Notice that the ellipticity ε,defined earlier, can be express in terms of moments of inertia as:

$$\varepsilon = \frac{a_3 - a_1}{\sqrt{a_1 a_3}} = \frac{Ma_3a_1 - Ma_1a_1}{Ma_1\sqrt{a_1a_3}} \approx \frac{I_3 - I_1}{I_1}, \tag{1.8}$$

where M is the mass of the star.

This gives us a value for the ellipticity as function of the ratio between precession angular velocity and rotation angular velocity:

$$\varepsilon = \frac{I_3 - I_1}{I_1} = \frac{\Omega}{\omega_3}. \tag{1.9}$$

Then using the values given in the introduction for the case of 1987A, we have ($P = 1/f$ is the period):

$$\varepsilon = \frac{\Omega}{\omega_3} = \frac{1/P_r}{1/P} = \frac{0.00214 \text{ seconds}}{1000 \text{ seconds}} = 2.1 \times 10^{-6}, \tag{1.10}$$

that is the estimated value for the ellipticity in the Middleditch *et al.*' paper.

The ellipticity for the pulsar PSR B1828-11 can be also easily estimated using the given observational data in that case are:

$$\varepsilon = \frac{\Omega}{\omega_3} = \frac{1/P_r}{1/P} = \frac{0.405 \text{ seconds}}{8.6 \times 10^7 \text{ seconds}} = 4.6 \times 10^{-9}$$

The more general case of ellipticity along more than one axis and the consequence for precession and gravity wave emission is discussed in a series of paper by Zimmerman [5-6].

APPENDIX 2
HOW THE EQUATION OF STATE WILL INFLUENCE THE VALUE OF THE ELLIPTICITY.

The above calculation assumes that the neutron star can be imagined as a rigid body. There are different model of neutron stars and they have in some cases very complicated equation of states. We can find in the literature some simpler models with easy expressions for the level of rigidity or stiffness of the equation of state in a neutron star. More rigid the equation of state closer is the star to a rigid body or at least to a star with a large solid core, solid crust and small fluid material in between. More soft is the equation more fluid is the interior of the star.

Now in one of earliest paper on the subject of rotating neutron star [5] there is a discussion of a model for a neutron stars that consists of a thick crust and a liquid interior. The liquid interior part is small in comparison with the crystalline crust. The shear modulus μ (that expresses the ability of the material to support shear stresses) for a Coulomb lattice is:

$$\mu \ll (Ze)N_z^{4/2}, \tag{2.1}$$

where N_z is the number density of nuclei of charge Z. Ruderman (an expert in neutron star physics) estimates:

$$\mu \ll 10^{30} \text{ dynes cm}^{-2}, \tag{2.2}$$

for typical neutron star mantles.

In this case if the star is set in free precession, the precession will not be as before $\varepsilon = \frac{I_3 - I_1}{I_1} = \frac{\Omega}{\omega_3}$ but:

$$\varepsilon = \frac{I_3 - I_1}{I_1} = \frac{\Omega}{\omega_3} \frac{19\mu + 2g\rho R}{19\mu} \gg \frac{\Omega}{\omega_3}, \tag{2.3}$$

where R is the radius of the neutron star, about 10^4 meters, $g = \frac{GM}{R^2}$ and $\rho \approx 10^{14} g/cm^3$ is the density of the star.

Playing around with different values of shear modulus, density and radii of neutron stars we can get an enhancement between 10^2 and 10^4 for the ellipticity. This is just to show that even a little softness in the equation of state will imply a bigger ellipticity that could be enough to make the neutron star generate enough gravitational radiation to be detectable by the improved ALLEGRO after one year or so of observation. In the case nothing is observed, the experiment will put strong limits on the equation of state of the neutron star left behind the Supernova 1987A, a non trivial astrophysical result.

APPENDIX 3
CODES IN MATLAB

3.1 Program # 1: Spectrum of the Noise for Two modes System. Spec_2mode.

```
%calculating the theoretical spectrum for the double resonant detector

and comparing it with the measured spectrum from the simulation

clear

xfs= 6.8404e-017; %normalization factor

w1=2*pi*f0x1;

w2=2*pi*f0x2;

k1=mass1*w1^2

k2=mass2*w2^2

b1=mass1*sqrt(k1/mass1)/Q1; %friction coefficients for springs

b2=mass2*sqrt(k2/mass2)/Q2;

%calculating the strength of the forces acting on the detector

Temp=4*10^-3;%temperature

Sfb=4*kb*Temp*mass1*sqrt(k1/mass1)/Q1;

%spectrum of force noise acting on the bar

Sft=4*kb*Temp*mass2*sqrt(k2/mass2)/Q2;

%spectrum of force noise acting on the transducer

Fb=sqrt(Sfb/(dT))%average size of force in Newtons on bar

Ft=sqrt(Sft/(dT))%average size of force in Newtons on transducer
```

```
Fnoiseb=Fb*randn(nfft,1);%this is the time sequence of the noise on the bar
Fnoiset=Ft*randn(nfft,1);%this is the time sequence of the noise on transducer
F1=Fnoiseb-Fnoiset;%this is the noise on x1
F2=Fnoiset;%this is the noise on x2
%force of the signal
mult=1000;%how many times the signal is bigger than average noise force on
bar
Fsign=mult*Fb;
% size of burst-signal force in Newtons on bar (mult times the average noise
force on bar)
F1sign=[zeros(10,1);Fsign;zeros(nfft-11,1)];
%the signal time sequence (one single force burst acting on bar)
F2sign=zeros(nfft,1);%no force on transducer in this case
%calculating the parameters of the normal modes trough linear algebra
GAMMA=[1/sqrt(mass1) 0;0 1/sqrt(mass2)] %the mass-normalizing Matrix
BETA=[b1 0; 0 b2];%the matrix of the friction coefficient in x1,x2 coordinates
BETAy=GAMMA*BETA*GAMMA;%transfrornation to y
OM=[-(w1^2+mass2/mass1*w2^2) sqrt(mass2/mass1)*w2^2;
sqrt(mass2/mass1)*w2^2 -w2^2]
%this is the omega matrix ,
%mass the normalized spring constant matrix OM=gamma K gamma
[A,D]=eig(OM);%spring constant and rotation Matrix
```

```
A

D

%transformations to eta coordinates (normal modes coordinates)

BETAeta=A'*BETAy*A%the friction coefficients matrix in eta1, eta2 coordinates


Qeta1=sqrt(-D(1))/BETAeta(1)%quality factor for normal mode1

Qeta2=sqrt(-D(4))/BETAeta(4)%quality factor for normal mode2

Forcemu=A'*GAMMA;%the transformation matrix for the force

Feta1=Forcemu(1)*F1+Forcemu(3)*F2;%noise force in eta coordinates

Feta2=Forcemu(2)*F1+Forcemu(4)*F2;

Feta1sign=Forcemu(1)*F1sign+Forcemu(3)*F2sign;%sign force in eta coordinates

Feta2sign=Forcemu(2)*F1sign+Forcemu(4)*F2sign;

om01=sqrt(-D(1));%resonant frequency of normal modes

om02=sqrt(-D(4));

f01=om01/(2*pi)

f02=om02/(2*pi)

theta=acos(A(1));

%%% specifing variables in terms of Papoulis H(s) function p.167

alphan1 = om01/(2*Qeta1) ;

betan1 = om01*sqrt( 1 - 1/(4*Qeta1^2) );

An1 = exp(-alphan1*dT)*sin(betan1*dT)/betan1;

bpn1 = 2*exp(-alphan1*dT)*cos(betan1*dT);
```

```
cn1 = exp(-2*alphan1*dT);

%%% calculate digital filter constants

bn1 = [0,An1*dT];

an1 = [1,-bpn1,cn1];

%the second mode

alphan2 = om02/(2*Qeta2) ;

betan2 = om02*sqrt( 1 - 1/(4*Qeta2^2) );

An2 = exp(-alphan2*dT)*sin(betan2*dT)/betan2;

bpn2 = 2*exp(-alphan2*dT)*cos(betan2*dT);

cn2 = exp(-2*alphan2*dT);

%%% calculate digital filter constants

bn2 = [0,An2*dT];

an2 = [1,-bpn2,cn2];

%%% make random force sequence

%f_noisebar =Forceex1(1)*randn(nfft,1);

%f_noiset=Forceex2(2)*randn(nfft,1);

%f_noise_eta1=f_noisebar-f_noiset;%force excting eta1

%f_noise_eta2=f_noiset;

%f_noise = [1; zeros(npts-1,1)];

%% calculate the entire output displacement sequence in eta coordinates

%this is the noise output sequence

eta_1 = filter(bn1,an1,Feta1);%filter gives initial and final condition of
```

```
delay
eta1=eta_1*weigth_un;%mass normalization (meters), mass=1
eta_2 = filter(bn2,an2,Feta2);%filter gives initial and final condition of
delay
eta2=eta_2*weigth_un;%mass normalization (meters)
%this is the signal sequence(no noise)
eta_1s = filter(bn1,an1,Feta1sign);%filter gives initial and final condition
of delay
eta1s=eta_1s*weigth_un;%mass normalization (meters), mass=1
eta_2s = filter(bn2,an2,Feta2sign);%filter gives initial and final condition
of delay
eta2s=eta_2s*weigth_un;%mass normalization (meters)
%save
%tranforming to y and then x coordinates
%noise
y1=A(1)*eta1+A(3)*eta2;
y2=A(2)*eta1+A(4)*eta2;
x1=1/sqrt(mass1)*y1;
x2=1/sqrt(mass2)*y2;
%signal (no noise)
y1s=A(1)*eta1s+A(3)*eta2s;
y2s=A(2)*eta1s+A(4)*eta2s;
```

```
x1s=1/sqrt(mass1)*y1s;

x2s=1/sqrt(mass2)*y2s;

difcoorn=x2-x1;

%difference in the two coordinates (the observable quantity) , just noise

difcoors=x2s-x1s;

%difference in the two coordinates (the observable quantity) , just signal

x_asn=10* 0.07*10^(-16);

x_white_noise =x_asn*randn(nfft,1);

%the squid white noise (comparable size to observable x2-x1)

xnoisetot=difcoorn+x_white_noise;

[spectn,frn]=psd(xnoisetot,nfft,samp_freq,hanning(nfft));

[spects,frs]=psd(difcoors,nfft,samp_freq,hanning(nfft));

figure(5)

semilogy(frn,spectn)

%filtering

%calculating the spectrum

S_xtot2m=spectn/samp_freq;

%the normalized spectral density of the noise

P=S_xtot2m;

s1=(1:(length(P)-1));% here we make a 2 sided

s2=(1:(length(P)-1)); %power spectrum :  psd will be nfft long

P1=P(s1+1)';
```

```
P2(length(P)-s2)=P(s2);

P=[P2,P1];

SXX=P';

PP=[P1,P2];

SXX1=PP';

Sw=x_asn^2*dT;

%Qeta1=Q1;

%Qeta2=Q2;

im=sqrt(-1);

om=2*pi*f1;

G11=cos(theta)^2./(mass1*(om01^2-im*om01.*om/Qeta1-om.^2))

+sin(theta)^2./(mass1*(om02^2-im*om02.*om/Qeta2-om.^2));

G12=-sin(theta)*cos(theta).

*1/(sqrt(mass1*mass2)*(om01^2-im*om01.*om/Qeta1-om.^2))

+sin(theta)*cos(theta)

.*1/(sqrt(mass1*mass2)*(om02^2-im*om02.*om/Qeta2-om.^2));

G22=sin(theta)^2./(mass2*(om01^2-im*om01.*om/Qeta1-om.^2))

+cos(theta)^2./(mass2*(om02^2-im*om02.*om/Qeta2-om.^2));

% the noise spectrum

Sptot=abs(G12-G11).^2*Sfb+abs(G22-2*G12+G11).^2*Sft+Sw;

figure(22)

semilogy(f1,SXX1,'bo-')
```

```
hold on

semilogy(f1, Sptot,'r-')

hold off

save spec_2mode_Sptot_4_3ln Sptot difcoors
```

3.2 Program # 2, Collapse of Events: Stat_events.mat

```
% statistc of collapsed events 2^18 = 1 minute of data%2 mode oscillator

%This subroutine creates a simulated record of data (with a preset

%length between 1-30 sec.)

%creates longer data set n minutes and creates statics of collapsed events

%calculating the spectrum

clear

Eev1_tot=0;

Eev_tot=0;

save f1_sh Eev1_tot Eev_tot


clear Fnoiseb Fnoiset GAMMA BETA BETAy OM A D


xfs=3.1682e-015;;%normalization factor

%xfs= 7.9839e-016;%for less noise

weigth_un=1;

kb=1.3806*10^(-23);%boltzmann constant
```

```
samp_freq =4096; % sampling frequency [1/s]

nfft=2^18;

npts=nfft;

%%% calculate derived paramters

dT = 1/samp_freq; % ''dT'' == the time (s) between samples

df = samp_freq/nfft;% the frequency spacing for ffts

t=linspace(0,2^18*dT,2^18);

f1 = df*[0:nfft/2, (-nfft/2+1):-1];% the storage order of ''fft'' function

%%% specify the parmeters of the damped harmonic oscillator

f0x1 =900; % the nominal frequency of the dho [Hz]

f0x2=900;%the frequency of the transducer;

Q1 =5*10^4; % the nominal quality factor of the dho [dimensionless]

Q2=5*10^4;

mass1 = 1000;

mass2=1;

w1=2*pi*f0x1;

w2=2*pi*f0x2;

k1=mass1*w1^2

k2=mass2*w2^2

b1=mass1*sqrt(k1/mass1)/Q1; %friction coefficients for springs

b2=mass2*sqrt(k2/mass2)/Q2;

%calculating the strength of the forces acting on the detector
```

```
Temp=4*10^-3;%temperature

Sfb=4*kb*Temp*mass1*sqrt(k1/mass1)/Q1;

%spectrum of force noise acting on the bar

Sft=4*kb*Temp*mass2*sqrt(k2/mass2)/Q2;

%spectrum of force noise acting on the transducer

Fb=sqrt(Sfb/(dT))%average size of force in Newtons on bar

Ft=sqrt(Sft/(dT))%average size of force in Newtons on transducer

Fnoiseb=Fb*randn(nfft,1);%this is the time sequence of the noise on the bar

Fnoiset=Ft*randn(nfft,1);%this is the time sequence of the noise on transducer

F1=Fnoiseb-Fnoiset;%this is the noise on x1

F2=Fnoiset;%this is the noise on x2

%force of the signal

mult=10^3;%how many times the signal is bigger than average noise force on

bar

Fsign=mult*Fb;

% size of burst-signal force in Newtons on bar (mult times the average noise

force on bar)

F1sign=[zeros(10,1);Fsign;zeros(nfft-11,1)];

%the signal time sequence (one single force burst acting on bar)

F2sign=zeros(nfft,1);%no force on transducer in this case

%F2sign=[zeros(10,1);Fsign/3;zeros(nfft-11,1)];

%F1sign_many=[zeors(10,1);Fsign;zeros(10,1)];
```

```
%calculating the parameters of the normal modes trough linear algebra
GAMMA=[1/sqrt(mass1) 0;0 1/sqrt(mass2)]%the mass-normalizing Matrix
BETA=[b1 0; 0 b2];
%the matrix of the friction coefficient in x1,x2 coordinates
BETAy=GAMMA*BETA*GAMMA;%transfrornation to y
OM=[-(w1^2+mass2/mass1*w2^2) sqrt(mass2/mass1)
*w2^2;sqrt(mass2/mass1)*w2^2 -w2^2]
%this is the omega matrix ,
%mass the normalized spring constant matrix OM=gamma K gamma
[A,D]=eig(OM);%spring constant and rotation Matrix
A
D
;%transformations to eta coordinates (normal modes coordinates)
BETAeta=A'*BETAy*A
%the friction coefficients matrix in eta1, eta2 coordinates
Qeta1=sqrt(-D(1))/BETAeta(1)%quality factor for normal mode1
Qeta2=sqrt(-D(4))/BETAeta(4)%quality factor for normal mode2
Forcemu=A'*GAMMA;%the transformation matrix for the force
Feta1=Forcemu(1)*F1+Forcemu(3)*F2;
%noise force in eta coordinates
Feta2=Forcemu(2)*F1+Forcemu(4)*F2;
Feta1sign=Forcemu(1)*F1sign+Forcemu(3)*F2sign;
```

```
%sign force in eta coordinates

Feta2sign=Forcemu(2)*F1sign+Forcemu(4)*F2sign;

om01=sqrt(-D(1));%resonant frequency of normal modes

om02=sqrt(-D(4));

f01=om01/(2*pi)

f02=om02/(2*pi)

theta=acos(A(1));

%%% specifing variables in terms of Papoulis H(s) function p.167

alphan1 = om01/(2*Qeta1) ;

betan1 = om01*sqrt( 1 - 1/(4*Qeta1^2) );

An1 = exp(-alphan1*dT)*sin(betan1*dT)/betan1;

bpn1 = 2*exp(-alphan1*dT)*cos(betan1*dT);

cn1 = exp(-2*alphan1*dT);

%%% calculate digital filter constants

bn1 = [0,An1*dT];

an1 = [1,-bpn1,cn1];

%the second mode

alphan2 = om02/(2*Qeta2) ;

betan2 = om02*sqrt( 1 - 1/(4*Qeta2^2) );

An2 = exp(-alphan2*dT)*sin(betan2*dT)/betan2;

bpn2 = 2*exp(-alphan2*dT)*cos(betan2*dT);

cn2 = exp(-2*alphan2*dT);
```

```
%%% calculate digital filter constants

bn2 = [0,An2*dT];

an2 = [1,-bpn2,cn2];

%%% make random force sequence

%f_noisebar =Forceex1(1)*randn(nfft,1);

%f_noiset=Forceex2(2)*randn(nfft,1);

%f_noise_eta1=f_noisebar-f_noiset;%force excting eta1

%f_noise_eta2=f_noiset;

%f_noise = [1; zeros(npts-1,1)];

%% calculate the entire output displacement sequence in eta coordinates

%this is the noise output sequence

eta_1 = filter(bn1,an1,Feta1);

%filter gives initial and final condition of delay

eta1=eta_1*weigth_un;%mass normalization (meters), mass=1

eta_2 = filter(bn2,an2,Feta2);

%filter gives initial and final condition of delay

eta2=eta_2*weigth_un;%mass normalization (meters)

%this is the signal sequence(no noise)

eta_1s = filter(bn1,an1,Feta1sign);

%filter gives initial and final condition of delay

eta1s=eta_1s*weigth_un;%mass normalization (meters), mass=1

eta_2s = filter(bn2,an2,Feta2sign);
```

```
%filter gives initial and final condition of delay

eta2s=eta_2s*weigth_un;%mass normalization (meters)

%save

%figure(1)

%subplot(2,1,1)

%plot(eta1)

%title('eta_1')

%subplot(2,1,2)

%plot(eta2,'r-')

%title('eta_2')

%tranforming to y and then x coordinates

%noise

y1=A(1)*eta1+A(3)*eta2;

y2=A(2)*eta1+A(4)*eta2;

x1=1/sqrt(mass1)*y1;

x2=1/sqrt(mass2)*y2;

%signal (no noise)

y1s=A(1)*eta1s+A(3)*eta2s;

y2s=A(2)*eta1s+A(4)*eta2s;

x1s=1/sqrt(mass1)*y1s;

x2s=1/sqrt(mass2)*y2s;

%figure(2)
```

```
%subplot(2,1,1)

%plot(x1)

%title('x_1')

%subplot(2,1,2)

%plot(x2,'r-')

%title('x_2')

difcoorn=x2-x1;

%difference in the two coordinates (the observable quantity) , just noise

difcoors=x2s-x1s;

%difference in the two coordinates (the observable quantity) , just signal

%figure(3)

%plot(difcoorn,'m-')

%figure(4)

%plot(difcoors,'m-')

difcoors1=[zeros(nfft/2,1);difcoors];

difcoors1=difcoors1(1:nfft);

x_white_noise = 4*10* 0.07*10^(-16)*randn(nfft,1);

%the squid white noise (comparable size to observable x2-x1)

xnoisetot=difcoorn+x_white_noise+difcoors1;

FFTsign=fft(difcoors );

%calculating transfer function G

%Qeta1=Q1;
```

```
%Qeta2=Q2;

im=sqrt(-1);

om=2*pi*f1;

G11=cos(theta)^2./(mass1*(om01^2-im*om01.*om/Qeta1-om.^2))

+sin(theta)^2./(mass1*(om02^2-im*om02.*om/Qeta2-om.^2));

G12=-sin(theta)*cos(theta)./(sqrt(mass1*mass2)*(om01^2-im*om01.*om/Qeta1-om.^2))

+sin(theta)*cos(theta)./(sqrt(mass1*mass2)*(om02^2-im*om02.*om/Qeta2-om.^2));

G22=sin(theta)^2./(mass2*(om01^2-im*om01.*om/Qeta1-om.^2))

+cos(theta)^2./(mass2*(om02^2-im*om02.*om/Qeta2-om.^2));

x_asn=10* 0.07*10^(-16);

Sw=x_asn^2*dT;

Sptot=abs(G12-G11).^2*Sfb+abs(G22-2*G12+G11).^2*Sft+Sw;

Gsignal=G11-G12;

InGsignal=1./Gsignal;

InGsignal2=1./abs(Gsignal).^2;

th=find(f1>700 & f1<1200);

WhtSignalom=InGsignal(th).*FFTsign(th)';

WhtSignalt=ifft(WhtSignalom);

figure(8)

semilogy(f1(th),1./abs( G11(th)-G12(th) ).^2 )

figure(9)

semilogy(f1(th),abs(WhtSignalom))
```

VITA

Giovanni Santostasi was born on February 2, 1967 in Genova, Italy to Saverio and Iolanda Santostasi. He was very interested in science and in particular astronomy since childhood. He built his first telescope at age 11. He graduated in 1986 from the Scientific High School, Liceo Scientifico " E. Fermi", in Genova. He studied in Padova and Bologna Universities in Italy. He received a full scholaship to study in Maharishi International University. He partecipated in undergraduate research in Mathematics and Phyiscs. In 1995 he won a state prize for the "outstanding undergraduate researcher" from the " Mathematical Association of America". He obatined a Bachelor of Science in Phyisics in 1995. He was awarded a graduate assistanship at Louisiana State University and started to work in the Experimetal Gravity Group of Professor W. Hamilton and W. Johnson. He received a Master in Science from LSU in 1999. He is currently a Ph. D. candidate at LSU.